Magazine of Civil Engineering

Online peer-reviewed open-access scientific journal in the field of Civil and Construction Engineering

Founder and Publisher: Peter the Great St. Petersburg Polytechnic University

This journal is registered by the Federal Service for Supervision of Communications, Information Technology, and Mass Media (ROSKOMNADZOR) in 2020. Certificate El No. FS77-77906 issued February 19, 2020.

Periodicity: 8 issues per year

Publication in the journal is open and free for all authors and readers.

Indexing: Scopus, Web of Sceince (ESCI, RSCI), DOAJ, Compendex, Google Academia, Index Copernicus, ProQuest, Ulrich's Serials Analysis System, CNKI

Corresponding address: 29 Polytechnicheskaya st., Saint Petersburg, 195251, Russia

Chief science editor: associate member of RAS, D.S. in Engineering, Vitaly V. Sergeev

Deputy chief science editors:
D.S. in Engineering, Galina L. Kozinetc

D.S. in Engineering, Sergey V. Korniyenko

Executive editor: Ekaterina A. Linnik

Translator, editor: Darya Yu. Alekseeva

DT publishing specialist:
Anastasiya A. Kononova

Contacts:
E-mail: mce@spbstu.ru
Web: http://www.engstroy.spbstu.ru

Date of issue: 03.04.2023

Contents

Contents

Research article

Performance of waste foundry sand concrete in sulfate environment

J. Singh[1] ✉ iD *, R. Siddique[2]* iD

[1] *Chitkara University Institute of Engineering and Technology, Chitkara University, Punjab, India*

[2] *Thapar Institute of Engineering & Technology (Deemed to be University), Patiala, India*

✉ *jagdeep.singh71717@gmail.com*

Abstract. Waste foundry sand is generated by the metal casting industry and has great potential to be used as a construction material. Nearly 70 % of the waste foundry generated is disposed of as a landfill which poses a threat to the surrounding environment. The negative impact of landfill disposal of waste foundry sand on the environment has invited the intentions of research faculty. In this research work, the impact of waste foundry sand as sand replacement on the properties of concrete cured in water as well as sulfate solution were explored. Test results indicate that the compressive strength of concrete cured in sulfate solution decreases with the use of waste foundry sand as partial substitution of natural sand. However, a chloride ion penetration resistance of concrete hikes on the accumulation of waste foundry sand. Up to 56 days, a concrete mixture made up of 15 % waste foundry sand showed optimum strength properties. Ultrasonic pulse velocities through concrete mixtures cured either in water or sulfate solution were almost identical. Energy dispersive spectroscopy analysis showed traces of sulfur in concrete mixtures cured in a sulfate solution.

Citation: Singh, J., Siddique, R. Performance of waste foundry sand concrete in sulfate environment. Magazine of Civil Engineering. 2023. 118(2). Article no. 11801. DOI: 10.34910/MCE.118.1

1. Introduction

Foundry sand (FS) is used to create molds for casting purposes in metal (ferrous and non-ferrous) casting industry. It is recycled and reused number of times till it loses its characteristics of consistency and cleanliness. When the foundry sand becomes unsuitable for reuse to create molds, it is discarded and disposed of as landfill. The non-usable foundry sand generated by foundries is called waste foundry sand. Worldwide, about 100 million tons of waste foundry sand [1] is engendered by the foundries by the year and India is the World's fourth-largest producer of waste foundry sand. Waste foundry is non-hazardous and is black in appearance. The physical properties of waste foundry sand are similar to river sand. The use of waste foundry sand in place of natural river sand will help in protecting the environment by reducing the mining of river sand.

Recently the researchers have made an attempt to utilize waste foundry sand as a substitute for natural sand in a concrete. Some published research studies by Khatib and Ellis [2], Aggarwal et al. [3], Guney et al. [4] and Naik et al. [5] show a decrease in concrete's strength characteristics made up of used foundry sand as a partial substitute of natural river sand. However, according to studies by Basar and Aksoy [6], Prabhu et al. [7], Prabhu et al. [8], and Torres et al. [9] without compromising mechanical properties of a concrete maximum 20 % waste foundry sand can be utilized as a substitute for natural sand. Another study by Mastella et al. [10] also reveals that the reduction in compressive strength of on concrete blocks containing up to 75 % waste foundry sand was not considerable. However, there are some studies by

Etxeberria et al. [11], Singh and Siddique [12], Kaur et al. [13], and Siddique et al. [14] show an increase in strength properties of concrete made with up to 20 % waste foundry sand. An investigation by Siddique et al. [15] exhibits a marginal increase in some strength properties of concrete incorporating waste foundry sand. According to the study by Siddique and Sandhu [16] higher compressive strength can be achieved with 10 % incorporation of used foundry sand in self-compacting concrete and concrete mixtures made with higher substitution levels i.e. 15 and 20 % exhibited lower compressive strength. Most of the studies on the use of waste foundry sand in concrete are focused on strength properties. Limited data is available related to the investigation on resistance of concrete made with waste foundry sand against chemical attacks such as acid, sulfate attack. However, these studies on resistance of concrete against sulfate attack show contradictory findings. According to the study by Prabhu et al. [8] reduction in compressive strength can be observed with the use of used foundry sand in the sulfate environment. Whereas, the study by Thaarini and Ramasamy [17] shows no negative effect on the resistance of geopolymer concrete made with waste foundry sand against sulfate attack. Another study by Smarzewski and Barnat-Hunek [18] indicates an improvement in the resistance of concrete against sulfate with use of waste foundry sand.

Intensive literature is available related to mechanical characteristics of concrete incorporating waste foundry sand. Limited data is available related to durability properties such as resistance of concrete incorporating waste foundry sand against acid and sulfate attack. The present investigation related to concrete has been carried out to assess the impact of waste foundry sand on sulfate resistance. The study evaluates the compressive strength, ultrasonic pulse velocity, chloride ion penetration, expansion, and microstructure of concrete incorporating waste foundry sand cured in water and 10 % sulfate solution.

2. Methods

2.1. Materials

In the study Ordinary Portland cement was used who's specifications are affirming to Indian code IS 8112: 2013. Cements characteristics were gauged as per Indian codes IS 4031(Part 1): 1996 and IS 4031 (Parts 3 to 6) and are presented in Table 1. Coarse aggregates with a maximum size of 20 mm confirming to IS 383:1970, was used. Physical characteristics of natural sand, coarse aggregate, as well as waste foundry sand were evaluated in line with Indian Standards IS 2386 (Part 3):1987 and are mentioned in Table 2. Waste foundry sand's chemical constitution is shown in Table 3. The grain size distribution curves of coarser aggregate, river sand as well as of waste foundry sand are presented in Fig. 1. Waste foundry sand's SEM morphology and EDS analysis is presented in Fig. 2 and 3, respectively. Properties of the sodium sulfate used in the investigation are mentioned in Table 4.
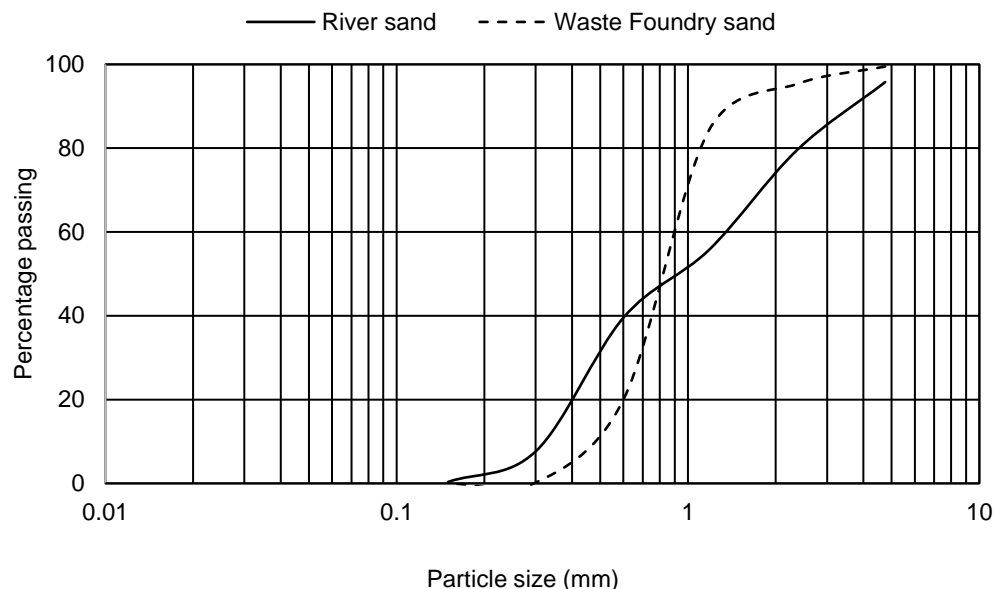
Figure 1. Particle size distribution curves of river sand and waste foundry sand.
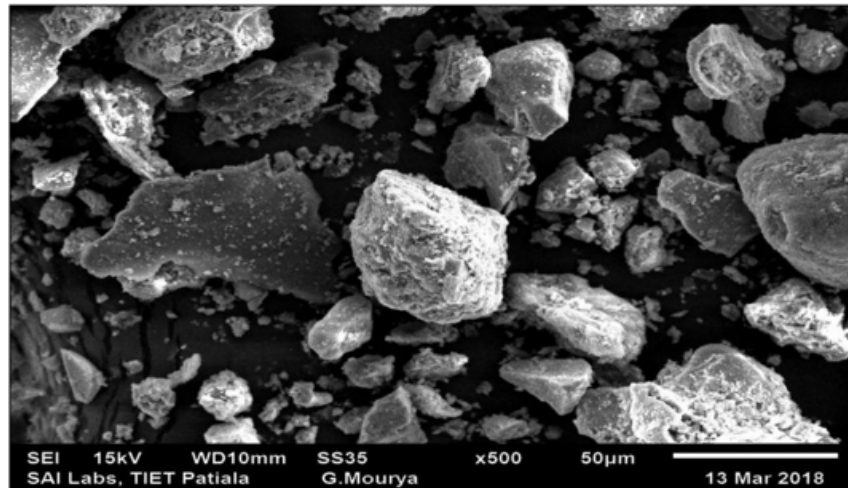
Figure 2. Scanning electron microscopy image of waste foundry sand.
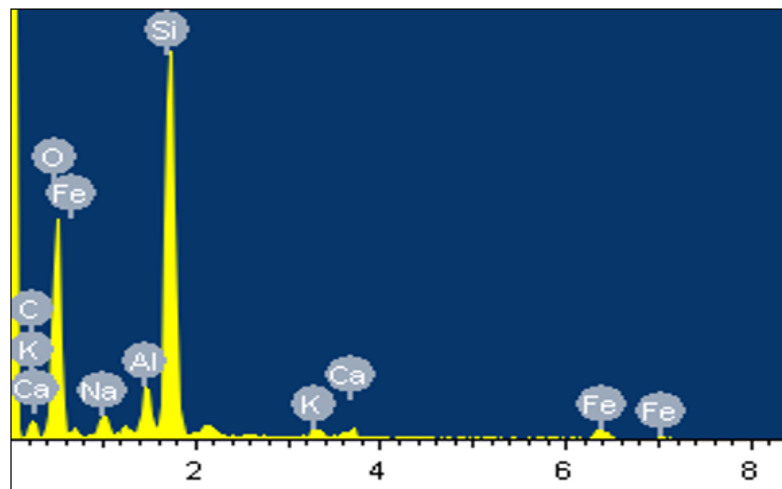
Figure 3. Energy dispersive X-ray spectroscopy chemical characterization spectrum of waste foundry sand.

Table 1. Properties of OPC.

Physical property	Result values	Standard values (BIS 8112: 2013)
Fineness (Retaining on 90 µ Sieve (%))	1.2	10 Max
Standard consistency (%)	29	–
Soundness (mm)	2.7	10 Max
Specific gravity	3.06	–
Initial setting time (min.)	75	30 Min
Final setting time (min.)	235	600 Max
Compressive strength 7-days (MPa)	32.6	33 Min
Compressive strength 28-days (MPa)	41.5	43 Min
Color	Gray	–

Table 2. Physical characteristics of coarse aggregate, river sand and waste foundry sand.

Property	Coarse aggregate		River sand	Waste Foundry sand
	10 mm	20 mm		
Specific gravity	2.68	2.59	2.54	2.8
Water absorption (%)	1.44	1.01	1.03	1.43
Fineness modulus	6.23	6.88	3.21	3.0
Bulk density (kg/m^3)	–	–	1784	1454

Table 3. Chemical properties of waste foundry sand.

Compound	Value (%)
SiO_2	77.22
Al_2O_3	1.84
FeO	8.10
CaO	6.4
TiO_2	0.23
MgO	0.25
Na_2O	2.59
K_2O	1.3
SrO	0.47
MnO	0.08

Table 4. Properties of sodium sulfate.

Property	Value
Chloride (%)	< 0.002
Heavy metals (%)	< 0.001
Arsenic (%)	< 0.0002
Calcium (%)	< 0.005
Iron (%)	< 0.001
Magnesium (%)	< 0.01
Loss on drying at 130ºC	< 1
PH (5% Water)	– 7.5

2.2. Mix proportioning, casting and curing

In the investigation concrete of strength 25 MPa after 28 days was considered as a control concrete and the concrete was designed as per IS 10262: 2009. 5, 10, 15, and 20 % quantity of waste foundry sand was used in the investigation as a substitute for natural river sand. In Table 5 the quantity of ingredients used in the concrete are mentioned. To evaluate the compression strength as well as the ultrasonic pulse velocity of concrete, cubes of size 150 mm were prepared. For determining the chloride-ion permeability cylindrical shaped samples of 200 mm length and 100 mm cross-section were used. Prism specimen of size 75×75×285 mm were cast to determine the expansion of concrete.

Table 5. Mix proportions of concrete.

Concrete mix	Cement (kg/m^3)	WFS (%)	Fine aggregate (kg/m^3)	WFS (kg/m^3)	Coarse aggregate (kg/m^3)		W/C ratio	Water (kg/m^3)
					10 mm	20 mm		
Control concrete (CC)	456.1	0	509.8	0	454.16	681.24	0.42	191.58
FS5	456.1	5	484.31	25.49	454.16	681.24	0.42	191.58
FS10	456.1	10	458.82	50.98	454.16	681.24	0.42	191.58
FS15	456.1	15	433.33	76.47	454.16	681.24	0.42	191.58
FS20	456.1	20	407.84	101.96	454.16	681.24	0.42	191.58

2.3. Testing procedure

Compressive strength was evaluated after proper curing as per Indian standard BIS 516: 1959. The procedure adopted to evaluate chloride-ion permeability was as per ASTM C 1202-12 [29] (Test standards are in Table 6) and the samples were tested after 7, 28, and 56 days. Expansion of concrete and ultrasonic pulse velocity were determined as per ASTM C 1012-10 [30] and ASTM C 597-02 [31], respectively. X-ray diffraction pattern of powdered concrete passing through 60 µm sieve was recorded with X-ray diffractometer with CuKα radiation (λ = 1.54 Å) at diffraction angle 2θ varies from 10° to 70° in steps of 2θ = 0.013°. X'PertHighScore Plus software tool was used to analyze the phases present in concrete. Scanning electron microscope instrument was used to examine the framework of different phases that exists inside the hard concrete.

Table 6. Chloride permeability classification (ASTM C 1202-12) [29].

Charge passed (coulomb)	Chloride permeability
< 100	Negligible
100-1000	Very low
1000-2000	Low
2000-4000	Moderate
> 4000	High

3. Results and Discussion

3.1. Characterization of material

Waste foundry sand is mainly composed of silica (77.22 %), iron oxide (8.14 %), calcium oxide (6.4 %), and aluminum oxide (1.84 %) and small traces of magnesium oxide, manganese oxide, potassium oxide. The fineness modulus and specific gravity of waste foundry sand were 3.0 and 2.8, compared to 3.21 and 2.54 of river sand, respectively. Water absorption of river sand is less comparative to waste foundry sand. The particles of waste foundry sand are sub-angular to angular in shape. Some platy particles of waste foundry sand were observed in the SEM image. The rough-surfaced particles of waste foundry sand improve the bond with the paste. All the above stated information is mentioned in the section 2.1. in detail.

3.2. Compressive strength

3.2.1. Concrete cured in water

Fig. 4 shows the compressive strength of concrete incorporating was as fine aggregates at 7, 28, and 56 days of normal water curing. It is evident from Fig. 4, that the compressive strength of concrete increases with an increase in up to 20 % waste foundry sand content. Concrete mixture FS15 displayed optimum compressive strength at the all curing periods. As compared to control mix (CC), different mixes named as FS5, FS10, FS15, and FS20 shows 1.14 %, 3.42 %, 7.6 %, and 0.8 % more compressive strength at a curing period of only 7-days, respectively. At 28-days, these concrete mixes exhibited compressive strength of 33.8, 34.7, 36.5, and 34.8 MPa, respectively, and the control mix (CC) shows 33.65 MPa strength. At 56-days, concrete mixtures FS5, FS10, FS15, and FS20 showed 3.8 %, 6.2 %, 10 %, and 2.1 %, respectively, higher compressive strength comparative to control mix (CC). The improvement in compressive strength of concrete having waste foundry sand can be attributed to the packing effect of particles of waste foundry sand. At 28-days, hike in the value of compression strength of different concrete mixes FS5, FS10, FS15, and FS20 with respect to that at 7 days was 27.06 %, 27.57 %, 28.97 %, and 31.3 %, respectively, compared to 27.94 % of control mix (CC). Similarly, at an age of 56-days, positive impact on compressive strength was observed as 51.12 %, 29.04 %, 50.05 %, and 43.01 %, respectively, 47.1 % of control concrete as compare to compressive strength at 7-days.
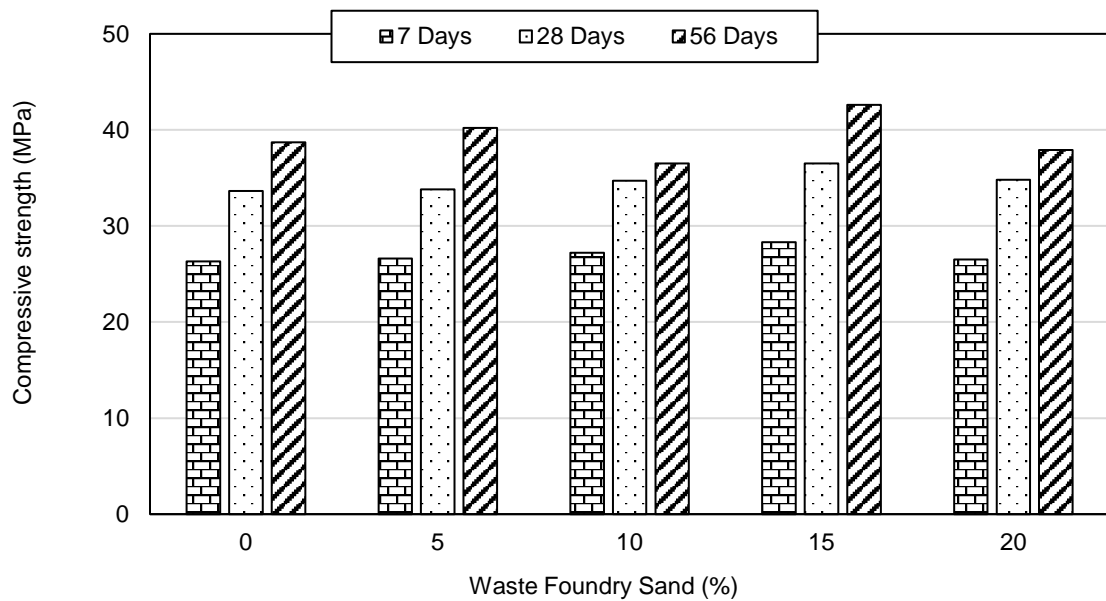
Figure 4. Compressive strength of water cured concrete mixtures.

3.2.2. Concrete immersed in 10 % sodium sulfate solution after initial 28 days of water curing

Concrete's compressive strength comprises of different waste foundry sand content cured in sulfate solution up to 7, 28, and 56 days is presented in Fig. 5. No negative impact of waste foundry sand on concrete's compression strength can be seen in Fig. 5 till 28-days of curing in 10 % sodium sulfate solution. A same increasing trend can be observed in all mixes till 56-days of curing in a sulfate solution. It can be noticed that till the replacement level of 15 %, compressive strength of waste foundry sand concrete improved even after immersion in 10 % sulfate solution up to 56 days. After 7 days of immersion, concrete mixtures FS5, FS10, FS15, and FS20 displayed compressive strength of 30.2, 33.6, 36.7, and 34.6 MPa, respectively and the control mix shows 27.4 MPa strength. Alike fashion was seen even after 28-days of sulfate curing. Hike in compression strength after 28-days sulfate curing of different mixes FS5, FS10, FS15 and FS20 with respect to control concrete was 6.60 %, 8.70 %, 16.81 % and 15.31 %, respectively. Strength of concrete mixes CC, FS5, FS10, FS15, and FS20 were 44.5, 41.1, 42.8, 44.6, and 39.2 MPa after 56-days of sulfate curing. From the results, it can be contemplated that concrete containing waste foundry sand shows more compressive strength even beyond 28-days of curing in sulfate medium. The concrete mixture FS15 exhibited optimum compressive strength at all the periods of curing in 10 % sulfate solution. This trend of compressive strength in all concrete mixtures indicates that the hydration process continued even during immersion in 10 % sodium sulfate solution.
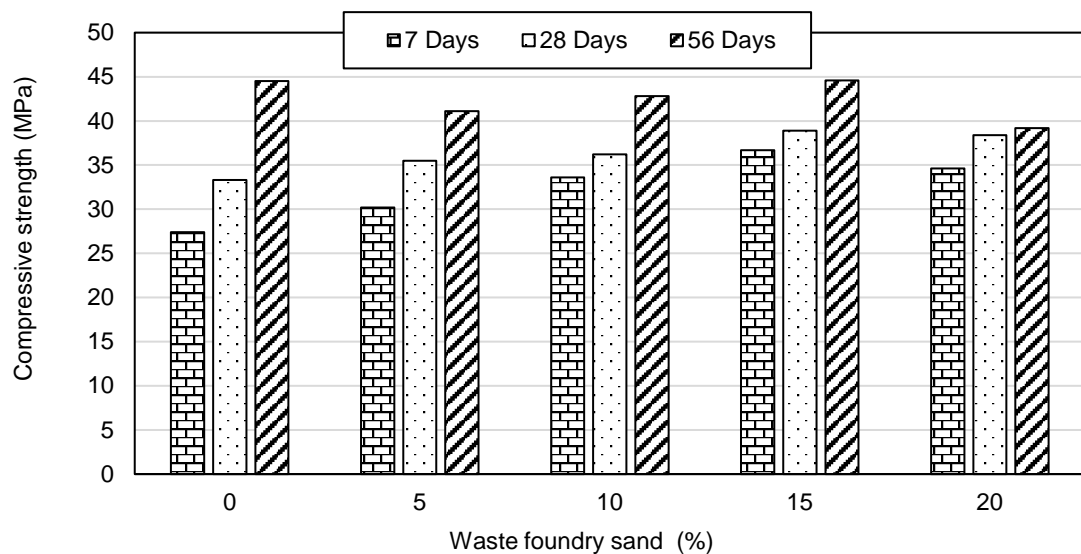
Figure 5. Compressive strength of concrete mixture after immersion in 10% sulfate solution.

3.2.3. Comparison of compressive strength of concrete cured in 10% sodium sulfate and normal water after initial water curing of 28 days

Before determining the compressive strength, all the concrete samples were firstly cured in normal water for 28-days and then some of the samples were water cured and some of they were cured in 10 % sodium sulfate solution, results are shown in Fig. 6 to 7. At 35 days of the total age of curing i.e. water curing for 28-days and sulfate curing for 7-days, concrete mixtures control concrete, FS5, FS10, FS15 and FS20 showed a decrease of 24.31, 19.25, 10.16, 3.4, and 5.72 % in compressive strength comparative to corresponding concrete mixtures cured in normal water. Similarly, at 56 days of age i.e. 28-days of water curing and 28-days of 10 % sulfate curing, a decrease in compression strength of these concrete mixes were 13.95, 11.69, 11.92, 8.69 and 1.28 % relative to those concrete samples which were normal water cured. At 84 days of age, the margins in concrete's compressive strength after water and 10 % sulfate solution curing reduced to 2.84, 3.29, 1.38, 4.29, and 2.73 %, respectively. In both types of curing conditions results reveal a similar trend of increase in compressive strength. But a rise in compressive strength of 10 % sulfate solution cured concrete was comparatively less than that of normal water cured concrete. It could be due to higher concentration of sulfate solution which may lead to more absorption of sulfate ions by C-S-H gel and thus make C-S-H gel of lower quality i.e. binding ability of the gel reduces [32]. High sulfate content also hinders in early hydration of binder or C_3A and thus results in lesser compressive strength [33, 34].

Figure 6. Compressive strength of concrete mixture after immersion in 10% sulfate solution and water at total age of 56 days.
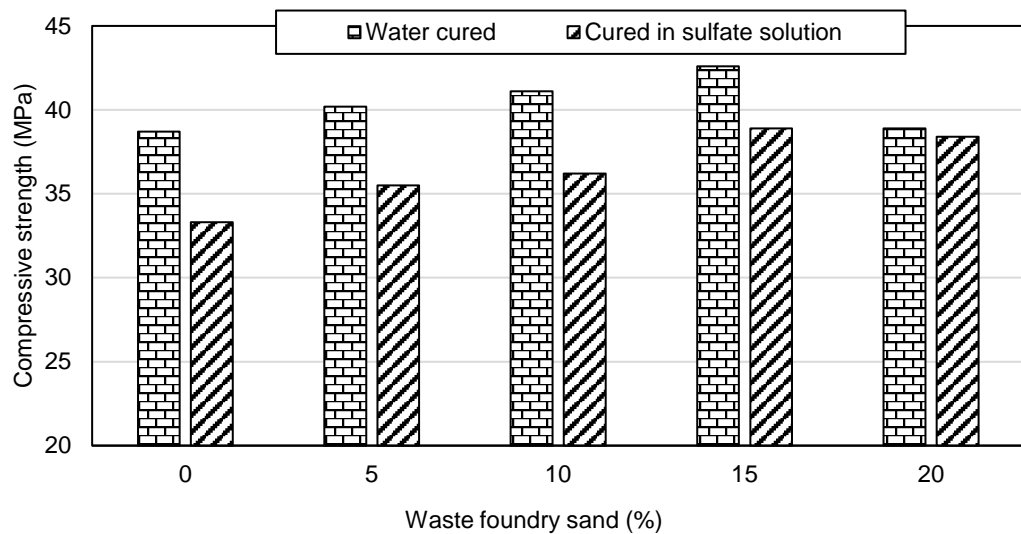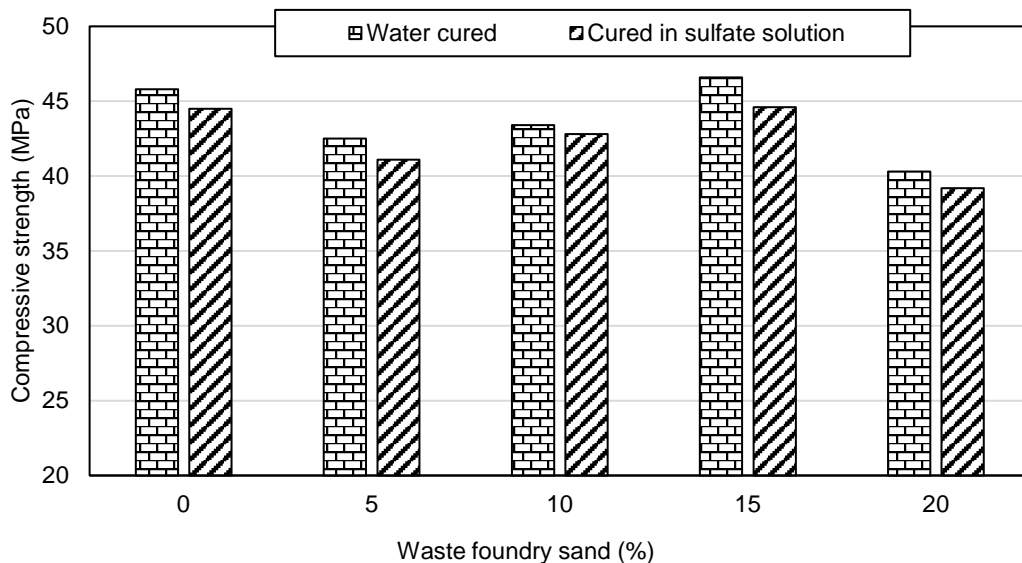

Figure 7. Compressive strength of concrete mixture after immersion in 10% sulfate solution and water at total age of 56 days 84 days.

3.3. Expansion of concrete specimens

3.2.4. Concrete cured in sulfate solution

Change in dimensions of a concrete specimen is a key factor to assess the impact of sulfate attack. The change in length of prism specimens of various concrete mixtures cured in 10 % sulfate solution after initially curing in water for 28 days is presented in Fig. 8. After curing for 28-days in 10 % sulfate solution, control concrete FS5, FS10, FS15 and FS20 exhibited expansion strain of 87.72×10^{-6}, 70.175×10^{-6}, 70.175×10^{-6}, 52.631×10^{-6} and 94.736×10^{-6}, respectively. After 56 days of immersion these figures increased to 105.263×10^{-6}, 87.72×10^{-6}, 98.245×10^{-6}, 70.175×10^{-6} and 105.263×10^{-6}, respectively.

As per the test results mixture FS15 exhibited minimum expansion whereas control concrete and FS20 mixtures showed maximum expansion after 56 days of immersion. The expansion of concrete cured in sulfate solution occurs due to formation of ettringites inside concrete on reaction with sulfate ions, these by-products formed so are expansive or swallowing in nature, so it may cause an expansion in concrete.
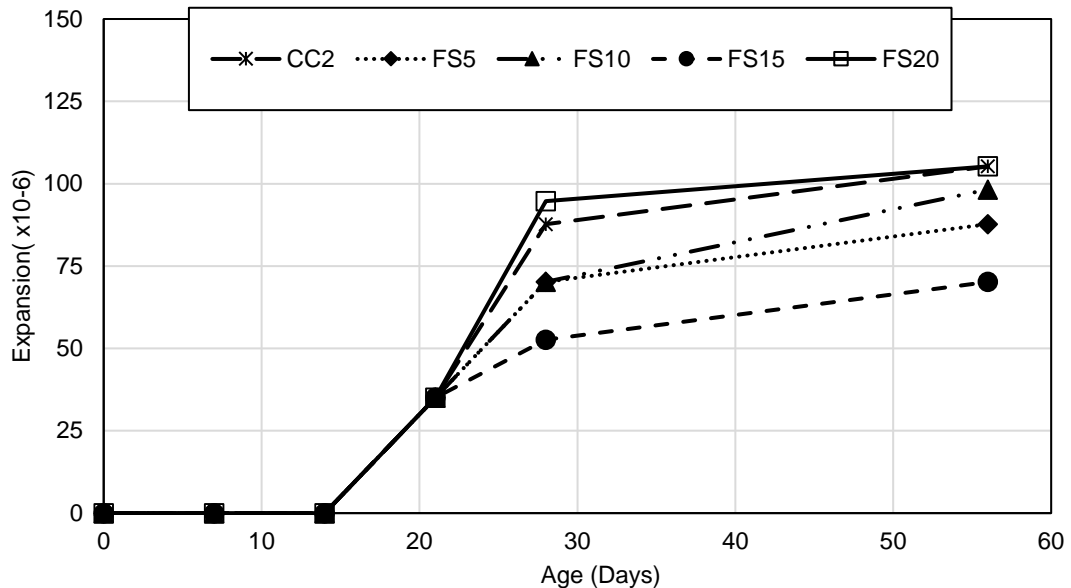
Figure 8. Concrete's expansion after cured in 10% sulfate solution.

3.2.5. Comparison of expansion of concrete cured in 10 % Sodium Sulfate and Water

Expansion of concrete prisms was also examined under water curing in a similar way as was done for concrete mixtures cured in 10 % sodium sulfate. After 84 (28+56) days of total age, control concrete, FS5, FS10, FS15 and FS20 cured in water exhibited expansion strain of 45.614×10^{-6}, 35.087×10^{-6}, 45.614×10^{-6}, 45.614×10^{-6} and 70.175×10^{-6}, compared to 105.263×10^{-6}, 87.72×10^{-6}, 98.245×10^{-6}, 70.175×10^{-6} and 105.263×10^{-6} expansion strain shown by these concrete mixes after curing in 10 % sulfate medium for a period of 56-days prior to this, 28-days normal water curing was done. The difference in expansion of concrete mixtures cured in sulfate solution and water can be considered as the expansion due to the action of sulfate. Afterward 56-days of 10 % sulfate solution curing, the net expansion of concrete mixes FS5, FS10, FS15, and FS20 due to sulfate attack was 52.633, 52.631, 24.561 and 35.088, respectively, compared to 59.649 of control concrete.

3.4. Chloride ion permeability

3.2.6. Concrete cured in water

The test results of Waste foundry sand concrete are presented in Fig. 9. It can be observed in Fig. 9 that with an increase in age and with the inclusion of waste foundry sand, chloride ion permeability reduces. Concrete mixture FS15 displayed the lowest chloride ion permeability at all the curing ages. Concrete mixes FS5, FS10, FS15, and FS20 showed 4.65, 14.95, 23.27, and 25 % reduction in total charge passed compared to that of control concrete after 7-days of curing. At 28-days of curing, charge flows across concrete mixes were 2196, 2078, 2042, and 2140 Coulomb, respectively, compared to 2205 Coulomb for control concrete (CC). At 56-days there was 9.57 %, 15.65 %, 20.37 %, and 12.4 %, reduction in charge flow in concrete mixes, compared to control concrete. With an increase in age from 7 days to 28 days of different concrete mixes, the reduction in charge flow was 37.7 %, 35 %, 31.05 %, 24.9 % and 19.45 % respectively. Similarly, at 56 days, chloride ion passing ability through these concrete mixtures reduced by 41.95 %, 44.95 %, 42.43 %, 39.75 % and 32.18 % compared to that at 7 days.
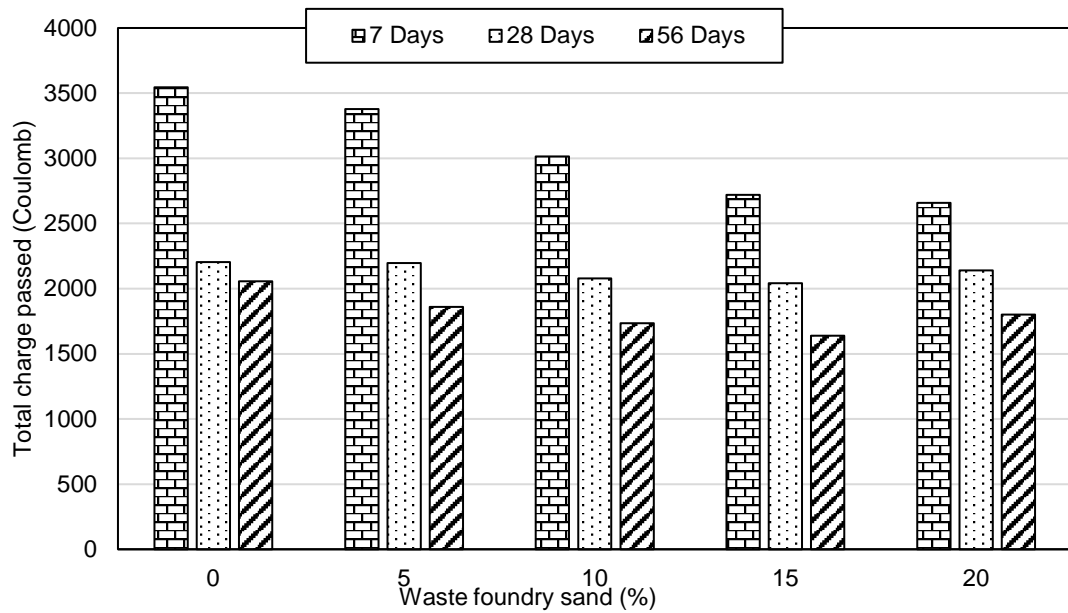
**Figure 9. Total charge passed through concrete mixtures cured
in water.**

3.2.7. Concrete immersed in 10 % sodium sulfate solution after initial 28 days of water curing

In Fig. 10 results of chloride ion permeability are shown, in which concrete mixes were firstly water cured for 28-days and then cured in 10 % sodium sulfate solution. Total charge passed through control concrete, FS5, FS10, FS15 and FS20 was 2125, 1998, 1822, 1668, and 1688 Coulomb, respectively, after 7-days of sulfate curing. Charge flows through concrete mixes was 1822, 1725, 1728, 1503 and 1561 Coulomb, respectively after 28-days of sulfate curing. Similarly, after 56-days of immersion, charge flow were 1522, 1199, 829, 811, and 964 Coulomb, respectively. According to ASTM C 1202-12 [29], after 7 and 28 days of immersion, concrete mixtures showed moderate chloride ion permeability. After 56 days of immersion, control concrete and concrete mixture FS5 showed low chloride ion permeability whereas concrete mixtures FS10, FS15, and FS20 exhibit very low chloride ion penetration in line with ASTM C 1202-12 [29]. The reduction in charge passing ability may be as sulfate solution penetrate inside microstructure of concrete and then sulfate particles may crystallize inside concretes voids or fissure and make concrete more impermeable.
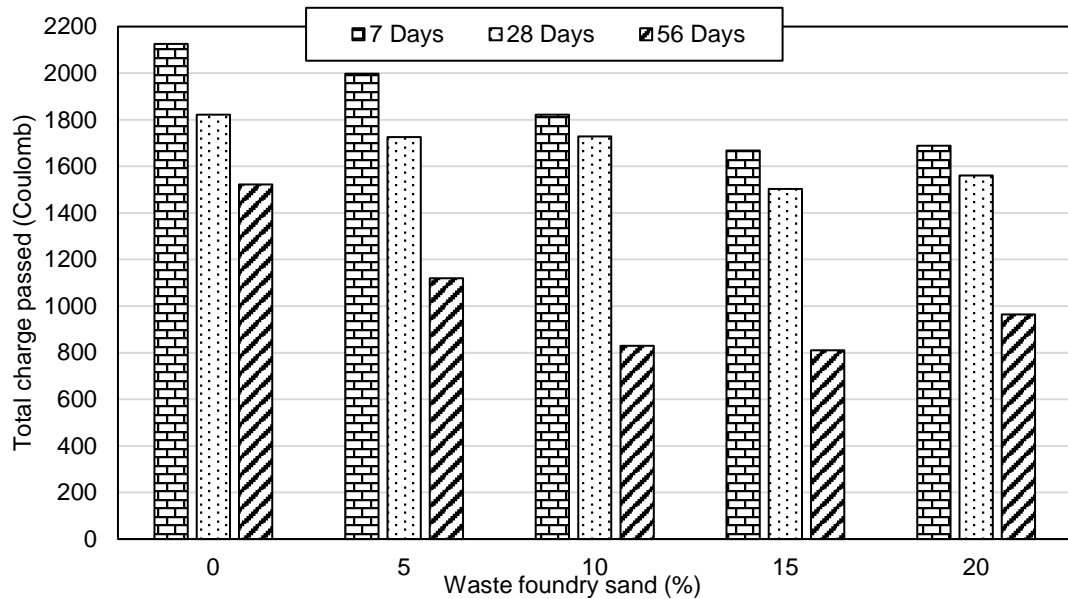
**Figure 10. Total charge passed through concrete mixtures cured
in 10% sulfate solution after initial water curing of 28 days.**

3.2.8. Comparison of chloride ion permeability of concrete cured in 10 % sulfate solution and water

To compare the chloride ion permeability of concrete mixtures cured in water and in 10 % sulfate solution, rapid chloride penetration tests were performed on different concrete mixes at an equivalent age. Total charge passed through concrete mixtures immersed in sulfate solution and cured in water are presented in Fig. 11 and 12. At 35 days of total curing age i.e. 28-days of initial water curing after that 7 days of sulfate curing, charge flow though control concrete, FS5, FS10, FS15, and FS20 was 2125, 1998, 1822, 1668, and 1688 Coulomb, respectively. When these concrete mixture was cured in water up to 35 days, the values of charge passed were 2168, 1908, 1889, 1702 and 1722 Coulombs, respectively. Similarly, at 84 days of total curing age, total charge passed through control concrete, FS5, FS10, FS15, and FS20 immersed in sulfate solution was 1522, 1119, 829, 811, and 964 Coulombs compared to 1481, 1407, 1238, 1189, and 1473 coulomb of charge passed through concrete mixtures cured in water. In both types of curing, a concrete mixture containing 15 % waste foundry sand displayed the lowest total charge passed.

After total curing of 56-days, mixes FS5, FS10, FS15, and FS20 cured in 10 % sulfate solution showed a decrease of 7.25, 6.5, 11.74, and 8.66 % in total charge passed comparative to corresponding concrete mixtures cured in normal water, respectively. The control concrete mixture displayed 8.8 % decrease in total charge passed when immersed in 10 % sulfate solution compared to charge flows through a water cured sample of concrete. Similar trend of decrease in chloride permeability was noticed after 84-days of curing. Less charge penetration through different concrete mixes cured in sulfate solution may be due to the formation of ettringite along with hydrates of calcium silicate in empty spaces in concrete microstructure and thus making the concrete more non-porous. Sulfate particles may also crystallize in voids in concrete and make the concrete more impermeable.
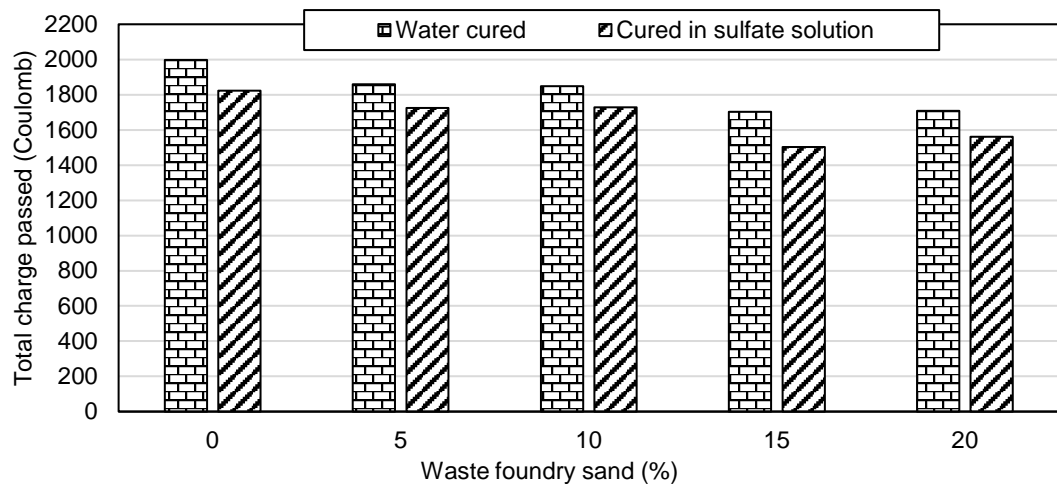
Figure 11. Total charge passed through concrete mixtures cured in water and 10% sulfate solution at total age of 56 (28+28) days.
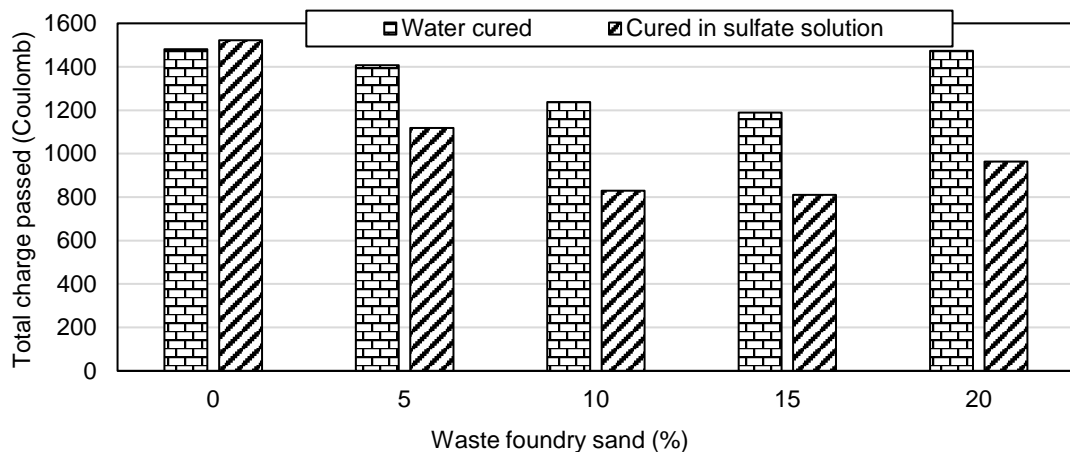
Figure 12. Charge flow through concrete mixes cured in water as well as in 10% sulfate solution at total age of 84 (28+56) days.

3.5. Ultrasonic Pulse Velocity

3.2.9. Concrete cured in water

Pulse velocity values of concrete incorporating waste foundry sand as a substitute of river sand are presented in Table 7. Concrete mixtures FS15 displayed optimum value of ultra-sonic pulse velocity at all curing ages. However, there were no major changes observed in pulse velocity values with the use of waste foundry sand in concrete. After 7-days of curing increase in the value of pulse velocity of different concrete mixes FS5, FS10, FS15, and FS20 were 0.32, 0.40, 0.73, and 0.32 % compared to that of control concrete. At 28 days of curing age, pulse velocity of waste foundry sand concrete mixtures was 6220, 6260, 6280, and 6255 m/s, compared to 6200 m/s of control concrete, respectively. At 56 days of curing age, pulse velocity of waste foundry sand concrete mixtures was higher by 0.47 %, 0.79 %, 1.26 %, and 0.79 % than that of control concrete. With the rise in curing duration from 7 days to 56 days, waste foundry sand concrete mixtures displayed 2.66 %, 2.9 %, 3.0 %, and 2.98 % increase in pulse velocity compared to control concrete whose rise is 2.5 %. Higher values of pulse velocity indicate that denser the microstructure of concrete mixtures.

Table 7. Comparison of pulse velocity of concrete mixtures immersed in 10% sodium sulfate solution after initial 28 days water curing and cured in water.

Age (days)	Sodium sulfate curing					Water curing				
	Pulse velocity (m/s)									
	CC	FS5	FS10	FS15	FS20	CC	FS5	FS10	FS15	FS20
28+7	6325	6333	6330	6360	6320	6300	6330	6360	6360	6272
28+28	6380	6380	6369	6440	6360	6335	6360	6380	6410	6360
28+56	6580	6580	6580	6610	6490	6520	6580	6520	6640	6520

3.2.10. Concrete immersed in 10 % sodium sulfate solution after initial 28 days of water curing

Pulse velocity values of concrete mixtures cured in 10 % sodium sulfate after the initial 28 days of water curing are mentioned in Table 7. Experimental results show that ultrasonic pulse velocity value increases with the rise in curing duration. However, it was observed that the pulse velocity of waste foundry sand concrete and control concrete as well, was almost the same at every age of immersion in a sulfate solution. This may be due to the reason that the sulfate particles may crystallize inside concretes voids and make concrete more impermeable and denser.

#### 3.2.11. Comparison of pulse velocity of concrete cured in 10 % sulfate solution and water

To compare the pulse velocity of concrete mixtures cured in water and in 10 % sulfate solution, ultrasonic pulse velocity tests were performed on concrete specimens cured in water at an equivalent age. The pulse velocity of concrete mixtures immersed in sulfate and cured in water are presented in Table 7. It is evident from the Table 7 that no major change in the pulse velocities of different concrete mixes cured either in normal water or in 10 % sulfate solution at every equivalent age. After 7-days of 10 % sulfate curing, concrete mixes FS5, FS10, FS15, and FS20 displayed pulse velocity of 6333, 6330, 6360, and 6320 m/s, respectively, compared to 6325 m/s for control concrete. These concrete mixtures, when cured in normal water for total duration of 35 days, displayed pulse velocity of 6330, 6360, 6360 and 6272 m/s, respectively, compared to 6300 m/s for control concrete. According to IS 13311 (part-1): 1992 [(Standards are mentioned in Table 8), the quality of concrete mixtures either immersed in sulfate solution or cured in water can be termed as excellent at all the ages.

Table 8. Pulse velocity as concrete's quality grading (BIS 13311 (part-1)).

Pulse velocity (km/sec)	Concrete quality grade
> 4.5	Excellent
3.5-4.5	Good
3.0-3.5	Medium
< 3.0	Doubtful

3.6. Microstructure Analysis

Scanning electron microscopy, as well as Energy Dispersive Spectroscopy analysis, were performed on a small fractured sample of control concrete and concrete specimens FS5, FS10, FS15, and FS20 after 28 days of sodium sulfate curing and normal water curing. The specimens were placed on the SEM stubs and the gold layer was applied over it. To determine chemical compositions of different phases of concrete microstructure EDS was performed which approximately tells about the oxide composition of different compounds. Fig. 13 and 14 show SEM micrographs and EDS spectrum of control concrete mixture cured

in 10 % sulfate solution. Fig. 15 and 16 show SEM micrographs and EDS spectrum of concrete mixture FS15 cured in 10 % sulfate solution. Fig. 17 and 18 show SEM micrographs and EDS spectrum of concrete mixture FS15 cured in water. The major phases present in concrete were Calcium silicate hydrate (CSH), Portlandite (Ca(OH)$_2$) and ettringnites etc. CSH looks like fibrous flakes, blocky mass, granular etc., calcium hydroxide appears like platy crystals and ettringnite were like a needle in shape. The morphologies of different phases have been identified and marked on SEM images. SEM images of concrete mixtures show CSH gel is uniformly scattered throughout the images. According to the study by Gurumoorthy and Arunachalam (2016) [36] CSH gel formation in concrete improves on the inclusion of waste foundry sand.
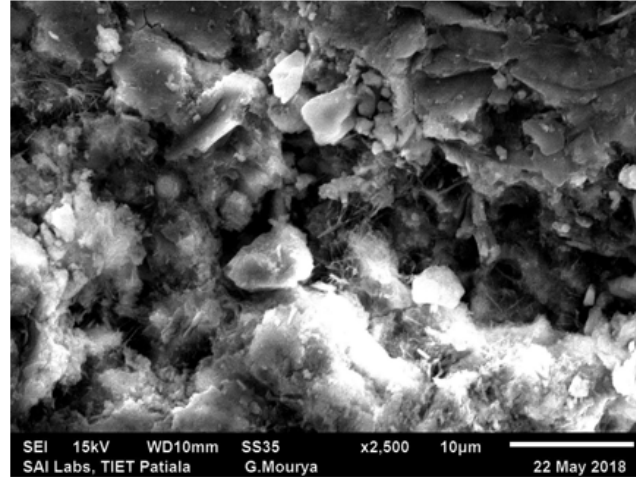
Figure 13. Scanning electron microscopy image of control concrete (CC) after 28 days of curing in sulfate solution after initial curing in water.
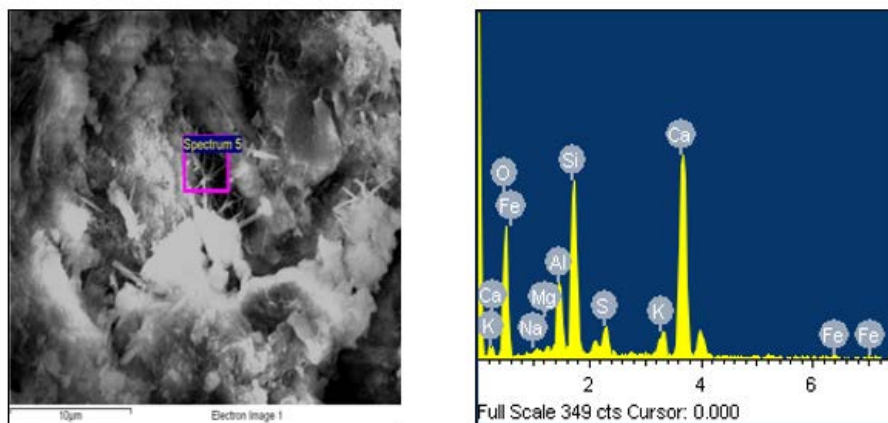
Figure 14. Energy dispersive X-ray spectroscopy spectrum of control concrete (CC) after 28 days of curing in sulfate solution after initial curing in water.
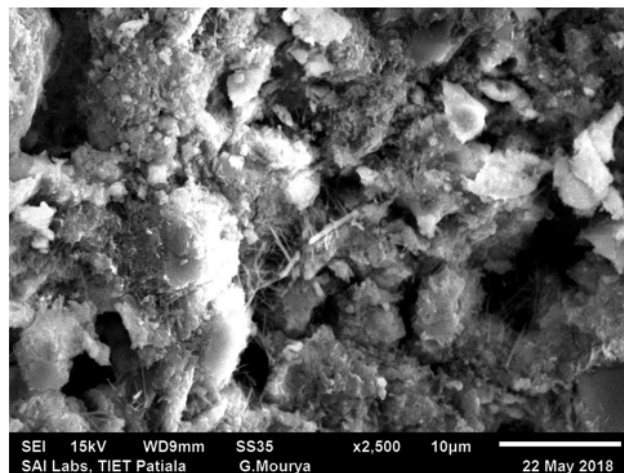
Figure 15. Scanning electron microscopy image of FS15 after 28 days of curing in sulfate solution after 28 days of initial water curing.
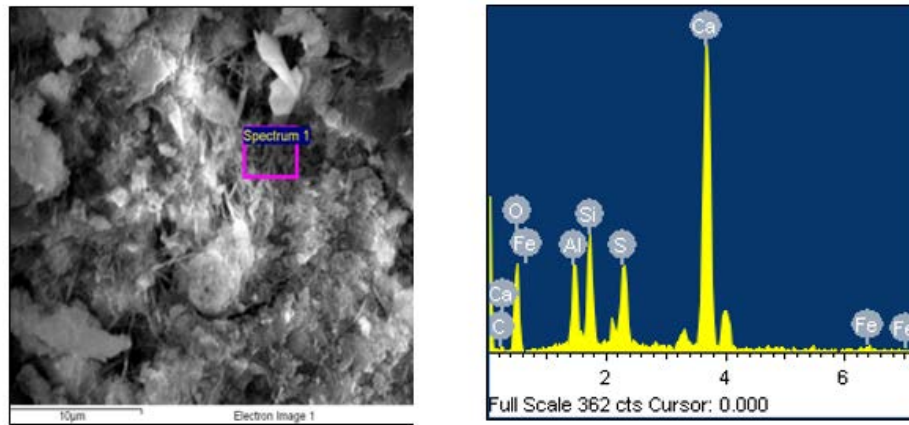
Figure 16. Energy dispersive X-ray spectroscopy spectrum of SF15 after 28 days of curing in sulfate solution after initial water curing.
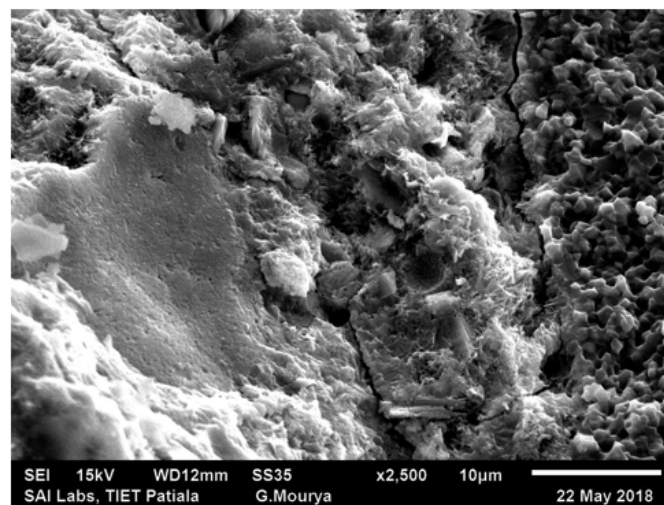
Figure 17. Scanning electron microscopy image of SF15 after 56 (28+28) days of water curing.
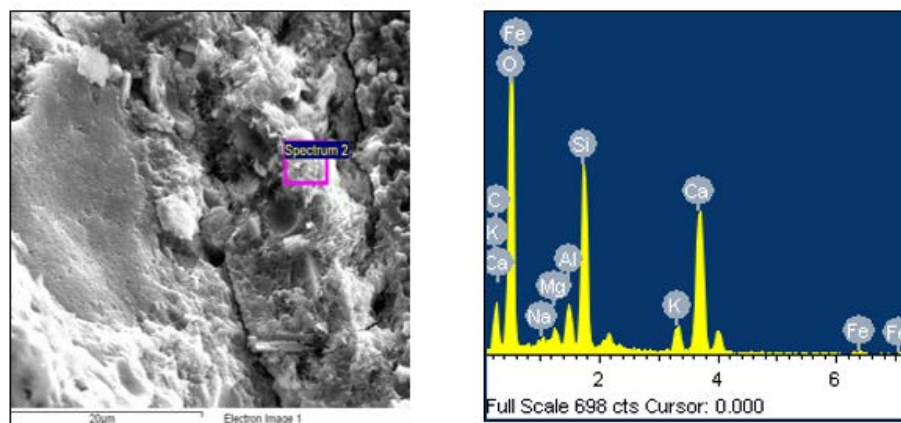
Figure 18. Energy dispersive X-ray spectroscopy spectrum of SF15 concrete after 56 (28+28) days of water curing.

Chemical characterization of concrete mixtures was determined at four/five locations on each sample by energy dispersive X-ray spectroscopy (EDS). The results of the elemental analysis carried out using EDS are presented in Table 9. The results show that no sulfur traces were detected in concrete mixtures except control concrete cured in water. Whereas, elemental analysis of concrete mixtures immersed in 10 % sulfate solution shows the presence of sulfur traces in all the concrete mixtures. Sulfur traces were detected at all the locations on control concrete, FS15, and FS20 concrete mixtures after sulfate curing. In the case of a concrete mixture FS10, sulfur traces were detected at three out of four locations. However, sulfur traces were detected at only one location on concrete mixture FS5 after immersion in a sulfate

solution. Traces of sulfur detected by EDS analysis in concrete mixtures immersed in sodium sulfate solution shows that sulfate ion (SO_4^{2-}) entered inside a concrete microstructure.

Table 9. Chemical configuration of concrete after sulfate solution and water curing.

Element	Cured in 10 % sodium sulfate solution					Cured in water				
	Maximum / minimum composition by weight (%)									
	CC	FS5	FS10	FS15	FS20	CC	FS5	FS10	FS15	FS20
Ca	30.63/ 16.96	27.38/ 17.31	53.40/ 2.58	41.28/ 25.34	32.27/ 19.97	43.45/ 20.15	23.19/ 5.57	48.77/ 16.72	17.26/ 17.11	31.98/ 18.97
Si	14.72/ 9.53	12.88/ 8.77	22.50/ 7.26	11.86/ 6.92	19.89/ 0.82	8.73/ 1.68	14.74/ 4.68	19.80/ 4.62	11.01/ 9.67	12.48/ 8.78
Al	6.33/ 2.66	5.38/ 1.70	16.98/ 2.66	4.67/ 2.60	13.10/ 2.71	2.51/ 0.42	11.21/ 2.12	7.7/ 0.88	5.26/ 2.21	4.17/ 2.32
K	2.73/ 1.17	2.01/ 1.09	2.66/ 2.33	1.59/ 1.46	2.32/ 1.82	3.62/ 0.07	1.35/ 0.74	–	2.62/ 1.69	2.24/ 1.48
O	59.85/ 45.49	60.31/ 51.63	49.97/ 23.94	52.28/ 36.56	57.47/ 41.44	55.86/ 51.34	60.23/ 53.47	52.17/ 34.42	61.92/ 59.02	56.92/ 49.22
C	8.29/ 0.88	10.13/ 0.79	6.66/ 1.68	3.10/ 1.34	4.71/ 2.93	8.25/ 1.59	5.71/ 0.58	7.99/ 3.35	6.13/ 0.25	0.46/ 0.13
S	2.47/ 0.56	1.46/ 0.0	7.0/ 1.65	6.37/ 0.81	2.37/ 0.42	0.31/ 0.10	–	–	–	0.57/ 0.0
Mg	0.78/ 0.26	0.67/ 0.19	1.13/ 0.46	0.76/ 0.18	1.59/ 0.10	0.89/ 0.11	1.49/ 0.14	0.30/ 0.08	0.76/ 0.63	2.77/ 0.27
Fe	3.14/ 0.72	3.38/ 0.96	3.04/ 0.62	1.91/ 1.20	2.56/ 1.43	0.91/ 0.0	25.99/ 1.17	4.01/ 0.41	1.68/ 1.07	4.29/ 2.67
Na	0.43/ 0.14	0.15/ 0.05	0.45/ 0.19	0.41/ 0.15	0.71/ 0.05	0.47/ 0.35	0.15/ 0.09	0.23/ 0.0	0.33/ 0.22	0.53/ 0.16

Fig. 19 to 22 present the XRD spectrum of concrete mixtures. The XRD spectrum of concrete mixtures shows weak peaks of ettringite and no peak of gypsum and thaumasite which indicates that no major damage was caused by sulfate attack till 28-days. Most commonly compounds seen in the analysis are quartz (Q), portlandite (P), CSH gel (CSH), calcite (C), and ettringnite (E). The presence of CH indicates the hydration process of cement and the absence of gypsum indicates that no reaction taken place between sulfate ions and portlandite in all sulfate cured samples. It can also be predicted that CSH gel absorbs sulfate ions and thus degrades its quality and binding ability, due to this content of sulfate ions reduced in the solution and thus gypsum will not form and $Ca(OH)_2$ remain unreacted [34].
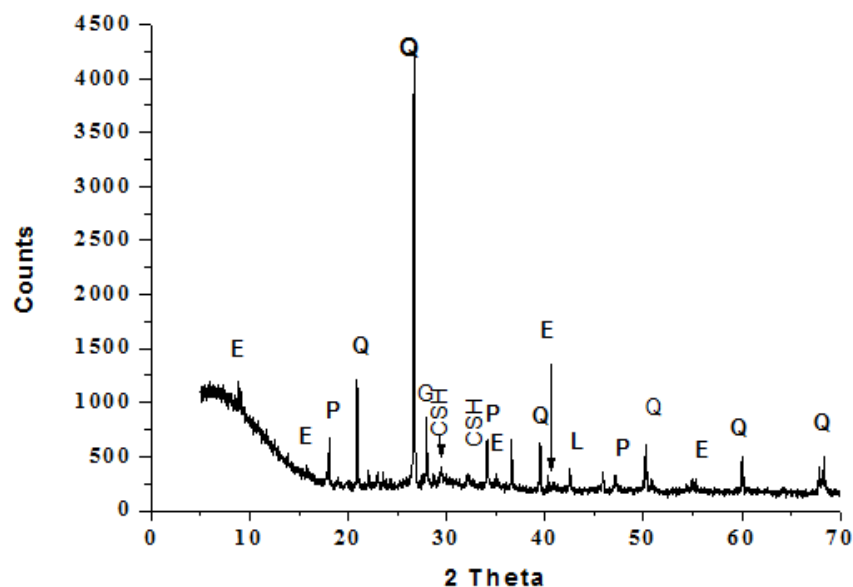
Figure 19. XRD spectrum of control concrete cured in sulfate solution for 28 days after curing in water for 28 days (E is Ettringite, Q is Quartz, P is Porlandite, C is Calcite, CSH is Calcium silicate hydrate, G is Gismondine).
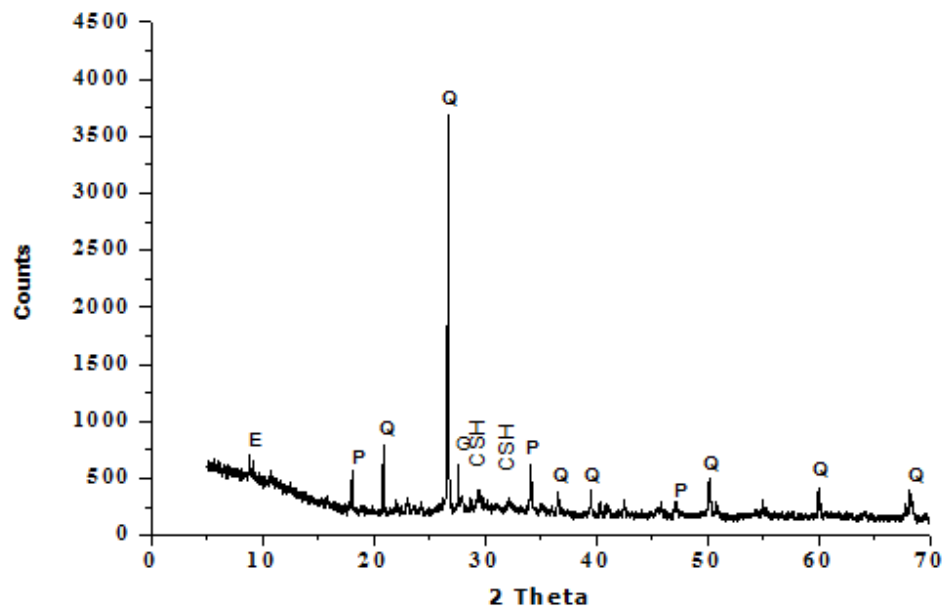
Figure 20. XRD spectrum of SF15 concrete cured in sulfate solution for 28 days after curing in water for 28 days (E is Ettringite, Q is Quartz, P is Porlandite, C is Calcite, CSH is Calcium silicate hydrate, G is Gismondine).
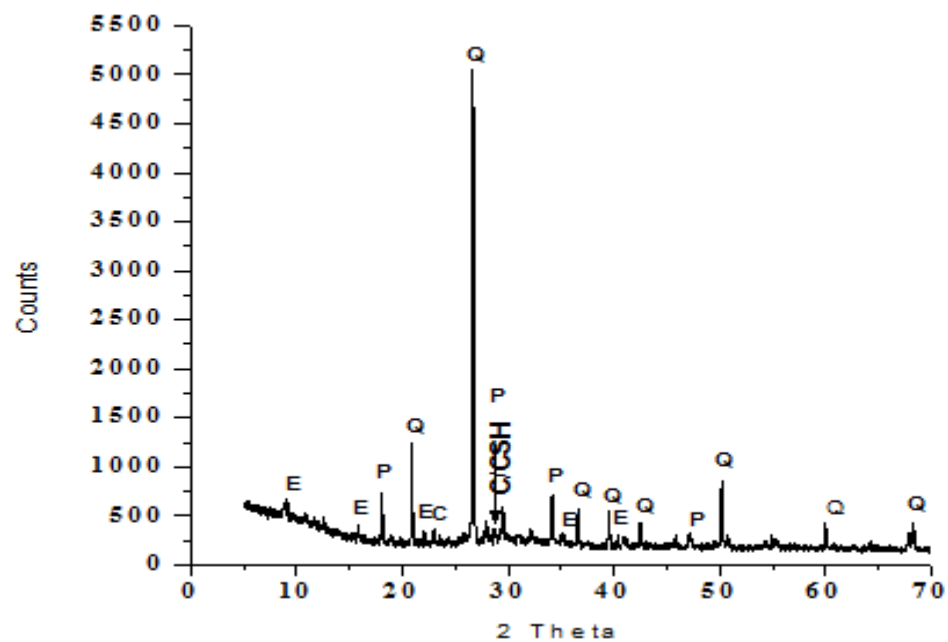
Figure 21. XRD spectrum of control concrete at 56 (28+28) days of water curing (E is Ettringite, Q is Quartz, P is Porlandite, C is Calcite, CSH is Calcium silicate hydrate, G is Gismondine).
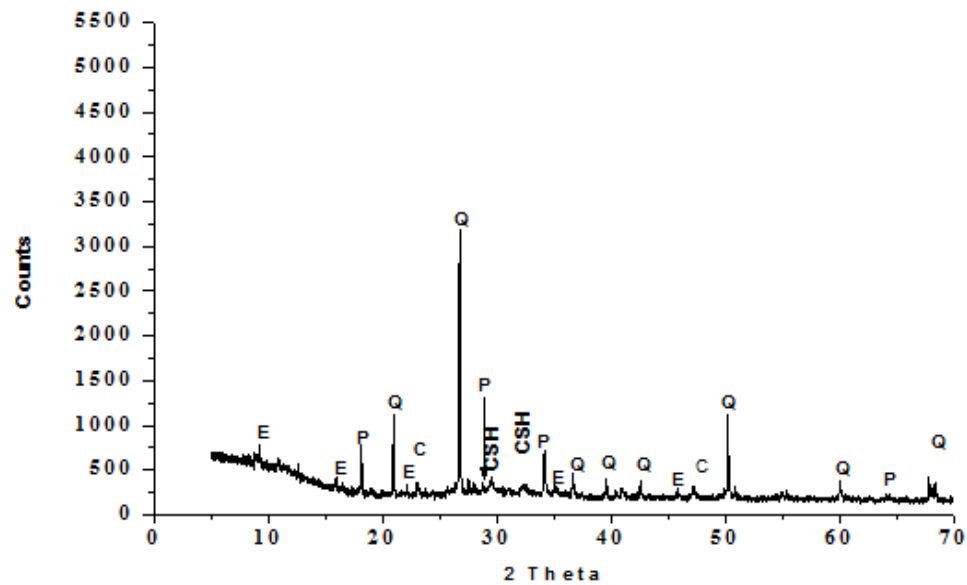
**Figure 22. XRD spectrum of SF15 concrete at 56 (28+28) days of water curing
(E is Ettringite, Q is Quartz, P is Porlandite, C is Calcite, CSH is Calcium silicate hydrate,
G is Gismondine).**

4. Conclusion

1. At all ages very slight change can be noticed in compressive strength values of control concrete and concrete containing maximum up to 20 % of waste foundry sand. As per results concrete containing 15 % waste foundry sand shows optimum results. Concrete mixtures cured in sulfate solution showed lower compressive strength compared to that of corresponding water cured concrete mixture at the same age.

2. Charge passing ability of water cured concrete mixtures reduces with the use of waste foundry sand at all the ages of curing. Concrete mixtures cured in sulfate solution displayed improvement in resistance against chloride ion penetration corresponding to water cured concrete mixtures at the same age.

3. No noteworthy variation in the ultrasonic pulse velocity of cured concrete mixtures in both water and sulfate solutions were observed.

4. Expansion of concrete mixtures cured in sulfate solution up to 56 days was greater than that of corresponding normal water cured concrete mixtures.

5. The Energy Dispersive Spectroscopy analysis validates the presence of sulfate ions in the concrete after immersion in a sulfate solution.

References

1. Carnin, R.L.P., Folgueras, M.V., Luvizão, R.R., Correia, S.L., da Cunha, C.J., Dungan, R.S. Use of an integrated approach to characterize the physicochemical properties of foundry green sands. Thermochimica Acta. 2012. 543. Pp. 150–155. DOI: 10.1016/j.tca.2012.05.018

2. Khatib, J.M., Ellis, D.J. Mechanical Properties of Concrete Containing Foundry Sand. ACI Special Publication. 2001. 200. Pp. 733–748.

3. Siddique, R., Aggarwal, Y., Aggarwal, P., Kadri, E.-H., Bennacer, R. Strength, durability, and micro-structural properties of concrete made with used-foundry sand (UFS). Construction and Building Materials. 2011. 25 (4). Pp. 1916–1925. DOI: 10.1016/j.conbuildmat.2010.1.065

4. Guney, Y., Sari, Y.D., Yalcin, M., Tuncan, A., Donmez, S. Re-usage of waste foundry sand in high-strength concrete. Waste Management. 2010. 30(8–9). Pp. 1705–1713. DOI: 10.1016/j.wasman.2010.02.018

5. Naik, T.R., Patel, V.M., Parikh, D.M., Tharaniyil, M.P. Utilization of Used Foundry Sand in Concrete. Journal of Materials in Civil Engineering. 1994. 6 (2). Pp. 254–263. DOI: 10.1061/(ASCE)0899-1561(1994)6:2(254)

6. Basar, H.M., Deveci Aksoy, N. The effect of waste foundry sand (WFS) as partial replacement of sand on the mechanical, leaching and micro-structural characteristics of ready-mixed concrete. Construction and Building Materials. 2012. 35. Pp. 508–515. DOI: 10.1016/j.conbuildmat.2012.04.078

7. Ganesh Prabhu, G., Hyun, J.H., Kim, Y.Y. Effects of foundry sand as a fine aggregate in concrete production. Construction and Building Materials. 2014. 70. Pp. 514–521. DOI: 10.1016/j.conbuildmat.2014.07.070

8. Ganesh Prabhu, G., Bang, J.W., Lee, B.J., Hyun, J.H., Kim, Y.Y. Mechanical and Durability Properties of Concrete Made with Used Foundry Sand as Fine Aggregate. Advances in Materials Science and Engineering. 2015. 2015. Pp. 1–11. DOI: 10.1155/2015/161753

9. Torres, A., Bartlett, L., Pilgrim, C. Effect of foundry waste on the mechanical properties of Portland Cement Concrete. Construction and Building Materials. 2017. 135. Pp. 674–681. DOI: 10.1016/j.conbuildmat.2017.01.028

10. Mastella, M.A., Gislon, E.S., Pelisser, F., Ricken, C., Silva, L. da, Angioletto, E., Montedo, O.R.K. Mechanical and toxicological evaluation of concrete artifacts containing waste foundry sand. Waste Management. 2014. 34 (8). Pp. 1495–1500. DOI: 10.1016/j.wasman.2014.02.001

11. Etxeberria, M., Pacheco, C., Meneses, J.M., Berridi, I. Properties of concrete using metallurgical industrial by-products as aggregates. Construction and Building Materials. 2010. 24 (9). Pp. 1594–1600. DOI: 10.1016/j.conbuildmat.2010.02.034

12. Singh, G., Siddique, R. Effect of waste foundry sand (WFS) as partial replacement of sand on the strength, ultrasonic pulse velocity and permeability of concrete. Construction and Building Materials. 2012. 26 (1). Pp. 416–422. DOI: 10.1016/j.conbuildmat.2011.06.041

13. Kaur, G., Siddique, R., Rajor, A. Influence of Fungus on Properties of Concrete Made with Waste Foundry Sand. Journal of Materials in Civil Engineering. 2013. 25 (4). Pp. 484–490. DOI: 10.1061/(ASCE)MT.1943-5533.0000521

14. Siddique, R., Singh, G., Singh, M. Recycle option for metallurgical by-product (Spent Foundry Sand) in green concrete for sustainable construction. Journal of Cleaner Production. 2018. 172. Pp. 1111–1120. DOI: 10.1016/j.jclepro.2017.10.255

15. Siddique, R., Schutter, G. de, Noumowe, A. Effect of used-foundry sand on the mechanical properties of concrete. Construction and Building Materials. 2009. 23 (2). Pp. 976–980. DOI: 10.1016/j.conbuildmat.2008.05.005

16. Siddique, R., Sandhu, R.K. Properties of Self-Compacting Concrete Incorporating Waste Foundry Sand. Leonardo Journal of Sciences. 2013. 12 (23). Pp. 105–124. U

17. Thaarrini, J., Ramasamy, V. Properties of Foundry Sand, Ground Granulated Blast Furnace Slag and Bottom Ash Based Geopolymers under Ambient Conditions. Periodica Polytechnica Civil Engineering. 2016. 60 (2). Pp. 159–168. DOI: 10.3311/PPci.8014

18. Smarzewski, P., Barnat-Hunek, D. Mechanical and durability related properties of high performance concrete made with coal cinder and waste foundry sand. Construction and Building Materials. 2016. 121. Pp. 9–17. DOI: 10.1016/j.conbuildmat.2016.05.148.

19. ASTM C1202-12. Standard Test Method for Electrical Indication of Concrete's Ability to Resist Chloride Ion Penetration. ASTM International, West Conshohocken, PA, 2012.

20. ASTM C1012 / C1012M-10. Standard Test Method for Length Change of Hydraulic-Cement Mortars Exposed to a Sulfate Solution. ASTM International, West Conshohocken, PA, 2010.

21. ASTM C597-02. Standard Test Method for Pulse Velocity Through Concrete. ASTM International, West Conshohocken, PA, 2002.

22. Divet, L., Randriambololona, R. Delayed Ettringite Formation: The Effect of Temperature and Basicity on the Interaction of Sulphate and C-S-H Phase 11Communicated by M. Moranville-Regourd. Cement and Concrete Research. 1998. 28 (3). Pp. 357–363. DOI: 10.1016/S0008-8846(98)00006-4

23. Tzouvalas, G., Rantis, G., Tsimas, S. Alternative calcium-sulfate-bearing materials as cement retarders: Part II. FGD gypsum. Cement and Concrete Research. 2004. 34 (11). Pp. 2119–2125. DOI: 10.1016/j.cemconres.2004.03.021

24. Fall, M., Pokharel, M. Coupled effects of sulphate and temperature on the strength development of cemented tailings backfills: Portland cement-paste backfill. Cement and Concrete Composites. 2010. 32 (10). Pp. 819–828. DOI: 10.1016/j.cemconcomp.2010.08.002

25. Gurumoorthy, N., Arunachalam, K. Micro and mechanical behaviour of Treated Used Foundry Sand concrete. Construction and Building Materials. 2016. 123. Pp. 184–190. DOI: 10.1016/j.conbuildmat.2016.06.143.

Information about authors:

Jagdeep Singh,
ORCID: *https://orcid.org/0000-0002-4966-9894*
E-mail: *jagdeep.singh71717@gmail.com*

Rafat Siddique, *PhD*
ORCID: *https://orcid.org/0000-0003-0128-6306*
E-mail: *siddique_66@yahoo.com*

Long-term strength and porosity of mortars based on ettringite binder

N.L. Nguyen[1] ✉ iD **, J.F. Georgin[2]** iD **, E. Prud'Homme[2]** iD

[1] Hanoi University of Civil Engineering, Hanoi, Vietnam

[2] National Institute of Applied Sciences of Lyon, Villeurbanne, France

✉ lamnn@huce.edu.vn

Abstract. Ettringite binder is widely used in mortars for technical applications such as patching mortars, self-leveling screeds, repair mortars thanks to their fast hardening ability and high early strength. However, depending on the amount and types of raw materials used in the composition, the properties of these types of binder have different behaviors at early-age and at long term. In this work, the influence of the nature and dosage of calcium sulfate in ettringite binder on the long-term strength of mortar in different curing conditions was determined. The results showed that the increase of calcium sulfate content in ettringite binder from 10–25 % improves the strength of mortars regardless of the calcium sulfate nature. In all curing conditions (endogenous, drying, outdoor), the strength of ettringite mortars with anhydrite is smaller than that of mortars containing hemihydrate. There is no major difference in the porosity of the mortars in different types of curing conditions before 28 days. However, after 28 days the porosity of mortar in drying condition is about 2–3 % higher than that of the mortars in endogenous and outdoor conditions.

1. Introduction

Within the last few decades, ettringite-based binders are used in applications that require a high compressive strength in a very short period of time to minimize construction times and disruption to the traveling public or user [1–5]. The binder system containing Portland cement (OPC), calcium aluminate cement (CAC) and calcium sulphate ($C\$H_x$) is often used when fast setting and hardening and high early strength development are required [5–7].

An ettringite binder is mainly based on the reaction between a calcium aluminate cement (CAC) and a calcium sulfate ($C\$Hx$), which lead to the formation of ettringite ($C_6A\$_3H_{32}$), aluminum hydroxide ($AH_3$):

$$3CA + 3C\$H_x + (38\text{-}3x)\ H \rightarrow C_6A\$_3H_{32} + 2AH_3 \tag{1}$$

$$3\ CA_2 + 3\ C\$H_x + (47\text{-}3x)\ H \rightarrow C_6A\$_3H_{32} + 5\ AH_3 \tag{2}$$

$$C_{12}A_7 + 12\ C\$H_x + (137\text{-}12x)\ H \rightarrow 4\ C_6A\$_3H_{32} + 3\ AH_3 \tag{3}$$
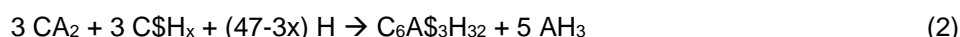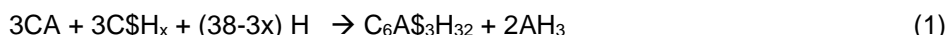
The rate of the reactions in the mixture in the fresh state is dependent on the ratio $CAC/C\$Hx$, the nature of the calcium sulfate and the presence or absence of admixtures [8, 9]. The setting time of ettringite-based binder is close to that of OPC, typically around 3 hours, but their hardening rate is in the range of 10 MPa to 20 MPa (compressive strength) per hour from setting. This rapidity is compatible with applications that require compressive strength from 10 MPa to 30 MPa after 4h to 6h. Therefore,

ettringite-based binders from ternary system (CAC – C$Hx – OPC) can be used in self-leveling mortars for underlayments and overlayments, screeds and repairing mortar, etc. [10, 11].

This combination with special additives makes a fast curing and drying possible, as well as shrinkage compensation of the cured mortar [12]. The mechanism is in many cases caused by ettringite formation, which is provided by blending CAC with calcium sulfates such as anhydrite, hemihydrate, gypsum or mixes thereof [13–15]. The calcium sulfate sources may vary in reactivity and have a large impact on the mechanical properties [16–18]. Although there are several papers on the study of these systems at early ages in the literature [19, 20], there appears to be a complete lack of studies about these systems as they reach older ages [21]. The carbonation of the ettringite binder was also studied, this process depends on weather conditions and occurs more or less quickly depending on several factors, especially the concentration of CO_2 in the weather [22–25].

The aim of this work is to clarify the influence of the nature and dosage of calcium sulfate in ettringite binder on the long-term strength and porosity of ettringite mortar in different curing conditions.

2. Materials and Methods

2.1. Materials

The binder of ettringite mortar consists of the calcium aluminate cement (CAC), Portland cement (CEM I) and 2 types of calcium sulfate: anhydrite (A) or hemihydrate α (P). The chemical composition of these raw materials is shown in Table 1:

Table 1. Chemical composition of raw materials in binder.

Raw material	Principal oxides / wt%										
	Al_2O_3	CaO	SiO_2	Fe_2O_3	MgO	TiO_2	K_2O	Na_2O	SO_3	MnO	L.O.I
CAC	69.68	29.78	0.26	0.16	0.15	0.04	–	0.23	0.27	0.01	–
CEM I – 42.5	5.30	67.28	20.22	0.20	1.02	0.18	0.26	0.20	2.63	0.06	–
Hemihydrate α	–	38.70	0.27	0.03	0.1	0.003	–	–	52.40	–	8.4
Anhydrite	–	42.69	–	0.07	0.05	0.002	–	–	56.83	0.006	3.9

The skeleton of ettringite mortars is composed of silica sand, slag and limestone fillers, whose average particle size is given in Table 2:

Table 2. Average particle size of the granular skeleton.

Raw material	Average diameter, D50 (µm)
Silica sand	88.19
Slag	11.95
Limestone fillers	13.17

2.2. Formulation of ettringite mortars

The formulation selected for studying ettringite mortars based on CAC and $C\$H_x$ is presented in Table 3. In order to grasp the influence of the nature of $C\$H_x$ (hemihydrate α or anhydrite) and the CAC/$C\$H_x$ ratio (75CAC/25$C\$H_x$ or 90CAC/10$C\$H_x$), the amount of each raw material was kept constant excepting for the nature of $C\$H_x$ and CAC/$C\$H_x$ ratio.

Table 3. Formulation of ettringite-based mortars in the research.

Raw materials		Percentage composition of raw materials, %	
		75CAC/25$C\$H_x$	90CAC/10$C\$H_x$
SKELETON	CAC	24.26	29.11
	$C\$H_x$	8.09	3.23
	CEM I – 42.5	3.97	3.97
	Silica sand		
	Carbonate powder	33.41	33.41
	Slag		
ADJUVANTS	Superplastifier		
	Viscosity agent	5.46	5.46
	Anti-shrinkage agent		
Retarder + Accelerator		0.238	0.238
Water		24.57	24.57
Water/Solid (W/S)		0.326	0.326

	Total	100	100

2.3. Research methods

2.3.1. Experimental conditions

The hydration process and structure of material, in general, depend on both the constituents and the conditions of casting and curing (temperature, humidity) where the material is hydrated versus time. In this study, the durability versus time of mortar based on ettringite binders in different curing conditions was investigated. The test protocol is as follows: after casting, the specimens are kept in endogenous condition for 24 hours (20 °C, Relative humidity – HR 100 %), then the mortar specimens are demoulded and stored in three different conditions:

- In endogenous condition (ENDO): the specimens were stored in sealed bags and placed in an air-conditioned room at 20 °C, 50 % RH.
- In drying condition (SEC): the specimens were placed in a temperature-controlled room at 20 °C and humidity 50 % RH.
- In outdoor condition (INT): the specimens were placed outdoors, their surfaces exposed to environment. Therefore, climatic conditions involve irregular changes of temperature and relative humidity (diurnal cycles, seasonal cycles, precipitation, and carbonation).

At desired age, the strength and porosity of ettringite mortars would be tested to evaluate the durability versus time of ettringite binders in different curing conditions.

2.3.2. Compressive strength and flexural strength

The freshly mixed mortars were cast into 40 mm×40 mm×160 mm mold for compressive strength and 3 point flexural strength tests. After 24 h, these specimens were unmolded and kept in three curing conditions mentioned above. The strength tests of ettringite mortars were performed at 1, 28, 90 and 330 days.

2.3.3. Mercury intrusion porosimetry test

Porosity was measured on fragments in the center of specimens (40×40×160 mm), which were first stopped hydration by grinding the samples of ettringite mortars at the required ages and putting the pieces obtained in an acetone bath for 2 days then filtered in a Buchner and placed in a dryer for 2 days to extract excess acetone and limit carbonation.

3. Results and Discussion

3.1. Observation of ettringite mortars

The main objective of this study is to investigate the influence of the curing conditions on the appearance of mortar using ettringite binder after a long-term weathering. Fig. 1 shows the surface of the mortars under outdoor exposure for 330 days.
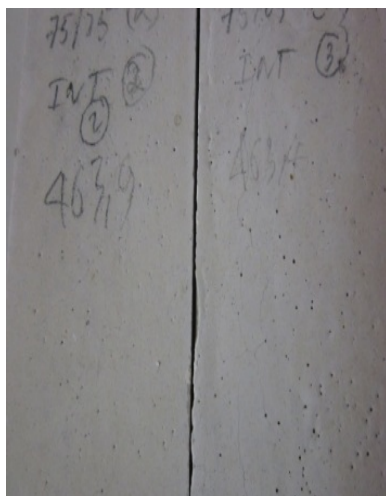
a) 75CAC/25P

b) 75CAC/25A
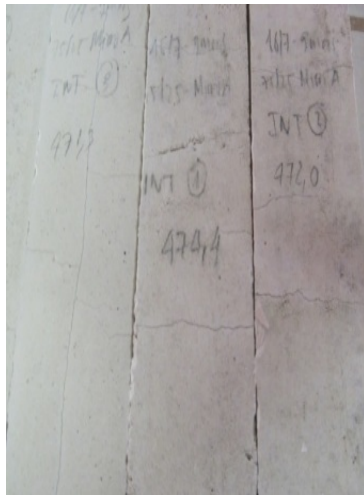
c) 90CAC/10P   **d) 90CAC/10A**

Figure 1. Surface of the ettringite mortars after 330 days outdoors exposure.

The results showed that cracks appeared at all the specimens except the composition 75CAC/25P. Meanwhile, the surfaces of mortars in endogenous condition or in drying condition are almost undamaged. It seemed that the cycle 'absorption – evaporation' of water in mortars occurs repeatedly due to outdoor weather conditions and is accompanied by dimensional variations that lead to local stresses causing cracks in the mortar structure.

3.2. Impact of curing conditions on the mechanical strength

Mechanical behavior is a very important property for construction materials. The results of compressive strength and flexural strength of the 4 compositions from 1 day to 330 days are shown in the Fig. 2:
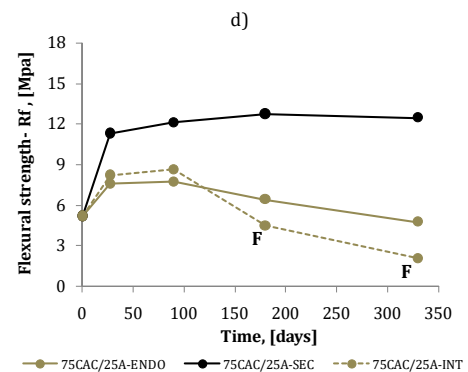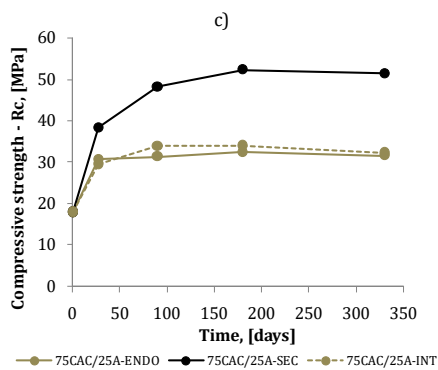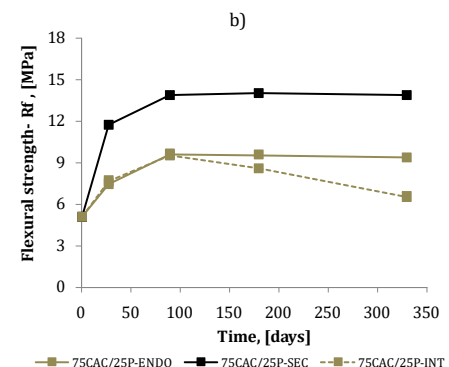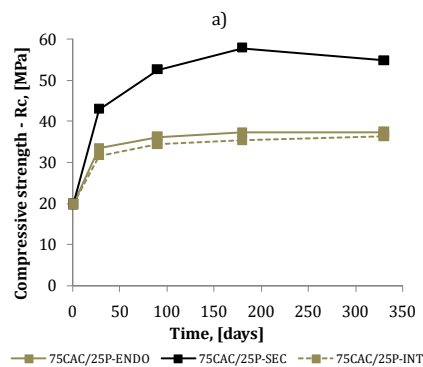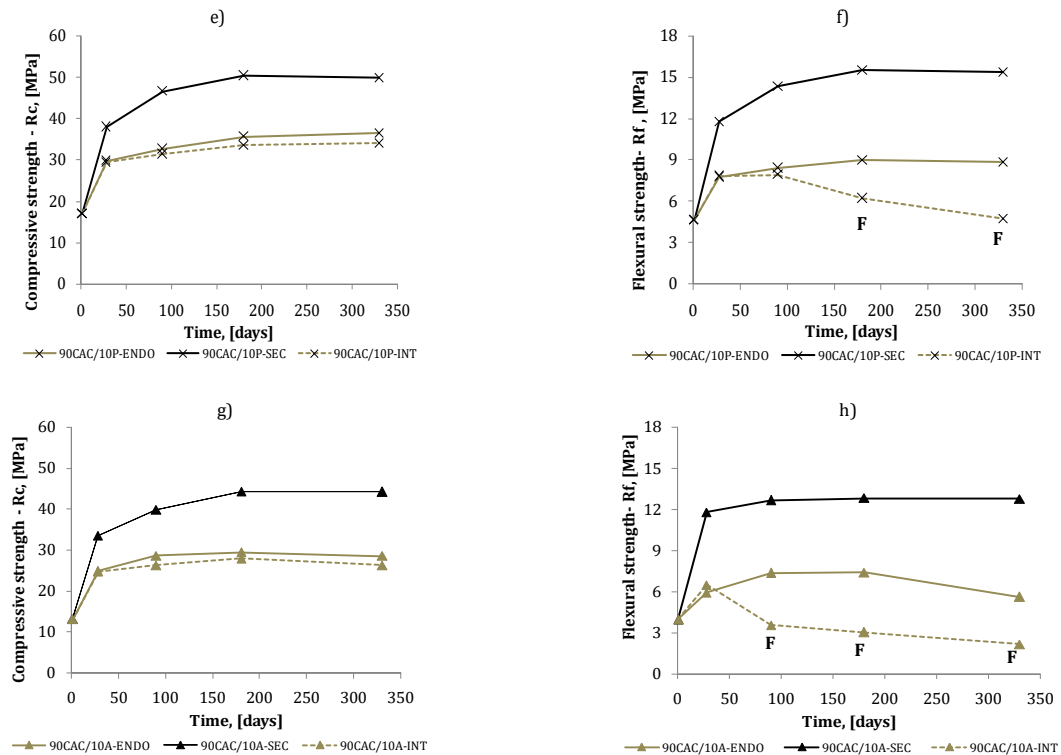
Figure 2. Strength of ettringite mortars in different curing conditions:
a) Compressive strength – 75CAC/25P; b) Flexural strength – 75CAC/25P;
c) Compressive strength 75CAC/25A; d) Flexural strength – 75CAC/25A;
e) Compressive strength – 90CAC/10P; f) Flexural strength – 90CAC/10P;
g) Compressive strength – 90CAC/10A; h) Flexural strength – 90CAC/10A.

The results in the Fig. 2 suggest that whatever the curing conditions, the compressive strength increases continuously versus time. Indeed, the compressive strength increases rapidly during the first 28 days then progress slowly. The strength of the composition 75CAC/25P is always more important than that of the other three compositions. In the contrast, the composition 90CAC/10A has the lowest strength, whereas the strengths of compositions 90CAC/10P and 75CAC/25A have the same values.

In the endogenous condition, except for composition 90CAC/10A, all samples achieved compressive strength above 30 MPa. For the flexural strength, it raises in the similar manner as compressive strength except for the compositions containing anhydrite: From 180 days, the flexural strength of the compositions containing anhydrite begin to decrease, the drop of flexural strengths is difficult to understand because there was no obvious evidence about the decrease in compressive strength.

In drying condition, the strength increases sharply during the first 28 days; then from 28 days until 180 days, it still continues increasing slightly and achieves the values higher than that in endogenous condition. The compositions with hemihydrate have flexural strength of about 15 MPa while compositions using anhydrite only achive about 12 MPa. Meanwhile, the compressive strength of samples 75CAC/25C$H achieve 50–60 MPa, but samples 90CAC/10C$H only have compressive strength of 40–50 MPa.

The strength of the 4 compositions cured outdoors in Fig. 2 also indicated clearly the influence of weathering processes on ettringite mortars in the research. The result shows that the compressive strength of the outdoor-exposed mortars evolves in the similar way as other curing conditions (endogenous or drying condition) in the following order:

$$R_c \text{ (75CAC/25P)} > R_c \text{ (75CAC/25A)} \approx R_c \text{ (90CAC/10P)} > R_c \text{ (90CAC/10A)}.$$

This trend of strength development is consistent with research results in the literature [16]. However, there is a drop in long-term flexural strength (the letter F in Fig. 2b, d, f, h is for cases of the micro-cracks visible). These micro-cracks are observed from 90 days for composition 90CAC/10A, 180 days for the compositions 90CAC/10P and 75CAC/25A. With the composition 75CAC/25P, a small decrease in flexural strength was remarked but there was no crack detected on the specimen surface. There may be micro-cracks in its structure.

3.3. Impact of curing conditions on the porosity of ettringite mortars

Porosity is one of the basic factors influencing durability of mortar and concrete. Fig. 3 shows the porosity of the 4 compositions at different curing conditions:
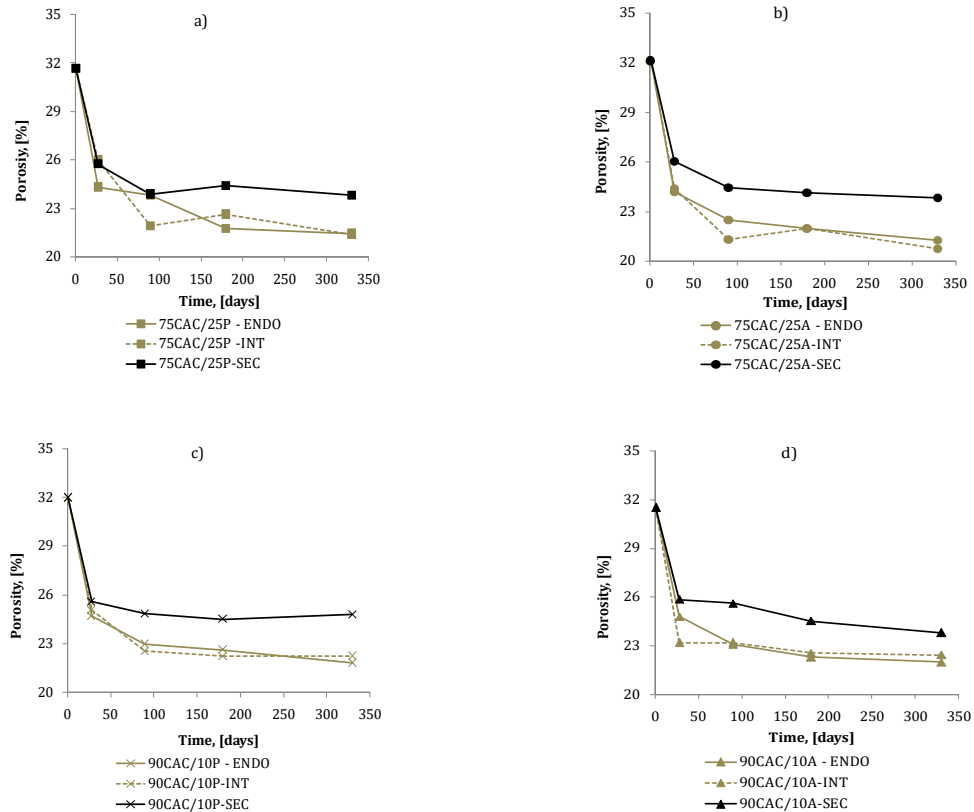
Figure 3. Evolution of the ettringite mortar porosity depending on the curing conditions: a) Composition 75CAC/25P; b) Composition 75CAC/25A; c) Composition 90CAC/10P; d) Composition 90CAC/10A.

The results indicated that there is no major difference on the porosity of the mortars in endogenous condition and outdoor exposure condition. This is explained by the fact that the water is always supplied for hydration when it rains for outdoor weathering specimens. Meanwhile, for the samples in drying condition (air-conditioned room at 20 °C, HR 50 %) the specimens are not rehydrated. Before 28 days, only the water at the surface of mortar specimens evaporates, so the difference in porosity between the different types of curing condition is not significant. However, after 28 days the porosity of mortar in drying condition is higher than that of the mortars in endogenous and outdoor condition about 2–3 % due to the evaporation of water in specimens, which becomes important. Besides, the main hydrates containing many water molecules (ettringite or carboaluminate) can lose a few water molecules in its formula because of a long-term drying period [26].

4. Conclusions

The study on long-term mechanical property and porosity of ettringite mortars leads to some key conclusions:

1. After 330 days, the surface of mortars in endogenous condition or in drying condition is still in good condition. In the contrast, the mortars stored outdoor have been discovered some micro-cracks on the surface. This phenomenon is more remarked on the compositions containing anhydrite.

2. Whatever the curing conditions, the compressive strength increases rapidly during the first 28 days but slightly at long-term age. The strength of the compositions containing hemihydrate is better than the strength of the compositions containing anhydrite.

3. The compressive strength of the specimens stored outdoors is the less important but still close to that in endogenous condition and the decrease in flexural strength maybe due to micro-cracks in the structure. The strength of mortar in drying condition is higher than that in endogenous condition or in outdoor condition although the porosity of mortar in drying condition is higher.

4. The difference of porosity at early age between the different types of curing condition is not significant. However, at later age after 28 days, the porosity of mortar in drying condition is higher than that of the mortars in endogenous and outdoor condition about 2–3 %.

References

1. Georgin, J.F., Prud'Homme, E. Hydration modelling of an ettringite-based binder. Cement and Concrete Research. 2015. 76. Pp. 51–61. DOI: 10.1016/j.cemconres.2015.05.009

2. Nguyen, H., Kinnunen, P., Gijbels, K., Carvelli, V., Sreenivasan, H., Kantola, A.M., Telkki, V.V., Schroeyers, W., Illikainen, M. Ettringite-based binder from ladle slag and gypsum – The effect of citric acid on fresh and hardened state properties. Cement and Concrete Research. 2019. 123. DOI: 10.1016/j.cemconres.2019.105800

3. Elodie Prud'homme, Ngoc Lam Nguyen, Marie Michel, Jean-François Georgin, J.A. Investigation of Ettringite Binder Hydration at Early Age for Glass Fiber Reinforced Concrete Application. Developments in Strategic Materials and Computational Design V: A Collection of Papers Presented at the 38th International Conference on Advanced Ceramics and Composites. 2014.

4. Edward G. Moffatt, Michael, D.A. Thomas. Effect of Carbonation on the Durability and Mechanical Performance of Ettringite-Based Binders. Materials Journal. 2019. 116 (1). Pp. 95–102.

5. Karen, L. Scrivener, A.C. Calcium Aluminate Cements. LEA's Chemistry of Cement and Concrete. Butterworth-Heinemann, 1998. Pp. 713–782.

6. Daimon, M., Rhee, K.H., Kondo, R. On the Hydration Mechanisms of Calcium Sulfate Hemihydrate. Journal of the Ceramic Association, Japan. 1970. 78 (900). Pp. 277–282. DOI: 10.2109/jcersj1950.78.900_277

7. Fernández, C., Lucía-Torrens, M., David, M.M., Laura, M.R., S.F. Evolution to carbonated compounds of phases developed on ternary systems materials. Cementing a sustainable future, XIII ICCC International Congress on the Chemistry of Cement. 2011. Pp. 345–352.

8. Klaus, S.R., Neubauer, J., Goetz-Neunhoeffer, F. Hydration kinetics of CA2 and CA – Investigations performed on a synthetic calcium aluminate cement. Cement and Concrete Research. 2013. 43 (1). Pp. 62–69. DOI: 10.1016/j.cemconres.2012.09.005

9. Martin, I., Patapy, C., Cyr, M. Parametric study of binary and ternary ettringite based systems Calcium aluminates. Calcium Aluminates: Proceedings of International Conference. 2014.

10. Kighelman, J. Hydration and structure development of ternary binder system as used in self-levelling compounds. EPFL. Lausanne, 2007. 224 p.

11. Lutz, H., Bayer, R. Dry Mortars15-07-2010.

12. Fredrik Paul Glasser, L., Zhang, Q.Z. Reaction of Aluminate Cements with Calcium Sulfate. Calcium Aluminates – Proceedings of the International Conference. 2001. Pp. 551–564.

13. Bayoux, J.P., Bonin, A., Marcdargent, S., Mathieu, A. and Verschaeve, M. Study of the hydration properties of aluminous cement and calcium sulfate mixes. Calcium Aluminate Cements. 1990. Pp. 320–334.

14. Goetz-Neunhoeffer, F.N.J. Refined ettringite structure for quantification of hydration in cement pastes. Proceedings of the 12th International Congress on the Chemistry of Cement. 2007.

15. Fryda, H., Estival, J., Berger, S., Bordet, F., Andreani, P.A.M.B. Ultra fast hydration opening new application fields: a comparison of different calcium aluminate technologies. Calcium aluminates – Proceedings of the international conference. 2014. Pp. 42–54.

16. Lamberet, S. Durability of ternary binders based on portland cement calcium aluminate cement and calcium sulfate. École Polytechnique Fédérale de Lausanne, 2005. 219 p.

17. Onishi, K., Bier, T.A. Investigation into relations among technological properties, hydration kinetics and early age hydration of self-leveling underlayments. Cement and Concrete Research. 2010. 40 (7). Pp. 1034–1040. DOI: 10.1016/j.cemconres.2010.03.004

18. Stabler, C., Breunig C., Goetz-Neunhoeffer F., Neubauer J., Fryda H., K.-E.F. Impact of different calcium sulfate sources on the early hydration of two different grades of calcium aluminate cement. Calcium aluminates Cements – Proceedings of the international conference. 2014. Pp. 177–188.

19. Le Saout, G., Lothenbach B., Winnefeld F., Taquet P., Fryda, H. Hydration study of Calcium aluminate cement blended with anhydrite. Calcium aluminates: Proceedings of the international conference. 2014. Pp. 165–175.

20. Bizzozero, J., Scrivener, K. Hydration and microstructure of rapid-strength binders based on OPC accelerated by early ettringite formation. Calcium aluminates – Proceedings of the international conference. 2014. Pp. 231–242.

21. Evju, C., Hansen, S. The kinetics of ettringite formation and dilatation in a blended cement with β-hemihydrate and anhydrite as calcium sulfate. Cement and Concrete Research. 2005. 35 (12). Pp. 2310–2321. DOI: 10.1016/j.cemconres.2004.09.012

22. Nishikawa, T., Suzuki, K., Ito, S., Sato, K., Takebe, T. Decomposition of synthesized ettringite by carbonation. Cement and Concrete Research. 1992. 22 (1). Pp. 6–14. DOI: 10.1016/0008-8846(92)90130-N

23. Xiantuo, C., Ruizhen, Z., Xiaorong, C. Kinetic study of ettringite carbonation reaction. Cement and Concrete Research. 1994. 24 (7). Pp. 1383–1389. DOI: 10.1016/0008-8846(94)90123-6.

24. Xie, L., Song, X., Tong, W., Gao, C. Preparation and structure evolution of bowknot-like calcium carbonate particles in the presence of poly(sodium 4-styrene sulfate). Journal of Colloid and Interface Science. 2012. 385 (1). Pp. 274–281. DOI: 10.1016/j.jcis.2012.06.076

25. Fernández-Carrasco, L., Torréns-Martín, D., Martínez-Ramírez, S. Carbonation of ternary building cementing materials. Cement and Concrete Composites. 2012. 34 (10). Pp. 1180–1186. DOI: 10.1016/j.cemconcomp.2012.06.016

26. Zhou, Q., Glasser, F.P. Thermal stability and decomposition mechanisms of ettringite at <120 °C. Cement and Concrete Research. 2001. 31 (9). Pp. 1333–1339. DOI: 10.1016/S0008-8846(01)00558-0

Information about authors:

Ngoc Lam Nguyen, *PhD*
ORCID: *https://orcid.org/0000-0003-2238-196X*
E-mail: *lamnn@huce.edu.vn*

Jean Francois Georgin, PhD
ORCID: https://orcid.org/0000-0002-4966-9894
E-mail: jean-francois.georgin@insa-lyon.fr

Elodie Prud'Homme, PhD
ORCID: https://orcid.org/0000-0001-9637-7125
E-mail: elodie.prudhomme@insa-lyon.fr

Influence of biological additives on the properties of cement systems

S.V. Dudynov ✉ iD

National Research Mordovia State University, Saransk, Russia

✉ *dsergey @mail.ru*

Abstract. The object of the research is cement systems, the materials most commonly used in the construction industry. Since people interact with construction materials all the time, they should only contain harmless components; this requirement applies to modifiers as well. The existing liquefiers are obsolete; there is a need for an alternative composition and production technology. The purpose of the research is, first, to theoretically design the structure of an environmentally friendly plasticizing additive for cement systems based on fragments of natural compounds – lipids and carbohydrates. Secondly, to select a non-pathogenic microbial culture capable of synthesizing this product and the conditions for its fermentation. And finally, to study the properties of cement systems containing the synthesized biomodifier. This paper proposes novel modifiers based on fragments of natural compounds. The production process should be based on biological synthesis running through the cellular structures of microorganisms growing in a synthetic nutrient medium. A non-pathogenic microbial culture was 'tamed' to synthesize this product. The authors further designed a synthetic nutrient medium and optimized the fermentation parameters. Ten hours after the onset of fermentation, a fat-like substrate is added to the nutrient medium so that *Leuconostoc mesenteroides* would be able to synthesize the hypothesized modifier. The output is an efficient glycolipid plasticizer. X-ray diffraction analysis, a plastometer, a flow table, a cone, a viscometer, a versatile press, and an ionometer were used in this research to find the parameters of the synthesized bioadditives and cement systems based on them. The bioplasticizer injection was noted to increase the fluidity of cement mixtures by a factor of 3 to 5. The novel modifiers greatly inhibit early cement hydration when dosed at >0.8 wt.%. However, while inhibiting early structuring, these liquefiers strengthen the material in the long term (3+ months). Injecting these biological additives in the mixture at up to 0.8 wt.% produces a material that is 20÷30 % stronger than the additive-free alternative and absorbs less water while being as resistant to frost. As per our hypothesis, the microbial synthesis did in fact produce efficient cement system modifiers for industrial and residential construction that would be subject to no environmental restrictions.

1. Introduction

All of us are in constant contact with construction materials over the course of our lives. For this reason, the environmental safety of such materials is of the utmost importance.

Although the range of modern construction materials is rather vast, those where Portland cement is the binding agent occupy pride of place. Due to their abundance, they are used practically everywhere, despite the fact that they have several peculiarities and drawbacks. With regard to the aforementioned, cement systems are the object of the research.

To attenuate or decrease the defects of the latter, measures of a technological and formulation nature are used. The fact that the classic composition, which includes cement, water, sand and gravel only, has disappeared from practice for the time being confirms this point. The mandatory component of modern cement mixtures includes modifying additives, the quantity of which is rather large, and it is continuously increasing [1–10].

The additives, as a rule, possess a polyfunctional activity or some additional effect. For example, they ensure the hardening process at temperatures below zero, accelerate it, and at the same time improve mixture mobility, ameliorate the protective properties with regard to steel reinforcement, etc. However, among such a broad range, one effect dominates the rest, and based on it the compound is designated into a certain group of modifying agents.

The products possessing a plasticizing effect – diluting agents, have a special status in the whole volume of additives. Such a standing is quite natural, since a small dose of the plasticizer is accompanied by substantial changes both in the production technology of the parts, items, constructions, and in the construction and technical characteristics of the ready-made material. Moreover, they are very accessible, their cost is comparatively low, and they usually belong to the group of surface-active agents (SAA).

According to the existing gradation, there are plasticizers, superplasticizers and hyperplasticizers. And superplasticizers on the melamine and naphthaline-formaldehyde basis, possessing high technical characteristics, are widely used in construction. However, the mentioned substances are highly hazardous, which makes their use in light of the toughening environmental requirements rather dubious [11–20].

From this point of view products based on polycarboxylate or acrylic polymers, which have another molecular structure, are more preferable. The serious drawback of such compounds, however, is their high cost, low accessibility, and heightened requirements towards qualitative figures of the used cements, which inevitably creates limit at ions for their use in mass construction.

It is also worth mentioning that most efficient diluting agents are produced artificially – by means of streamlined chemical synthesis. Such a method naturally envisages the production of the target compound using special, often unique equipment, and is based on individual technology, and the chemical processes, in any case, result in often dangerous byproducts, the utilization of which is also rather expensive.

The aforementioned expressly justifies the topicality of the research of cement composites with plasticizers, since existing diluting agents have become exhausted, and must be changed both in their composition and production technology [21–33].

We believe that natural substances or materials produced using their fragments have good potential in terms of environmental figures. These are proteins, carbohydrates, lipids, nucleic acids, their derivatives and complexes. The method of producing the mentioned compounds – the source of commercial production, becomes rather important here.

In our view, the technological solution of the issue is in using biotechnology for producing the compounds with a set structure, and the subsequent (as applicable) task-oriented transformation of the produced products using the later ones as the initial raw material.

Biotechnology is based on the use of live cells – plant, animal ones, including the cells of microscopic creatures for certain purposes. In this case we suggest the fermentative cultivation of microorganisms for the synthesis and accumulation of desirable metabolites with the set composition and structure, with the subsequent use of the produced compounds as modifying agents in the cement compositions.

The microorganisms synthesize various compounds, some of which possess surface activity. Due to the large value of the surface v/s volume ratio, they are promising products capable of considerably broadening the range of additives for concretes currently used.

A live cell may be compared to a very complex system of shops, with a change of containers with organic and aqueous media, which contain various reagents. The cellular structures provide the required sequence of the successive metabolic reactions, which, if decomposed, are interrupted, and the effect begins to be produced only by hydrolytic enzymes.

The suggested concept is rather logically explained by the circumstance that a set of technological advantages is appropriate to the substances of microbial synthesis:

1. due to complete biological destruction, the products of microbial synthesis cannot contaminate the environment;
2. retain efficiency in a wide range of temperatures, pH;
3. are renewable resources;
4. have unlimited resource sources.

The use of biotechnology from the technological point of view is quite justified. We will substantiate this statement in more detail.

Alternative production processes always require huge material and financial costs to equip the factory with the necessary materials. Moreover, the installed mechanisms, engineering facilities and appliances usually cannot be used for producing other products.

By contrast, biotechnology is based on single-type processes, appliances and devices. The correct choice of the strain-producer is the main thing here. The optimization of the cultivation process is not very complex and will not take much time. Moreover, if necessary, the whole system may be reset relatively easily and quickly for the production of another target product using the same equipment and the analogous scheme, when a simple exchange of the microbial population strain and/or growing medium for its cultivation is required.

The main difficulty involves correctly determining the microorganism-producer able to generate the target compound, since this synthesis can be produced by various microscopic creatures. This compound can be constructed theoretically at the beginning, and then the required conditions for its generation must be created using the selected microbial strain.

In principle, for biosynthesis of the required product there is a theoretical possibility of using a producer from any taxonomic group: bacteria, fungi, yeast fungi, microalgae, molds, etc. The unique peculiar feature of the biotechnology must be emphasized here, which is represented as follows.

If the microbial colony does not generate the required fragment, it will be sufficient to introduce a specific reagent into the growth medium composition, thus changing the cultivation conditions in the bioreactor, forcing the producer to absorb a new substrate. The microorganisms, adapted in their development to such an unusual source of nourishment, subsequently start synthesizing it in large quantities (in such cases, the term 'accustomed to' is used).

Furthermore, the conditions required for biotechnological processes differ greatly from those under chemical effects. In particular, the main difference is that in such a case the following will not be necessary: high temperature; high pressure; catalysts, etc. Moreover, biosynthesis usually takes place at room temperature and under regular atmospheric pressure, making the production cycle much safer, easier, and making it possible to organize the production of environmentally friendly products in any climate conditions with relatively low material costs and investments.

As a rule, plasticizers are products from the surface-active agents (SAA) group.
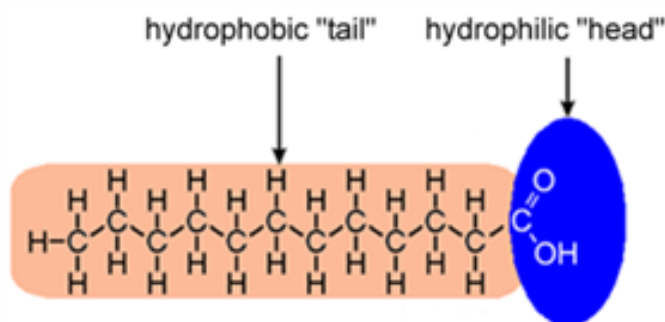
Figure 1. Structure of surface-active agents.

The structure of surface-active agents is composed of a hydrophilic constituent, represented usually by the polar group – carboxyl (—COOH), amino- (—NH_2), nitro- (—NO_2), oxi- (—OH), sulfo- (—SO_3H) and so on, and a hydrophobic hydrocarbon radical. Such a two-fold nature of SAAs gives to them special properties, in particular, the ability to adsorb at the phase boundary. Moreover, with the concentration being increased, the molecules of the surface-active agents are united into specific associates – micellae, changing their form when the critical micelle concentration (CMC) is reached.

It is known that the SAA properties are determined by the construction of diphilic components and their mutual position in the molecule. The influence of the hydrocarbon radical length and activity of functional groups are distinguished here first of all.

In our view, the compound may demonstrate plasticizing properties when the missing structural component is introduced into its composition, thereby transforming the compound into a diphilic one. That is, for the reagents having a polar group, the hydrocarbon fragment must be injected; and vice versa, the characteristic group must be added to the product containing the hydrocarbon radical. Such changes transfer any compound into the category of a surface-active agent.

As stated, the surface activity of the SAAs at other equal conditions depends on the properties of the diphilic components. Hence, we believe that the surface activity of the substance can be increased by substituting the functional groups for more active ones, increasing their number in the compound macromolecule, or by injecting additional or longer hydrocarbon radicals.

Carbohydrates account for a large share of the total number of natural compounds. Studying the structure of carbohydrates, it is easy to notice that they have an excess of hydrophilic components. However, though the mobility of the concrete mixture after the injection of carbohydrates changes, its value in this case is negative. According to our research tests, adding sugars (for example, dextrans and dextrins) to the cement mixtures decreases the mobility of the latter, with a simultaneous decrease in the strength of the hardened material.

Therefore, it is rather logical to assume that to produce an efficient sugar-based plasticizer, a hydrocarbon chain of lipids must be implanted into the latter, which may consist, for example, of a fatty acid. Injection of the hydrophobic link into the carbohydrate molecule will be accompanied by a change in the structure and molecular mass of the compound, its lyophilic-lyophobic balance, CMC, which, in turn will influence the properties of the final product, and, if the latter is injected into construction mixtures, will produce a plasticizing effect.

The synthesis of bioSAA, in our view, may take place during the development of the microbial colony only after the injection into the growing medium at a certain stage of fermentation of special ingredients – fatty acids, vegetable oil or other lipoids. This is due to the fact that, after a certain period of time, the sufficient quantity of developed cells with accumulated carbohydrates is contained in the producer population. Adding the fat-containing substrate to the growing medium composition changes the cultivation conditions, breaching the C/N ratio in favor of carbon, thus stimulating the formation of lipids [37–40].

It should be pointed out that over the course of various development stages, all types of microbial creatures must generate and accumulate carbohydrates as an auxiliary material and source of energy. Adding the reagent containing the lipid fraction (vegetable oil, oleic acid, etc.) changes the cultivation conditions, forcing the bacteria to absorb the new component. The subsequent generations of microorganisms cultivated in such conditions will be 'accustomed to' synthesizing it. The process of intensified accumulation of lipids is further enhanced by the intensive growth in the number of senescent cells, which are characterized by an increased fat content. Given the ability to maintain optimal existence conditions, the population of microorganisms tends to use the available material to construct new cells. Biochemical transformations take place simultaneously in cellular structures, accompanied by the integration of fatty acid molecules into the structure of oligomer links in the carbohydrate fragments. New glycolipid type molecules, having the following structure, are formed and accumulated during the transformation of initial substrates:
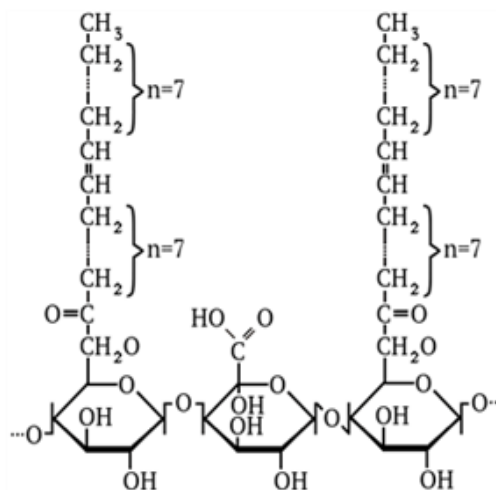
Figure 2. Structure of new glycolipid type molecules.

It is easy to notice that the structure produced is analogous to that of glycolipids. Glycolipids, as is known, possess the highest surface activity among natural SAAs [34–40].

Based on the proposed theoretical concept, we have successfully synthesized non-hazardous biomodifiers for construction mixtures.

The task of the work is to develop efficient and environmentally friendly plasticizers for construction purposes, which include or are composed of the fragments of natural compounds: 1) using the methods of

biotechnology, namely streamlined microbial synthesis; 2) modification of the existing ones, without producing reagent byproducts.

To achieve the set task, the following issues must be solved:

to demonstrate the possibility of transforming the initial compounds into SAAs by means of streamlined microbiological reconstruction of their composition and structure;

to search for substances possessing the surface-active properties among natural products, i.e. those being potential plasticizers for the cement systems;

to demonstrate the expedience of using biotechnology for the synthesis of compounds with the set composition and structure;

to find strains of microorganisms suitable for cultivation in such processes;

to study the rheological properties of cement compositions with bioSAAs;

to examine the construction and technological characteristics of the cement systems with the produced biomodifiers.

2. Materials and Methods

Cement mixes were prepared using several cements, the technical performance of which is demonstrated in Tables 1 and 2.

Table 1. Cements chemistry.

Cement No.	Composition, %					
	CaO	SiO$_2$	Al$_2$O$_3$	Fe$_2$O$_3$	MgO	SO$_3$
1	2	3	4	5	6	7
Z1	58.7	28.31	4.21	3.44	1.41	2.3
Z2	60.27	24.55	4.50	4.05	0.82	2.64
Z3	63.46	20.58	4.74	4.23	1.74	3.21
Z4	64.9	20.8	4.2	3.5	1.1	3.0

Table 2. Cements mineralogy.

Cement No	Composition, %			
	C$_3$S	C$_2$S	C$_3$A	C$_4$AF
1	2	3	4	5
Z1	57.73	23.3	5.01	10.46
Z2	61.6	17.1	4.9	13.3
Z3	62.99	15.01	5.51	14.35
Z4	73.0	8.7	5.3	11.6

The specific surface area of the cements is 2370–2850 cm^2/g.

Samples, forms, equipment and test methods comply with EN 12350, EN 12390, CR 13901, EN 196, EN 934.

To study the structural changes in cement systems, an X-ray phase analysis was performed on the X-ray diffractometer with X-ray intensity ionization registration. Copper K_{α_1}-radiation and nickel filter were used in the study. Powder diagram was taken at room temperature in the following mode: tube current is 16 mA; voltage is 30 kV; RC time is 2 s; diagram chart speed is 720 mm/hour; recording scale range is 1000 imp/s. When determining the hydration degree (α) was in the (2Θ) 8–57⁰ range of angles with a counter speed of 1 ⁰/min twice with the sample repacking.

The base cement from which the cement stone of the control composition was obtained, was used as an external standard for determination of the degree of hydration of clinker minerals. In this case, α clinker of minerals is determined from the formula:

$$\alpha = \left(1 - \frac{J_\tau}{J_0}\right) \times 100\%, \tag{1}$$

where J_0 is line intensity of a given phase in the base unhydrated cement; J_τ is line intensity of the same phase in the hydrated cement.

The cement stone was formed during the hardening of the cement paste prepared with a constant water-cement ratio and a corresponding proportion of modifier additive.

By comparing the intensities of analytical lines selected for each crystal formation in time we determined the amount of unhydrated substance of cement clinker minerals.

The degree of C₄AF hydration was not determined.

To calculate the hydration of clinker minerals, the line of average intensity with d = 2.204 Å was chosen as the analytical line for C₃A; α-C₂S is the line with d = 3.869 Å; β-C₂S is the strong line with d = 2.189 Å, not overlapping the lines of other minerals; C₃S is the strongest line of intensity "100" on the 100-point scale with d = 2.776 Å.

The mobility of the concrete mix was determined by the standard cone slump. The comparison was made with the control composition.

The effect of additives on the mobility of cement mortar was made by comparing the spreads of the control composition and compositions with the additives obtained from the experiments on the shaker apparatus.

The water absorption of the material was determined by the storage of samples in water during the specified time.

The study of the structure formation process was carried out on a cone plastometer. The method consists of determining the mechanical properties of the cement mix and the nature of their change over time. Here the controlled item of the system is its plastic strength, which is calculated on the readings recorded when the cone is penetrated at the same depth. The plastic strength of the cement paste "P_m" was calculated as per the formula (2)

$$P_m = K_\alpha \times \frac{P}{h_m^2}, \ \text{MPa,} \qquad (2)$$

where P is load on the cone, kN; h_m^2 is cone penetration depth, cm; K_α is cone constant, moreover,

$$K_\alpha = \frac{1}{\pi} \times \cos\frac{\alpha}{2} \times \cot\frac{\alpha}{2}, \qquad (3)$$

where α is cone-apex angle (in its axial plane).

During concreting, the process of material hardening can occur both under normal conditions (t = 291-–294 K, W = 95–100 %), and in curing. Bearing this in mind, the following curing mode was adopted (in hours): preliminary curing + temperature rise + isothermal warming + temperature drop = 2 + 3 + 7 + 4. The temperature of isothermal warming is 353±2 K [41–44].

Generally, bioadditive production technology includes the following operations:

- preparation of a sterile synthetic medium;
- sowing fermentation – inoculum cultivation;
- fermentation.

When choosing a producer culture for biomodifiers, not only its ability to synthesize the necessary compounds fast and in great numbers, but also their localization is of significant importance. According to this indicator, microorganisms can be divided into two groups: 1 – microorganisms that accumulate metabolic products inside the cell (intracellular); 2 – microorganisms that get them into the cultural liquid (extracellular). It stands to reason that to extract intracellular metabolites, it is necessary to destroy cellular structures someway, which naturally complicates the process at the instrument level. Therefore, in some cases, less productive cultures that produce extracellular metabolites may be preferable to highly productive ones that accumulate biosynthesis products in cellular organoids. Here, the individual peculiarities of the microbial population can be crucial in terms of the choice of a particular species [45–48].

Leuconostoc mesenteroides bacteria cultivated on a synthetic medium were selected as a producer. The basis for this decision is the following factors:

The first and most important factor is that the microbial culture is not pathogenic.

Second, biosynthesis compounds formed during the cultivation of colonies are localized not in cellular organoids, but outside them. That is, we will not require additional operations for their extraction subsequently. Consequently, the process chain becomes much shorter and simpler at the instrument level.

Third, *Leuconosloc mesenteroides* accumulates metabolic products encapsulated. Moreover, the walls of the capsule consist of structures that are easily destroyed by the exposure of even weakly alkaline media. Thus, after fermentation, additional stages for extracting the preparations will not be required, since the hydration reaction of the cement clinker is accompanied by the formation of calcium hydroxide, which gives the pore liquid pH = 7 or more, which is why the biomodifiers get into the cement system directly. Therefore, the additive can be introduced in the form of a cultural liquid at a particular.

Fourth, the use of a synthetic (artificial), rather than a natural medium for the growth of the microbial population ensures the stability of the properties of the synthesized product.

We used the following composition of the medium: potassium chloride is 0.1 g; magnesium sulfate is 0.1 g; potassium phosphate monobasic is 1.0 g; disodium hydrogen phosphate is 2.5 g; ammonium chloride is 0.5 g; Mohr's salt is 0.01 g; paraaminobenzoic acid is 0.05 g; peptone is 0.2 g; refined sugar is 100 g; apyrogenic water (water for injection) is 1000 ml; oleic acid – 0.14 g (for the synthesis of the product with the index "O-1"); – 0.18 g (for the synthesis of the product with the index "O-2"). A sterilization stage is required to prevent the development of other microbial organisms, including wild ones. Sterilization was carried out in one of the temperature conditions: 378 K – 20 minutes or 390 K – 10 minutes.

To get glycolipid plasticizers, the bacterial culture was grown in flasks with a medium in a shaking mode (160 rpm). The culture medium was inoculated as 1 tube with seed per 100 ml of medium. Ten hours after the start of cultivation, a specific substrate (vegetable oil or oleic acid) was added to the medium.

The duration of the cultivation period was 24–48 hours at a temperature of 296–298 K. Considering the fact that the number of accumulating lipids in the individual cells of the producer colony increases with aging, the preference should be given to processes with a longer duration. After completion of the fermentation, the surfactant of the microbial synthesis of the glycolipid base is ready for use as an additive in cement systems. If the components containing a fat-like substrate (vegetable oil, oleic acid, etc.) are excluded from the composition of the medium, the selected bacterial strain that is not "accustomed" to the synthesis of the lipid fraction accumulates only polysaccharides, and the biomodifier is not formed.

During the experiments on the selection of parameters for fermentation, the following factors significantly influence on the indicators of the resulted substances:

- the oxygen concentration and carbon dioxide in the cultural liquid;
- stimulating additives;
- time of specific substrate introduction;
- cultivation duration;
- mixer rotation speed.

Moreover, when introducing the type and dosage of the added reagent have a significant impact on the quality indicators of the synthesized biomodifier.

3. Results and Discussion

Without insight into metabolic reactions occurring in the course of fermentation, we should note that chemically the resulting compounds are typical surfactants.

Therefore, the operating principle of the resultant biomodifiers can be briefly described as follows.

By adsorbing on cement system's components with a polar «head» and an outward-orientated «tail», surfactant molecules smoothen sharp edges, angles, and surface roughness, thereby making grains more rounded, which in turn makes the mix more flowing. In addition to the above, we should note that with the hydrocarbon «tails» being orientated outwards the hydrophobic repulsive forces occur between them that hinder the grain aggregation process. I.e., synergism effect is obvious here that intensifies the plasticizing effect.

But an adsorbed surfactant layer has also another effect.

Hydrocarbon chain "pale fencing" intrinsically hinders water molecules' penetration to the surface of clinker grains, which extends the time of setting and solidifying. This fact is supported by hydration process deceleration, which is clearly seen when comparing charts that demonstrate plastic strength changing of the reference (plain) cement system and mixes with a biomodifier.
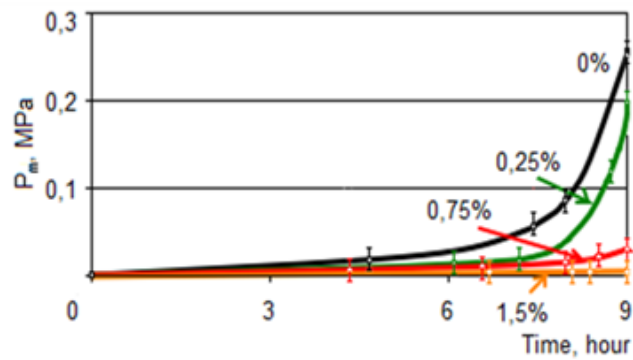
Figure 3. Structure formation of a cement paste with a glycolipid additive (% of cement).

In terms of plasticizing effect comparison, it should be highlighted that this effect is determined by a quantitative dosage of the fluxing agent added and is not influenced by a qualitative composition – paste, mortar, or concrete mix. That means that developed modifiers increase the flowability of cement pastes, cement mortars, and concrete mixes. The same plasticizing technique from the proposed bioadditives emerges in systems prepared using the different cements, though their quantitative characteristics vary widely.
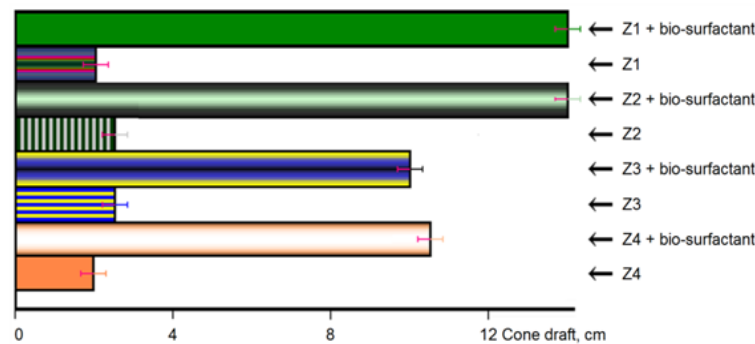
Figure 4. Bioflux effect on the flowability of systems prepared using the different cements.

In general, though, greater importance of fluxing is characteristic of poly-cement mixes.

In-process devices and designs are often exposed to negative environmental factors, specifically – to sub-zero temperatures. Moreover, the concrete freeze-thaw resistance is significantly impacted by the number of open water penetrable pores. The biosurfactant use in certain dosage appeared to not compromise the freeze-thaw resistance. This parameter of a modified concrete in the dosage of 0.2~0.3 % of cement mass retains the level of a plain composition, as demonstrated by sample compression test results after multiple freeze-thaw cycles (see Fig. 5).
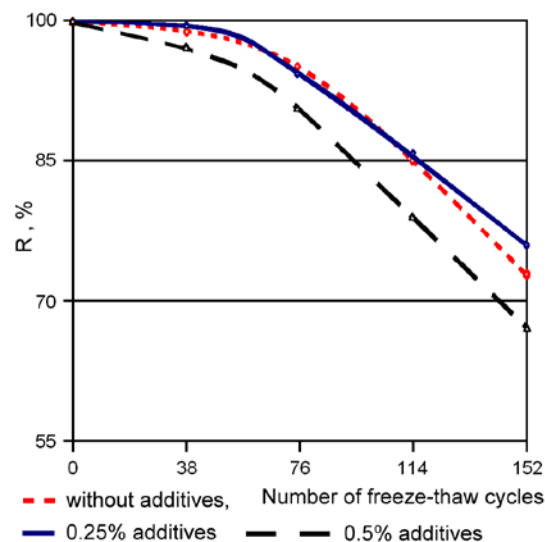
Figure 5. Material strength change with exposure to various biomodifier dosages after alternating freezing and thawing.

When exposed to sub-zero temperatures, the structure of a construction materials undergoes negative changes. Ultimately, developing destructive processes cause material breakage regardless of the initial mechanical strength value. With that in mind, one of the most significant features of concrete is its porosity [49–51]. In addition, we can have a certain understanding of a pore space within the structure of hardened concrete via its water absorption kinetics. The nature of charts shows that the use of an additive does not result in a drastic concrete porosity change.
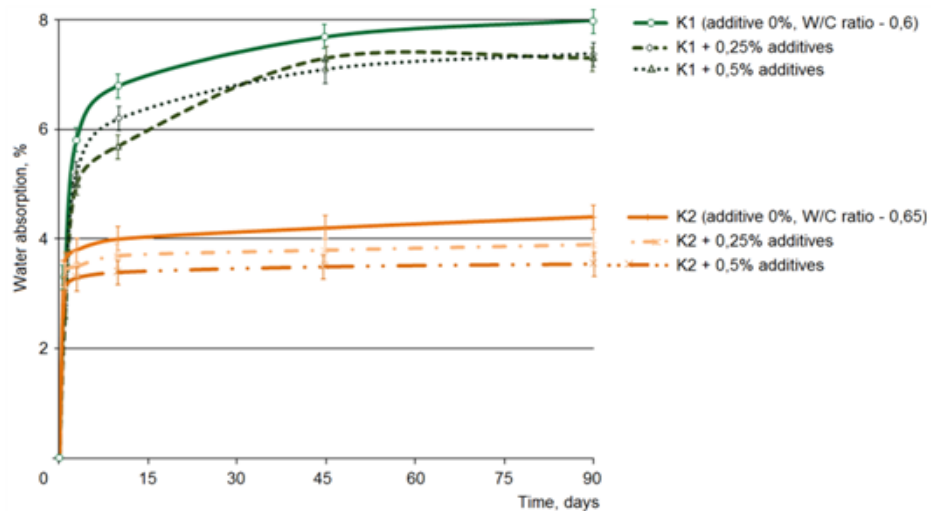
Figure 6. Concrete water absorption kinetics versus different bioadditives' dosages.

Lines showing the mass increase of samples formed of concrete mixes with various glycolipid modifier dosage and reference (plain) composition are strictly synchronous. It proves that the pore size has not changed. However, general porosity of a material with added fluxing agent is lower than in a concrete made of similar blank mix compositions, which is evidenced by a higher position of the reference composition line.

There are rather interesting results with changes in strength characteristics of a material with various content of biomodifier hardening in normal conditions.
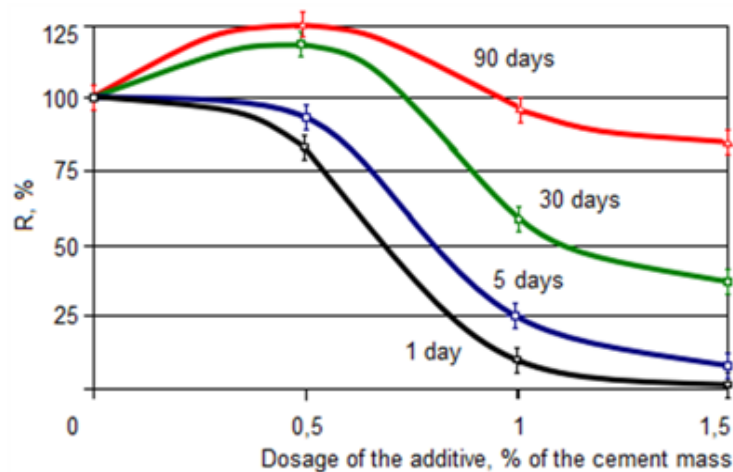
**Figure 7. Time variation of the strength of a cement mortar
with a glycolipid additive under normal hardening condition.**

Apparently, short-term strength of blocks formed of mixes with an additive is more than 0.8 % lower than corresponding values of a reference lot (plain). However, this difference gradually fades away over time and with the lapse of three months the strength characteristics of samples made of the blank mix no longer exceed those of compositions with a plasticizer.

The findings are a solid proof of screening effect of the adsorbed biosurfactant layer on the surface of cement grains.

On the basis of these findings, we can conclude that it is quite possible to add glycolipid bioadditive of up to 0.8 % of cement mass. Such dosages make the modified material strength not only comparable to similar parameters of a reference composition, but even higher by up to 25 % at three months.

The cement clinker minerals hydration in mixes containing a glycolipid modifier after hygrothermal processing may be evaluated by the resulting X-ray phase analysis of diffraction patterns shown on.
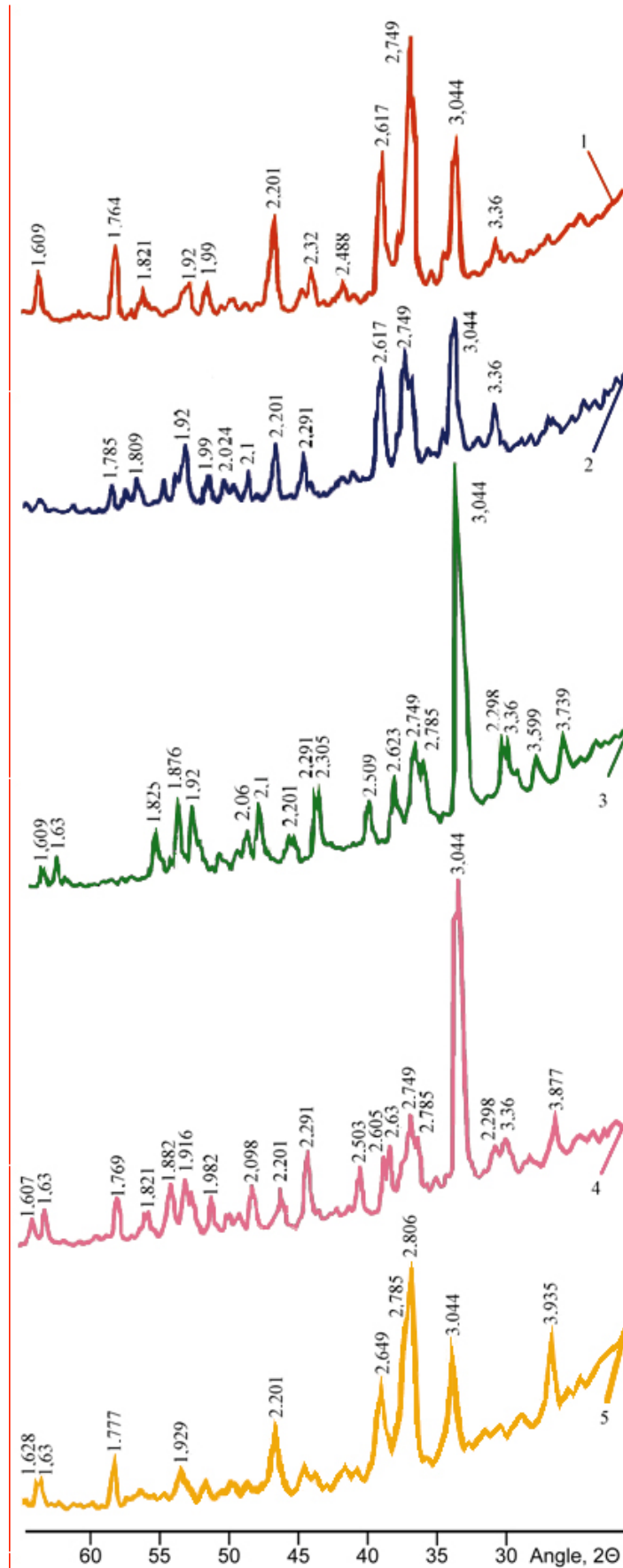
Figure 8. X-rays of a cement stone with a glycolipid plasticizer after hygrothermal processing. Additivecontent (% ofcement): 1 – 0; 2 – 0.1; 3 – 0.25; 4 – 0.5; 5 – 1.

The glycolipid additive compositions show the lower degree of hydration of base minerals than in a reference (plain) composition mix with a higher crystalline hydrate content than in any other mixes.

Thus, the use of biosurfactants hinders the hydration of clinker minerals during hygrothermal processing of a material, with the perfectly structured compounds to form. The latter is confirmed by predominance of single peaks on powder diffraction patterns of compositions with an additive compared to fuzzy apexes on the reference composition X-ray.

Occurring changes may be the result of additive sorbing on hydration products and hindering structure forming processes. Hydration inhibition by an adsorption layer of a modifier has the most significant impact on the material strength at early stages of hardening. During this period there are significantly less hydrated newgrowths formed in mixes with a bioflux, which means their strength characteristics are lower. In the course of time the negative impact of an additive (on strength characteristics) weakens. It is quite possibly related to activation of hydration products' surfaces by modifier's molecules followed by embedding of these molecules into the forming material structure.

Structure forming inhibition will inevitably affect the cement system flowability as well. Cement agent hydration deceleration along with newgrowths forming processes leads to release of a portion of water, which is an additional factor for plasticizing effect increase. These are the conditions that are created by introduction of glycolipid modifiers into the composition of cement mixes.

One may evaluate the extent of impact of a fluxing agent dosage on the flowability of a mortar mix by the charts shown on Fig. 9.
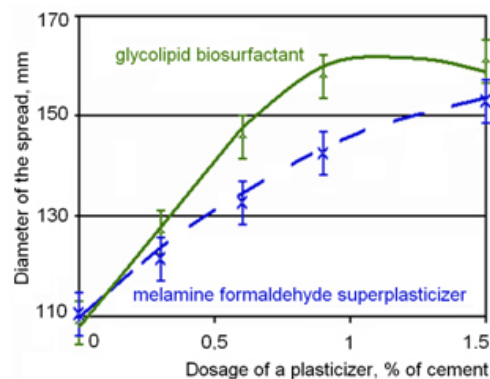
Figure 9. Impact of a modifier on the mortar spread (cement – Z1, mortar:sand = 1:3, W/C = 0.64).

As we can see, the most significant increase in flowability is observed at the consumption rate of a plasticizer of up to 1.5 % of cement mass, while its higher amount is not so effective. In fact, a higher additive dosage is not reasonable, as fluxion is disproportionate to its consumption rate. We believe that these observations are related to saturation of surfaces of cement paste newgrowths at agent introduction of no more than 1.5 % of cement mass. Further concentration of plasticizer molecules in a dispersion medium doesn't lead to its fluxion increase, but only hinders the formation of new phase contacts instead, which inhibits the new structure forming [52–55].

This fact is especially obvious on the charts of cement paste setting in the presence of bioadditives.

Therefore, molecules of the fluxing agent in a dispersion system are adsorbed on surfaces of highly-dispersive components by polar groups, creating a molecular layer with outward-orientated hydrocarbon radicals. Due to worsening of hydration conditions the structure forming processes are decelerated, and strength development shifts to the long run.

Notably, the most significant effect of biomodifier's adsorption layers is observed in mixes with highly-dispersive grains and anisometric particles with sharp edges, angles, and defective surfaces. In this case the grain shape is changed due to smoothening of sharp edges, angles, and surface irregularities by adsorbed layers of biosurfactant molecules that simultaneously create a structural-mechanical barrier. Cement paste, the most active concrete mix component, is such a system. That is why, additive's molecules adsorbed on surfaces of concrete mix disperse components draw them aside, acting as a kind of lubricant as well. In turn, highly-dispersive grains covered with an adsorption surfactant layer along with particles that have anisometric shape hinder aggregation of larger components, thereby enhancing cement system fluxing.

This is a general, basic, and brief description of the essence of processes that take place in cement systems with added biomodifiers.

The existing liquefiers are obsolete; there is a need for an alternative composition and an alternative production technology.

Alternative modifiers should be found among natural compounds or synthesized from their fragments; industrial production of such modifiers should use biotechnology.

The authors theorized upon a cement plasticizer based on fragments of natural compounds, lipids and carbohydrates, and theoretically constructed its structure.

They picked a non-pathogenic microbial culture, *Leuconosloc mesenteroides*, and 'tamed' it to synthesize this product.

The authors further designed a synthetic nutrient medium and optimized the fermentation parameters.

Experiments showed that adding the newly made biological surfactants to the cement composition delayed the structuring. Higher doses (>0.8 wt.%) resulted in the most prominent delay in the early hydration of crystalline cement formations. The additives would be adsorbed on the finely dispersed components of the binder, thus preventing the water-clinker interface.

Cement systems with these biomodifiers showcased absorption combined with chemical effects, i.e. chemisorption. Chemisorption was the first of all of the characteristics of the components in the surficial active centers. As a result, the most active components were neutralized early in hydration.

Thus, the microbially synthesized surfactant had a strong liquefying effect on cement systems of any composition regardless of the binder concentration.

The authors found that a high dosage (>0.8 wt.%) is strongly not recommended for glycolipid liquefiers. The reason is that it not only inhibits clinker hydration but also reduces the strength of the cured concrete.

On the other hand, while early structuring may be slower, such biomodifiers do strengthen the cured material in the long term. Experiments showed that the optimal dosage of the liquefier (up to 0.8 % wt.%) produced a material that was 20÷30 % stronger than its additive-free counterpart. Frost resistance was not compromised. In addition, cement composites with the glycolipid additive were noted to absorb less water.

Based on the theoretical concept put forward, the authors successfully synthesized friendly biomodifiers for construction mixes.

Thus, microbial synthesis produced efficient cement system modifiers that would be subject to no environmental restrictions for industrial and residential construction.

References

1. Gambhir, M.L. Concrete Technology: Theory And Practice. 5th Edition. McGraw Hill Education (India). New Delhi, 2013. 792 p.

2. Kalashnikov, V.I., Tarakanov, O.V., Kusnetsov, Y.S., Volodin, V.M., Belyakova, E.A. Next generation concreteon the basis of fine-grained dry powder mixes. Magazine of Civil Engineering. 2012. 34(8). Pp. 47-53. (rus). DOI: 10.5862/MCE.34.7.

3. Nagrockienė, D., Girskas, G., Skripkiūnas, G. Properties of concrete modified with mineral additives. Construction and Building Materials. 2017. 135. Pp. 37–42. DOI: 10.1016/j.conbuildmat.2016.12.215

4. Vu, Q.H., Pham, G., Chonier, A., Brouard, E. et al. Impact of different climates on the resistance of concrete to natural carbonation. Construction and Building Materials. 2019. 216. Pp. 450–467. DOI: 10.1016/j.conbuildmat.2019.04.263

5. Guadalupe Sierra-Beltran, M., Jonkers, H.M., Schlangen, E. Characterization of sustainable bio-based mortar for concrete repair. Construction and Building Materials. 2014. 67 (C). Pp. 344–352. https://doi.org/10.1016/j.conbuildmat.2014.01.012

6. Ikumapayi, C.M., Adeniji, A.A., Obisesan, A.A. et al. Effects of Carbonation on the Properties of Concrete. Scientific Review. 2019. 5(12). Pp. 205–214.

7. Yoshihiko Ohama. Additives to concrete and mortars. WilliamAndrew. 1995. 246 p.

8. Li, Q., He, Ch., Zhou, H. et al. Effects of polycarboxylate superplasticizer-modified graphene oxide on hydration characteristics and mechanical behavior of cement. Construction and Building Materials. 2021. 272(22). DOI: 10.1016/j.conbuildmat.2020.121904

9. Casagrande, C.A., Jochem, L.F., Ongherob, L. et al. Effect of partial substitution of superplasticizer by silanes in Portland cement pastes. Journal of Building Engineering. 2020. 29. DOI: 10.1016/j.jobe.2020.101226

10. Stark, J. Recent advances in the field of cement hydration and microstructure analysis. Cement and Concrete Research. 2011. 41(7). Pp. 666–678. DOI: 10.1016/j.cemconres.2011.03.028

11. Bungey, J.H., Grantham, M.G. Testing of Concrete in Structures. Taylor and Francis. 4th edition.CRC Press. London, 2014. 352 p.

12. Morin, V., Tenoudji, F., Cohen, A., Feylessouli et al. Superplasticizer effects on setting and structuration mechanisms of ultra-high-performance concrete. Cement and Concrete Research. 2001. 31. Pp. 63–71.

13. Han, S., Van, P.Y., Kong, X.M. Study on the compatibility of cement-superplasticizer system based on the amount of free solution. Technological Sciences. 2011. 54 (1). Pp. 183–189. DOI: 10.1007/s11431-010-4174-2

14. Wang, K., Jansen, D.C., Shah, S.P. et al. Permeability study of cracked concrete. Cement and Concrete Research. 1997. 27(3). Pp. 381–393.

15. Rubio-Hernández, F.J., Adarve-Castroa, A., Velázquez-Navarrob, J.F. et al. Influence of water/cement ratio, and type and concentration of chemical additives on the static and dynamic yield stresses of Portland cement paste. Construction and Building Materials. 2020. 235. 117744. DOI: 10.1016/j.conbuildmat.2019.117744

16. Khaemba, D.N., Azam, A., See, T.-L., Neville, A. et al. Early strength development in concrete using preformed CSH nano crystals. Tribology International. 2020. 146. 106243. DOI: 10.1016/j.triboint.2020.106243

17. Kiski, S.S., Ageyev, I.V., Ponomarev, A.N., Kozeyev, A.A., Yudovich, M.Ye. Investigation of carboxylate plasticizer modification potential in modified fine-grained concrete mixes. Magazine of Civil Engineering. 2012. 34(8). Pp. 42–46. (rus). DOI: 10.5862/MCE.34.6.

18. Sakai, E., Kakinuma, Y., Yamamoto, K., Daimon, M. Relation between the Shape of Silica Fume and the Fluidity of Cement Paste at Low Water to Powder Ratio. Journal of Advanced Concrete Technology.2009. 7(I). Pp. 13–20. DOI: 10.3151/jact.7.13

19. Choi, Y.W., Kim, Y.J., Shin, H.C., Moon, H.Y. An Experimental Research on the Fluidity and Mechanical Properties of High-Strength Lightweight Self-Compacting Concrete. Cement and Concrete Research. 2006. 9. Pp. 1595–1602. DOI: 10.1016/j.cemconres.2004.11.003

20. Azam, A., Dorgham, A., Khaemba, D.N., Salehi, F.M. Understanding the role of surface textures in improving the performance of boundary additives, part II: Numerical simulations. Tribology International. 2020. 152:106252. DOI: 10.1016/j.triboint.2020.106252

21. Weichert, D., Ponter, A. (Eds.). Limit States of Materials and Structures: Direct Methods. Springer Netherlands. 2009. 320 p.

22. Young, J.F. A review of the mechanisms of set-retardation in Portland cement pastes containing organic admixtures. Cement and Concrete Research. 1972. 2(4). Pp. 415–433.

23. Chaudhari, O.A., Biernacki, J., Northrup, S.H. The Effect of Select Organic Compounds on Hydration of Portland Cement: Molecular Scale Insights. Annual Conference: American Ceramic Society. Cement Division. 2016. Evanston, Illinois.

24. Das, S., Ray, S., Sarkar, S. Early strength development in concrete using preformed CSH nanocrystals. Construction and Building Materials. 2020. 233. 117214. DOI: 10.1016/j.conbuildmat.2019.117214

25. Okamura, H., Ozawa, K., Ouchi, M. Self-compacting concrete. 2000. 1 (1). Pp. 3–17. DOI: 10.1680/STCO.2000.1.1.3

26. Wiktor, V., Jonkers, H.M. Quantification of crack-healing in novel bacteria-based self-healing concrete. Cement and Concrete Composites. 2011. 33 (7). Pp. 763–770. DOI: 10.1016/j.cemconcomp.2011.03.012

27. Maruya, E., Osaki, M., Igarashi, H. Relationships between Rheological Constant of Cement Paste and Fluidity of High-Fluidity Concrete. Journal of Advanced Concrete Technology. 2006. 4 (2). Pp. 251–257. DOI: 10.3151/jact.4.251

28. Han, B., Zhang, L., Ou, J. Self-Compacting Concrete. In: Smart and Multifunctional Concrete Toward Sustainable Infrastructures. 2017. Pp. 11–36.

29. Wingender J., Neu T.R., Flemming H.C. What are bacterial extracellular polymeric substances? Microbial Extracellular Polymeric Substances. Springer. Berlin Heidelberg. 1999. Pp. 1–19.

30. Sierra-Beltran, L., Jonkers, H.M. Crack self-healing technology based on bacteria. Journal of Ceramic Processing Research. 2015. 16(S1). Pp. 33–39.

31. Tziviloglou, E., Tittelboom, K.V., Palin, D., Wang, J. Bio-Based Self-Healing Concrete: From Research to Field Application. Advances in Polymer Science. 2016. Pp. 345–385. DOI: 10.1007/12_2015_332

32. Jonkers, H.M. Self-healing concrete: a biological approach. In: van der Zwaag S. (Ed.). Self-Healing Materials: An Alternative Approach to 20 Centuries of Materials. Springer Science. 2007. Dordrecht. Pp. 195–204.

33. Jonkers, H.M., Thijssen, A., Muyzer, G., Copuroglu, O. et al. Application of bacteria as self-healing agent for the development of sustainable concrete. Ecological Engineering. 2010. 36(2). Pp. 230–235. DOI: 10.1016/j.ecoleng.2008.12.036

34. Lim, J.L.G., Ramanb, S.N., Lai, F.-Ch., Mohdet, M.F. al. Synthesis of nano cementitious additives from agricultural wastes for the production of sustainable concrete. Journal of Cleaner Production. 2018. 171. Pp. 1150–1160. DOI: 10.1016/j.jclepro.2017.09.143

35. Christofi, N., Ivshina, I. Microbial Surfactants and Their Use in Soil Remediation. In: Bioremediation of Aquatic and Terrestrial Ecosystems. 2005. Pp. 311–327. DOI: 10.1201/b11002-10

36. Gunther IV, N.W., Nuñez, A., Fett, W., Solaiman, D.K.Y. Production of Rhamnolipids by Pseudomonas chlororaphis, a Nonpathogenic Bacterium. Applied and Environmental Microbiology. 2005. 71 (5). Pp. 2288–2293. DOI: 10.1128/aem.71.5.2288-2293.2005

37. Lima, T.M.S., Procopio, Ch., Brandão, F.D., de Carvalho, A.M.X. et al. Biodegradability of bacterial surfactants. Biodegradation. 2011. 22(3). Pp. 585–592. DOI: 10.1007/s10532-010-9431-3

38. Jiang, T., Gao, Ch., Ma, C., Xu, P. Microbial lactate utilization: enzymes, pathogenesis, and regulation. Trends in Microbiology. 2014. 22 (10). Pp. 589–599. DOI: 10.1016/j.tim.2014.05.008

39. John, R.P., Nampoothiri, K.M., Pandey, A. Fermentative production of lactic acid from biomass: an overview on process developments and future perspectives. Applied Microbiology and Biotechnology. 2007. 74(3). Pp. 524–534. DOI: 10.1007/s00253-006-0779-6

40. Fakas, S. Lipid biosynthesis in yeasts: A comparison of the lipid biosynthetic pathway between the model non-oleaginous yeast Saccharomyces cerevisiae and the model oleaginous yeast Yarrowia lipolytica. Engineering in Life Sciences. 2017. 17. Pp. 292–302. DOI: 10.1002/elsc.201600040

41. Chi, J.M., Huang, R., Yang, C.C. Effects of carbonation on mechanical properties and durability of concrete using accelerated testing method. Journal of Marine Science and Technology. 2002. 10 (1). Pp. 14–20.

42. Edvardsen, C. Water Permeability and Autogenous Healing of Cracks in Concrete. Aci Materials Journal. 1999. 96(4). Pp. 448–454. DOI: 10.14359/645

43. Plank, J., Hirsch, Ch. Impact of zeta potential of early cement hydration phaseson superplasticizer adsorption. Cement and Concrete Research. 2007. 37 (4). Pp. 537–542. DOI: 10.1016/j.cemconres.2007.01.007

44. Mander, J., Adams, L.D., Larkin, E.E. A Method for the Determination of Some Minor Compounds in Portland Cement and Clinker by X-Ray Diffraction. Cement and Concrete Research. 1974. 4. Pp. 533–544.

45. Groot, W.J., Borén, T. Life cycle assessment of the manufacture of lactide and PLA biopolymers from sugarcane in Thailand. The International Journal of Life Cycle Assessment. 2010. 15(9). Pp. 970–984. DOI: 10.1007/s11367-010-0225-y

46. Bazan, N.G. (Eds.). Function and Biosynthesis of Lipids. Springer. 2012. 646 p.

47. Van Hamme, J.D., Ward, O.P. Physical and Metabolic Interactions of Pseudomonas sp. Strain JA5-B45 and Rhodococcus sp. Strain F9-D79 during Growth on Crude Oil and Effect of a Chemical Surfactant on Them. Applied and Environmental Microbiology. 2001. 67(10). Pp. 4874–4879. DOI: 10.1128/AEM.67.10.4874-4879.2001

48. Mors, R.M., Jonkers, H.M. Feasibility of lactate derivative based agent as additive for concrete for regain of crack water tightness by bacterial metabolism. Industrial Crops and Products. 2017. 106. Pp. 97–104. DOI: 10.1016/j.indcrop.2016.10.037

49. Fantilli, A.P., Kwon, S., Mihashi, H., Nishiwaki, T. Synergy assessment in hybrid Ultra-High Performance Fiber-Reinforced Concrete (UHP-FRC). Cement and Concrete Composites. 2018. 86. Pp. 19–29. DOI: 10.1016/j.cemconcomp.2017.10.012

50. Fernández, Á., García Calvo, J.L., Alonso, M.C. Ordinary Portland Cement composition for the optimization of the synergies of supplementary cementitious materials of ternary binders in hydration processes. Cement and Concrete Composites. 2018. 89. Pp. 238–250. DOI: 10.1016/j.cemconcomp.2017.12.016

51. Nguyen, H., Adesanya, E., Ohenoja, K., Kriskova, L. et al. Byproduct-based ettringite binder – A synergy between ladle slag and gypsum. Construction and Building Materials. 2019. 197. Pp. 143–151. DOI: 10.1016/j.conbuildmat.2018.11.165

52. Flatt, R., Schober, I. Superplasticizers and the rheology of concrete. Understanding the Rheology of Concrete. Woodhead Publishing Series in Civil and Structural Engineering. 2012. Pp. 144–208. DOI: 10.1533/9780857095282.2.144

53. Bauchkar, S.D., Chore, H.S. Effect of PCE superplasticizers on rheological and strength properties of high strength self-consolidating concrete. Advances in Concrete Construction. 2018. 6 (6). Pp. 561–583. DOI: 10.12989/acc.2018.6.6.561

54. Superplasticizers and Other Chemical Admixtures in Concrete. Proceedings Eleventh International Conference. Editors: V. Mohan Malhotra, Pawan R. Gupta, Terence C. Holland. Ottawa. ON. 2015. 513 p.

55. Plank, J., Ilg, M. The Role of Chemical Admixtures in the Formulation of Modern Advanced Concrete. 3rd International Conference on the Application of Superabsorbent Polymers (SAP) and Other New. 2019. 24. Pp. 143–157.

Information about author:

Sergey Dudynov, *Doctor of Technical Science*
ORCID: https://orcid.org/0000-0002-0934-549X
E-mail: dsergey@mail.ru

Method for determining the thermal fluctuation constants of the generalized Zhurkov equation

A.V. Erofeev ✉ iD , **T.I. Gorokhov** iD

Tambov State Technical University, Tambov, Russia

✉ *AV.Erofeev @yandex.ru*

Abstract. Reliable forecasting of the service life of building materials and products allows you to lay down the costs of repair work in a timely manner, which in modern economic realities is undoubtedly an urgent task. This paper presents the results of a study on the development and comparison with existing methods for determining the thermal fluctuation constants of the generalized Zhurkov equation. A new method is proposed for determining the thermal fluctuation constants of the generalized Zhurkov equation. Practical application of the methodology will make it possible to reliably predict the service life of building materials. The main goal is to develop a method for determining the thermal fluctuation constants of the generalized Zhurkov equation, characterized by higher reliability by reducing the number of operations entailing errors, while increasing the number of experiments conducted under identical conditions (increasing the sample when determining durability under constant operating conditions). To achieve this goal, it is necessary to solve a number of tasks: 1) analyze the main provisions of the thermal fluctuation concept; 2) develop a method for determining the thermal fluctuation constants; 3) to conduct a comparative analysis of the obtained results of determining the thermal fluctuation constants. The object of the study is the constants of thermal fluctuation. The subject of the study is a new method for determining thermal fluctuation constants. The main methods of scientific knowledge used in the development of the methodology are hypothetical (the hypothesis of a linear dependence of the change slope of direct temperatures in the coordinates of the logarithm of durability - stress) and experiment (determination of durability of samples under transverse bending under specified operating conditions). A new method was developed for determining the thermal fluctuation constants of the generalized Zhurkov equation. It allows you to determine constants by plotting only one straight line temperature and one control point at a different temperature. Application of the proposed technique allows increasing the number of samples tested in identical conditions while reducing labor costs for experimental research. An increase in the sample leads to an increase in the accuracy and reliability of predicting the service life of building materials.

1. Introduction

The problem of reliably predicting the durability of building materials, which is understood as the time before the onset of the limiting state, is one of the complex problems of construction science. The classical mechanical concepts of the strength of a material interpret the process of destruction as a critical event, the arrival of which is irreversible when the selected criterion of strength reaches its maximum value [1–5]. Otherwise, destruction is considered impossible, which contradicts reality [6–8]. In the middle of the last

century, many researchers have experimentally established, especially for polymer materials, the effect on the strength of the material not only by the time of stress action, but also by the ambient temperature [6, 9–13]. Thus the destruction occurred at values of stresses lower than the critical ones, however, such destruction took time.

S.N. Zhurkov was able to describe the observed temperature-time force equivalence of the destruction process by the formula, which was later named after him [6, 9]:

$$\tau = \tau_0 \exp\left(\frac{U_0 - \gamma \cdot \sigma}{R \cdot T}\right). \tag{1}$$

And he was also able to reveal the physical meaning of the constants included in the resulting equation [6, 9]: τ_0 is constant, numerically close to the period of thermal vibrations of atoms; T is the absolute temperature; R is Boltzmann's constant; γ is structural-mechanical constant characterizing the geometric parameters of the material and the mechanical component of the fracture process; U_0 activation energy of the destruction process.

It was they who were proposed to consider the thermal motion of the kinetic units of a solid as a decisive factor in the process of destruction, while the mechanical component only ordered the process of oscillation of particles. This postulate formed the basis for the formation of first a kinetic and, subsequently, a thermofluctuation concept of fracture and deformation of solids.

S.B. Ratner and V.P. Yartsev modernized the Zhurkov equation (1) by introducing into it the limiting temperature of the existence of a rigid body without changing the interpretation of the role of thermal motion [14]. The equation is called the generalized Zhurkov equation:

$$\tau = \tau_m \cdot \exp\left[\frac{U_0 - \gamma \cdot \sigma}{R} \cdot \left(T^{-1} - T_m^{-1}\right)\right], \tag{2}$$

where, τ is the durability of the material or the time until one of the limit states occurs, c; R is universal gas constant, kJ / mol • K; σ is stress, MPa; T is temperature, K; τ_m, U_0, γ, T_m are physical constants of the material, having the following physical meaning for the classical case of convergence in a straight beam (Fig. 1.3, a): τ_m is the minimum time of destruction of a solid, characterized by the oscillation period of a particular kinetic unit (atom, group of atoms or segments), c; U_0 is the maximum activation energy of the destruction process, which is determined by the energy of bonds that prevents the loss of body integrity; moreover, in metals it is close to the sublimation energy, in polymers – to the activation energy of the thermal destruction process, i.e. the maximum activation energy of the destruction process is numerically close to the value of the activation energy for the decay of interatomic bonds in solids, kJ/mol; γ is structural-mechanical constant characterizing the efficiency of a mechanical field when a load is applied to the body kJ/(mol • MPa); T_m is the limiting temperature of the existence of a solid at which it decomposes in one thermal vibration, K.

Thus, it is possible to predict the durability of building materials within the framework of the thermofluctuation concept of fracture and deformation using formula (2). To predict the durability, it is necessary to know the four thermal fluctuation constants included in the generalized Zhurkov equation, which are determined by the graphic-analytical method from the experimentally obtained data on the dependence of durability (logarithm of durability) on the acting stresses and ambient temperature. To date, these constants have been established for a whole range of building materials [15–20]. However, the existing method for their determination is not distinguished by a high degree of reliability. This is due to the fact that according to the existing method for determining the constants, it is required to determine the durability (logarithm of durability) for each of three temperatures at five voltages. This is also due to the need to work in semi-logarithmic coordinates, when even minor deviations of the logarithm of durability in the zone of low durability (the range of experiments) leads to significant errors in further calculations of the durability of the material. The studies carried out on the example of polyvinyl chloride boards show that the values of the constants determined by different methods (graphical, graphic-analytical and mathematical) show significant discrepancies [21]. As well as the values of the constants obtained by different researchers on an identical array of initial data [22].

Thus, the main goal is to develop a method for determining the thermal fluctuation constants of the generalized Zhurkov equation, which is characterized by increased reliability due to a reduction in the number of operations entailing the appearance of errors, while increasing the number of experiments

conducted under identical conditions (increasing the sample when determining the durability under constant operating conditions).

To achieve this goal, it is necessary to solve a number of tasks:

1) to analyze the main provisions of the thermofluctuation concept;

2) to develop a method for determining thermofluctuation constants;

3) to carry out a comparative analysis of the results of determining the thermofluctuation constants obtained.

The object of study is thermoeluktuation constants.

The subject of the study is a new method for determining thermoeluctation constants.

2. Methods

To achieve this goal, it is necessary to check the hypothesis put forward (a hypothetical research method) that in the case of the invariability of the material structure in the entire temperature range, the tangent of the slope of direct temperatures in the coordinates $\lg \tau - \sigma$ obeys a linear relationship. The hypothesis put forward is verified theoretically, by the reverse method and experimentally.

For experimental verification of the hypothesis, polyvinyl chloride plates were chosen as the object of the study. This choice is due to the fact that it has a homogeneous structure and the presence of temperature-time force equivalence of the destruction process is clearly traced for it.

The dependence of durability (logarithm of durability) on stress and temperature was determined for polyvinyl chloride plates with transverse bending according to the following algorithm:

1. Determination of the critical load at which the durability is minimal.

2. Selection of the boundaries of temperature-force conditions based on the obtained critical load.

3. Determination of the durability of the material in the selected temperature and power conditions.

The studies were carried out on a six-position stand according to the standard method [20, 23]. The temperatures at which the measurements were carried out were 15, 30, 45 °C. For each temperature, five voltages are selected in the range from 0.75 to 0.95 of breaking. To obtain each point, at least 8 samples were tested under similar conditions. The results obtained were subjected to statistical processing according to the method according to Russian State Standard GOST R 8.736-2011 to eliminate gross errors and establish the boundaries of the confidence interval.

Thermofluctuation constants of the generalized Zhurkov equation were determined graphically, graphically, analytically, and mathematically according to the standard method [21].

3. Results and Discussion

The dependence of the logarithm of the durability on the effective voltage at constant temperature is linear and in general form can be written as follows:

$$\lg \tau (\sigma) = a \cdot \sigma + b, \tag{3}$$

where a is slope or tangent of the angle of inclination of a straight line, the physical meaning of which is the rate of the process; b is free term of the equation determining the logarithm of the life in the absence of stresses.

The absence of stresses in a solid is physically impossible, since the body's own weight creates stress in it. If in the idealized model we neglect the stresses from its own weight, then the value of the free term of equation (3) will determine the durability of the body in the absence of other types of stress.

When the temperature changes, the values of the coefficients of Eq. (3) will also change, and with increasing temperature a it increases, and b – decreases. With decreasing temperature, they respectively decrease and increase. The temperature of a body can vary in the range from absolute zero (0 K), which in practice, based on the provisions of thermodynamics, is unattainable, and the maximum temperature of the existence of a solid. Thus, the straight line of temperature corresponding to the temperature of absolute zero is located parallel to the ordinate of the graph plotted in the coordinates "logarithm of durability – stress" (Fig. 1). In this case, the coefficients of equation (3) tend to infinity, which is consistent with one of the main postulates of the thermofluctuation concept: the decisive factor in the destruction of a solid is the

thermal motion of kinetic units, and at a temperature of absolute zero, the process of motion stops [24]. The straight line of the maximum temperature of existence of a solid is parallel to the abscissa axis (stress axis) (Fig. 1). Consequently, the value of the logarithm of the durability is a constant value, which is equal to the oscillation period of the kinetic unit of a solid, and does not depend on the voltage. Thus, it seems logically justified to consider the change in durability between these limiting temperatures, since a negative temperature is impossible, and the study of behavior at temperatures above the temperature of the existence of a material has no physical meaning: the destruction of a solid requires a minimum time.
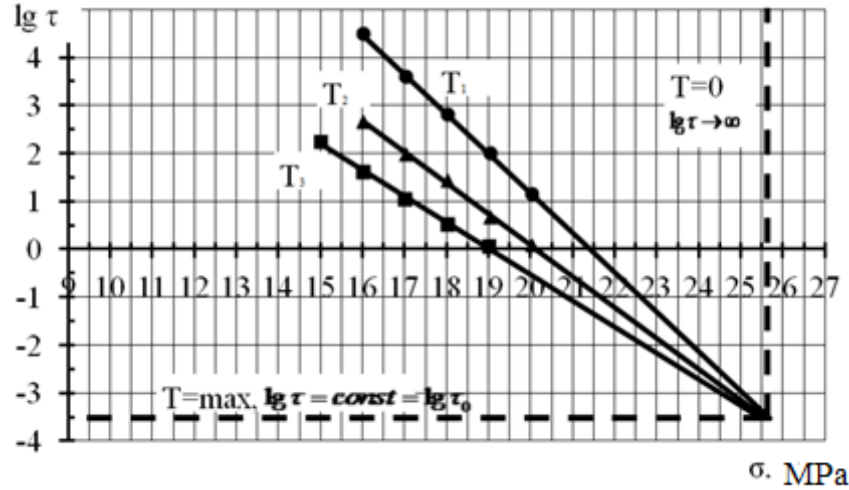
Figure 1. Example of a straight beam with boundary conditions.

If the structure of the material does not change over the entire temperature range under consideration, i.e. the thermal fluctuation constants of the generalized Zhurkov equation remain constant, according to the hypothesis put forward, the dependence of the change in the coefficient a of equation (1) on temperature or its inverse value is linear:

$$a = c \cdot T + d \tag{4}$$

or

$$a = c^* \cdot \frac{1}{T} + d^* \tag{5}$$

moreover, the dependence of the change in the coefficient b on temperature or its inverse value is also linear:

$$b = k \cdot T + \mu \tag{6}$$

or

$$b = k^* \cdot \frac{1}{T} + \mu^*. \tag{7}$$

Straightness occurs only in the operating temperature range. So, when considering the dependence of the coefficient a on temperature at a temperature of absolute zero, the coefficient a tends to infinity (vertical asymptote), and at temperatures above the temperature of existence of a solid, the dependence has no physical meaning, since the body itself ceases to exist. In the case of considering the dependence of this coefficient on the reciprocal temperature, then at absolute zero the coefficient a linearly goes to infinity, and at the temperature of existence it crosses the abscissa axis and in the first positive half-quarter at temperatures above the temperature of existence of a solid body also has no physical meaning. The linear dependence of the coefficient b on temperature is also valid only up to the temperature of existence of a solid, at which it becomes an asymptote $\lg \tau_0$.

The hypothesis put forward is tested, as indicated earlier, in three ways: theoretical, proof from the opposite and practical. Let the dependences of the change in the coefficients of equation (3) be linear and described by equations (4) and (6), respectively, then substituting them into equation (3) we obtain:

$$\lg \tau = (c \cdot \sigma + d) \cdot T + k \cdot T + \mu \tag{7}$$

resolving which with respect to a variable T (temperature), taking into account that the voltage is in this case a constant value $(\sigma = const)$, it turns out:

$$\lg \tau = (c \cdot \sigma + k) \cdot T + (d \cdot \sigma + \mu). \tag{8}$$

Thus, we have a linear relationship.

Similar actions with formulas (5) and (7) lead to a similar result:

$$\lg \tau = \left(c^* \cdot \sigma + k^*\right) \cdot \frac{1}{T} + \left(d^* \cdot \sigma + \mu^*\right). \tag{9}$$

Thus, the resulting equations (8) and (9) are forward stress equations constructed in the coordinate system of the logarithm of durability versus temperature (reciprocal temperature), which are obtained by rebuilding the graph in the coordinate system "$\lg \tau - \sigma$" into the coordinate system "$\lg \tau - T$" ("$\lg \tau - \dfrac{1}{T}$") practice. Consequently, the hypothesis put forward is confirmed.

In the case of proof from the opposite, let the dependences of the change in the coefficients of Eq. (3) are not linear, but obey, say, parabolic dependences. Then, solving equation (3) with respect to a variable at a constant voltage, the dependence of the logarithm of durability on temperature (reciprocal temperature) will not have a linear form, which contradicts the experimental data.

For polyvinyl chloride boards during transverse bending tests, the following direct temperatures of the dependence of the logarithm of durability on stress were obtained:

$$T = 15\ °C - \lg \tau(\sigma) = -2.484 \cdot x + 15.766;$$
$$T = 30\ °C - \lg \tau(\sigma) = -1.822 \cdot x + 11.366;$$
$$T = 45\ °C - \lg \tau(\sigma) = -1.68413 \cdot x + 10.4504.$$

When constructing straight lines, the approximation method is used [25].

The change in the coefficient a obeys a linear relationship: $a(T) = 0.0267 \cdot T - 10.077$ $\left(a\left(\dfrac{1}{T}\right) = -2466.6 \cdot \dfrac{1}{T} + 6.1573\right)$, whose correlation coefficient is $R^2 = 0.8749$ $\left(R^2 = 0.8932\right)$. The change in the coefficient b also obeys a linear relationship: $b(T) = -0.1772 \cdot T + 66.215$ $\left(b\left(\dfrac{1}{T}\right) = 16390 \cdot \dfrac{1}{T} - 41.652\right)$, which confirms the hypothesis put forward.

The constant T_m can be obtained from the boundary condition, at $a = 0$. Thus, the maximum temperature for the existence of PVC boards is 380 K (400 K). Substituting the limiting temperature in the dependence of the change in the coefficient b on temperature (return temperature), is determined $\lg \tau_0$. For polyvinyl chloride boards, it is:

$$b(T) = -0.1772 \cdot 380 + 66.215 = -1.121;$$
$$b\left(\frac{1}{T}\right) = 16390 \cdot \frac{1}{400} - 41.652 = -0.677.$$

The remaining two constants are proposed to be found by solving a system of equations in which the operating conditions (set from the operating conditions) and two constants are already known. For polyvinyl chloride boards, such a system of equations may look like this:

$$\begin{cases} 7.28 = 0.076 \cdot \exp\left[\dfrac{U_0 - \gamma \cdot 6.3}{8.314 \cdot 10^{-3}} \cdot \left((273 + 15)^{-1} - 380^{-1}\right)\right] \\[4mm] 107.152 = 0.076 \cdot \exp\left[\dfrac{U_0 - \gamma \cdot 5.3}{8.314 \cdot 10^{-3}} \cdot \left((273 + 45)^{-1} - 380^{-1}\right)\right] \end{cases};$$

$$\begin{cases} 7.28 = 0.215 \cdot \exp\left[\dfrac{U_0 - \gamma \cdot 6.3}{8.314 \cdot 10^{-3}} \cdot \left((273+15)^{-1} - 400^{-1}\right)\right] \\ 107.152 = 0.215 \cdot \exp\left[\dfrac{U_0 - \gamma \cdot 5.3}{8.314 \cdot 10^{-3}} \cdot \left((273+45)^{-1} - 400^{-1}\right)\right] \end{cases}.$$

Whence it follows that U_0 = 409 kJ/mol, γ = 72.6 kJ/mol MPa when working with a direct temperature and U_0 329 kJ / mol, γ = 50 kJ / mol MPa when considering the reverse temperature.

The obtained thermal fluctuation constants of the generalized Zhurkov equation by all methods are summarized in Table 1.

Table 1. A summary table of the found thermal fluctuation constants.

Method of determination	T_m, К	τ_m, с	U_0, kJ/mol	γ, kJ/mol·MPa
Mathematical method [20–22]	400	0.177	313.4	47.15
Graphoanalytical method [20–22]	431	0.011	327.0	48.00
Graphical method [20–22]	390	0.180	370.0	58.00
According to the proposed method	380 (400)	0.076 (0.215)	409.0 (329.0)	72.6. (50.00)

Analysis of the values in Table 1 shows that the thermal fluctuation constants obtained by the proposed method correspond to the constants obtained by the previously used methods, including for other materials [7, 14, 15, 18, 19]. The smallest scatter associated with inevitable determination errors is observed when calculating the constants using the dependence of the inverse temperature on other parameters. The proposed technique allows reducing the errors in determining the constants due to the failure of working with graphs, and also simplifies mathematical calculations. At the same time, the high number of required experiments, each of which is associated with the appearance and accumulation of errors, remains the same. Even in studies that are not the largest in terms of volume, the number of necessary experiments exceeds a hundred. This fact does not greatly affect when working with a rapidly disintegrating material, but with an increase in the durability of the material, the time for conducting a single experiment greatly increases. All this results in many labor costs when receiving input data. Therefore, the next step is to reduce the number of experiments required to determine the thermal fluctuation constants of the generalized Zhurkov equation while maintaining high reliability of the results obtained.

The limiting temperature of existence can be obtained from the pole displacement equation:

$$\frac{1}{T_m} = \frac{c}{A \cdot \rho^2} + \alpha, \tag{10}$$

where c is heat capacity; α is thermal coefficient of linear expansion; ρ is density; A is characteristic of the forces of interatomic attraction.

Dependence (10) was theoretically substantiated by S.B. Ratner. S.N. Zhurkov also established a connection U_0 and γ with the fundamental characteristics of a solid:

$$U_0 = \left(\frac{c}{\alpha}\right) \cdot \varepsilon_0, \tag{11}$$

$$\gamma = \left(\frac{c}{\alpha \cdot E}\right) \cdot k, \tag{12}$$

where c is heat capacity; α is thermal coefficient of linear expansion; E is elastic modulus; ε_0 is the relative value of the limiting change in the interatomic distance leading to rupture; k is local link overload factor.

Determining the characteristics A, ε_0 and k in practice, cause difficulties and therefore the use of formulas (10), (11), (12) for determining the thermal fluctuation constants is limited. However, the limiting temperature of the existence of a solid can be obtained from the derivatogram.

The derivatogram is constructed in a research method called derivatography. Derivatography is based on a combination of differential thermal analysis with physical or physicochemical methods, such as thermogravimetry, dilatometry, mass spectrometry and emanation thermal analysis. Along with the transformations of the substance, which occur under the influence of the thermal effect, the change in the mass [26–28].

Thus, knowing the value of the limiting temperature of existence from the derivatogram, it seems possible and sufficient to determine the remaining thermal fluctuation constants to experimentally obtain a straight line of only one temperature in the "$\lg\tau - \sigma$" coordinate system and the coordinates of one point at any other temperature. Knowing the values of the temperature (inverse temperature) and the value of the coefficient a of equations (4) and (5), as well as the limiting temperature of the existence of a solid, at which $a = 0$, it is necessary to solve the system of equations for c and c и d (c^* и d^*):

$$\begin{cases} a = c \cdot T + d \\ T_m = \dfrac{-d}{c} \end{cases}, \qquad (13)$$

when, substituting the obtained coefficients into Eqs. (4) and (5), it seems possible to find the value of the coefficient a at the temperature (reciprocal temperature) at which the point is obtained experimentally. Then substituting the obtained coefficient into the formula (3), Further, substituting the obtained coefficient into formula (3), for which the operating conditions ($\lg\tau$ and σ) are known, the coefficient b is determined. Thus, the equation of the second line is obtained. The point of intersection of the lines gives the value of the coefficient $\lg\tau_0$. The remaining two thermal fluctuation constants are determined by solving the system of equations, which was shown earlier.

The required number of experiments to obtain one point, as well as the condition for the choice of the control temperature, at which only one point is determined, requires further study and justification.

4. Conclusion

1. A method has been developed for determining the constants of thermal oscillations of the generalized Zhurkov equation, based on the construction of only one direct temperature and one control point at another temperature.

2. It was found that the proposed technique allows to reduce the errors in determining constants due to the failure of working with graphs.

3. It is proved that the proposed method allows to reduce the number of experiments by almost 3 times.

4. It is established that the developed technique allows to increase the number of studies conducted at each point in comparison with the existing method at lower labor costs, which increases the accuracy of forecasting the durability of building materials.

5. It is established that the proposed method simplifies mathematical calculation.

References

1. Mushchanov, V.P., Orzhekhovskii, A.N., Zubenko, A.V., Fomenko, S.A. Refined methods for calculating and designing engineering structures. Magazine of Civil Engineering. 2018. 78(2). Pp. 101–115. DOI: 10.18720/MCE.78.8

2. Travush, V.I., Konin, D.V., Krylov, A.S. Strength of composite steel and concrete beams of high-performance concrete. Magazine of Civil Engineering. 2018. 79(3). Pp. 36–44. DOI: 10.18720/MCE.79.4

3. Lo, K.H., Miyase, A., Wang, S.S. Failure strength predictions for closed-cell polyvinyl chloride foams. Journal of Composite Materials. 2018. 52(30). Pp. 4185-4201. DOI: 10.1177/0021998318777049

4. Koyankin, A.A., Mitasov, V.M. Stress-strain state of precast and cast-in place buildings. Magazine of Civil Engineering. 2017. 74(6). Pp. 175–184. DOI: 10.18720/MCE.74.14

5. Sokova, S., Smirnova, N. Reliability assessment of waterproofing systems of buildings underground parts. IOP Conf. Series: Materials Science and Engineering. 2018. 365. 052028. DOI: 10.1088/1757-899X/365/5/052028

6. Zhurkov, S.N., Abasov, S.A. The temperature and the time dependence of the strength of polymer yarns. Polymer Science. Series A. 1999. 41(12). Pp. 1276–1282.

7. Yartsev, V.P., Kiselyova, O.A., Plotnikova, E.E. Influence of temperature, humidity and ultraviolet irradiation on durability and durability of modified wood. Scientific Herald of the Voronezh State University of Architecture and Civil Engineering. Construction and Architecture. 2011. 9. Pp. 4–10.

8. Yartsev, V.P., Nikolyukin, A.N, Danish, A.B., Aljaboobi, D., Giyasov, B., Giyasov, T. Analytical modeling of glass composite and metal reinforcement adhesion with cements and concrete. E3S Web of Conferences. 2019. 01046. DOI: 10.1051/e3sconf/201911001046

9. Zhurkov, S.N., Narzullaev, B.N. Time dependence of the strength of solids. Journal of Applied Mechanics and Technical Physics. 1953. 23(10). 1677. (rus)

10. Zhurkov, S.N., Korsukov, V.E. Atomic mechanism for the destruction of stressed polymers. Soviet Physics, Solid State. 1974. 15. 1379.

11. Zhurkov, S.N. The question of the nature of physical strength. Solid State Physics. 1980. 22(11). 3344.

12. Regel, V.R., Slutsker, A.I., Tomashevskiy, E.Ye. Kineticheskaya priroda prochnosti tverdykh tel [Kinetic nature of the strength of solids]. M.: Nauka. 1974. 560 p.

13. Potapova, L.B., Yartsev, V.P. Mekhanika materialov pri slozhnom napryazhennom sostoyanii. Kak prognoziruyut predelnyye napryazheniya? [Mechanics of materials under complex stress state. How are limit stresses predicted?]. Moscow: «Izdatelstvo Mashinostroyeniye-1». 2005. 244 p.

14. Yartsev, V.P., Kiseleva, O.A. Prediction of the building materials performance in products and structures. Advanced Materials and Technologies. 2019. 4. Pp. 35-51. DOI: 10.17277/amt.2019.04.pp.035-051

15. Zagorodnikova, M.A., Yartsev, V.P., Rupyshev, V.G. Strength and Durability of Roofing PVC Membranes in the Conditions of Climate Impacts. Advanced Materials and Technologies. 2019. 2. Pp. 41–47. DOI: 10.17277/amt.2019.02.pp.041-047

16. Sapov, A.V., Zimnukhov, A.N., Yartsev, V.P. The Structure and Operational Characteristics of Bitumen. Voprosy sovremennoy nauki i praktiki. Universitet im. V.I. Vernadskogo. 2017. 2. Pp. 180–186. DOI: 10.17277/voprosy.2017.02.pp.180-186

17. Yartsev, V.P. Stareniye i razrusheniye stabilizirovannykh termoplastov v napryazhennom sostoyanii [Aging and destruction of stabilized thermoplastics in a stressed state]. Vestnik Tambovskogo gosudarstvennogo tekhnicheskogo universiteta. 2005. 11(2). Pp. 470-474.

18. Bera, P.K., Majumdar, S., Ouillon, G., Sornette, D., Sood, A.K. Quantitative earthquake-like statistical properties of the flow of soft materials below yield stress. Nature Communications. 2020. 11(1). Article no. 9. DOI: 10.1038/s41467-019-13790-2

19. Zagorodnikova, M. A., Mamontov, S.A., Yartsev, V.P. Assessment of maintainability and resistance to external influences of PVC waterproofing membrane systems. IOP Conference Series: Materials Science and Engineering. 2019. 687(2). 022012. DOI: 10.1088/1757-899X/687/2/022011

20. Drannikov, R.N., Yerofeyev, A.V., Gorokhov, T.I. Opredeleniye iskhodnykh dannykh dlya rascheta termofluktuatsionnykh konstant obobshchennogo uravneniya Zhurkova polivinilkhloridnykh plit [Determination of the initial data for calculating the thermal fluctuation constants of the generalized Zhurkov equation of polyvinyl chloride plates]. Sovremennaya nauka: teoriya, metodologiya, praktika. Materialy 2-oy Vserossiyskoy (natsionalnoy) nauchno-prakticheskoy konferentsii [Scientific conference] . 2020. Pp. 116–119.

21. Yerofeyev, A.V., Gorokhov, T.I., Drannikov, R.N. Vliyaniye metodiki obrabotki dannykh na poluchayemyye velichiny termofluktuatsionnykh konstant na primere polivinilkhloridnykh plit [Influence of the data processing technique on the obtained values of thermal fluctuation constants on the example of polyvinyl chloride plates]. Stroitelstvo: novyye tekhnologii – novoye oborudovaniye. 2020. 7. Pp. 36–41.

22. Yerofeyev, A.V., Drannikov, R.N., Gorokhov, T.I. Rol chelovecheskogo faktora v opredelenii termofluktuatsionnykh konstant obobshchennogo uravneniya Zhurkova graficheskim sposobom [The role of the human factor in determining the thermal fluctuation constants of the generalized Zhurkov equation graphically]. Stroitelnyye materialy oborudovaniye tekhnologii XXI veka. 2020. 7-8. Pp. 25–28.

23. Miyase, A., Wang, S.S. Test method development and determination of three-dimensional stiffness properties of polyvinyl chloride structural foams. Journal of Composite Materials. 2018. 52(5). Pp. 679–688. DOI: 10.1177/0021998317713588

24. Kovshov, A.G. Kineticheskaya, termofluktuatsionnaya priroda razrusheniya poverkhnostey treniya tverdykh tel pri iznashivanii [Kinetic, thermofluctuational nature of the destruction of friction surfaces of solids during wear]. Izvestiye Samarskogo nauchnogo tsentra Rossiyskoy akademii nauk. 2020. 22(3). Pp. 37–43. DOI: 10.37313/1990-5378-2020-22-3-37-43

25. Chumachenko, K., Raitoharju, J., Iosifidis, A., Gabbouj, M. Speed-up and multi-view extensions to subclass discriminant analysis. Pattern Recognition. 2021. 111. 107660. DOI: 10.1016/j.patcog.2020.107660

26. Kienzler, D., Wan, Y., Erickson, S.D., Wu, J.J., Wilson, A.C., Wineland, D.J., Leibfried, D. Quantum Logic Spectroscopy with Ions in Thermal Motion. Physical Review X. 2020. 10(2). Article no. 021012. DOI: 10.1103/PhysRevX.10.021012

27. Prokopchuk, N.R. Issledovaniye termostoykosti polimerov metodom deritografii [Study of the thermal stability of polymers by the method of derivatography]. Izvestiye akademii nauk Belorusskoy SSR. Seriya khimicheskikh nauk. 1984. 4. Pp. 119–121.

28. Chumachenko, K., Raitoharju, J., Iosifidis, A., Gabbouj, M. Speed-up and multi-view extensions to subclass discriminant analysis. Pattern Recognition. 2021. 111. Article no. 107660. DOI: 10.1016/j.patcog.2020.107660

Information about authors:

Alexander Erofeev, *PhD in Technical Sciences*
ORCID: https://orcid.org/0000-0002-1035-887X
E-mail: AV.Erofeev@yandex.ru

Timofey Gorokhov,
ORCID: https://orcid.org/0000-0002-1410-9520
E-mail: gorohowt@yandex.ru

Experimental behavior of novel GFRP reinforcing bars under compressive loads

A. Almerich-Chulia[1] ✉ iD **, P. Martin-Concepcion**[1] iD **, J.M. Molines-Cano**[2] iD **, J. Moreno-Puchalt**[1] iD

[1] *Universitat Politecnica de Valencia, Valencia, Spain*

[2] *Universitat Jaume I, Castelló, Spain*

✉ *analchu@mes.upv.es*

Abstract. Glass fiber-reinforced polymer (GFRP) bars have been used in RC structures due to their high tensile strength capacity and resistance to corrosion in comparison with steel. However, international standards do not recommend their use in RC structure elements subjected to compressive loads. Currently, there is no standard method to determine the compressive characteristics of FRP bars. This article presents a new type of GFRP bars designed specially to support compressive loads: they have additional winding GFRP layers around the longitudinal fibers. An exhaustive experimental study was carried out to obtain compressive properties of the bars: compressive strength, Young's modulus and stress-strain relation. After post-processing the experimental results of the study, this paper showed compressive strength between 50% and 60% of tensile strength, which allows employing the bars as internal reinforcement in RC structures. Their obtained Young's modulus is the same in both tensile and compression, which enables the linear stress-strain relation to be extended to the entire range of deformations. This is most advantageous for structural analysis procedures in the linear elastic regime. Finally, based on the experimental results of failure modes, some limitations about the cross-sectional area or the slenderness were proposed for the use as internal reinforcing in RC structures, which helps the researchers in the design procedure for members reinforced with FRP bars.

1. Introduction

Rapid technological advances in building materials have contributed to significant progress in civil engineering in areas like security, economy, and functionality. They serve society's needs by improving people's standard of living. One of them has been used since the early 1940s. Still, it has recently drawn the engineers' attention in the construction of civil structures: composite material made of fibers embedded in polymeric resin, also known as fiber-reinforced polymer (FRP).

Conventional concrete structures are reinforced with non-prestressed or prestressed steel. Initially, the alkalinity of concrete protects steel and usually results in durable and serviceable construction.

However, many structures like bridges, parking garages, and marine structures are subjected to aggressive environments with salt, moisture, chlorides, and temperature changes. These conditions reduce concrete's alkalinity and allow corrosion to build up on reinforced steel. Finally, the corrosion process causes concrete deterioration and loss of serviceability.

Composite materials offer considerable benefits if correctly applied, given their cost and durability. These materials provide other advantages like high tensile strength, stiffness-to-weight ratio, ability to resist corrosion and chemical attack, controllable thermal expansion, damping conditions, and higher electromagnetic neutrality compared to other materials.

The use of fiber-reinforced polymer bars is one technique that enhances conventional reinforced concrete structures [1, 2]. In particular, FRP bars offer a very high potential to be used as reinforcement under conditions in which concrete reinforced with steel offers unacceptable service conditions [3–7].

The study of FRP bar behavior as a reinforcement of concrete structures has undoubtedly evolved since 1954, when Brandt Goldsworthy spoke of this material's high potential for specific construction applications. Since that time and until 1970s, only a few studies have analyzed the feasibility of using GFRP rods as reinforcement of reinforced concrete.

Since 1980s and early 1990s, the FRP reinforcement use in civil engineering applications promoted the development of scientific research, and methods were tested on bars. Collections of documents and published reports describe the research and work done in Europe, the USA, Japan, and Canada. International interest in investigating the use of FRP bars as internal reinforcement for reinforced concrete has quickly grown and led to an increasing number of publications about hundreds of studies and tests conducted in this field [1, 8–11].

Table 1. International codes and guidelines FRP design.

	Codes – Guidelines
USA	ACI 440R-07 "Report on Fiber-Reinforced Polymer (FRP) Reinforcement for Concrete Structures", ACI Committee 440, American Concrete Institute, 2007.
	ACI 440.1R-15 "Guide for the Design and Construction of Structural Concrete Reinforced with FRP Bars", ACI Committee 440, American Concrete Institute, 2015.
	ACI 440.5-08 "Specification for Construction with Fiber-Reinforced Polymer Reinforcing Bar", ACI Committee 440, American Concrete Institute, 2008.
	ACI 440.6-08 "Specification for Carbon and Glass Fiber-Reinforced Polymer Bar Materials for Concrete Reinforcement", ACI Committee 440, American Concrete Institute, 2008.
	ACI 440.3R-04 "Guide for Test Methods for Fiber Reinforced Polymers (FRP) for Reinforcing and Strengthening Concrete Structures", ACI Committee 440, American Concrete Institute, 2004.
	BDGS-GFRP "AASHTO LRFD Bridge Design Guide Specifications for GFRP-Reinforced Concrete", 2nd Edition, 2018.
CANADA	CSA-S806-12 (R2017) "Design and Construction of Building Components with Fibre-Reinforced Polymers", Canadian Standards Association, 2012.
	CSA-S6-06 "Canadian Highway Bridge Design Code" Canadian Standards Association, 2006.
	CSA S807-19 "Specification for fibre-reinforced polymers", 2019.
	Design Manual No. 3 "Reinforcing Concrete Structures with Fiber Reinforced Polymers"*
JAPAN	Japan Society of Civil Engineers (JSCE) "Recommendation for Design and Construction of Concrete Structures Using Continuous Fiber Reinforced Materials", Concrete Engineering Series 23, Research Committee on Continuous Fiber Reinforcing Materials, 1997.
EUROPE	fib Bulletin N° 40 "FRP reinforcement in RC structures", Technical Report. France, 2007
	CNR-DT 203/2006 "Guide for the Design and Construction of Concrete Structures Reinforced with Fiber-Reinforced Polymer Bars". Italy, 2006

* The Canadian Network of Centers of Excellence on Intelligent Sensing for Innovative Structures (ISIS CANADA).

This FRP reinforcement behavior knowledge has resulted in several design codes or guidelines (Table 1) for FRP-reinforced concrete (FRP-RC) systems.

These guidelines or standards provide the limit states to design reinforced concrete with FRP. In fact, of current design guidelines and codes of practice for FRP-RC systems, only the Japan Society of Civil

Engineers (JSCE) has established a design procedure for FRP-RC columns. ACI 440.1R does not recommend employing FRP bars in columns, while CSA S806 ignores the compression contribution of FRP bars owing to their little compression [12, 13]. In this design of FRP-RC systems, all these standards reach the same conclusion when compression reinforcement is required: none considers its contribution to the design of these elements. International tests show that the compression strength of GFRP bars is lower than tensile. There are many kinds of research on FRP bars used as reinforcement in columns, flexural members, and reinforced walls in which GFRP bars are subjected to compressive stresses contribution [14–18]. However, they all indicate that the compressive strength of GFRP bars should be neglected, thus requiring further research in this area.

Many studies have shown the effectiveness of using GFRP bars in compression for RC elements [19–23]. Researchers describe some attempts made to evaluate the compressive strength of GFRP bars. Moreover, no generalizations can be made about the results because different researchers have employed a limited number of specimens, a single bar diameter, or a specific slenderness ratio. Further research into this and a more systematic approach are needed to examine the compressive behavior of GFRP bars. Moreover, the linear behavior of FRP bars until failure creates a significant concern for design engineers regarding safety.

The main objective of this research is to investigate the compressive behavior of new GFRP bars and provide technical information to design engineers seeking guaranteed solutions for using GFRP bars as internal reinforcement of reinforced concrete. This paper presents an experimental compressive strength study for new GFRP bars for RC structures (Fig. 1). This study aims to obtain ultimate compressive strength, compressive loads, modulus of elasticity, and stress-strain relation for specimens with different diameters. The experimental results show that these bars' specific design regarding compressional behavior enables their use as concrete reinforcement with compression loads according to the theoretical conditions set by international standards.

Figure 1. RTHp GFRP bars.

1.1.   Case study: new GFRP bars

FRP bars' mechanical behavior differs from traditional reinforced steel. FRP bars' mechanical properties depend on several factors: fiber quality, orientation, fabric reinforcement, fiber-resin volume ratio, resin type, manufacturing process, curing time, etc. FRP materials are anisotropic due to fibers' orientation in rebars, and FRP bars do not possess plastic behavior (yielding).

Tested bars are a new-patented technology No. ES2325011B1 [24] was designed specially for compressive loads for concrete reinforcement in FRP-RC systems, provided by RTH Pultrusystems (RTHp) [25].

A pultrusion process manufactures the employed experimental bars with fiberglass and vinyl ester resin. They are glass-fiber-reinforced polymers (GFRP). The percentage of fiberglass per volume on the core is 77 % and 23 % of vinyl ester, as reported by the manufacturer.

In the early stages of this research, these bars only had a high tensile strength like more classical GFRP rebars. After an exhaustive study, it was eventually possible to design a new GFRP bar to support specific compression loads and obtain its performance as compression reinforcement. Fig. 2 illustrates this final solution.
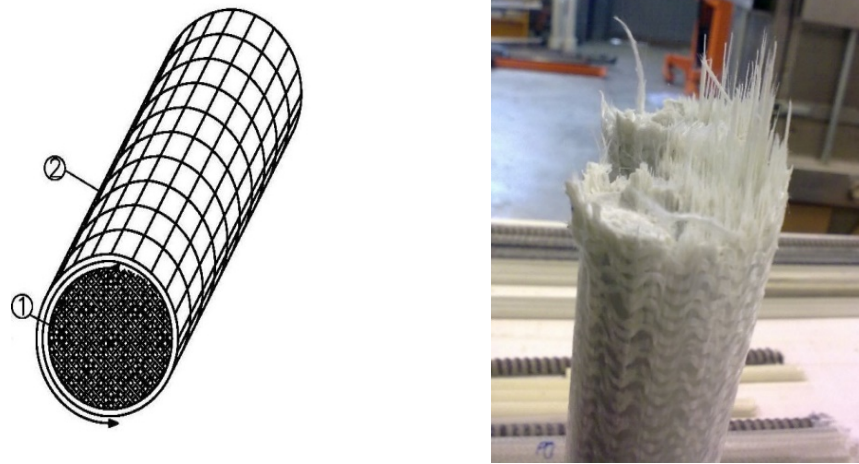
Figure 2. Configuration RTHp bar: (a) Schematic: (1) central core of fiberglass rovings, (2) fiberglass fabrics; (b) Real.

In this structural solution, not all the fiber is longitudinally arranged. There is a central core of fiberglass rovings (1), bonded together through polymeric resins, and a second zone composed of fiberglass fabrics (2), which covers the entire surface to act as a blanket and to provide a strapping to the longitudinal fibers in the first zone. The employed fabric type is taffeta (very tight mesh). Expressly, this woven mesh confers longitudinal rovings stability to work under compression. This is the main contribution of these bars to the products on the market.

Table 2 shows this solution according to the bar's diameter, which includes a variable number of fiberglass rovings, type 4800TEX, arranged longitudinally for the central core, coaxed by woven rovings of different widths and grammage for the second zone.

Table 2. GFRP bar composition.

	UD	Ø 8	Ø 10	Ø 12	Ø 16	Ø 20	Ø 25	Ø 32
Diameter	mm	8	10	12	16	20	25	32
pultrusion core (kg/m)	kg	0.100	0.156	0.225	0.400	0.625	0.975	1.596
Nº rovings 4800 TEX	--	12	21	29	54	110	136	230
Weight woven roving	gr/m^2	220	300	300/220	300/220	300/220	300/300	300/300
Width woven roving	mm	60	80	80/40	80/60	80/60	120/140	140/120
Nº woven rovings	--	1	1	2	2	2	2	2

Finally, an outer layer of silica-based granules with a variable granulometry bonded using resin to the second zone. This outer layer allows the bar to adhere to the reinforced concrete.

2. Method

Currently, there is no standard method to determine the compressive characteristics of FRP bars. This document provides a model test method to determine the mechanical compression properties of bars. The compression test was done according to ISO 5893 [26], UNE 13706-2 [27], and ISO 604 [28]. This last European standard is similar to ASTM D695-10 (compression test) [29] but with some modifications because this standard is not applicable to round GFRP bars.

This research aims to determine the critical compressive properties, including modulus of elasticity, yield strength, strain beyond yield strength, and compressive strength. The specimen was subjected to a compressive load along its longitudinal axis at a constant speed to failure during the test. The evaluation and analysis of these values will allow us to know the compressive mechanical characteristics of the bars as an internal reinforcement for RC systems, which helps in the design procedure for members reinforced with FRP bars.

2.1. Specimen dimensions

Using bars as the internal reinforcement of reinforced concrete elements establishes their dimensions. For example, limiting bars' unbraced length is necessary as internal reinforcement of reinforced concrete elements.

The researchers used various test fixtures to characterize GFRP bars in compression. The free length varies from test to test. Deitz studied the effect of the slenderness ratio, with unbraced lengths ranging from 50 to 380 mm [30], and another study investigated bars with a low slenderness ratio [31]. Chaallal and Benmokrane tested three different diameters with a slenderness ratio of 11 [32]. Khan studied GFRP bars with a slenderness ratio of 5 for compression [33]. Bruun varied the unbraced lengths from 50 mm to 600 mm as the potential unbraced length used in reinforced concrete (RC) columns [34]. Khorramian and Sedeghian are considered free length two times diameter as indicated in ISO 604 and ASTM D695-10 [35]. AlAjarmeh et al. studied the effects of the bar diameter and the unbraced length-to-bar diameter ratio for high modulus GFRP bars [36] and under elevated temperatures [37].

Standards for the compressive testing of materials define limitations on the free length to the diameter or the width ratio to avoid buckling and reach material failure.

Nevertheless, ACI standards offer no recommendations for compression tests. ACI tensile test for FRP reinforcement describes the recommended specimen's free length according to the FRP bar's diameter, which should be no less than 40-fold effective bar diameter [38, 39]. For FRP-reinforced concrete (FRP-RC) systems, when FRP bars in the compression zone cannot be avoided, ACI recommends that the transverse reinforcement should have a spacing more minor than the least cross-sectional dimension or 16 longitudinal bar diameters [12].

For Eurocode 2 [40] and Concrete Spanish Code [41], the unbraced length for steel-RC systems should be less than 15-fold the bar's diameter in a typical environmental situation. Still, it should be less than 12-fold the bar's diameter for the structures located in seismic risk zones or exposed to wind effects.

According to the last recommendations, researchers conducted several tests with different slenderness. Finally, they took an unbraced specimen length of 12-fold the tested diameter, L_0, which is the minimum free length between stirrups in reinforcement concrete, conforming with the Spanish code.

$$L_0 = 12 \cdot \phi. \tag{1}$$

For each diameter, the total length was calculated following the formula:

$$L_T = L_1 + L_0 + L_1, \tag{2}$$

where L_0 is the free distance between anchorages, unbraced length, and L_1 is anchor length embedded in steel sleeves, whose depth is required to bond the bar to steel tube and was established as 50 millimeters [39]. The gap between the bar and sleeves was filled with epoxy resin, and the ends of the sleeves were cut facing so they would be parallel and smooth. All these features allowed bars to be placed on compression plates.

Table 3 presents and tabulates bars' length values (in millimeters) for the compression test. The total length of the specimen is the free length plus two times the anchor length (Fig. 3). For the Ø8 mm and Ø10 mm diameter rods, two series of different lengths were made: Serie 1 with L_0 (fc) length to obtain the compression strength values; Serie 2, L_0 (E) length to get Young's modulus, being able to place the extensometer (Fig. 4).

Table 3. Lengths of the GFRP bars in the compression test: Serie 1, Serie 2.

Ø (mm)	L1 (mm)	Serie 1: fc		Serie 2: E	
		L_0 (fc)	L_T (fc)	L_0 (E)	L_T (E)
8	50	38	138	102	202
10	50	70	170	102	202
12	50	102	202	102	202
16	50	166	266	166	266
20	50	230	330	23	330
25	50	310	410	310	410
32	50	470	570	470	570
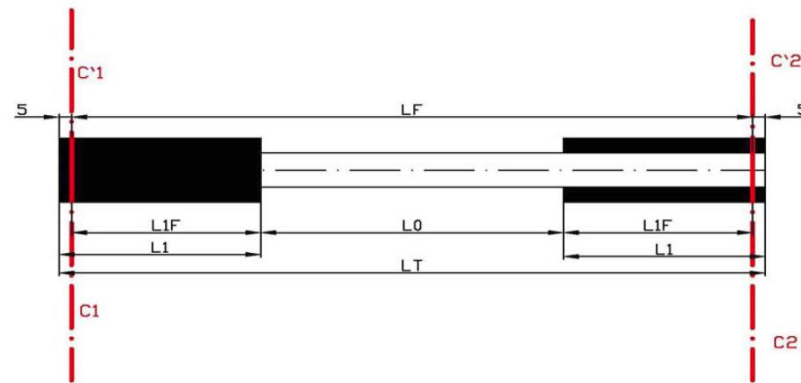
Figure 3. Length of the GFRP bars.

Figure 4. Bars for the compression test. Serie 2.

2.2. Test procedure

According to ISO 5893, a testing machine was used that maintains a constant speed of 5 mm/minute as recommended by ISO 604, while recording axial load, strain, and displacement values. To perform the compression test, it was necessary to design and build a set of plates for each bar family. These plates were made of hardened steel (Fig. 5), with a concentric hole for the required diameter to hold steel sleeves in position and align FRP bars properly. These plates are essential and need to ensure that bars are subjected to pure compression during tests and, thus, disregard any bending produced by possible eccentricity upon load application, which contributes to the consistency of the results.

Figure 5. Compression test plate.

The testing machine transmits a compression load through these plates, which lies the perpendicular plane parallel to the loading axis. Specimen and plates are coupled by a free-rotation joint so that the load on the tested bar is entirely axial. Fig. 6 shows the bar's deformation upon a rupture with the set of plates in motion.

Figure 6. Compression test. Set of plates.

According to ISO 604, there were nine test specimens for each diameter, except for Ø8 and Ø10 mm, for which there were five. If a tested bar failed, another test was carried out with another bar taken from the same lot as the failed specimen.
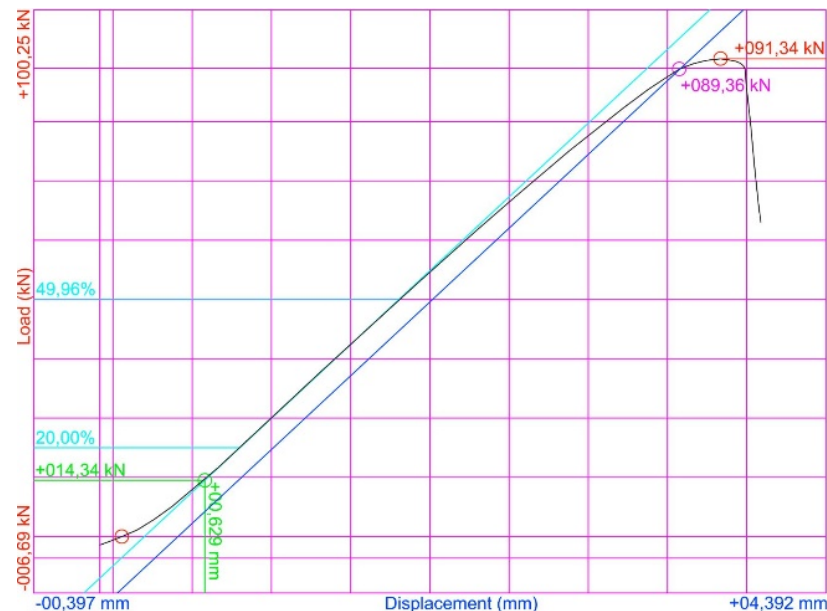
Figure 7. Curve load/elongation compression test: Ø16 mm.

The universal press employed to conduct the experimental research has an acquisition system of analog data that records the maximum compression load Fu (kN) and the shortening corresponding to breakage ΔL (mm). The PC2K software, by SERVOSIS, was used to establish an automatic recording system, resulting in the compression test's load/elongation curve (Fig. 7).

Moreover, researchers employed an extensometer to determine the relative variation of the specimen's reference length in each instant. Its reference length was 50 mm, defined in ISO 5893. The extensometer was placed in the test free length's center (Fig. 8). It was delay-free due to both inertia and the specified test speed, and it could measure the variation of the reference length at an accuracy of 1 %.

Then, with the tested information and geometric data obtained from the bars, namely specimen length, nominal diameter (mm), and cross-section (mm²), the researchers were able to determine compression strength, modulus of elasticity, and the stress-strain relation for the compression test based on brittle materials' linear elastic mechanical behavior.

Figure 8 Extensometer.

3. Results and Discussion

In this section, after carrying out the test campaign and the post-processing of the experimental data, the results of the compressive tests on the performance of GFRP pultruded bars are presented and discussed in detail.

3.1. Mechanical compression test results

This performance of glass fiber reinforced polymer (GFRP) bars subjected to compression loads was investigated by repeating the process two times. Table 4 shows the results obtained in the compression tests for each tested diameter (Serie 1), where:

- P (kN) is the compression load applied.
- $f_{u,c}$ (MPa) is the ultimate compressive strength obtained by dividing the peak compressive load by the specimen's cross-section.
- E_c (MPa) is the modulus of elasticity in compression, obtained by the linear regression of the stress-strain curve between 20 % and 50 % of ultimate stress.

Table 4. Experimental results of the compression testing of GFRP bars – Serie 1.

		#1	#2	#3	#4	#5	#6	#7	#8	#9	σ	SD	$\delta\%$	Fk
Ø8	P	22.63	23.38	24.61	23.00	22.88								
	$f_{u,c}$	467.6	483.1	499.5	469.2	468.0					477.48	11.06	2.32	451.48
	E_c	46753.5	46020.3	41863.1	38748.6	38512.2					42380	3205.90	0.08	34846
Ø10	P	34.06	35.47	38.09	34.39	34.51								
	$f_{u,c}$	448.8	461.7	493.8	446.8	449.2					468.9	14.17	3.02	435.61
	E_c	53551.0	47080.9	52450.6	47923.9	42135.5					48628	3497.93	0.07	40408
Ø12	P	52.70	49.81	50.40	54.01	51.68	57.32	53.88	57.09	51.20				
	$f_{u,c}$	444.1	452.4	482.4	463.1	515.4	482.0	512.4	457.3	444.1	475.61	19.94	4.19	438.52
	E_c	46237.8	47134.3	40658.8	40027.2	39612.3	40916.3	40139.5	43019.5	46237.8	42351	2311.26	0.05	38052
Ø16	P	90.89	92.14	88.45	92.42	91.14	88.24	86.28	91.50	91.54				
	$f_{u,c}$	454.9	461.1	442.7	462.5	456.1	441.6	431.8	457.9	458.1	451.88	8.78	1.94	435.54
	E_c	48358.2	51079.0	48153.7	52558.3	54512.4	53671.3	51735.7	49306.2	50566.1	51105	1791.00	0.04	47773

		#1	#2	#3	#4	#5	#6	#7	#8	#9	σ	SD	δ%	Fk
Ø20	P	138.03	137.94	140.78	136.62	150.42	130.76	139.52	139.85	140.45				
	$f_{u,c}$	452.8	452.6	461.9	448.2	493.5	429.0	457.7	458.8	460.8	457.26	10.31	2.26	438.07
	E_c	48918.1	49056.8	47253.2	44035.7	44875.9	44229.5	45378.8	47545.6	43606.8	46100	1860.78	0.04	42639
Ø25	P	171.97	181.42	184.39	181.69	184.63	186.09	183.52	189.06	180.35				
	$f_{u,c}$	360.4	380.2	386.4	380.7	386.9	389.9	384.6	396.2	377.9	382.56	6.91	1.81	369.71
	E_c	40517.5	46901.1	43393.5	43187.1	42549.4	44782.1	40702.1	44511.2	42687.5	43248	1465.81	0.03	40522
Ø32	P	261.45	253.04	266.81	265.46	258.76	247.06	248.34	250.26	180.35				
	$f_{u,c}$	332.3	321.6	339.1	337.4	328.9	314.0	315.7	318.1	329.4	326.28	7.94	2.43	311.51
	E_c	43606.1	44503.2	43974.5	41716.1	41008.7	38270.9	43948.5	41149.2	43126.9	42367	1627.46	0.04	39340

As glass fiber composition differs for each diameter, according to UNE 66040 [42], an estimator was used to ensure a minimum value of the tested characteristic, with a 95 % confidence interval (95 % CI) determined according to:

$$M = \sigma - (1 - \delta \cdot t_{1-\alpha}) \tag{3}$$

where σ is the arithmetic mean of the experimentally requested values, δ is the rate between the arithmetic mean, the standard deviation (SD) as %, and $t_{1-\alpha}$ is the t-Student coefficient for confidence α = 95 %.

3.2. Discussion

Unlike steel bars, FRP bars have no constant value but a variable dependent on the cross-sectional area. The characterization process shows that the bearing capacity and modulus of elasticity vary per bar diameter, which rose as the diameter decreased.

Table 5 shows the final rebars' mechanical behavior values. They can be regarded as mechanical characteristic values for designing and checking reinforced concrete sections with this novel GFRP bars.

Table 5. Characteristic values.

	Tensile				Compression			
	f_u (MPa)		E (MPa)		$f_{u,c}$ (MPa)		E_c (MPa)	
Ø	Mean	Charact	Mean	Charact	Mean	Charact	Mean	Charact
8	855.8	799.9	38276	36107	463.5	416.9	39934	32713
10	779.1	731.0	42634	38488	449.5	387.0	46295	38492
12	637.9	614.5	41125	39573	469.7	397.6	41894	35966
16	695.5	626.5	42477	40140	449.1	417.5	50804	46302
20	723.7	691.1	43590	40970	443.6	394.6	44861	40791
25	722.8	627.3	39929	35453	371.9	342.8	41993	37956
32	720.1	611.6	39681	33370	319.2	291.9	40766	36590

Table 6 gives a comparison of the mechanical properties of steel [41] and this novel GFRP rebars [25].

Table 6. Mechanical properties Steel versus GFRP bars.

Property	Steel	GFRP
Yielding strength fy (MPa)	246 – 517	--
Tensile strength fu (MPa)	550	600 – 800
Compression strength fu,c (MPa)		290 – 420
Tensile modulus E (GPa)	200	38 – 42
Compression modulus Ec (GPa)		32 – 45

a) Compressive strength

According to the literature, GFRP bars exhibit meager compressive strength [30], [33], [34], [43], [44], and International Standards do not usually recommend their use in RC structures under compression. The reported results (Table 5) show that the tested bars' compressive strength was 50-60% of the tensile strength for all the diameters [45]. However, the presented experimental results support their use as reinforcement bars in RC structures under compression loads. Thus, tested bars can sustain compression loads, and ignoring their compressive contribution to concrete members is not reasonable.

b) Modulus of elasticity.

Each specimen was equipped with an extensometer to measure the changes in length as the applied load varied. In this way, it was possible to determine the modulus of elasticity, which does not depend on specimen length as a material's property (Table 5). No buckling stability problems occurred as the values were taken between 20 % and 50 % of the load (Fig. 7). The modulus of elasticity in compression is similar to the elasticity modulus of tension, so it should be a material property.

c) Mechanics of failure

It is known that crushing is a localized failure mode related to the material's properties (fiber and resin), while buckling depends on these and specimen length [36, 46, 47].

Euler's Equation can model the response of a compressed element to predict critical load.

$$P_{cr} = \frac{\pi^2 EI}{(\alpha L)^2} \tag{4}$$

Although this formula does not apply to GFRP for being non-homogeneous material, it is a good approximation. Given the experimental characteristic values (Table 5), it is possible to obtain Euler's critical load. The experimental rupture loads are lower than the critical load for the adopted slenderness ratio, except with larger diameters, where failure occurs by buckling $\left(f_{u,c} > f_{Euler} \right)$ (Table 7). Fig. 9 shows the different failure modes for the compression test.

Table 7. Comparative Critical Loads.

Ø (mm)	L_0 (mm)	E_c (Mpa)	$f_{u,c}$ (MPa)	P_{crit} (kN)	f_{Euler} (MPa)
8	38	32713	416.9	91.75	1825.23
10	70	38492	387.0	77.67	988.91
12	102	35966	397.6	70.87	626.67
16	166	46302	417.5	108.88	541.51
20	230	40791	394.6	121.98	388.29
25	310	37956	342.8	152.54	310.76
32	470	36590	291.9	171.73	213.53

Figure 9. Different failure modes: (a) Crushing, (b) Splitting[1], (c) Buckling.

d) Spacing/unbraced length

According to the experimental characteristic values, Table 8 shows the maximum theoretical unbraced length $\left(L_{\text{max\_theoretical}}\right)$ to avoid buckling failures compared to the experimentally used L_0. Based on the experimental results, bars with a larger diameter do not comply.

Also, in the Spanish regulation [41], the maximum allowed unbraced length for steel reinforcement is 12-fold the diameter in extreme situations, called $L_{\text{normalized}}$. As in the previous case, bars with a larger diameter do not comply. Likewise, this standard does not recommend employing bars smaller than 12 mm for compression reinforced concrete elements.

Table 8. Comparative Unbraced Length

Ø	L_0 (mm)	Experimental Values			Length		
		E_c (Mpa)	$f_{u,c}$ (MPa)	P (kN)	Max. theoretical (mm)	Normalized (mm)	Recommended (mm)
8	38	32713	416.9	21.39	78.70	96	80
10	70	38492	387.0	31.27	110.31	120	100
12	102	35966	397.6	47.33	124.82	144	120
16	166	46302	417.5	85.79	187.00	192	160
20	230	40791	394.6	128.43	224.16	240	200
25	310	37956	342.8	172.39	291.60	300	250
32	470	36590	291.9	241.11	396.65	384	320

4. Conclusions

This study is focused on the compression behavior of a novel GFRP bar through experimental and theoretical analysis, with the aim of contributing to the experimental database and providing a comprehensive understanding on the variables involved.

An experimental program was planned and carried out to check the new configuration of the GFRP bar to predict the compression mechanical characteristics. The material properties (ultimate compressive strength, compressive loads, modulus of elasticity, and stress-strain relation) for specimens with different diameters were obtained. The experimental results have been compared and discussed. Finally, an analytical discussion on unbraced length has been introduced and evaluated.

After this research, it is possible to affirm that the new tested bars display the correct behavior for compression loads. Although it is possible to optimize compression tests, this study and research recommend their use as internal longitudinal reinforcement in columns, flexural members, and reinforced walls where GFRP bars are subjected to compressive stresses with no loss of other properties. Knowledge of these characteristics helps analyze and design structural reinforced concrete elements with GRP bars.

In addition, this study assumed that bars' elastic modulus in compression is similar to their elastic modulus in tension. The tension and compression behavior of bars are linearly elastic until failure. After a detailed examination of failure modes, some limitations were proposed for using as internal reinforcing in RC structures, which helps the researchers in the design procedure for members reinforced with GFRP bars with safety:

- cross-sectional area: use a minimum diameter of 12 mm for internal longitudinal reinforcement for columns and flexural members.
- slenderness: the maximum distance of stirrups, unbraced length, must be less than 10-fold the bar's diameter, as $L_{\text{recommended}}$ (see Table 8).

This research helps to optimize and standardize the GFRP rebars by maximizing its physical/mechanical performance.

References

1. Benmokrane, B., Masmoudi, R., Chaallal, O. Flexural Response of Concrete Beams Reinforced with FRP Reinforcing Bars. ACI Structural Journal. 1996. 93 (1). Pp. 46–55. DOI: 10.14359/9839

---

[1] Combination of crushing and buckling

2. Nanni, A. Flexural Behavior and Design of RC Members Using FRP Reinforcement. Journal of Structural Engineering. 1993. 119(11). Pp. 3344–3359. DOI: 10.1061/(ASCE)0733-9445(1993)119:11(3344)

3. Labossière, P., Neale, K. Advanced composite materials in bridges and structures. Canadian Society for Civil Engineering, Quèbec, Canada, 1992. ISBN: 9780921303411.

4. Nanni, A., Dolan, C.W. Fiber-reinforced-plastic reinforcement for concrete structures. ACI SP-138, International Symposium on Fiber-Reinforced Plastic Reinforcement for Concrete Structures. 1993. 177.

5. Tavassoli, A., Sheikh, S., Liu, J. Glass Fiber-Reinforced Polymer-Reinforced Circular Columns under Simulated Seismic Loads. ACI Structural Journal. 2015. 112(1). DOI: 10.14359/51687227

6. Sheikh, S., Kharal, Z. GFRP-Reinforced Concrete Columns Subjected to Seismic Loads. ACI Symposium Publication. 2018. 326. Pp. 56.1–56.10.

7. Robert, M., Cousin, P., Benmokrane, B. Behaviour of GFRP reinforcing bars subjected to extreme temperatures. Proceedings, Annual Conference – Canadian Society for Civil Engineering. 2009. 3 (4). Pp. 1587–1596. DOI: 10.1061/(asce)cc.1943-5614.0000092

8. Nanni, A. Fiber-Reinforced-Plastic (GFRP) Reinforcement for Concrete Structures: Properties and applications. Developments in Civil Engineering. 1993. 42. Pp. 450. DOI: 10.1016/c2009-0-09136-3

9. Alsayed, S.H. Flexural behaviour of concrete beams reinforced with GFRP bars. Cement and Concrete Composites. 1998. 20(1). Pp. 1–11. DOI: 10.1016/S0958-9465(97)00061-9

10. Bakis, C.E., Bank, L.C., Brown, V.L., Cosenza, E., Davalos, J.F., Lesko, J.J., Machida, A., Rizkalla, S.H., Triantafillou, T.C. Fiber-Reinforced Polymer Composites for Construction-State-of-the-Art Review. Journal of Composites for Construction. 2002. 6(2). Pp. 73–87. DOI: 10.1061/(ASCE)1090-0268(2002)6:2(73)

11. Benmokrane, B., Eisa, M., El-Gamal, S., El-Salakawy, E., Thebeau, D. First Use of GFRP Bars as Reinforcement for Continuous Reinforced Concrete Pavement. Fourth International Conference on FRP Composites in Civil Engineering (CICE2008). 2008.

12. ACI 440.1R: Guide for the Design and Construction of Structural Concrete Reinforced with FRP Bars. Farmington Hills, MI, USA, American Concrete Institute, 2015.

13. CAN/CSA S806. CAN/CSA S806: Design and construction of building components with fibre reinforced polymers. Toronto, Ontario, Canadian Standards Association, 2012.

14. Toutanji, H., Saafi, M. Flexural Behavior of Concrete Beams Reinforced with Glass Fiber-Reinforced Polymer (GFRP) Bars. ACI Structural Journal. 2000. 97 (5). Pp. 712–719. DOI: 10.14359/8806

15. De Luca, A., Matta, F., Nanni, A. Behavior of Full-Scale Glass Fiber-Reinforced Polymer Reinforced Concrete Columns Under Axial Load. ACI Structural Journal. 2010. 107(5). Pp. 589–596.

16. Maranan, G.B., Manalo, A.C., Benmokrane, B., Karunasena, W., Mendis, P. Behavior of concentrically loaded geopolymer-concrete circular columns reinforced longitudinally and transversely with GFRP bars. Engineering Structures. 2016. 117. Pp. 422–436. DOI: 10.1016/j.engstruct.2016.03.036

17. Hales, T.A., Pantelides, C.P., Reaveley, L.D. Analytical buckling model for slender FRP-reinforced concrete columns. Composite Structures. 2017. 176. Pp. 33–42. DOI: 10.1016/j.compstruct.2017.05.034

18. Fillmore, B., Sadeghian, P. Contribution of longitudinal glass fiber-reinforced polymer bars in concrete cylinders under axial compression. Canadian Journal of Civil Engineering. 2018. 45 (6). Pp. 458–468. DOI: 10.1139/cjce-2017-0481.

19. Tobbi, H., Farghaly, A., Benmokrane, B. Concrete Columns Reinforced Longitudinally and Transversally with Glass Fiber-Reinforced Polymer Bars. ACI Structural Journal. 2012. 109 (4). Pp. 551–558. DOI: 10.14359/51683874

20. Manalo, A., Benmokrane, B., Park, K.-T., Lutze, D. Recent developments on FRP bars as internal reinforcement in concrete structures. Concrete in Australia. 2014. 2 (40). Pp. 46–56.

21. Mohamed, H.M., Afifi, M.Z., Benmokrane, B. Performance Evaluation of Concrete Columns Reinforced Longitudinally with FRP Bars and Confined with FRP Hoops and Spirals under Axial Load. Journal of Bridge Engineering. 2014. 19 (7). Pp. 04014020. DOI: 10.1061/(asce)be.1943-5592.0000590

22. Khorramian, K., Sadeghian, P. Experimental and analytical behavior of short concrete columns reinforced with GFRP bars under eccentric loading. Engineering Structures. 2017. 151. Pp. 761–773. DOI: 10.1016/j.engstruct.2017.08.064

23. Duy, N.P., Anh, V.N., Hiep, D.V., Anh, N.M.T. Strength of concrete columns reinforced with Glass fiber reinforced polymer. Magazine of Civil Engineering. 2021. 101(1). Pp. 10108–10108. DOI: 10.34910/MCE.101.8.

24. Rovira Soler, J., VIALOBRA, Tecniques de Pultrusió, Tadipol. Barra a base de polímeros reforzados con fibras para el armado del hormigón. Patent ES 2 325 011 B1. 2009.

25. RTH Pultrusystems (RTHp). Technical Specifications of GFRP. 2012.

26. ISO 5893: Rubber and plastics test equipment. Tensile, flexural and compression types (constant rate of traverse). Specification. International European Committee for Standardization, Brussels, Belgium, 2019.

27. UNE-EN 13706-2: Standard Reinforced plastics composites – Specifications for pultruded profiles – Part 2: Methods of test and general requirements. Standardization Organization, Spain, 2017.

28. ISO 604: Standard Plastics - Determination of compressive properties. European Committee for Standardization, Brussels, Belgium, 2017.

29. ASTM D695: Standard Test Method for Compressive Properties of Rigid Plastics. American Society for Testing and Materials, 2015.

30. Deitz, D.H., Harik, I.E., Gesund, H. Physical Properties of Glass Fiber Reinforced Polymer Rebars in Compression. Journal of Composites for Construction. 2003. 7 (4). Pp. 363–366. DOI: 10.1061/(ASCE)1090-0268(2003)7:4(363)

31. Deitz, D., Harik, I.E., Gesund, H. GFRP Reinforced Concrete Bridge Decks (KYSPR 96-169). Kentucky Transportation Center Research Report 297. 2000. DOI: 10.13023/KTC.RR.2000.09

32. Chaallal, O., Benmokrane, B. Physical and mechanical performance of an innovative glass-fiber-reinforced plastic rod for concrete and grouted anchorages. Canadian Journal of Civil Engineering. 1993. 20 (2). Pp. 254–268. DOI: 10.1139/l93-031

33. Khan, Q., Sheikh, M., Hadi, M. Tension and compression testing of fibre reinforced polymer (FRP) bars. Faculty of Engineering and Information Sciences – Papers: Part A. 2015. Pp. 5008. URL: https://ro.uow.edu.au/eispapers/5008

34. Bruun, E. GFRP Bars in Structural Design: Determining the Compressive Strength versus Unbraced Length Interaction Curve. Canadian Young Scientist Journal. 2014. 2014 (1). Pp. 22–29. DOI: 10.13034/cysj-2014-003

35. Khorramian, K., Sadeghian, P. New Testing Method of GFRP Bars in Compression. CSCE Annual Conference. 2018.

36. AlAjarmeh, O.S., Manalo, A.C., Benmokrane, B., Vijay, P.V., Ferdous, W., Mendis, P. Novel testing and characterization of GFRP bars in compression. Construction and Building Materials. 2019. 225. Pp. 1112–1126. DOI: 10.1016/J.CONBUILDMAT.2019.07.280

37. AlAjarmeh, O., Manalo, A., Benmokrane, B., Schubel, P., Zeng, X., Ahmad, A., Hassanli, R., Sorbello, C.D. Compression behavior of GFRP bars under elevated In-Service temperatures. Construction and Building Materials. 2022. 314. Pp. 125675. DOI: 10.1016/J.CONBUILDMAT.2021.125675

38. ACI 440.3R: Guide Test Methods for Fiber-Reinforced Polymer (FRP) Composites for Reinforcing or Strengthening Concrete and Masonry Structures. Farmington Hills, MI, USA, American Concrete Institute, 2012.

39. ASTM D7205: Standard Test Method for Tensile Properties of Fiber Reinforced Polymer Matrix Composite Bars. American Society for Testing and Materials, 2016.

40. Eurocode 2. "Design of concrete structures". Part 1-1: General rules and rules for buildings. Brussels, Belgium, 2004.

41. Instrucción de Hormigón Estructural 2008. EHE. Madrid, Spain, Comisión Permanente del Hormigón. Ministerio de Transportes, Movilidad y Agenda Urbana, 2008.

42. UNE 66040: Standard Statistical interpretation of test results. Estimation of the mean. Confidence interval. Standardization Organization, Spain, 2003.

43. Robert, M., Benmokrane, B. Physical, mechanical, and durability characterization of preloaded GFRP reinforcing bars. Journal of Composites for Construction. 2010. 14 (4). Pp. 368–375. DOI: 10.1061/(ASCE)CC.1943-5614.0000104

44. Sadeghian, P., Khorramian, K. Material characterization of GFRP bars in compression using a new test method. Journal of Testing and Evaluation. 2019. 49 (2). DOI: 10.1520/JTE20180873

45. Almerich Chulia, A., Martin Concepcion, P., Molines Cano, J.M., Rovira Soler, J. New GFRP bars as internal reinforcement in concrete Structures. ECCM 2012 – Composites at Venice, Proceedings of the 15th European Conference on Composite Materials. 2012.

46. Papia, M., Russo, G., Zingone, G. Instability of Longitudinal Bars in RC Columns. Journal of Structural Engineering. 1988. 114 (2). Pp. 445–461. DOI: 10.1061/(asce)0733-9445(1988)114:2(445). URL: 29114%3A2%28445%29

47. Bae, S., Mieses, A.M., Bayrak, O. Inelastic Buckling of Reinforcing Bars. Journal of Structural Engineering. 2005. 131 (2). Pp. 314–321. DOI: 10.1061/(asce)0733-9445(2005)131:2(314)

Information about authors:

Ana Almerich-Chulia, *Doctor of Engineering*
ORCID: https://orcid.org/0000-0002-4508-4733
E-mail: analchu@mes.upv.es

Pedro Martin-Concepcion, *Doctor of Engineering*
ORCID: https://orcid.org/0000-0001-8857-3249
E-mail: pmartin@mes.upv.es

Jose M. Molines-Cano, *Doctor of Arts*
ORCID: https://orcid.org/0000-0002-3721-5369
E-mail: molines@uji.es

Jesica Moreno-Puchalt, *Doctor of Arts*
ORCID: https://orcid.org/0000-0001-9262-7916
E-mail: jemopuc@mes.upv.es

Research article

UDC 69.04

DOI: 10.34910/MCE.118.6

Modelling of thin-walled members with restrained torsion considering the section properties

T.H. Gebre[1] ✉ iD **, V.V. Galishnikova[2]** iD **, E.V. Lebed[2]** iD **, E.M. Tupikova[1]**

[1] Peoples' Friendship University of Russia, Moscow, Russia

[2] Moscow State University of Civil Engineering (National Research University), Moscow, Russia

✉ tesfaldethg@gmail.com

Abstract. Various engineering structures include lightweight or thin-walled beam structures that are used in a complex loading situation which includes restrained torsion of closed or open section. The importance of restrained torsion of thin-walled cross-sections is significant as the deformations and stresses caused by torsion affect the behaviour of the structures with open as well as closed section. The aim of this study is to demonstrate and compare different methods used to develop stiffness matrix for the finite element beam calculation of open and closed thin-walled sections with restrained torsion. The beam stiffness matrices are presented and graphically compared in order to choose the most convenient method for advanced structural analysis of thin-walled 3D beams with restrained torsion. The interpolation functions containing hyperbolic and approximate functions are considered, which satisfy the governing differential equation for torsion, with different value of characteristic number of torsion (ka). Comparing both methods, we can conclude that both are similar for small value of ka and this is commonly considered for open thin-walled section as their value of ka is small. The percentage of error between the results obtained by two methods of element stiffness matrix development for torsion with restrained warping is given graphically. Based on this study, numerical examples are considered and compared with results obtained by different finite element software. The examples include restrained and free torsion which are nonuniform and uniform torsion, respectively.

Citation: Gebre, T.H., Galishnikova, V.V., Lebed, E.V., Tupikova, E.M. Modelling of thin-walled members with restrained torsion considering the section properties. Magazine of Civil Engineering. 2023. 118(2). Article no. 11806. DOI: 10.34910/MCE.118.6

1. Introduction

Steel members are widely used in civil engineering because of its high strength, excellent ductility, fast construction, and effective space partition. Normally steel members are manufactured as thin-walled structures. The behaviour of a thin-walled bar in torsion depends strongly on the topology of its section. If the network of the section does not contain any loop, the section is called open whereas if the network of the section contains at least one loop, the section is called closed. This geometric property is used to develop special methods for the computation of their torsion and warping constants. It will be shown that the torsion properties of open thin-walled sections differ significantly from those of closed thin-walled sections. This difference has an effect for the structural response of the beam, most importantly when it comes to shear and torsion behaviour. The importance of restrained torsion of thin-walled cross-sections is significant as the deformations and stresses caused by torsion affect the behaviour of the whole structure. The present study deals with beam member subjected to torsion and uses different finite element approach.

The governing equations are solved to calculate displacements and internal forces and moments for the structure.

It is well known that the effect of non-uniform torsion must be considered in structural analysis of thin-walled beams with open cross-sections. It was unusual to check the influence of torsion on load carrying structural elements, but today it is quite often that the stresses and deformations caused by torsion will determine the studs of the structures. The importance of restrained torsion of thin-walled cross-sections has grown significantly as the deformations and stresses caused by torsion will affect the behaviour of the structures with open as well as closed section [1]. It is well known that the effect of non-uniform torsion must be considered in structural analysis of thin-walled beams with open cross-sections. It was unusual to check the influence of torsion on load carrying structural elements, but today it is quite often that the stresses and deformations caused by torsion will determine the studs of the structures. Thin-walled sections do not behave according to the law of the plane sections employed by Euler-Bernoulli-Navier however, the general theory of thin-walled section is developed by Vlasov and In addition, thin-walled structures like plates and shells associated with finite element formulations are the most common construction elements in nature and technology [2–4]. When a thin-walled beam is undergoing flexure and torsion simultaneously, transverse and torsional shear deformations would be coupled [5].

If the structures are designed using only the effect of Saint Venant torsion resistance thus the analysis may ignore the torsion part in the members and the design may be underestimated. To overcome this inaccuracy, several researchers tried to develop stiffness matrix with four degrees of freedom for a member subjected to a restrained torsion [6–11]. This additional stiffness matrix considers the warping degree of freedom at the ends of the member with thin-walled section. This study deals with the member finite element method subjected with torsion and it is done by considering beam element and equation which are necessary for the computing deformations will be derived thus to calculate the displacements and internal forces and moments for the structures.

A Number of researchers have dealt with restrained torsion of thin-walled beams with open and closed cross sectional types [12–17]. Different thin-walled torsion hypotheses have been developed to account for the shear deformation due to restrained torsion of open thin-walled section with the assumption in which the derivative of shear stress in middle surface is constant along the length of the member as they much used in engineering structures [18–23]. A finite element model is studied based on mixed variational formulation in order to improve convergence and provide an explicit way to calculate internal forces and stresses in thin- walled bar [24]. Also, different studies are developed a numerical method of thin-walled bar systems design by different theories and formulated matrixes of the stiffness of thin-walled finite elements [25–27]. The bending and torsion behaviour of cold-formed steel bars was studied experimentally based on the strengths of unbraced cold-formed steel channel beams loaded eccentrically [28–29]. Many design methods have been developed to deal with or without restrained torsions. There are different commercial softwares commonly consider with two degrees of freedom at each node of a member for a space frame without considering the effect of warping restraint at the ends of the members [30–33]. The warping part of the first derivative of the twist angle has been considered as the additional degree of freedom in each node at the element ends which can be regarded as part of the twist angle curvature caused by the warping moment [34–35]. Numerous studies developed the 4×4 member stiffness matrix including warping as an additional degree of freedom and commonly with open thin-walled section [11, 36, 37].

In this contribution, which is an extension of previous studies on thin-walled structure different 3D finite elements for open and closed sections are compared based on their section properties. Currently, many residential, social and sports buildings are being built using a steel frame, the application field of steel frame is expanding. Results of this research are applicable for software implementation, that is an advantage in respect to analogous jobs. There is lack of papers devoted to numerical solutions of the problem, that proves insufficient development of the topic and so that the investigation is relevant.

So, the first objective of this study is to consider the stiffness matrices including additional degrees of freedoms at the nodes and added to member displacement vector, apply these matrices for analysis and assess them by considering several examples and validate by comparing different finite element software.

One more objective is to analyze the effect of changing interpolation function, the same test example numerical experiments are conducted. First interpolation function type considered is hyperbolic, it contains hyperbolic functions of deflection. Such function satisfies the governing differential equation for torsion exactly and use above derivatives of stiffness matrix. The alternative approach is considered too, which is using approximate shape function. The second approach has an advantage for varying cross sections and non-linear problems and compared results with different studies [20, 38].

The last objective of the study is conducting of verification examples by commercial software. The examples of open and closed section members under uniformed and non-uniformed torsion are considered

and compared to results obtained by the new approaches introduced in this paper. Comparing both methods, we can conclude that both are similar for small value of ka and this is commonly considered for open thin-walled section as their value of ka is small. The percentage of errors between the two methods of element stiffness matrix for torsion with restrain torsion are given graphically.

2. Methods

2.1. Governing equations for 3D thin-walled beams with restrained torsion

The differential equation of restrained torsion of thin-walled beams can be obtained by the following expression and the total free warping torsion and total restrained torsion are corresponding to uniform warping rotation and nonuniform or restrained rotation, respectively. The governing equation for non-uniform torsion is used to study the behaviour of a bar with restrained torsion and it is derived for bars with thin-walled sections with local coordinate systems y_1, y_2, y_3 as shown in Fig. 1.
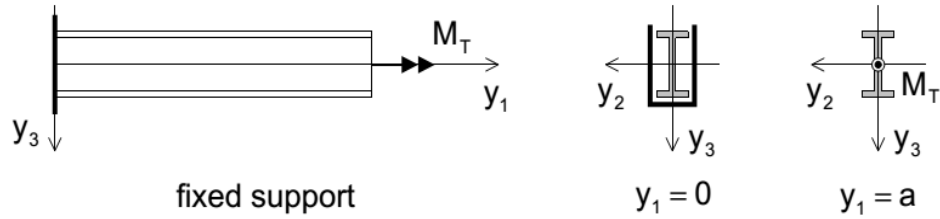

Figure 1. Prismatic bar subjected to torsion

$$EJ_\omega \frac{d^4\theta_1}{dy_1^4} - GJ_t \frac{d^2\theta_1}{dy_1^2} = 0,$$

$$\frac{d^4\theta_1}{dy_1^4} - (k)^2 \frac{d^2\theta_1}{dy_1^2} = 0, \qquad (1)$$

$$ka := a\sqrt{\frac{GJ_t}{EJ_\omega}},$$

when θ_1 is angle of twist; E, G are elastic constant; J_ω is warping constant; ka is characteristic number for torsion; J_t is torsion constant; m_T is twisting load per unit length of bar; a is length of the bar.

The general solution for the homogeneous equation (1) is satisfied by the following assumed twisting angle function $\theta_1(y_1)$ and it yields to the exact solutions of the angle of twists of a node as it is defined in the following expression:

$$\theta_1 = c_1 sinh ky_1 + c_2 cosh ky_1 + c_3 ky_1 + c_4. \qquad (2)$$

The governing equations for a member and frame are derived by applying the principle of virtual work to the beam. The differential governing equations for the generalized member displacements are satisfied for arbitrary virtual displacements and expressed as follows:

$$EJ_\omega \theta_{1,1111} - GJ_t \theta_{1,11} - m_1 - m_{\omega,1} = 0. \qquad (3)$$

The sum over the members of the virtual work δW_m of the inner forces in (1) equals the sum over the members of the virtual work δW_{md} of the member loads.

$$\sum_{m=1}^{M} \delta W_m = \sum_{m=1}^{M} \delta W_{md} + \delta W_n \int_0^a \left(EI_\omega \delta\psi_{,1}\psi_{,1} + GI_t \delta\theta_{1,1}\theta_{1,1} \right) dy_1. \qquad (4)$$

The nodal displacement and corresponding nodal moments vectors can be expressed as follow:

$$v_m^T = \boxed{\theta_{1A} \mid \psi_A \mid \theta_{1B} \mid \psi_B},$$

$$q_m^T = \boxed{M_{1A} \mid M_{\omega A} \mid M_{1B} \mid M_{\omega B}},$$

where M_1 and M_ω are the torsion moments and the warping moments respectively at the nodal points.

The positive directions of the member end moments and node rotations are shown in Fig. 2.
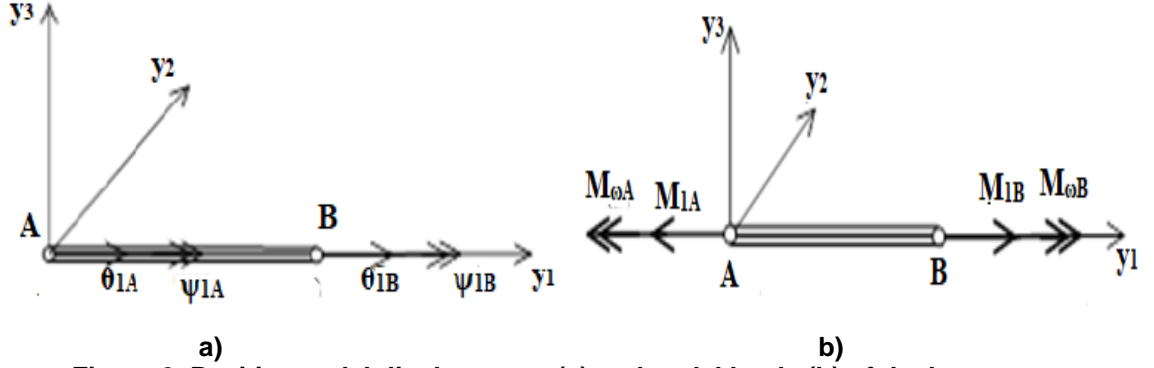

a)   **b)**
Figure 2. Positive nodal displacement (a) and nodal loads (b) of the bar.

As it is known, the relationship between the generalized force vector q_m and displacement vector v_m is established by the stiffness matrix K_m of the element as show below.

$$q_m = K_m \cdot v_m, \tag{5}$$

where K_m is the stiffness matrix of current torsion element and for non-uniform torsion.

A trigonometric interpolation and approximation solutions of rotation θ_1 are used as an initial parameter and finally compared based on the nature of section type. For non-uniform torsion, a trigonometric interpolation of rotation β_1 is used as an initial parameter and finally compared with the approximation solution. To consider the warping of the restrained member, additional degrees of freedoms are introduced at the nodes and added to member displacement vector. An interpolation function containing hyperbolic functions of y_1, which satisfies the governing differential equation for torsion considered as given below:

$$\theta_1(y_1) = g(y_1)^T b$$

$$g^T = \boxed{g_1(y_1) \mid g_2(y_1) \mid g_3(y_1) \mid g_4(y_1)}$$

$$b^T = \boxed{\theta_{1A} \mid \theta_{1,1A} \mid \theta_{1B} \mid \theta_{1,1B}}$$

$$\beta_1 = h_\omega^T C$$

$$h_\omega^T = \boxed{\begin{array}{c} \sinh ky_1 \\ \cosh ky_1 \\ y_1 \\ 1 \end{array}} \qquad C = \boxed{C_1 \mid C_2 \mid C_3 \mid C_4}$$

The interpolation functions are substituted into the left-hand side of (4) and the integration over the length of the member is performed for axial and bending loads but separately considered for torsion as it developed based on the two different methods. The contribution of torsion to the internal virtual work of the governing differential equation is given as the following expressions:

$$\int_0^a (E J_\omega \delta\theta_{1,11} \theta_{1,11} + G J_t \delta\theta_{1,1} \theta_{1,1}) \, dA = \delta b^T (K_{\omega 1} + K_{\omega 2}) b$$

where $K_{\omega 1}$ is component of stiffness matrix with warping restrained

$K_{\omega 2}$ is component of stiffness matrix without warping restraint.

The Stiffness matrices components $K_{\omega 1}$ and $K_{\omega 2}$ are added to the member stiffness matrix K_m in the usual manner.

$$K_T = \frac{EJ_\omega}{a^3}
\begin{array}{|c|c|c|c|}
\hline
k_{T1} & k_{T2} & k_{T3} & k_{T4} \\
\hline
k_{T2} & k_{T6} & k_{T7} & k_{T8} \\
\hline
k_{T3} & k_{T7} & k_{T11} & k_{T12} \\
\hline
k_{T4} & k_{T8} & k_{T12} & k_{T16} \\
\hline
\end{array},$$

$$K_{T1} = K_{T11} = S * ka\,sinh\,ka, \quad K_{T6} = K_{T16} = S*(cosh\,ka - \frac{sinh\,ka}{ka})*a^2, \tag{6}$$

$$K_{T2} = K_{T4} = S*(cosh\,ka - 1)*a, \quad K_{T8} = S*\left(\frac{sinh\,ka}{ka} - 1\right)*a^2,$$

$$S = \left(\frac{ka^2}{Q}\right), \quad Q = 2(1 - cosh\,ka) + ka\,sinh\,ka, \quad K_{T3} = -K_{T1}, \quad K_{T7} = K_{T12} = -K_{T2}.$$

An alternative to the above derivatives of stiffness matrix can be replaced by using approximate shape function and it has an advantage for varying cross sections and non-linear problems. The element stiffness matrix for torsion with restrain warping can be used by divided into two matrices. The parameters K_{T1}, K_{T2}, K_{T6} and K_{T8} can be replace by approximation as shown below:

$$K_{T1} = 12 + \frac{6}{5}*ka^2, \qquad K_{T2} = 6 + \frac{1}{10}*ka^2$$
$$K_{T6} = 4 + \frac{2}{15}*ka^2, \qquad K_{T8} = 2 - \frac{1}{30}*ka^2 \tag{7}$$

Considering the above series expressions, the alternative matrices can express as shown below:

$$K_T = \frac{EC_\omega}{a^3}
\begin{array}{|c|c|c|c|}
\hline
12 & -6a & -12 & 6a \\
\hline
6a & 4a^2 & 6a & 2a^2 \\
\hline
-12 & -6a & 12 & 6a \\
\hline
6a & 2a^2 & 6a & 4a^2 \\
\hline
\end{array}
+ \frac{GJ}{30a}
\begin{array}{|c|c|c|c|}
\hline
36 & -3a & -36 & -3a \\
\hline
-3a & 4a^2 & 3a & -a^2 \\
\hline
-3a & 3a & 36 & 3a \\
\hline
-3a & -a^2 & 3a & 4a^2 \\
\hline
\end{array} \tag{8}$$

3. Results and Discussions

3.1. The assessment of the exact and approximate methods for different value of ka

Comparing both methods, we can conclude that both are similar for small value of ka, and this is commonly considered for open thin-walled section as their value of ka is small as shown in Fig. 3. Referring equation 6, the components of stiffness matrix are generated based on the trigonometric and approximate methods. The percentage of error between the two methods of element stiffness matrix for torsion with restrain warping is given graphically as shown below in Fig. 3.

a)

b)

c)

d)
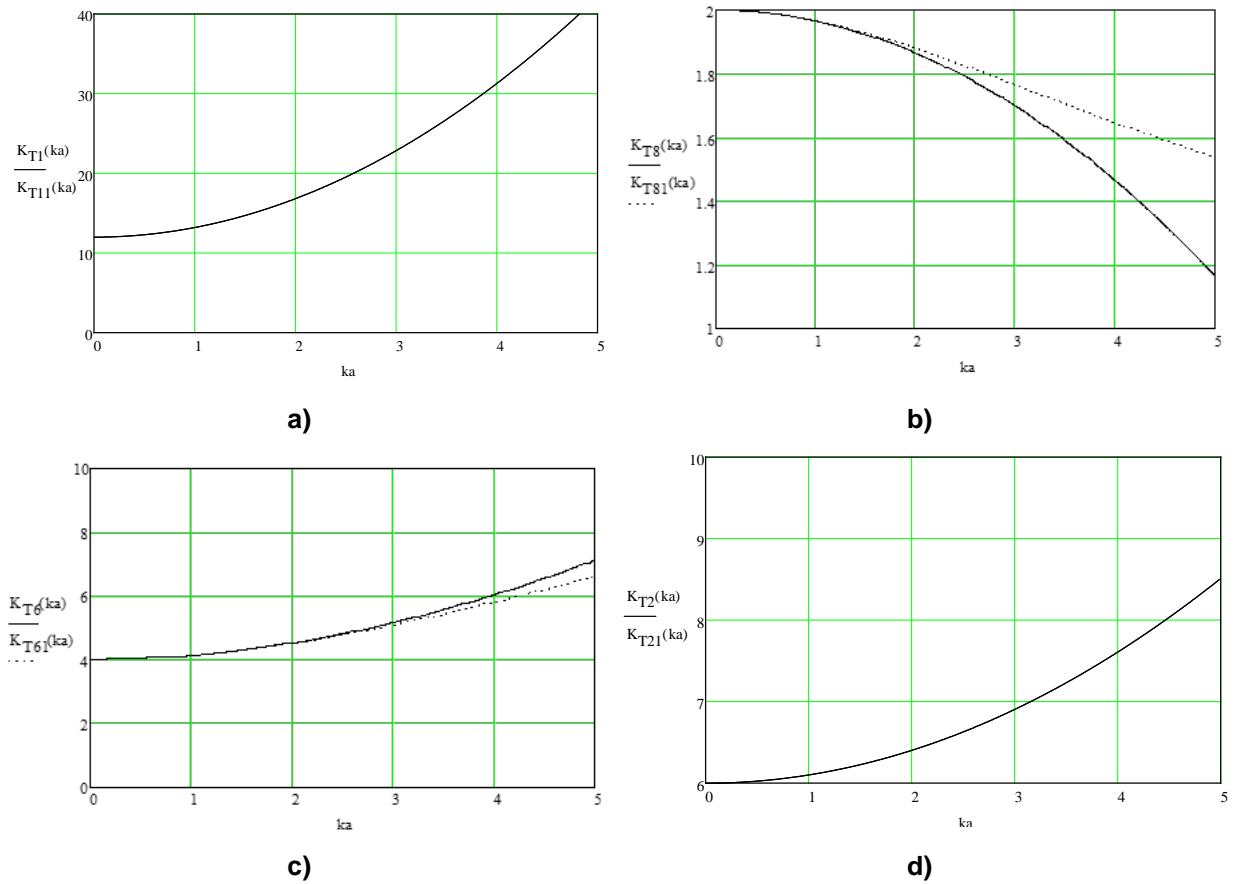
Figure 3. Evaluation of the exact and approximate methods for different value of ka.

Referring Fig. 4, for ka =1 and 2 the errors range between 6.7 % to 9.7 % which is considered reasonable and both methods are acceptable for open thin-walled sections. So, the lengths of the member can be limited based on the section type and should be chosen for small value of ka.
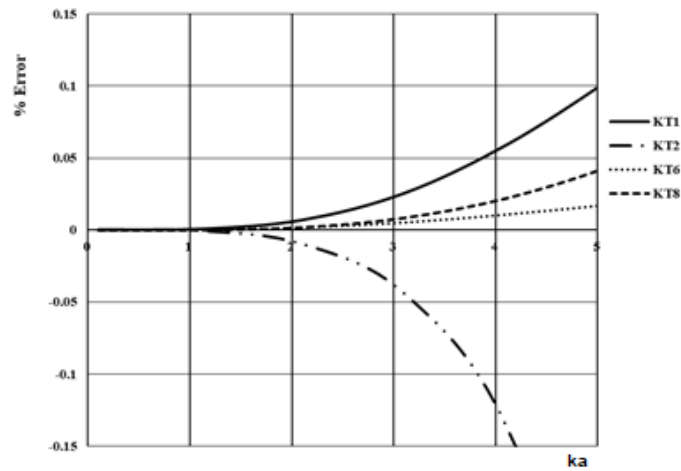
Figure 4. Approximation error graph for the values of K_{T1}, K_{T2}, K_{T6} and K_{T8}.

Considering the results of Fig. 3 and 4, the lengths of the member can be limited based on the section type and should be chosen for small value of ka = 2 as given below.

$$a \leq 0.1925 * \sqrt{\frac{J_t}{J_\omega}}.$$

If the member is free to warp, C_w = 0 and the torsional moment is carried by St Venant's torsion which is considered as uniform torsion. Considering Expression 8, only the second part of the matrix or the uniform torsion stiffness matrix can be used as given below.

$$\boldsymbol{K}_T = \frac{GJ_t}{a} \begin{array}{|c|c|} \hline 1 & -1 \\ \hline -1 & 1 \\ \hline \end{array} \quad \text{or} \quad \boldsymbol{K}_T = \frac{GJ_t}{30a} \begin{array}{|c|c|c|c|} \hline 36 & -3a & -36 & -3a \\ \hline -3a & 4a^2 & 3a & -a^2 \\ \hline -3a & 3a & 36 & 3a \\ \hline -3a & -a^2 & 3a & 4a^2 \\ \hline \end{array}$$

The local element stiffness matrix after formation must be transformed to global coordinate system. The transformation is performed by extended transformation matrix and can be formally expressed as follow:

$$\boldsymbol{K}_{mx} = \boldsymbol{R}_m \boldsymbol{K}_{my} \boldsymbol{R}_m^T,$$

where $\boldsymbol{R}_m$ is member rotation matrix.

The member load vector is transformed by analogy to the member displacement vector:

$$\boldsymbol{q}_{mx} = \boldsymbol{R}_m \boldsymbol{q}_{my},$$

where $\boldsymbol{q}_{mx}$ is member load vectors refereed to the global coordinate system; $\boldsymbol{q}_{my}$ is member load vectors refereed to the member coordinate system.

A system displacement vector $\boldsymbol{u}_s$ and a system load vector $\boldsymbol{q}_s$ are defined for the frame, which contain the nodal displacement and load coordinates in an order that is favorable for the solvers of the algebraic system equations. The member displacement and load vectors are related to the corresponding system vectors with topology matrices $\boldsymbol{T}_m$:

$$\boldsymbol{u}_m = \boldsymbol{T}_m \boldsymbol{u}_s, \quad \boldsymbol{q}_m = \boldsymbol{T}_m \boldsymbol{q}_s.$$

This study considers several section types, including the I section, rectangular hollow section, and channel section. Considering the prismatic bar of Fig. 1 as it is fixed at vertex $y_1 = 0$ and subjected to a twisting moment of M_T without warping restraint at vertex $y_1 = a$. The section properties, displacements, rotations, stresses are to be compared for all cases and compared their distribution within the span based on the required value of ka. The value of ka for the closed and open sections differs largely, accordingly for closed section the shear stress is constant while for open section varies its direction and magnitude across the thickness. The section property for open and closed sections varies with respect to torsional and warping constants thus the value of ka differs. For small value of ka both torsion mechanisms contribute to M_T throughout the beam in both cases but with the increasing of the value of ka the influence of the twisting moment differs. For value of ka greater than 10, the total torsional moment is restricted to small length (approximately *0.2a*) near to the support and its magnitude changes rapidly in both cases. A combined graphs for M_{TP}, M_{TS}, and M_ω for the values of $ka = 1$ and $ka = 10$ are shown in the Fig. 5. Referring Fig. 5, the values of M_{TP}, M_{TS}, and M_ω differ for $ka = 1$ and for $ka = 10$. For $ka = 1$, the total torsional moment components are extent throughout the span of the beam as shown in Fig. 5 (a) and its magnitude changes gradually as the value of ka is small. If the value of ka is small, it is most common for open sections. For $ka = 10$, the total torsional moment is restricted to small length near to the support and its magnitude changes rapidly as shown in Fig. 5 (b). If value of ka is large, it is most common for closed sections.
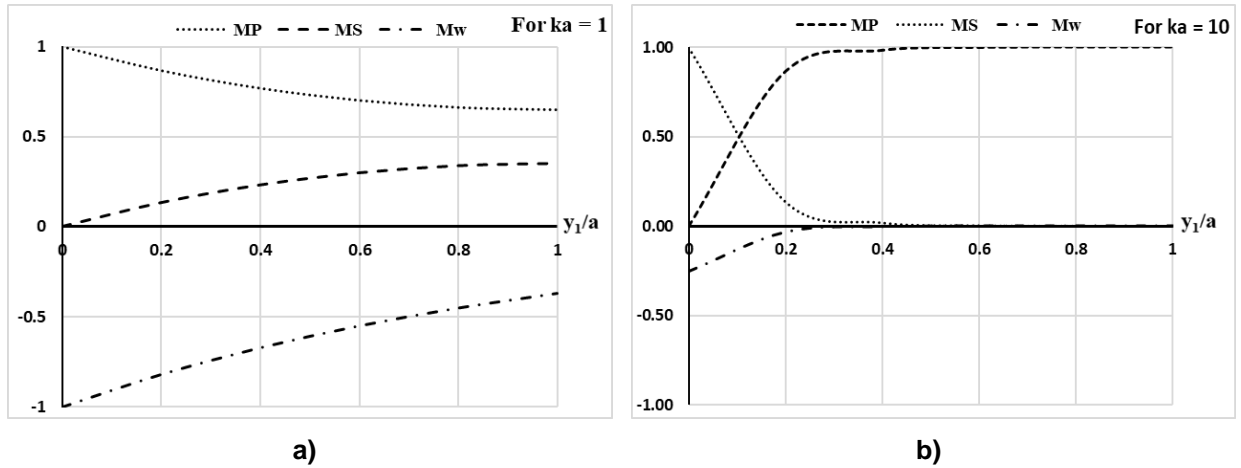
Figure 5. Combined M_{TP}, M_{TS} and M_ω for value of ka = 1 (a), and ka = 10 (b).

The variation of M_{TP}, M_{TS}, and M_T on the axis of the bar are shown in Fig. 6. Both M_{TP} and M_{TS} contribute to M_T through the span of the beam and the torsional stresses are due to St Venant shear stresses and the restraint of warping. The applied twisting moment is resisted entirely by the secondary twisting moment at support $\left(y_1 = 0 \right)$ and entirely by the primary twisting moment at $y_1 = a$. In addition, the variation of the uniform angle of twist, non-uniform angle of twist, M_{TP}, M_{TS}, and M_T on the axis of the bar are shown in Fig. 6. The rotation at vertex $y_1 = a$ due to non-uniform torsion is around 50 percent of the rotation for uniform torsion of an I-section. Both M_{TP} and M_{TS} contribute to M_T through the span of the beam and the torsional stresses are due to St Venant shear stresses and the restraint of warping. The applied twisting moment is resisted entirely by the secondary twisting moment at support $\left(y_1 = 0 \right)$ and entirely by the primary twisting moment at $y_1 = a$. The distribution of the total moment between uniform and non-uniform torsion at intermediate points is shown in Fig. 6.
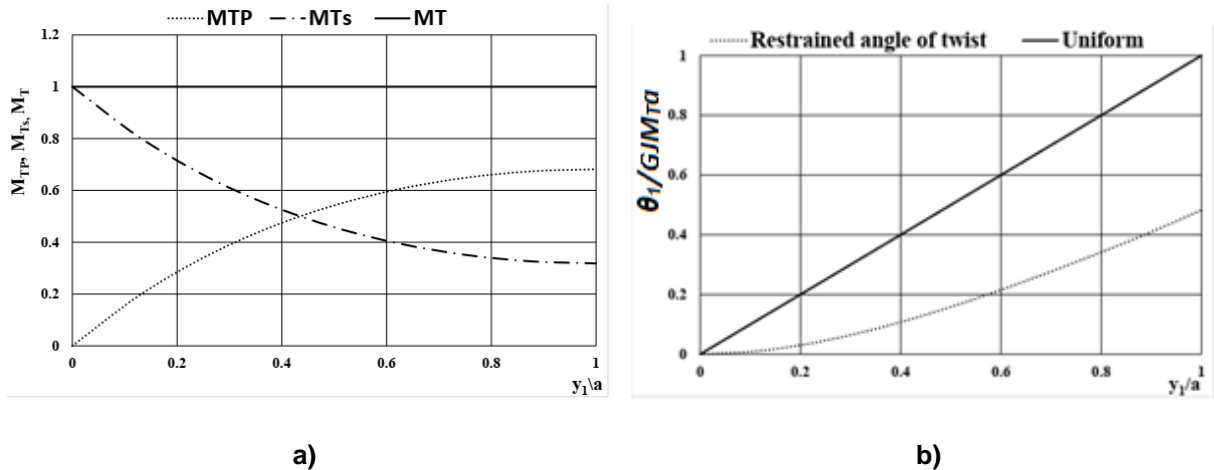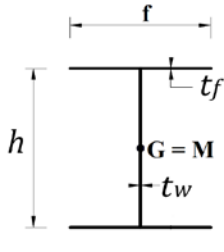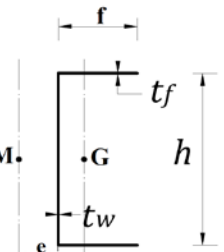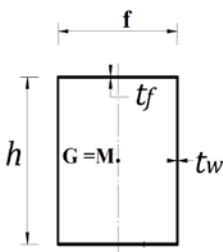
Figure 6. The normalised graphs of θ_1, (a) M_{TP}, M_{TS} and M_T of restrained I-beam section (b).

3.2. Numerical Examples

Based on the studies of the stiffness matrix for finite element procedure, the two methods are considered for the analysis of the uniform and non-uniform torsion behaviour of steel beam. The theory of restrained torsion is applied to a cantilever beam of length L subjected to external distributed torque. The two approaches of stiffness matrixes for the finite element methods compared in the previous sections, several problems of thin-walled beams with external torque applied on shear centre are presented to demonstrate the applicability of the methods. Three different sections of thin-walled beams loaded with external torque applied on shear centre are considered and compared with different methods as shown in Table 1. The accuracy of the presented model is illustrated by three examples using most commonly finite element software. The twisting effects and stresses are calculated, and the angle of twisting are presented graphically furthermore we considered the axial stress σ_z variation within individual section types.

Table 1. Different section types considered in this study

Section type			
h(mm)	400	400	400
f(mm)	180	180	180
t_f(mm)	11	11	11
t_w(mm)	8	8	8

$$E = 200*10^6 \text{ kN}/\text{m}^2 \qquad M_T = 1.0 \text{ kN m} \qquad G = 77*10^6 \text{ kN}/\text{m}^2$$

For the above numerical examples, we considered different methods for comparison and validation of the results for uniform and nonuniform torsions. The verification of the model was conducted by means of FEM software ANSYS, Abaqus, Mathcad and current theory. Six models were created for three restrained and three uniformly twisted beams with I-section, Channel, and rectangular sections. The finite element BEAM 189 was used for Ansys because it can consider warping by entering special key options. Similarly, the non-homogeneous torsion is evaluated in ABAQUS by using of a shell model. A shell model is used because a thin-walled spatial beam is investigated and it works with the reduced number of finite elements in a way that less equations to solve. The following model is considered using ANSYS software and each model consists of 100 linear elements, the section is divided by 10 points in each direction and the results for each one is available. Such meshing is sufficient for the purposes of this analysis. One end of the cantilever beam is fixed for all degree of freedom and the torque moment is applied at another end by M_T command in the shear centre of the beam center.

a)   b)
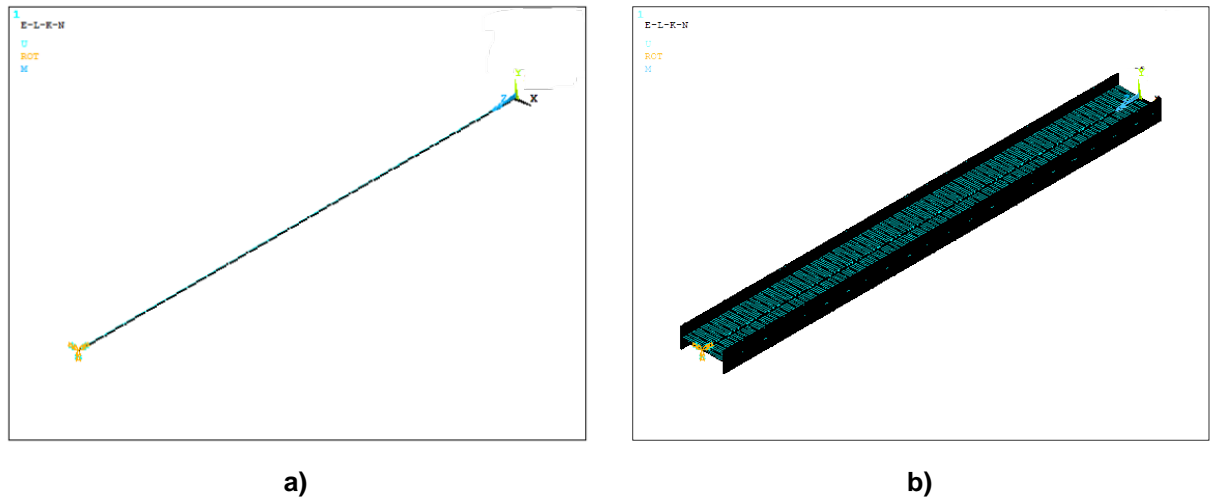
Figure 7. The load and support scheme for an I section.

The section properties, displacements, rotations, stresses are to be calculated for all cases and compared their distribution with the span based on the required value of ka. The variation of the uniform and non-uniform angle of twist (restrained torsion) on the axis of the three section types of the bar are shown in Table 2. The rotations at vertex $y_1 = a$ due to non-uniform torsion are around 49, 39 and 95 percent of the rotation for uniform torsion of the I section, channel section and rectangular hollow sections respectively. The rotation at vertex $y_1 = a$ due to uniform and non-uniform torsion is almost the same for the rectangular hollow cross section and its magnitude is negligible.

Table 2. Comparison of uniform and uneven torsion for different types of cross sections.

Methods	Applied torsion	I-Section	Chunnel Section	Rectangular Section

Current theory	Restrained	1.09E-01	47.7%	9.32E-02	38.9%	3.27E-04	98.2%
	Uniform	2.28E-01		2.40E-01		3.33E-04	
Ansys	Restrained	1.12E-01	49.3%	9.10E-02	38.7%	3.36E-04	91.8%
	Uniform	2.27E-01		2.35E-01		3.66E-04	
Mathcad 7DOF FEM	Restrained	1.19E-01	52.4%	9.21E-02	38.8%	3.31E-04	94.7%
	Uniform	2.28E-01		2.38E-01		3.50E-04	
Abaqus	Restrained	1.10E-01	48.1%	9.21E-02	38.6%	3.33E-04	97.6%
	Uniform	2.28E-01		2.39E-01		3.41E-04	

The variation of the non-uniform angle of twist (restrained torsion) on the axis of the three different cross-sections of the bar are shown in Table 2. The values of rotation angle in each node of restrained and uniformed cases were used for constructing comparison diagram. The rotation at vertex $y_1 = a$ due to non-uniform torsion is around 50 percent of the rotation for uniform torsion of an I-section. For I-cross-section as the value of ka is small and the magnitudes of the angle twist are extent throughout the span of the beam and its magnitude changes gradually as the value of ka is small as shown in Fig. 8 and 9.

Figure 8. Variation of angle of twisting for an I-section of thin wall structure.
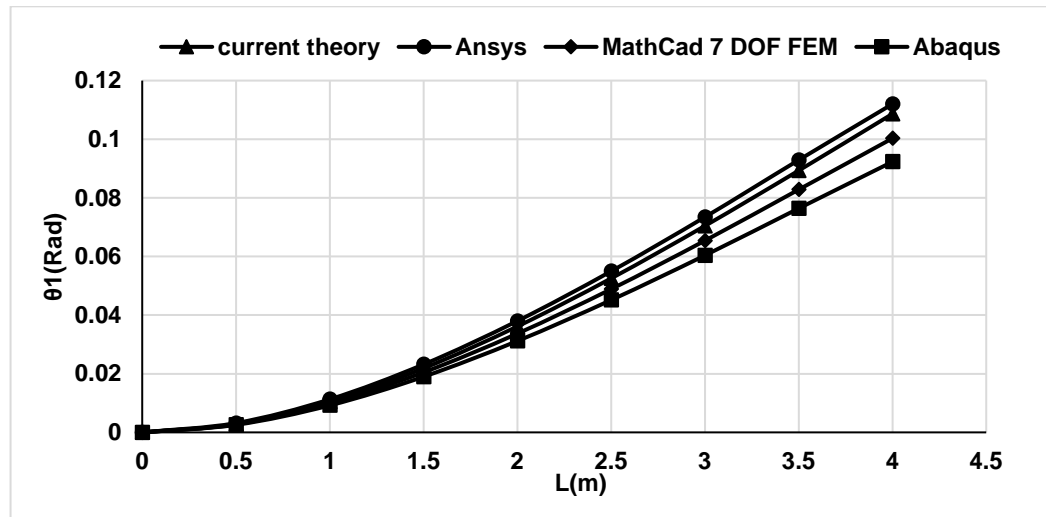
Figure 9. Rotations along the longitudinal direction of the I-section of thin wall structure.

For rectangular hollow cross-section as the value of ka is large and the angle of twist is very small in its magnitude. The angle of twist at points nearer to the support has significant magnitude as shown in the Fig. 10 and 11 and suddenly drops to a small value at the free end.

Figure 10. Variation of angle of twisting for rectangular section of thin wall structure.
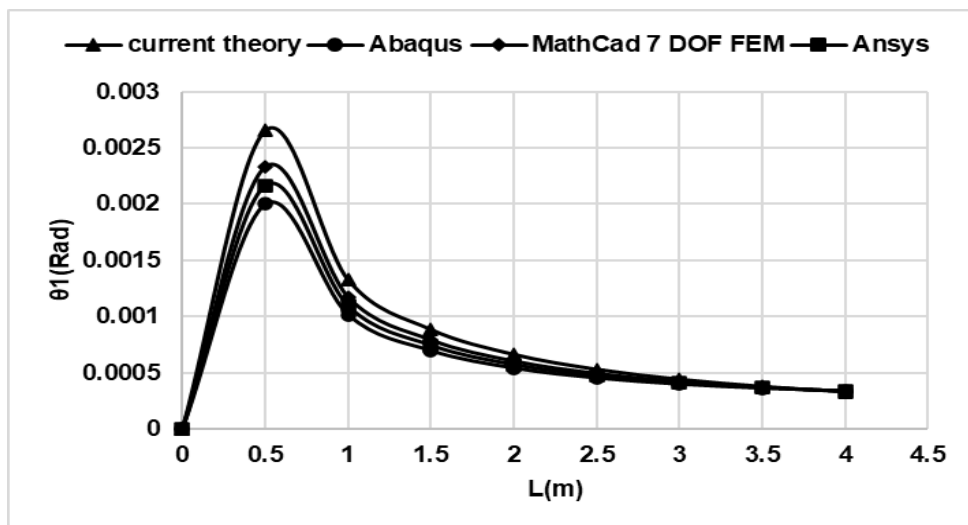
Figure 11. Rotations along the longitudinal direction of rectangular section of thin wall structure.

The variation of the non-uniform angle of twist (restrained torsion) on the axis of the channel section of a bar is shown in Fig. 12 and 13. The rotation at vertex $y_1 = a$ a due to non-uniform torsion is around 40 percent of the rotation for uniform torsion of the channel section.
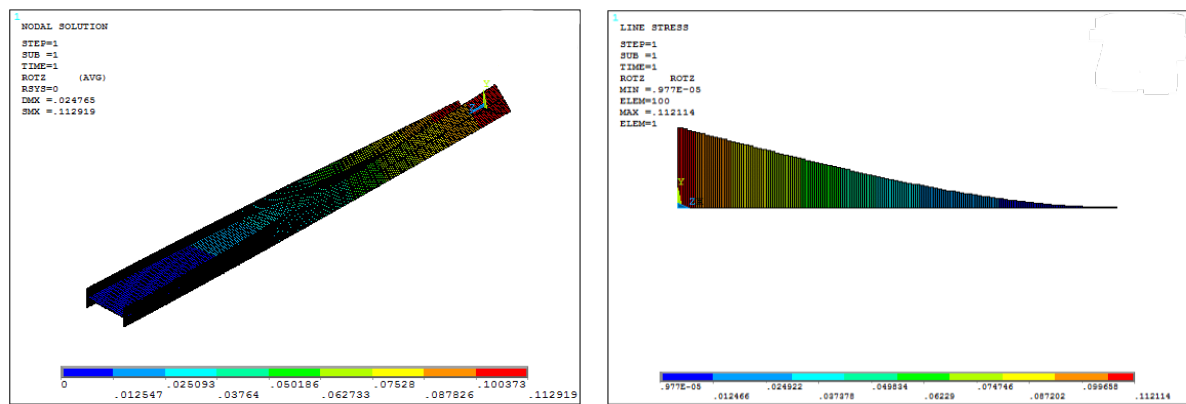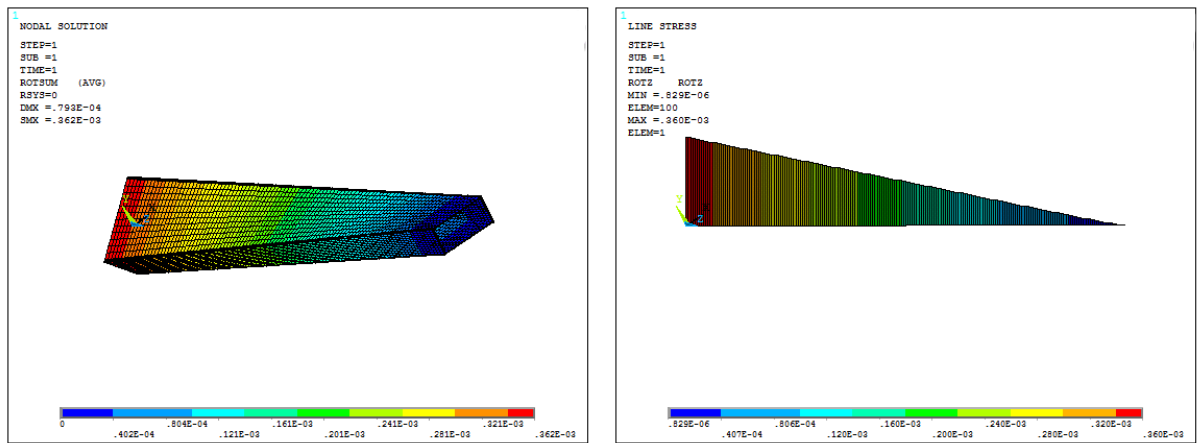

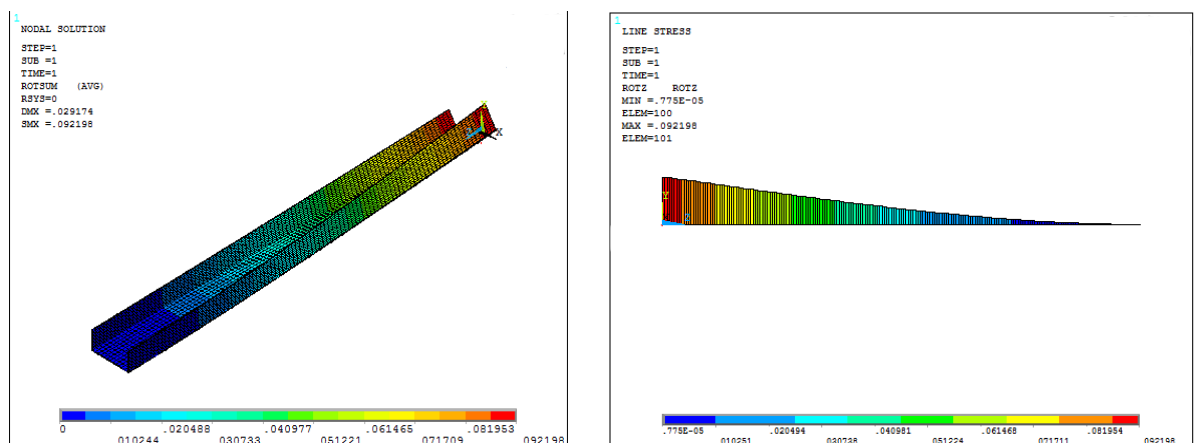**Figure 12. Variation of angle of twisting for channel section of thin wall structure.**
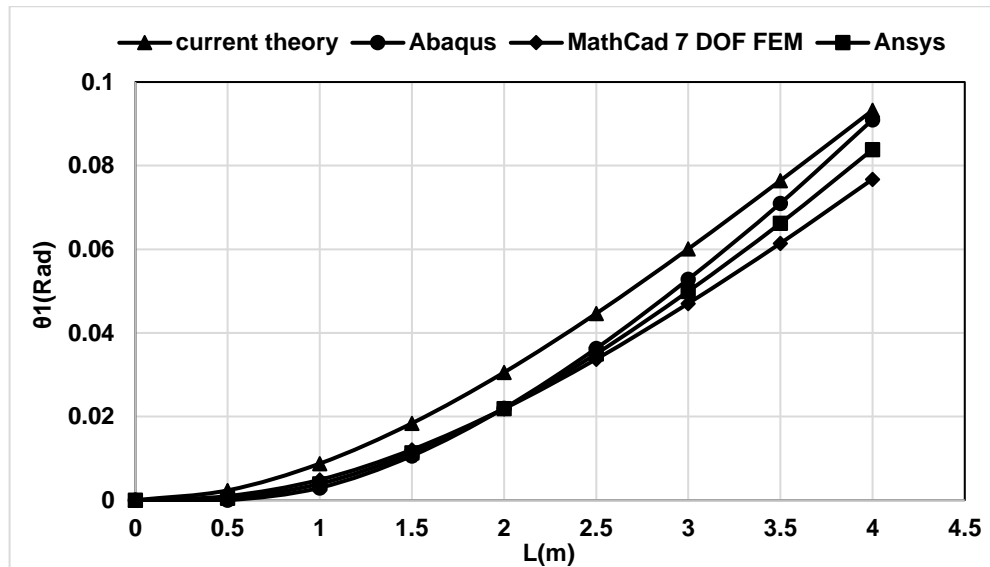
Figure 13. Rotations along the longitudinal direction of channel section of thin wall structure.

The study is compared with different research works which are considered for open thin-walled sections. The section properties are considered as the main criteria to compare the two different stiffness matrix and presented their comparison graphically. Associating both methods, we can achieve that both are similar for small value of ka and this is commonly considered for open thin-walled section as their value of ka is usually small and all results are compared with different studies [6, 10, 13, 18, 24, 38, 40]. For closed sections, the rotations are very small and are considered negligible but comparing to different studies, it shows that the effect of warping must be considered in the case of non-uniform torsion of closed-section beams [38–39].

4. Conclusion

In this study, two methods of stiffness matrix for the thin-walled structures with restrained torsion are used based on the exact and approximate methods. Based on different studies and design practices the two methods are successfully applied for the design of thin-walled structures with restrained torsion as part of finite element methods. According to this study, it is concluded that:

1. Comparing both methods, we can conclude that both are similar for small value of ka and this is commonly considered for open thin-walled section as their value of ka is small.

2. The percentage of error between the two methods of element stiffness matrix for torsion with restrain warping is negligible for the value of ka less than 2.

3. As the variation of the total torsional components depends on the value of ka and we can consider different section types. For $ka = 1$ and 2 the errors range between 6.7 % to 9.7 %, which is considered reasonable and both methods are acceptable for open thin-walled sections. So, the lengths of the member can be limited based on the section type and should be chosen for small value of ka.

4. For small value of ka both torsion mechanisms contribute to M_T throughout the beam in both cases but with the increasing of the value of ka the influence of the twisting moment differs. For value of ka greater than 10, the total torsional moment is restricted to small length (approximately 0.2a) near to the support and its magnitude changes rapidly in both cases.

5. For $ka = 1$, the total torsional moment components are extent throughout the span of the beam as shown in Fig. 4 and its magnitude changes gradually as the value of ka is small. If the value of ka is small, it is most common for open sections.

6. The angle of twist of non-uniform torsion differs from uniform torsion by 50, 1.8, and 41 percent for the I-section, rectangular tube, and channel section, respectively.

7. For $ka = 10$, the total torsional moment is restricted to small length near to the support and its magnitude changes rapidly. If value of ka is large, it is most common for closed sections.

References

1. Gebre, T.H., Galishnikova, V.V. The impact of section properties on thin-walled beam sections with restrained torsion Journal of Physics: Conference Series. 2020. 1687(1). DOI: 10.1088/1742-6596/1687/1/012020

2. Vlasov, V.Z. Thin-walled Elastic Beams. Springfield, Va.: National Technical Information Service, Virginia, 1984. 493 p.

3. Murin, J., Sedlar, T., Kralovic, V., Goga, V., Kalas, A., Aminbaghai, M. Numerical analysis and measurement of non-uniform torsion 99. Pp. 1–18. DOI: 10.4203/ccp.99.11

4. Sapountzakis, E.J. Bars under Torsional Loading: A Generalized Beam Theory Approach. ISRN Civil Engineering, 2013. Pp. 1–39. DOI: 10.1155/2013/916581

5. Xiao-Feng, W., Qi-Lin, Z., Qing-Shan, Y. A new finite element of spatial thin-walled beams Applied Mathematics and Mechanics 2010. 31(9). Pp. 1141–1152. DOI: 10.1007/s10483-010-1349-7

6. Qi, H., Wang, Z., Zhang, Z. An Efficient Finite Element for Restrained Torsion of Thin-Walled Beams Including the Effect of Warping and Shear Deformation. IOP Conference Series: Earth and Environmental Science. 2019. 233 (3). DOI: 10.1088/1755-1315/233/3/032029

7. Bradford, M.A., Ronagh, H.R. Generalized Elastic Buckling of Restrained I-Beams by FEM. Journal of Structural Engineering, 1997. 123 (12). Pp. 1631–1637. DOI: 10.1061/(asce)0733-9445(1997)123:12(1631)

8. Sapountzakis, E.J. Solution of non-uniform torsion of bars by an integral equation method. Computers and Structures. 2000. 77(6). Pp. 659–667. DOI: 10.1016/S0045-7949(00)00020-1

9. Bani, D., Turkalj, G., Brni, J. Finite element stress analysis of elastic beams under non-uniform torsion. Transactions of Famena, 2016. 40 (2). Pp. 71–82. DOI: 10.21278/TOF.40206

10. Wang, Z.-Q., Zhao, J.-C. Restrained Torsion of Thin-Walled Beams. Journal of Structural Engineering, 2014. 140(11). Pp. 04014089. DOI: 10.1061/(asce) st.1943-541x.0001010

11. Wang, Z.Q., Zhao, J.C., Zhang, D.X., Gong, J.H. Restrained torsion of open thin-walled beams, including shear deformation effects. Journal of Zhejiang University: Science A. 2012. 13 (4). Pp. 260–273. DOI: 10.1631/jzus.A1100149

12. Galishnikova, V., Gebre, T.H. The behaviour of thin-walled beam with restrained torsion. Magazine of Civil Engineering. 2022. 110(2). DOI: 10.34910/MCE.110.9

13. Li, X., Wan, S., Shen, K., Zhou, P. Finite beam element with exact shape functions for torsional analysis in thin-walled single- or multi-cell box girders. Journal of Constructional Steel Research. 2020. 172. Pp. 106189. DOI: 10.1016/j.csr.2020.106189.

14. Tusnin, A. Finite Element for Calculation of Structures Made of Thin-Walled Open Profile Rods. Procedia Engineering. 2016. 150. Pp. 1673–1679. DOI: 10.1016/j.proeng.2016.07.149.

15. Alsafadie, R., Hjiaj, M., Battini, J.M. Three-dimensional formulation of a mixed corotational thin-walled beam element incorporating shear and warping deformation. Thin-walled structures. 2011. 49 (4). Pp. 523–533. DOI: 10.1016/j.tws.2010.12.002.

16. Floros, M.W., Smith, E.C. Finite element modeling of open-section composite beams with warping restraint effects. AIAA Journal. 1997. 35(8). Pp. 1341–1347. DOI: 10.2514/2.242

17. El Fatmi, R. Non-uniform warping, including the effects of torsion and shear forces. Part II: Analytical and numerical applications International Journal of Solids and Structures. 2007. 44 (18–19). Pp. 5930–5952. DOI: 10.1016/j.ijsolstr.2007.02.005

18. Pavazza, R. Torsion of thin-walled beams of open cross-section with the influence of shear. International Journal of Mechanical Sciences, 2005. 47(7). Pp. 1099–1122. DOI: 10.1016/j.ijmecsci.2005.02.007

19. Aminbaghai, M., Murin, J., Kuti, V., Hrabovsky, J., Kostolani, M., Mang, H.A. Torsional warping elastostatic analysis of FGM beams with longitudinally varying material properties. Engineering Structures, 2019. 200 (April). Page 109694. DOI: 10.1016/j.engstruct.2019.109694

20. Fujitani, Y., Fujii, D. A structural analysis method of framed structures with thin-walled open section members based on the bending-torsional theory of beams. Page 1 of 10, 1998.

21. Proki, A. Thin-walled beams with open and closed cross-sections. Computers and Structures. 1993. 47 (6). Pp. 1065–1070. DOI: 10.1016/0045-7949(93) 90310-A

22. Murin, J., Aminbaghai, M., Hrabovsky, J., Mang, H. Second-order torsional warping modal analysis of thin-walled beams. COMPDYN 2017: Proceedings of the 6th International Conference on Computational Methods in Structural Dynamics and Earthquake Engineering. 2017. 1. Pp. 1–19. DOI: 10.7712/120117.5406.16926 Earthquake Engineering. 2017. 1. Pp. 1–19. DOI: 10.7712/120117.5406.16926

23. Brunetti, M., Lofrano, E., Paolone, A., and Ruta, G. Warping and Ljapounov stability of non-trivial equilibria of non-symmetric open thin-walled beams. Thin-walled Structures. 2015. 86. Pp. 73–82. DOI: 10.1016/j.tws.2014.10.004

24. Lalin, V.V., Rybakov, V.A., Ivanov, S.S., Azarov, A.A. Mixed finite-element method in V.I. Slivker's semi-shear thin-walled bar theory. Magazine of Civil Engineering. 2019. 89 (5). Pp. 79–93. DOI: 10.18720/MCE.89.7

25. Dyakov, S.F., Lalin, V.V. Postroyeniye i analiz konechnykh elementov sterzhnya otkrytogo profilya s uchetom deformatsiy sdviga i krucheniya [Construction and investigation of open cross-section bar finite element with account of shear and torsion]. Vestnik Permskogo gosudarstvennogo tekhnicheskogo universiteta. Okhrana okruzhayushchey sredy, transport, bezopasnost zhiznedeyatelnosti. 2011. 2. Pp. 130–140. (rus)

26. Lalin, V.V., Rybakov, V.A. The finite elements for the design of building walls made of thin-walled beams. Magazine of Civil Engineering. 2011. 8(26). Pp. 69–80. (rus)

27. Lalin, V.V., Rybakov, V.A., Morozov, S.A. Issledovaniye konechnykh elementov dlya rascheta tonkostennykh sterzhnevykh sistem [The finite elements research forcalculation of thin-walled bar systems]. Magazine of Civil Engineering, 2012. 1(27). Pp. 53–73. (rus)

28. Tsipiras, V.J., Sapountzakis, E.J. Secondary torsional moment deformation effect in inelastic nonuniform torsion of bars of doubly symmetric cross section by BEM. International Journal of Non-Linear Mechanics. 2012. 47(4). Pp. 68–84. DOI: 10.1016/j.ijnonlinmec.2012.03.007.

29. Janevski G., Kozić P., Pavlović R. Moment Lyapunov exponents and stochastic stability of a thin-walled beam subjected to eccentric axial loads. Journal of Theoretical and Applied Mechanics. 2012. 50(1). Pp. 61–83.

30. Bogdan, M.P, Pi, Y., Trahair, N.S. Bending and Torsion of Cold-Formed Channel Beams. Journal of Structural Engineering .1999. 9445 (May). DOI: 10.1061/(ASCE)0733-9445(1999)125

31. Tusnin, A.R., Tusnina, O.A. Vychislitelnaya Sistema «Stalkon» dlya rascheta i proyektirovaniya sterzhnevykh konstruktsiy iz tonkostennykh sterzhney otkrytogo profilya [Software complex "Stalkon" for analysis and design of thin-walled opened cross-section bar structures]. Promyshlennoye i grazhdanskoye stroitelstvo. 2012. 8. Pp. 62–64. (rus)

32. Tusnin, A.R. Nekotoryye voprosy rascheta tonkostennykh stalnykh konstruktsiy [Some approaches of thin-walled steel structure's analysis]. Nauchnoye obozreniye. 2015. 11. Pp. 79–82. (rus)

33. Gebre, T., Galishnikova, V., Tupikova, E. Warping Behavior of Open and Closed Thin- Walled Sections with Restrained Torsion. Engineering letters. 2022. 30 (1).

34. Askandar, N.H., Mahmood, A.D., Kurda, R. Behaviour of RC beams strengthened with FRP strips under combined action of torsion and bending. European Journal of Environmental and Civil Engineering. 2020. Pp. 1–17. DOI: 10.1080/19648189.2020.1847690.

35. Al-Rousan, R., Abo-Msamh, I. Impact of anchored CFRP on the torsional and bending behaviour of RC beams. Magazine of Civil Engineering. 2020. 96(4). Pp. 79–93. DOI: 10.18720/MCE.96.7

36. Galishnikova, V.V, Gebre, T.H., Tupikova, E.M., Niazmand, M.A. The design guide for space frames with or without warping restraint at nodes. AIP Preceedings. 2022. 05001.

37. Ubaydulloyev, M.N. Calculations of strengthened open profile thin-walled element enclosing structures. Magazine of Civil Engineering. 2014. 52(8). DOI: 10.5862/MCE.52.6

38. Lalin, V., Rybakov, V., Sergey, A. The finite elements for design of frame of thin-walled beams. Applied Mechanics and Materials. 2014. 578–579. Pp. 858–863. DOI: 10.4028/www.scientific.net/AMM.578-579.858

39. Wang, X., Yang, Q.S. A new finite element of spatial thin-walled beams. Applied Mathematics and Mechanics. 2010. 31(9). Pp. 1141–1152. DOI: 10.1007/s10483-010-1349-7

40. Selyantsev, I.M., Tusnin, A. Cold-formed steel joints with partial warping restraint. Magazine of Civil Engineering. 2021. 101. 10101. DOI: 10.34910/MCE.101.1

Information about authors:

Tesfaldet Gebre, PhD in Technical Sciences
ORCID: https://orcid.org/0000-0002-7168-5786
E-mail: tesfaldethg@gmail.com

Vera Galishnikova, Doctor of Technical Sciences
ORCID: https://orcid.org/0000-0003-2493-7255
E-mail: galishnikovaVV@mgsu.ru

Evgeny Lebed, PhD in Technical Sciences
ORCID: https://orcid.org/0000-0003-3926-8701
E-mail: evglebed@mail.ru

Evgeniya Tupikova, PhD in Technical Sciences
E-mail: emelian-off@yandex.ru

Research article

Regularity of natural oscillations characteristics change of tall earth dams

A.A. Vartanyan[1] ✉ [iD] **, A.A. Sarukhanyan[2]** [iD] **, G.G. Veranyan[2]** [iD] **, H.V. Tokmajyan[3]** [iD]

[1] *Moscow Aviation Institute, Moscow, Russia*

[2] *National University of Architecture and Construction of Armenia, Yerevan, Republic of Armenia*

[3] *Shushi University of Technology, Yerevan, Republic of Armenia*

✉ *arevshadvartanyan@mail.ru*

Abstract. A preliminary assessment of the strength of earth dams under dynamic loads is one of the most important tasks associated with the design of such massive hydraulic structures. The present study is devoted to predicting the deformation of earth dams under the influence of strong earthquakes, which are possible in the immediate vicinity of the dam location. Recently, a number of large earthquakes have occurred in the world, which led to severe destruction and indicate high seismic risks associated with the potential instability of existing large earth dams. Under intense seismic impacts, the response of the dam depends on various factors, including its geometric dimensions, as well as the type of structure. A number of existing dams, which were designed and built according to the normative rules of their time, do not take into account modern real operating conditions, in particular, potential seismic loads. This article examines the influence of these factors on the stability and strength of earth dams, taking into account the real properties of the soils of the dam body and the base of the bottom of the hydraulic structure in accordance with the new regulatory requirements. On the basis of the proposed mathematical model, verification calculations for the strength and stability of such earth dams located in the seismic zone were carried out. To assess seismic safety of high earth dams built and operating in regions of complex climatic conditions, including frequent earthquakes, the proof of the method choice capable of reliable and valid results in terms of adopted assessment criteria is required. Correct mathematical model choice ensures, on the basis of computations, strength indices of the hydraulic structure under study. In particular, comparison and analysis of calculated date obtained in case of the plane calculation model and spatial model with the field measurements results and spectral analyses of the Sarsang dam accelerograms showed the suggested calculation models provided reliable strength indices results for the earth dams in the operating reservoirs. The use of more complex models of the physical and mechanical properties of the dams' soil leads to reliable results that are in good agreement with real field tests.

1. Introduction

The subject of this research is verification of earth dam slopes stability of built and running dams, as well as adjustment of the safety factor, which are aimed at providing not only solutions to urgent safety problems but also are of great economic importance. These problems are especially of vital importance in earthquake-prone areas where the loads calculated for the strength and stability of structures are due to

seismic alternating-sign dynamic forces. Under these conditions, the discovery of the stress-strain model and on this basis the solutions to the problems of strength and stability of earth dams are of significant theoretical and economic importance.

Earth dams are the main hydraulic structures in those territories where their construction with other building materials is economically unjustified [1, 2]. This explains the fact that in Armenia and Nagorno Karabagh Republic earth dams have mainly been built. Compared to concrete or other types of dams, earth dams have not been deeply studied, which is associated with the constant refinement and adjustment of earth dams foundation soils and bodies' physical and mechanical properties [3, 4]. To assess the real state of earth dams in terms of strength and stability, the decisive factor is the choice of a mathematical model of the current stress-strain state of the soils of the foundation and the body of the dam [4, 5]. However, obtaining data on the current physical and mechanical state of soils requires the use of expensive measuring instruments and the availability of highly qualified operating personnel, which ultimately leads to an increase in the cost of the structure.

Due to the high risk of strong earthquakes in seismic zones, much attention is paid to the design, construction and operation of hydrotechnical dams in such places, namely, they constantly improve calculation methods to determine their strength and stability. These tasks are especially relevant in regions where, in addition to constant loads, there are alternating seismic loads.

The issues of stability of dams with vibrational effects of a hydraulic turbine are considered in [1]. Recommendations have been received to ensure the safe operation of dams with hydro-turbine units that cause strong vibrations. The influence of environmental vibrations on concrete dams with very diverse geometric characteristics has been studied. Methods have been developed for calculating the strength of concrete dams, taking into account the vibration of the environment [2]. The well-known finite element method for calculating the stability of slopes is sufficiently accurate and universal. Slope destruction occurs through zones in which the shear strength of the soil is insufficient to resist shear stresses. In [3], on the basis of the finite element method, an analysis of the stability of slopes was carried out in comparison with other methods. Finite element method and slope stability analysis is claimed to be a more accurate method.

The paper [4] considers methods for calculating buried structures for overall stability, taking into account arbitrary dynamic loads acting on an elastic herd. Methods for determining the mechanical properties of soils in the field under the action of static and dynamic loads, as well as the results of some experiments, are outlined.

Based on the results of experimental studies of the strength and deformation properties of soils in a complex stress state, a mathematical model has been developed, on the basis of which a complex method for calculating dams from soil materials under static and dynamic loads and a comparison of natural and calculated data are given [5].

Seismic characteristics of existing hydraulic structures can be determined by destructive and non-destructive methods. In [6], the seismic behavior of these structures is studied. In particular, by conducting a non-linear analysis, it is possible to calculate displacements, damages and stress distributions, on the basis of which it is recommended to develop engineering measures to preserve these structures.

In [7], an assessment of the stress state of earth dams in a three-dimensional formulation is proposed. To assess the stress-strain state and dynamic characteristics of earth dams, mathematical model, methodology and calculation algorithm have been developed based on finite elements. To ensure the required accuracy in assessing the stress state and dynamic characteristics of earth dams, it is proposed to carry out calculations using a three-dimensional model.

When designing and, especially, building earth dams, all technical requirements provided for by regulatory documents must be met. Only with strict observance of all requirements during the operation of earth dams can we expect their reliable and safe operation. Often, in order to increase the strength of soils, composite materials are used, a mixture of which with local materials provides high strength necessary for the construction of the core of earthen dams or the foundation of buildings and roads [8]. In [9], a review of the literature on assessing the state of earth dams under the influence of earthquakes was carried out. Using soft computing methods, two models have been developed to predict the slope deformations of earth dams during various earthquakes.

A technique has been developed to identify the patterns of the stress-strain state of soils based on the results of standard triaxial tests, including primary loading, unloading and repeated loading [10]. The impact of seismic loads on historical monuments located in the Imperial Valley was studied in [11], where the authors performed a deformation analysis using the finite element method.

The monograph [12] is devoted to the improvement of the basic concepts of seismic action, methods of calculation, design, erection and reinforcement of buildings and structures, as well as the development

of methods for predicting accelerograms of strong soil movements depending on the seismic characteristics of the terrain.

According to the theory of random fields and the autocorrelation function, a modeling method was proposed to study the stress-strain state of the parameters of gravity dams, taking into account their spatial variability [13]. The modulus of elasticity and ultimate tensile strength are chosen as random variables. Based on the plasticity model of concrete damage, the influence of spatial variability of parameters on the dynamic characteristics of gravity dams in terms of damage development, residual displacement and energy dissipation was studied. The influence of the average value, coefficients of variation and seismic effects on structural damage was studied.

The attenuation of peak acceleration near the source according to the accelerograms of strong earthquakes that occurred from 1957 to 1993 is given in the materials of the Fifth US National Conference on Seismic Stability Issues [14].

In some special structures, when calculating seismic loads on structures, in addition to the three translational seismic excitations along the coordinate axes, rotational components around the axes should also be taken into account. The paper [15] presents the results of numerical calculations of seismic loads on a mine derrick.

To determine the dynamic characteristics of the arch dam, the optimal locations of the sensors were identified by testing for environmental vibration using a large number of acceleriometers. Based on the analysis of these dynamic characteristics, the optimal number of sensors was determined to reveal the dynamic characteristics of a structure [16].

The stress-strain response observed in monotonic and cyclic tests is captured by an elastoplastic critical state model used as a virtual simulation of experiments to determine the effect of the initial state on soil response. This dependence is introduced in equivalent linear elastic-ideally plastic models as a function of the state variable to study the propagation of shear waves through horizontally layered dumps and embankments. Seismic actions on dams with different soil densities and geometries are analyzed to see the role of these factors in soil response and embankment slip resistance. The study revealed the exceptionally high resistance of gravel, which allows embankments with steep abutments to withstand strong earthquakes [17].

The effects of strong forced vibrations through the railway embankment and natural soil are transferred to the structure of surrounding buildings, causing deformation and inconvenience to residents. In [18], methods have been developed to mitigate these vibrations by pumping drilling fluid during strong ground movements.

The study of the characteristics of polymer impervious layers of earthen dams under the influence of seismic loads is of great practical importance. The results of the seismic performance of an earth dam with a polymer impervious wall, together with a comparison of the response characteristics of earth dams with a concrete core, show that such an earth dam has good resistance to seismic failures [19, 20].

Under strong seismic actions, the response of the dam depends on various factors, including the geometric dimensions and type of the dam. In [21], the influence of these factors is studied by comparing the seismic characteristics of two idealized earth dams: homogeneous and with a core. The seismic response of the dams was evaluated using a non-linear dynamic analysis that used the same real-time ground motion input. It is shown that for strongly inelastic systems, such as those under consideration, in addition to the compatibility criteria with the calculated elastic response spectrum, it is necessary to take into account the duration of the input motion. The article highlights the features in the behavior of such earth dams, gives recommendations for a rational assessment of their seismic characteristics.

What are the reasons that lead to the assumption that the stress-strain state of the dam's body and as a result the necessity of carrying out investigations on verification of the dam body strength and stability and formation of appropriate conclusions.

First, during the design phase on the basis of calculation techniques were used simplest models which did not fully reflect running in reality processes.

Second, to perform calculations the basic equations were linearized and their some members were simplified, and influence of static and dynamic loads were considered as constants.

Third, in case of forced vibrations the dam was considered as an elastic body, hence, as a result plastic deformations occurring in the body were neglected. In consequence of this the degree of the dam stability reliability was artificially increased.

On the basis of insufficient substantiations of described model of the problem study, a method was suggested which allows to obtain reliable calculation criteria. Structures designed applying these criteria will have guaranteed strength and stability.

Methods for earth dams' slopes stability calculation have been developed under dynamic loading conditions of the soil [10, 11]. However, in the above mentioned calculation methods the stress state of the soil is considered under linear regularity. During earthquakes due to Earth crust fluctuations [12, 13], the change of the soil stress-strain state differs from the linear regulation [14], therefore, calculation of the earth dams' slopes stability and strength under nonlinear regularity conditions [4, 5] is not only of practical importance but also pursues the goal of precise determination of such structures dimensions.

In recent decades, strong earthquakes have occurred, resulting in a high seismic risk associated with the potential instability of existing earth dams. Under intense seismic impacts, the response of the dam depends on various factors, including the spatial geometric dimensions of the dam. In addition, regulatory requirements for taking into account seismic loads, due to various circumstances, often increase and it becomes necessary to check the strength and stability of existing dams. From this point of view, the task of developing a methodology for calculating the stability of existing earth dams under new, more stringent regulatory conditions is relevant. To obtain reliable results, it is necessary, in addition to seismic characteristics, to take into account also the physical and mechanical properties of the soil under the influence of dynamic loads and the geometric dimensions of the structure.

The proposed method enables to reveal the stress-strain state of the earth dam body, taking into account the actual stress state of the soil, can provide more accurate data.

2. Theoretical Basis

The earth dams under design and construction, in accordance with the current regulatory requirements for recording and assessment of man-made and natural disasters, corresponding to real indicators, have sufficient strength and stability ensuring their long and safe operation lifetime [15, 16]. However, most of the existing hydraulic structures, which were designed and built according to regulatory documents that do not take into account the real dynamic loads arising during earthquakes, were in an indefinite state [17, 18]. Thus, dams built on the territory of Armenia and Nagorno Karabakh Republic, according to the old regulatory documents, have been designed for seismic loads corresponding to a horizontal acceleration of 0.2 g.

However, after the 1988 Spitak earthquake, this normative indicator was significantly changed and increased to 0.43 g. It is clear that with a sharp deviation from this indicator, no active earthen structure can remain unharmed.

To check the real state of the existing eart dams according to the new regulatory requirements, the authors, on the basis of the proposed mathematical model, carried out verification calculations for the strength and stability of earth dams built on the territory of the Nagorno Karabakh Republic. The purpose of the calculations was to identify the real state of these structures, if necessary, to develop preventive measures to increase their reliability. An extremely unique structure is the Sarsang Dam, which is the tallest earth structure on the European continent [19, 22].

The Sarsang Dam is the most important strategic object in the Republic of Nagorno Karabakh and ensuring the requirements for its safe operation is of particular importance for the national economy. Based on the need of identifying the technical state of the Sarsang Dam, a 3D model of the relief of the dam foundation and lateral prisms was developed and to carry out computations of natural oscillations, spatial and flat design models were developed [23–25]. By numerical expansion of the DWG (drawing), the general plan of the structure was adjusted and the horizontals were restored, using new topographic data (Fig. 1).

Figure 1. Corrected master plan of the Sarsang dam.

To estimate the real values of the accelerations of the propagation of elastic waves on the territory of platinum, experiments were carried out, the results of which are shown in the Table 1.

Table 1. Results of the Sarsang dam's area microzoning.

Site name	Oscillation period, s	Maximum expected horizontal acceleration A			
		Engineering-geological analogy	Acoustic stiffness	Impact	Final
Foot of the dam	0.09 – 0.28	0.4	0.45	0.45	0.45
Left-bank site	0.1 – 0.3	0.4	0.432	0.419	0.434
Right-bank site			0.434	0.421	

In the calculations, the mechanical parameters of the soil were obtained by the dynamic method [12], and the densities and physical and mechanical properties of the soil of the dam body and foundation were obtained making use of the results of laboratory studies of prototypes delivered from different depths of the dam body and the bottom of the hydraulic structure. The results of laboratory studies are shown in Table 1.
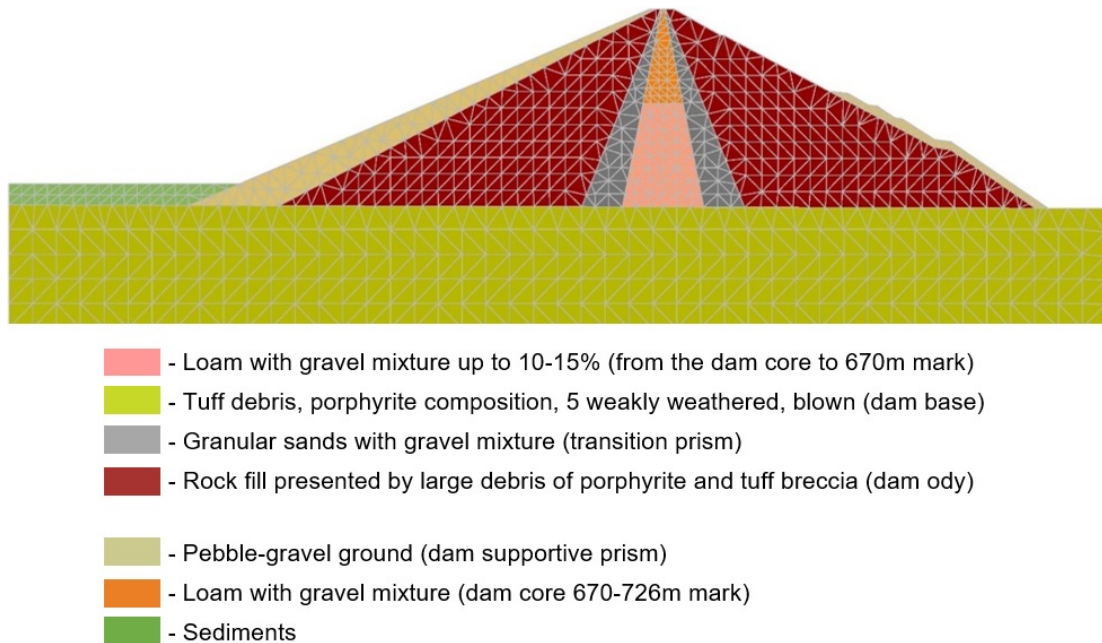
Table 2. Physical-mechanical properties of the dam body's soil and base.

N	Layer name	γ_{nat}, KN/m^3	V_e, m/s	V_s, m/s	μ	E, MPa	G, MPa	Logarithmic decrement
1	Loam and gravel mixtures up to 10–15% (from the core base to the mark 670m)	20.85	500	200	0.4	700	25	0.20
2	Loam and gravel mixtures (dam core, mark 670–726.0m)	20.3	450	190	0.39	600	22	0.22
3	Gruss-sandy soil (transitional prism)	17.5	550	300	0.29	1200	450	0.25
4	Gravelly-pebble soils (retaining prisms)	20.6	650	400	0.2	2300	950	0.26
5	Rock fill (body of the dam)	22.0	700	450	0.15	3000	1300	0.27
6	Tuffbreccia, detritus, weakly crumbling (base of the dam)	24.0	1450	800	0.28	11000	4500	0.3
7	Sediment	20.6	650	400	0.2	2300	950	0.24

To achieve the set goal, quantitative relationships of natural oscillations were identified depending on the relief forms and their comparative assessment was given using spectral accelerograms recorded by strong earthquakes.

3. Materials and Methods

First, a flat calculation model of the dam was built (Fig. 2).

- Loam with gravel mixture up to 10-15% (from the dam core to 670m mark)
- Tuff debris, porphyrite composition, 5 weakly weathered, blown (dam base)
- Granular sands with gravel mixture (transition prism)
- Rock fill presented by large debris of porphyrite and tuff breccia (dam ody)

- Pebble-gravel ground (dam supportive prism)
- Loam with gravel mixture (dam core 670-726m mark)
- Sediments

Figure 2. Design cross-section of the dam divided into finite elements.

From the master plan (Fig. 1) of the site and using the ArcGis program, a survey of the raster relief was built, placed in the computational grid (Fig. 3). Cartesian coordinates are defined in the center of each cell. By these coordinates and using the Mathematica program, triangular elevation models were built (Fig. 4). Further, the relief with triangular cells was entered into the AutoCAD program and a spatial site model was built (Fig. 5), on which the dam model was also built (Fig. 6), as well as the calculated plane model of the dam, taking into account the two most dangerous cross-sections, as a result of which the dam has the greatest height.
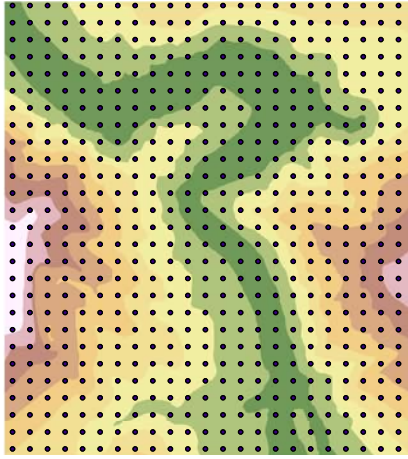
Figure 3. Raster grid by the middle points.
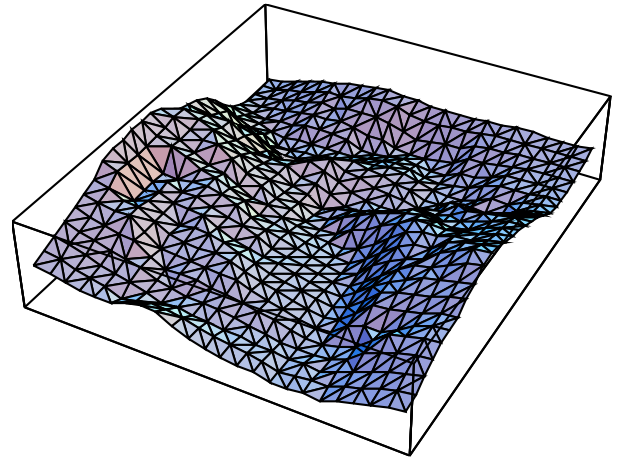
Figure 4. Triangular spatial model of the relief.
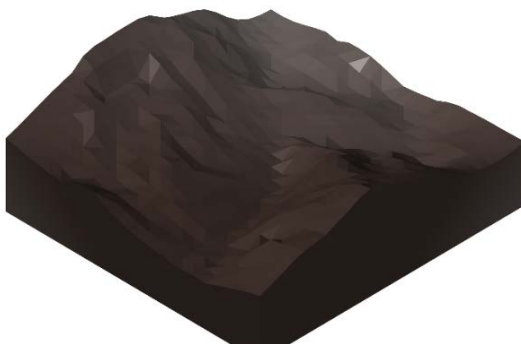
Figure 5. Spatial model of the site.
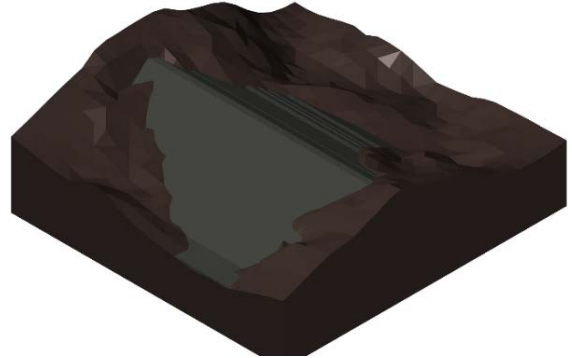
Figure 6. Spatial model of the dam and the site.

Since the building codes are based on elastic linear soil models [12], the proposed calculations was based on the methods of the theory of elasticity in order to be able to compare the calculation results with the results obtained according to regulatory documents.

A comparative analysis was carried out of the periods of natural oscillations, calculated by spatial flat models with the data of field measurements. It is important here to compare the results of spectral analyzes of accelerograms of strong earthquakes with the parameters of natural oscillations of earth dams. Accelerograms were used as accelerograms of strong earthquakes that occurred in Spitak (Armenia, 1988) (Fig. 7) and Izmir (Turkey, 1999) (Fig. 8), the scales of which are estimated at 0.45 g [10].
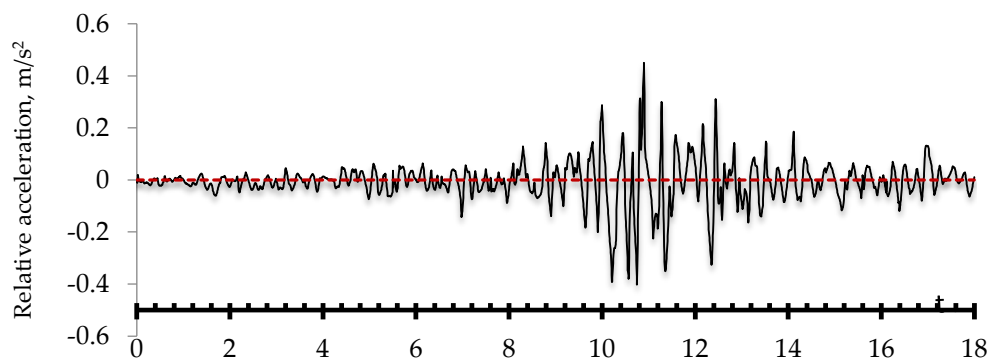
Figure 7. Accelerogram of horizontal accelerations of the 1988 Spitak earthquake on a scale of 0.45g.
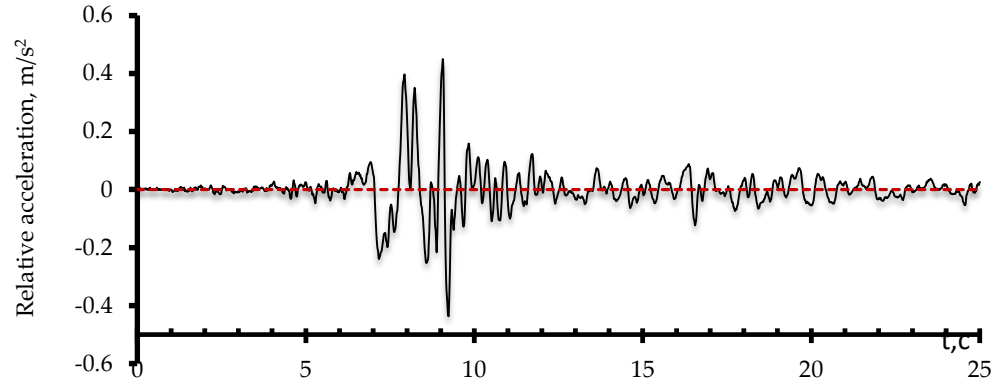
**Figure 8. Accelerogram of horizontal accelerations
of the 1999 Izmir earthquake at a scale of 0.45 g.**

Accurate estimation of hydraulic structures stability is especially important from seismic impacts considerations. Toward this end it is necessary to solve a dynamic equilibrium equation in matrix form

$$[M]\{\ddot{a}\}+[D]\{\dot{a}\}+[K]\{a\}=\{F\},$$ (1)

where $[M]=\int_s \rho\{N\}^T\{N\}dS$ is the matrix of the mass, ρ is the specific mass, $[D]=\alpha[M]+\beta[K]$

is the damping matrix representing resistance of the material (extinction forces), $[K]=\int_s[B]^T[C][B]dS$

is the stiffness matrix $\{F\}=\{F_b\}+\{F_L\}+\{F_n\}+\{F_g\}$ is the force vector at the node, $\{F_g\}$ is gravi-

tation force, $\{\ddot{a}\}$ is the acceleration vector at the node, $\{\dot{a}\}$ is the velocity vector at the node, and $\{a\}$
is the node displacement matrix [14].

In case of elastic linear problems the constructive matrix $([C])$ is calculated according to Eq. (1.4)
[15, 20]. Since real soils have non-linear properties, then the constructive matrix is calculated for each
loading stage.

$$[C]=\frac{E}{(1+\nu)(1-2\nu)}\begin{bmatrix}1-\nu & \nu & \nu & 0\\ \nu & 1-\nu & \nu & 0\\ \nu & \nu & 1-\nu & 0\\ 0 & 0 & 0 & \frac{1-\nu}{2}\end{bmatrix}.$$ (2)

Dynamic (cyclic) loading increases porous pressure leading to the effective stress-strain state
change of the body. That change is conditioned by respective change of mechanical properties of the material, i.e. the strength of soil material in case of dynamic loading acquires kinematic properties [11, 21].

The periods of natural oscillations of the dam and their shapes are determined by numerical integration of equation (1). However, in the case of considering the dam as an elastic body, Eq. (1) is modified in
the form

$$[M]\{\ddot{a}\}+[K]\{a\}=0.$$ (3)

To integrate Eq. (3) by a physicomechanical method, taking into account the longitudinal and transverse components of the wave propagation velocity, Poisson's ratios (m) and Young's modulus (E) were

determined. Using the data of the experiments carried out by formula (2), the stiffness matrix $[G]$ is calculated. The dynamic characteristics of soils are obtained from the reference book. Soil slip modulus and
Poisson's ratio are determined by empirical formulas

$$G=\rho\times V_s^2,$$ (4)

$$\mu = \frac{0.5 - \gamma_v^2}{1 - \gamma_v^2}, \quad \gamma_v = \frac{V_s}{V_p}, \tag{5}$$

if $\sigma_z > 0.2$ MPa, then the value of V_s and V_p is determined by the following formulas

$$V_{p,s} = 1.3 \times V_{p_0, s_0} \times \left(\frac{\sigma_z}{\sigma_{z_0}}\right)^{1/6}, \tag{6}$$

$$G = 1.7 \times V_{s_0}^2 \times \left(\frac{\sigma_z}{\sigma_{z_0}}\right)^{1/3}, \tag{7}$$

where zero values of V_{s_0} and V_{p_0} are given in Table 2.

4. Results and Discussions

Equation (3) was integrated for the plane and spatial problems at various modes of oscillation, characteristic of the structure under consideration. However, the recommended forms of oscillation clearly do not correspond to the nature of the passing processes [20, 21]. In order to identify the true form of oscillations, calculations were carried out to determine the periods of oscillation.

As a result, oscillation periods were obtained for 20 different modes of oscillation (Fig. 8). Fig. 9 shows one of the modes of oscillations of the dam in the case of a plane problem, and in Fig. 10 – the same in the case of a spatial problem.
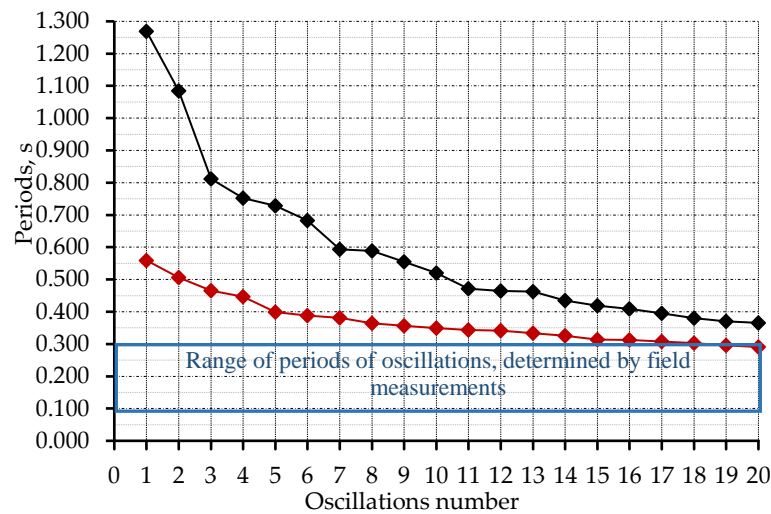
Figure 9. Graphs of periods of natural oscillations for different modes of oscillation:
the graph above is the periods of natural oscillations for the plane problem,
the graph below – the same for the spatial problem.

Fig. 10–13 show the results of calculations of natural vibrations for 4-puzzle flat design sections.
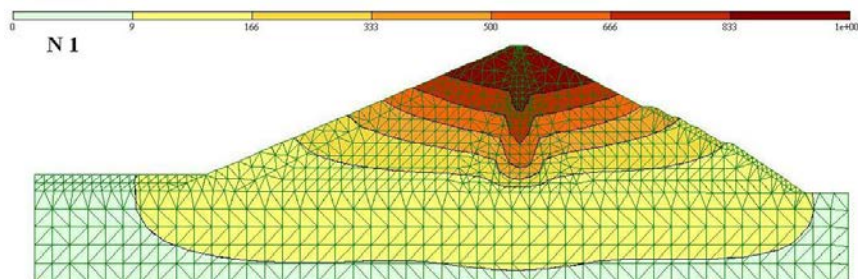
Figure 10. The form of natural oscillations of the dam
in the design section for the plane problem. Form 1.
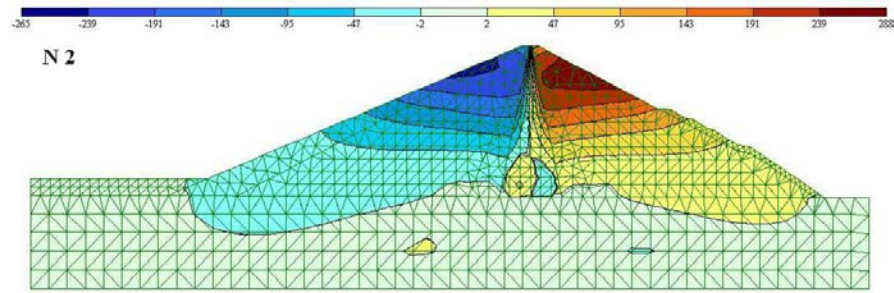
**Figure 11. The form of natural oscillations of the dam
in the design section for the plane problem. Form 2.**
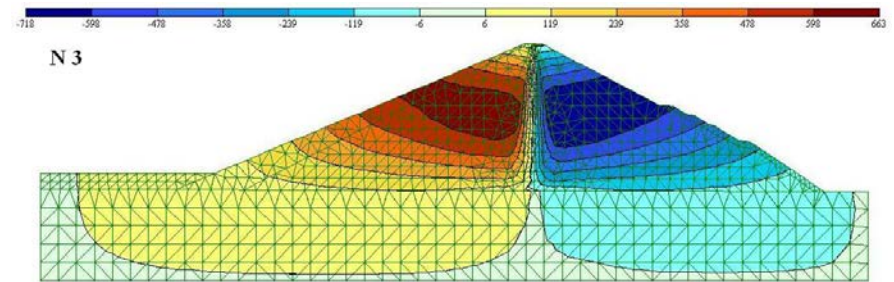
**Figure 12. The form of natural oscillations of the dam
in the design section for the plane problem. Form 3.**
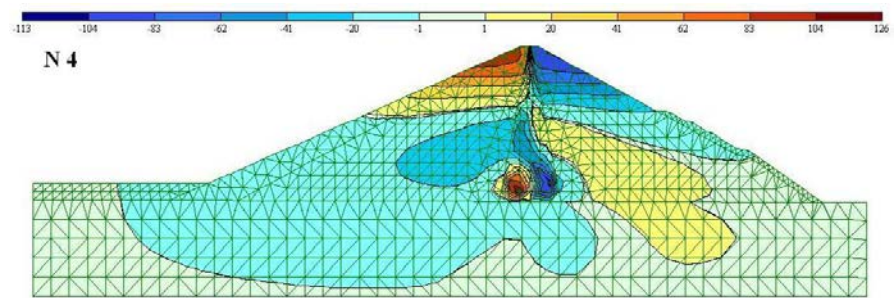
**Figure 13. The form of natural oscillations of the dam
in the design section for the plane problem. Form 4.**
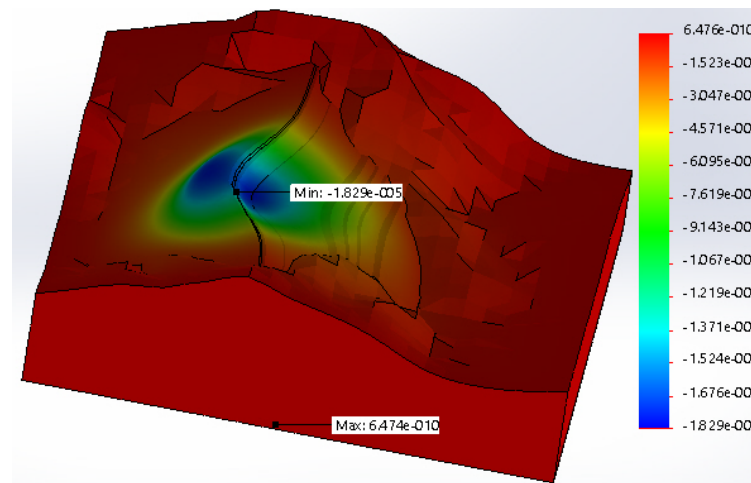
Figure 14. The form 1 of natural oscillations of the dam for the spatial problem.
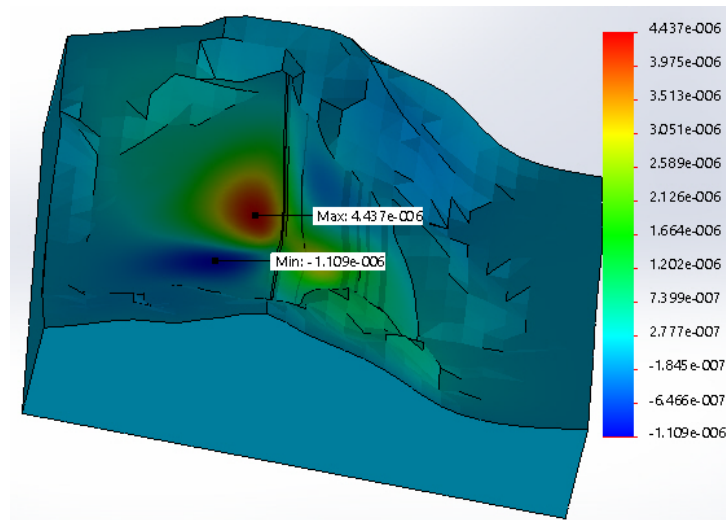
Figure 15. The form 2 of natural oscillations of the dam for the spatial problem.
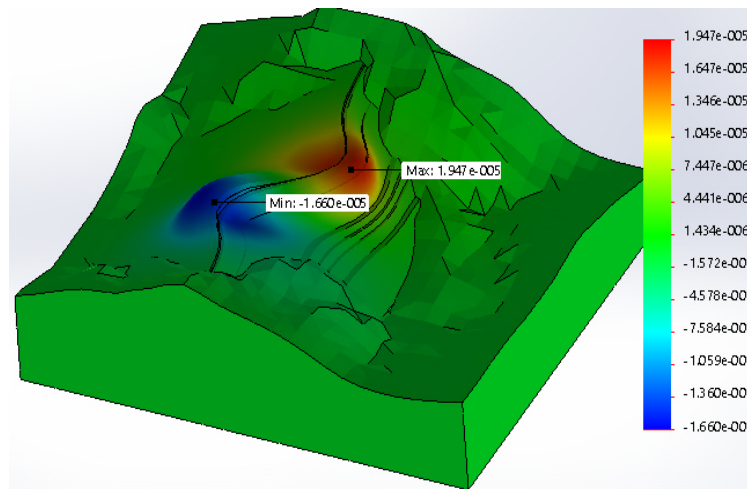
Figure 16. The form 3 of natural oscillations of the dam for the spatial problem.
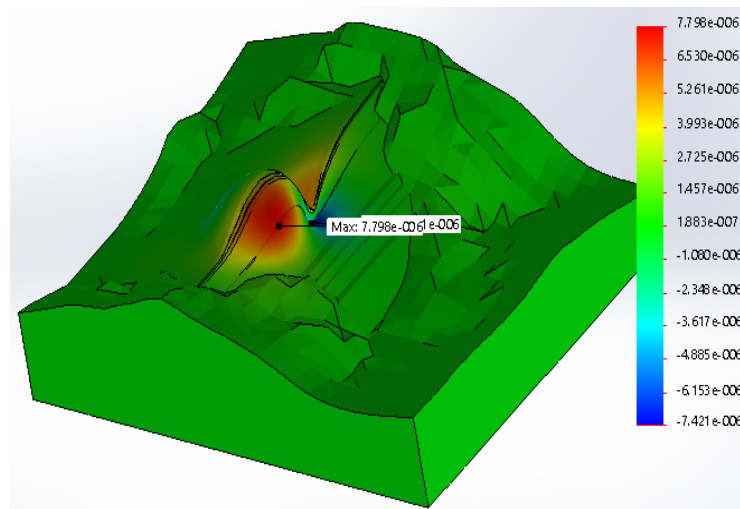
Figure 17. The form 4 of natural oscillations of the dam for the spatial problem.

The results of spectral analyzes of the Spitak and Izmir earthquakes accelerograms, carried out by the method of discrete Fourier transforms, are shown in Fig. 11 and Fig. 12. The calculations were carried out at different values of the logarithmic decrement, which correspond to the values of the soil properties of the dam body and foundation.
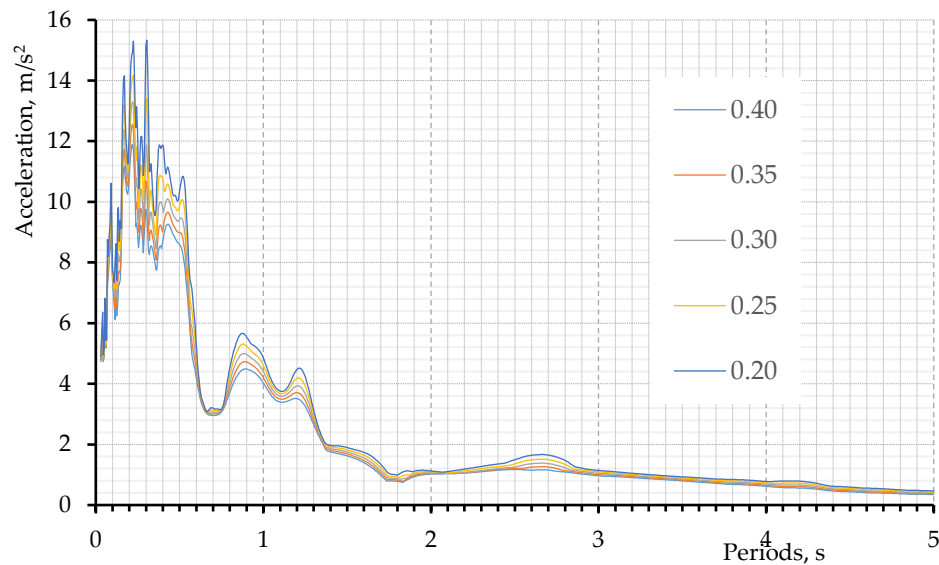
**Figure 18. Spectral analysis of the asceliogram of the Spitak earthquake
with an acceleration of 0.45g in the interval of the logarithmic determinant 0.2..0.4.**
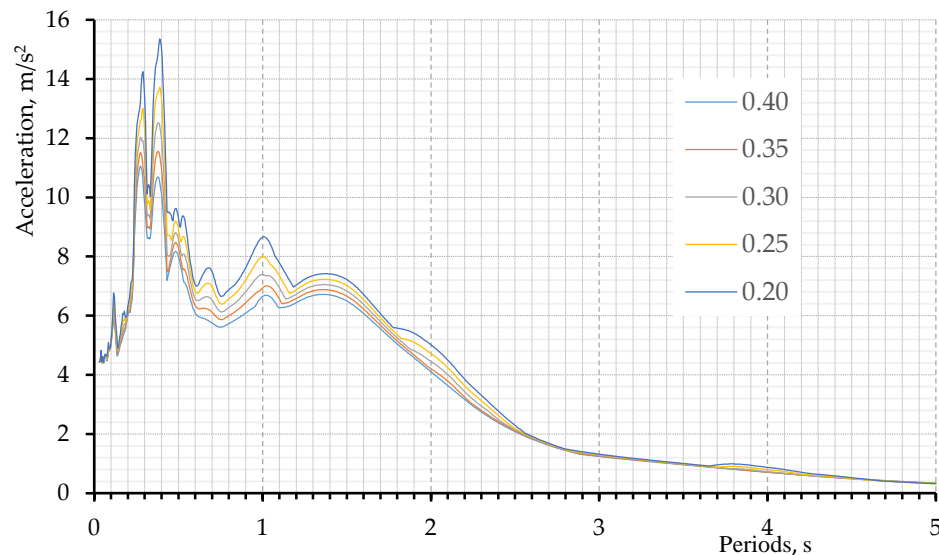
**Figure 19. Spectral analysis of the asceliogram of the Izmir earthquake
with an acceleration of 0.45g in the interval of the logarithmic determinant 0.2..0.4.**

The analysis of the results obtained shows that the maximum horizontal accelerations are obtained in the interval of the oscillation period of 0.3 ... 0.4 s.

5. Conclusions

Comparison of calculated and measured data reveals the essence of dynamic phenomena and gives comparable results. In the case of an approximate plane problem, an excessively large range of periods of natural oscillations is obtained, which indicates an excessively elastic property of the structure. The spatial model gives more approximate values of the periods of natural oscillations. However, here we also neglect the nonlinear properties of the soil and the decay coefficient. It should be noted that in elastic models, where the effect of the decay coefficient is neglected, the value of natural oscillations becomes close to their maximum values.

The results of in-situ measurements by natural oscillations are obtained less than their calculated values. This means that, in reality, the properties of the soil are non-linear, and the process has a damping character.

The results of spectral analysis of accelerograms have shown satisfactory agreement with the results of natural oscillations field measurements, but there are some risks of resonance.

References

1. Yaseen, Z.M., Ameen, A.M.S., Aldlemy, M.S., Ali, M., Abdulmohsin Afan, H., Zhu, S., Sami Al-Janabi, A.M., Al-Ansari, N., Tiyasha, T., Tao, H. State-of-the Art-Powerhouse, Dam Structure, and Turbine Operation and Vibrations. Sustainability. 2020. 12(4). 1676 p.

2. Pereira, S., Magalhães, F., Cunha, Á., Moutinho, C., Pacheco, J. Modal identification of concrete dams under natural excitation. Journal of Civil Structural Health Monitoring. 2021. 11 (2). Pp. 465–484.

3. Griffiths, D.V., Lane, P.A. Slope Stability Analysis by Finite Elements. Geotechnique. 1999. 49 (3). Pp. 387–403.

4. Glushkov, G.I. Statika i dinamika sooruzheniy, zaglublennykh v grunt [Statics and dynamics of structures buried in the ground]. Stroyizdat. Moscow. 1967. Pp. 171–207.

5. Zaretsky, Yu.K., Lombardo, V.N. Statika i dinamika gruntovykh plotin [Statics and dynamics of earth dams]. Energoatomizdat. Moscow. 1983. 247 p.

6. Altiok, T.Y., Demir, A. Collapse mechanism estimation of a historical masonry minaret considered soil-structure interaction. Earthquakes and Structures. 2021. 21 (2). Pp. 161–172.

7. Mirsaidov, M.M., Toshmatov, E.S. Spatial stress state and dynamic characteristics of earth dams. Magazine of Civil Engineering. 2019. 89 (5). Pp. 3–15.

8. Tabari, M.K., TaghaviGhalesari, A., Choobbasti, A.J., Afzalirad, M. Large-scale experimental investigation of strength properties of composite clay. Geotechnical and Geological Engineering. 2019. 37 (6). Pp. 5061–5075.

9. Javdanian, H., Pradhan, B. Assessment of earthquake-induced slope deformation of earth dams using soft computing techniques. Landslides. 2019. 16 (1). Pp. 91–103.

10. Duncan, J.M., Chang, C.Y. Nonlinear analysis of stress and strain insoils. Journal of the Soil Mechanics and Foundations Division. 1970. 96 (5). Pp. 1629–1654.

11. Gu, W.H., Morgenstern, N.R., Robertson, P.K. Postearthquake deformation analysis of Wildlife site. Journal of Geotechnical Engineering. 1994. 120 (2). Pp. 274–289.

12. Khachiyan, E.E. Seismic Effects and Prognosis of structures Behavior. Gitutyun. Yerevan., 2015, 555 p.

13. Lu, X., Wu, Z., Pei, L., He, K., Chen, J., Li, Z., Yang, Z. Effect of the spatial variability of strength parameters on the dynamic damage characteristics of gravity dams. Engineering Structures. 2019. 183. Pp. 281–289.

14. Campbell, K.W., Bozorghia, Y. Near-Source Attenuation of Peak Acceleration from Worldwide Accelerograms Recorded from 1957 to 1993. Proceedings of Fifth U.S. National Conference on Earthquake Engineering. 1994. 3. Pp. 283–292.

15. Bońkowski, P.A., Kuś, J., Zembaty, Z. Seismic rocking effects on a mine tower under induced and natural earthquakes. Archives of Civil and Mechanical Engineering. 2021. 21 (2). Pp. 1–11.

16. Altunisik, A.C., Sevim, B., Sunca, F., Okur, F.Y. Optimal sensor placements for system identification of concrete arch dams. Advances in concrete construction 2021. 11 (5). Pp. 397–407.

17. Modoni, G., Albano, M., Salvatore, E., Koseki, J. Effects of compaction on the seismic performance of embankments built with gravel. Soil Dynamics and Earthquake Engineering. 2018. 106. Pp. 231–242.

18. Khan, M.R., Dasaka, S.M. Spatial Variation of Ground Vibrations in Ballasted High-Speed Railway Embankments. Transportation Infrastructure Geotechnology. 2020. 7 (3). Pp. 354–377.

19. Li, J., Zhang, J., Xu, J., Wang, F., Wang, B., Li, Q. Dynamic behavior of polymer antiseepage wall for earth dam by centrifuge test. International Journal of Geomechanics. 2018. 18 (12). 04018179 p.

20. Sarukhanyan, A.A., Vartanyan, A.A., Vartanyan, G.G., Tokmajyan, H.V. Estimation of hydraulic structures safety by comparison of strength and stability theories. IOP Conference Series: Earth and Environmental Science. 2021. 677 (4). 042085 p.

21. Masini, L., Rampello, S., Donatelli, R. Seismic performance of two classes of earth dams. Earthquake Engineering & Structural Dynamics. 2021. 50 (2). Pp. 692–711.

22. Li, J., Zhang, J., Wang, Y., Wang, B. Seismic Response of Earth Dam with Innovative Polymer Antiseepage Wall. International Journal of Geomechanics. 2020. 20 (7). 04020079 p.

23. Belkova, I.N., Glagovskiy, V.B., Pavlovskaya, L.N., Radchenko, V.G. Otsenka fil'tratsionnoy prochnosti gruntovoy plotiny na primere Irganayskoy GES [Evaluation of the seepage strength of an earth dam on the example of the Irganay hydroelectric power station]. Izvestiya Vserossiyskogo nauchno-issledovatel'skogo in-stituta gidrotekhniki im. BE Vedeneyeva. 2011. 264. Pp. 3–12.

24. Zhilenkov, V.N., Belkova, I.N. Sposob regulirovaniya osadok tyazhelykh sooruzheniy, fundiruyemykh v vodonosnoy tolshche neskal'nykh slabopronitsayemykh gruntov [A method for regulating the settlement of heavy structures funded in the aquifer of non-rocky, poorly permeable soils]. Izvestiya Vserossiyskogo nauchno-issledovatel'skogo instituta gidrotekhniki im. B.E. Vedeneyeva, 2009. 256, Pp.10–22.

25. Bakanovichus, N.S., Klimovich, V.I., Lyalina, A.A., Sosnina, S.A. (2021). Issledovaniya gidrodinamicheskikh i ledovykh vozdeystviy na morskiye GTS i ikh ustoychivost' [Studies of hydrodynamic and ice effects on marine hydrotechnical structures and their stability]. Gidrotekhnicheskoye stroitel'stvo. 2021. 9. Pp. 25–32.

Information about authors:

Arevshad Vartanyan, *PhD in Physical and Mathematical Sciences, Doctor of Economics*
ORCID: https://orcid.org/0000-0002-0317-7296
E-mail: arevshadvartanyan@mail.ru

Arestak Sarukhanyan, *Doctor of Technical Sciences*
ORCID: https://orcid.org/0000-0003-4928-9960
E-mail: sarukhanyan.arestak@mail.ru

Gevorg Veranyan, PhD in Technical Sciences
ORCID: *https://orcid.org/0000-0001-9093-2271*
E-mail: *g.g.veranyan@mail.ru*

Hovhannes Tokmajyan, Doctor of Technical Sciences
ORCID: *https://orcid.org/0000-0002-2315-7233*
E-mail: *tokmadzhyan_hv@mail.ru*

Neural prediction of mechanical properties of fiber-reinforced lightweight concrete containing silica fume and nano-silica

H.R. Moradi [iD] , *S.A.H. Hashemi* [✉] [iD]

Department of Civil Engineering, Qazvin Branch, Islamic Azad University, Qazvin, Iran

✉ *hashemi@qiau.ac.ir*

Abstract. Experimenting to acquire the optimum result for producing a product in a real environment takes a long time and has various costs. Numerical simulations help save time and improve accuracy in implementing numerous complex tests. The present study exploits neural networks in MATLAB to calculate the mechanical properties of fiber-reinforced lightweight concrete under different fractions of silica fume and Nano silica, steel and polypropylene fibers, cement, and scoria. Concrete specimens were constructed under different mix designs and subjected to 7- and 28-day compressive, tensile, flexural, and initial and ultimate water absorption tests. Then, a multilayer perceptron (MLP) was used as the neural network. Furthermore, 70 % of the specimens were utilized as the training data samples, 15 % were exploited as the validation data samples, and the remaining 15 % were employed as the testing data samples. The MLP was trained for seven inputs, one hidden layer, and 20 neurons. The model training, testing, and overall accuracy were 100 %, 97.3 %, and 99.5 %, respectively, indicating the model is efficient and effective.

1. Introduction

As the upper structures became lighter, the foundation volume and construction time will be reduced, leading to lower costs. By using natural or synthetic lightweight aggregates in the concrete, the concrete weight and thus, the foundation dimensions would be reduced, less bars would be needed, forming and bracing would cost less during section construction, better thermal isolation and sound absorption would be achieved, the transportation costs would decrease, the fire resistance would increase, and the freeze/thaw cycles would improve, compared to conventional concrete. Fiber-reinforced concrete can be used for a wide range of applications due to its high ductility, profound strength, high energy absorption capacity, and high cracking resistance.

Nowadays, technology has come to the aid of humans to perform their tasks faster, with higher accuracy and lower cost. Here, we intend to employ an artificial neural network (ANN) and experimental experience to take a step in that direction. ANN and experimental data are used in this study to predict the mechanical properties of lightweight fiber-reinforced concrete.

The use of lightweight concrete (LWC) has been a feature of construction for the past several decades. LWC has higher seismic resistance particularly for buildings located in the seismic regions. A recent study in Iran shows that destruction of most buildings is due to great inertial force and lack of structural tolerance for the load [1]. Therefore, lightweight concrete is employed in light of its unique properties in several applications, including high-rise structures, large multi-span bridges, and buried military structures for energy absorption and dissipation [2]. Lightweight concrete can be fabricated using

various methods, including removing fine-grained aggregates and creating air bubbles through chemical foam admixtures. Lightweight aggregates (LWAs) are the most common method of fabricating lightweight concrete [3, 4]. Scoria is a porous igneous rock with an edged appearance resulting from volcano eruptions and rapid cooling in the air, typically appearing in red to brown [5]. Structural lightweight aggregate concrete [SLWAC] criterion of ACI standard requires a 28-day cylinder compressive strength of 17 MPa and air-dry unit weight of less than 1840 kg/m^3. However, maximum unit weight of SLWC in some European standards such as DIN-4219, PN-91, ENV92 is defined as 2000 kg/m^3 and in PREN 206 is taken to be 2100 kg/m^3 (Euro light concrete 1998) [6]. Silica fume (also known as micro-silica) is an amorphous micro-scaled material, which improves the stability and strength of concrete. Shannag [7] demonstrated that the addition of silica fume at a fraction of 15 % enhanced concrete strength. Moreover, nanosilica may react with Ca(OH)$_2$ crystals and produce the calcium silicate hydrate (C-S-H) gel, increasing the early strength of hardened cement paste and concrete [8]. Qing et al. [9] compared nanosilica to silica fume in strength enhancement and reported that nanosilica had much higher pozzolanic activity than silica fume at early ages. Li [10] showed that a small fraction of nanosilica enhanced concrete compressive and flexural (bending) strengths and abrasion resistance. Ji et al. [11] found that the simultaneous use of silica fume and steel fibers enhanced the concrete compressive strength. Gesog̃lu et al. [12] concluded that the combined effect of SF and steel fibers may increase the compressive strength. Mahoutiyan et al. [13] studied the effects of steel and polypropylene fibers on concrete and found that polypropylene fibers had lower contributions than steel fibers to compressive strength enhancement. Hajmohammadi Baghba et al. [14] evaluated the effects of polypropylene fibers on self-compacting concrete (SCC) with recycled aggregates and reported a rise in polypropylene fibers enhanced impact strength, tensile strength, and energy absorption. In addition, soft computing can be employed to accurately predict the strength of asphalt mixtures. Accordingly, Zehtabchi et al. [15] employed fuzzy logic and predicted the marshal stability of polymer-modified asphalt mixtures with an error below 5 %. The type, quality, and amount of materials in concrete fabrication strongly influence its compressive strength. For example, the water-cement ratio and chemical and/or mineral admixture types and fractions are influential parameters. Since these parameters can cover relatively wide ranges, it is difficult to predict the concrete behavior. Therefore, advanced modeling is required to cope with this challenge. Artificial neural network (ANN) models are efficient instruments inspired by the biological neural network as a complex nonlinear regression model for minimizing the cost of predicting concrete behavior. Computers have enabled computational algorithms in the past several decades. Numerous studies have been conducted by computer scientists, engineers, and mathematicians on the computational behavior simulation of the human brain, which are classified into artificial intelligence (AI) and ANN sub-branch. Ruslan Ibragimov et al. [16] conducted a case study on construction material titled "The effect of metal and polypropylene fiber on technological and physical-mechanical properties of activated cement compositions" to study the effect of the fiber of various materials and sizes on the rheological properties of concrete mixtures and the physical and mechanical properties of self-compacting concrete and mortar obtained by the activation of Portland cement in the vortex layer device. According to the results, the metal fiber increases the shear stress of the concrete mixture obtained from activation by 1.56 times, which is higher than the polypropylene fiber (up to 1.34 times). In addition, Polypropylene fiber increases the crack resistance by 1.57 times, but metal fiber increases the impact strength of fine-grained concrete by 2.6 times. Oguzhan Yavuz Bayraktar et al. [17] studied the impact of recycled coarse aggregate (RCA) and fly ash (FA) on the mechanical properties and durability of polypropylene fiber-reinforced concrete exposed to freeze-thaw cycles and MgSO4 with artificial neural network (ANN) modeling experimentally. It was found that the combined use of 50 % RCA and PPF exhibited the best performance in terms of abrasion resistance. The principal result of this study is that using RCA, FA, and PPF in concrete can provide better mechanical and durability performance compared to conventional concrete. They also suggested that mixing ratios of concretes with RCA, FA, and PPF could be reliably determined by using Bayesian regularized ANN models. Based on this model, the mixing ratios of concrete can be determined based on the desired properties. Alaa M. Morsy et al. [18] conducted a case study named "predicting mechanical properties of engineering cementitious composite reinforced with PVA using artificial neural network". They designed an artificial neural network (ANN) to predict the mechanical properties of engineered cement composites (ECC), such as compressive strength, flexural strength, and direct tensile stress-strain curve. The used data set was 151, 76, and 44 test results for compressive strength, flexural strength, and direct tensile stress-train curve collected from recently published research. Based on the results, which include regression of all data, 98.4 % for compressive strength, 97.7 % for compressive strength, 98.4 % for tensile strength, relative minimum error of (0.15:9.40 ⁒) for compressive strength, (0.05:4.71 ⁒) for flexural strength, and (1.40:5.00 ⁒) for tensile strength, the artificial neural network can predict these parameters with great proximity. Al-Shiri et al. [19] evaluated the strength of lightweight concrete in a structure using neural networks. They used lightweight expanded clay aggregate (LECA) to reduce the weight of the concrete. The experiments were conducted for 3, 7, 14, and 28-day specimens, and they were able to provide a good approximation of lightweight concrete strength using sand, water/cement ratio, lightweight fine aggregate, lightweight coarse aggregate, silica fume used in solution, silica fume used in addition to cement, superplasticizer, and curing period as the input. They employed one

input layer, two hidden layers, and one output layer for their network. The hidden layers are composed of 14 and 6 neurons, sequentially, and the output layer is composed of four neurons. The neural network prediction results indicate that the experimental data were measured and estimated by the network with an appropriate accuracy. Alton and his colleagues [20] used a neural network to estimate the strength of the steel fiber-contained lightweight concrete. A total of 126 specimens of 150×300 mm were made in the laboratory. The input parameters of the neural network were steel fibers, water, water/cement ratio, sand, and superplasticizer. They used multilayer perceptron neural network (MLP) in their study. They also used multiple linear regression (MLR) method, a statistical technique to estimate data, to compare the results with MLP. The algorithm used in this experiment is the Levenberg-Marquardt algorithm (LM). The results showed that the neural network offered a good estimation of the data. In case of better neural network training, the results could even improve in their estimation. Regarding the high correlation coefficient and the diversity of parameters, it can be expected that the neural network can offer a wider range of solutions than complex statistical techniques. In a research, Saudi and his colleagues [21] tried to predict the creep deformation of asphalts modified with polymer, using an artificial neural network. They suggested that a proper neural network architecture with an error correction approach can predict the output parameter (i.e., creep rate) with a small error using various input parameters (e.g., temperature, rubber contents, loading stress, and compactness). Abdullah [22] studied the application of artificial neural networks to predict concrete properties. The selected network input parameters are water/cement ratio, aggregate/cement ratio, and slump values. According to the results, the average absolute error (AAE) value was found to be less than 3.46 % for the proposed model and the NRMSE value was the lowest 0.0011, indicating that artificial neural networks are an invaluable modeling technique. In a research, Ofrikhter and his colleagues [23] employed artificial neural networks to estimate the mechanical parameters of soils based on known physical characteristics. As a result of this research, an artificial neural network has been obtained that makes it possible to predict the angle of friction and the specific cohesion of clay soils with reasonable accuracy.

ANNs were proposed by Yang (1903) [24]. The inception of artificial neurons can be traced back to 1943 when Warren McCulloch, a neuroscientist, and Walter Pitts, a mathematician, put forth a model of a neuron in their article entitled "A Logical Calculus of Ideas Immanent in Nervous Activity." Their proposed model was a simplistic computational framework grounded on propositional logic that offered a blueprint for how neurons operate to accomplish intricate tasks. Their work demonstrated that a network of neurons has the capability to compute any mathematical or logical function [25]. The initial scientific application of neural networks began to take shape during the latter part of the 1950s. In this epoch, Frank Rosenblatt formulated the concept of perceptron networks and their associated learning rules. In 1957, Rosenblatt introduced an algorithm that initializes parameter values and subsequently updates them toward optimal parameters by analyzing distinct input values. Moreover, Rosenblatt and his colleagues conducted experiments that showed that perceptron networks have the ability to recognize patterns. In essence, perceptron acquire a set of input signals and if their linear combination surpasses a predetermined threshold value, the perceptron becomes activated, while if it falls below this value, the perceptron remains deactivated [26]. Civil engineers started using ANNs in 1990. Rajasekaran et al. [27] published papers on utilizing fuzzy neural networks in civil engineering. Lai et al. [28] estimated the concrete compressive strength using neural networks in 1996. Basma et al. [29] and Oh et al. [30] employed backpropagation neural networks to estimate the mix design of typical concrete and the cement hydration degree. Mousavinejad et al. [31] explored the effects of micro-silica (MS) and Nano silica on the mechanical properties of fiber-reinforced lightweight concrete. The present study used the data of Mousavinejad et al. [31], as reported in Tables 1 and 2.

The main objective of this study is to evaluate the performance of the artificial neural network (ANN) approach to predict the mechanical properties of lightweight fiber-reinforced concrete with adequate precision. The ANN was composed of 7 input layers and 1 hidden layer, and it was trained using 20 neurons. The estimations were reasonably accurate, indicating the proper efficiency and accuracy of the chosen network.

2. Methods

2.1. Mix designs and specimen fabrication

Initially, a water-cement ratio of 0.3 was applied to all the specimens, with 10% and 15% silica fume fractions. Then, hooked steel (50 mm) and polypropylene (12 mm) fibers were used, and some water was mixed with dry LWAs for 30 min pre-wetting to fabricate the specimens. In the following procedure, sand was added and mixed with LWAs before adding cement. Finally, water and the superplasticizer were added to the mixture. The concretes were molded and cured in the laboratory at 20–25 °C for 24 h. Table 1 shows the mix designs [31].

Table 1. Mix designs [31].

Specimen	Cement	Silica Fume	Nano silica	Water	Sand	Scoria	Superplasticizer	Polypropylene Fiber	Steel Fiber
Control	500	0	0	150	705	676	2.5	0	0
MS 10	450	50	0	150	705	661	4	0	0
MS10 PP2	450	50	0	150	705	657	4	1.8	0
MS10 PP2 S4	450	50	0	150	705	649	5	1.8	31.4
MS10 PP2 S8	450	50	0	150	705	641	6	1.8	62.8
MS 15	425	75	0	150	705	653	5	0	0
MS15 PP2	425	75	0	150	705	650	5	1.8	0
MS15 PP2 S4	425	75	0	150	705	641	6	1.8	31.4
MS15 PP2 S8	425	75	0	150	705	633	7	1.8	62.8
MS10 Na3	435	50	15	150	705	646	5	0	0
MS10 Na3 PP2	435	50	15	150	705	643	5	1.8	0
MS10 Na3 PP2 S4	435	50	15	150	705	635	6	1.8	31.4
MS10 Na3 PP2 S8	435	50	15	150	705	627	7	1.8	62.8
MS10 Na5	425	50	25	150	705	638	5	0	0
MS10 Na5 PP2	425	50	25	150	705	635	5	1.8	0
MS10 Na5 PP2 S4	425	50	25	150	705	627	6	1.8	31.4
MS10 Na5 PP2 S8	425	50	25	150	705	618	7	1.8	62.8

Table 2. Compressive, flexural, and tensile strengths and water absorption [31].

Specimen	7-Day Compressive Strength (MPa)	28-Day Compressive Strength (MPa)	Initial Water Absorption (%)	Ultimate Water Absorption (%)	Tensile Strength (MPa)	Flexural Strength (MPa)
Control	19	22	2.21	3.89	2.49	3.78
MS 10	24	29	1.58	2.31	3.11	4.8
MS10 PP2	23	27.8	1.62	2.37	3.3	5.28
MS10 PP2 S4	26	31.3	1.77	2.51	3.72	6.06
MS10 PP2 S8	25.8	32	1.89	2.65	3.97	6.66
MS 15	22.5	26.5	1.79	2.66	2.79	4.44
MS15 PP2	21.2	25.8	1.84	2.74	2.98	4.74
MS15 PP2 S4	23.8	28.5	1.97	2.82	3.16	5.58
MS15 PP2 S8	25	29	2.09	2.98	3.41	6.06
MS10 Na3	26.8	31.5	1.42	1.95	3.31	5.16
MS10 Na3 PP2	25.5	30	1.44	2	3.57	5.64
MS10 Na3 PP2 S4	28.8	34	1.58	2.11	3.85	6.78
MS10 Na3 PP2 S8	29	35	1.76	2.3	4.08	7.26
MS10 Na5	24.5	28	1.74	2.53	2.88	4.56
MS10 Na5 PP2	23.2	27	1.75	2.62	3.07	4.92
MS10 Na5 PP2 S4	26	30	1.91	2.78	3.41	6.12
MS10 Na5 PP2 S8	26.5	30.8	2.02	2.83	3.62	6.48

2.2. Artificial Neural Network (ANN)

ANNs consist of simple parallel operation elements inspired by the biological neural system. Neural Networks function is determined through the connection of elements in nature. Therefore, it is possible to construct an artificial structure based on natural networks where the connections are weighted to determine the relationships of its elements. A multilayer perceptron (MLP) is a basic neural network model that simulates the transmission process of the human brain and focuses on the network behavior and signal propagation of the human brain. Therefore, MLPs are sometimes known as feedforward ANNs since two or more neurons can be combined into a layer. A neural network may consist of several layers with a unique weight matrix, bias vector, and output. The layers positioned between the input and output layers are the hidden layers. Fig. 1 depicts a schematic of a feedforward ANN.
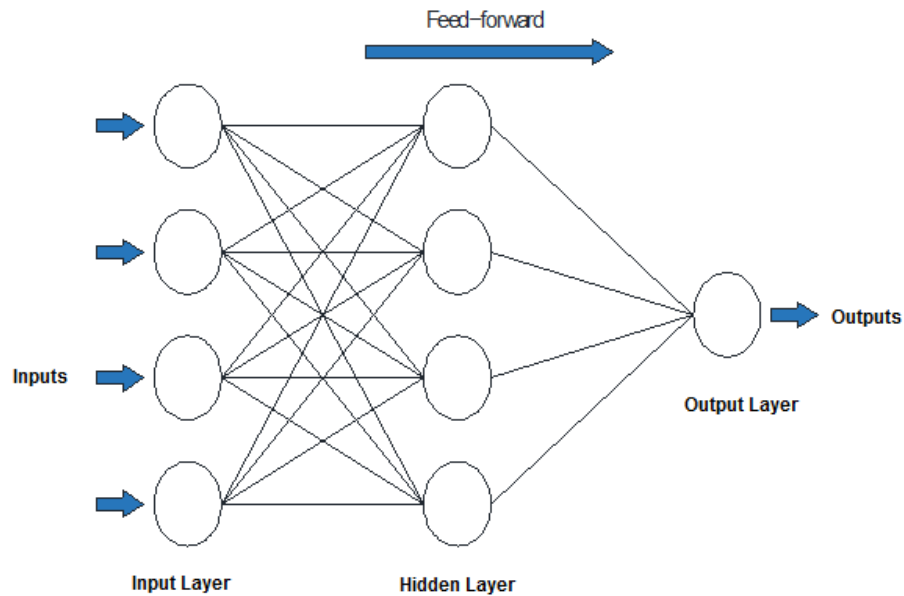
Figure 1. Schematic of a feedforward ANN.

2.3. Model description and training

2.3.1. Dataset

An efficient ANN requires sufficient and detailed data of the critical parameters. Thus, the present study employed 17 experimental concrete specimens of various mix designs. The cement, Silica Fume, Nano-silica, scoria, superplasticizer, and polypropylene and steel fiber quantities were used as the inputs, whereas the 7- and 28-day compressive strength, initial and ultimate water absorptions, tensile strength, and flexural strength were assumed to be the outputs (Table 1 and Table 2).

An ANN seeks to learn through variations in the weights and biases performed via iterations. In other words, a training dataset is introduced several times to the algorithm, which recognizes differences in the training data by changing the weights and deviations. Backpropagation is one of the most commonly used iteration approaches in neural networks consisting of feedforward and backpropagation stages. The input data are multiplied by the corresponding weights and summed up with the biases. Then, the output, which is likely to differ from the actual output, is obtained to calculate the error in the first iteration. Once the error has been found through the weights and deviations, the algorithm moves to the second stage in one iteration, updating the weights and biases to diminish the error in the next iteration. These iterations continue until the output approaches the actual output for all the training data.

2.3.2. Optimal ANN structure

The networks with two hidden sigmoid and linear output neurons were investigated to identify the optimal ANN topology. The performance of ANNs was evaluated for different numbers of neurons, and the numbers of neurons were set based on trial and error. This study adopted the root-mean-square error $(RMSD)$ as the evaluation criterion, which is calculated as:

$$RMSD = \sqrt{\dfrac{\sum\limits_{i=1}^{N}\left(X_i - \bar{X}\right)}{N}}, \tag{1}$$

where X_i presents the actual data point, $\bar{X}$ represents the estimated data point, and N denotes the number of data points.

The MLP model with seven inputs, one hidden layer, and 20 neurons was trained, as shown in Fig. 2.
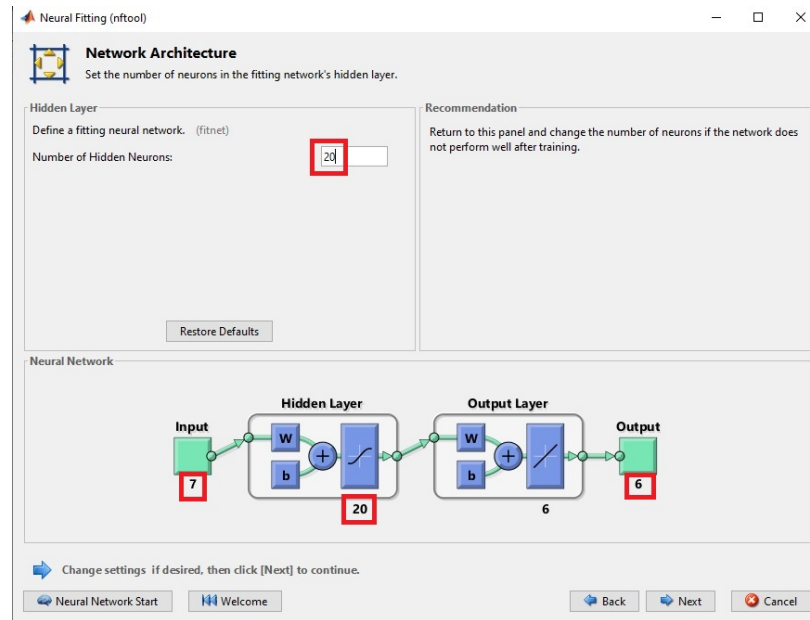
Figure 2. MLP architecture with inputs, output, and neurons in MATLAB.

Bayesian neural networks are a method based on neural networks in modeling nonlinear and complicated problems through specific algorithms and statistical methods. It can be used to model cause and effect relationships of a process, analyze the circumstance, and predict the future status of a system. Bayesian regularization was used to train the MLP model and determine the coefficients. Furthermore, the data were divided into training (70 %), validation (15 %), and testing (15 %) dataset, respectively. Table 3 summarizes the ANN parameters.

Table 3. ANN parameters.

ANN	MLP
Type	Feedforward
Training algorithm	TRAINLM
Error algorithm	Backpropagation
Optimization function	Bayesian regularization
Training data	70 %
Validation data	15 %
Testing data	15 %

3. Results and Discussion

The correlation coefficient R was used for evaluating the model. The optimized trained model accurately predicted the 7- and 28-day compressive strengths, flexural strength, tensile strength, and initial and ultimate absorptions. In this context, testing (simulation) was carried out on 3 data never used in ANN. From these results, the model yields sufficient reliability as the training regression was 100 %, testing regression was 97.3 % and all data regression was 99.5 %. Fig. 3 compares the actual and predicted regression values of the training, validation, and testing datasets. As can be seen, the model was found to have high performance.
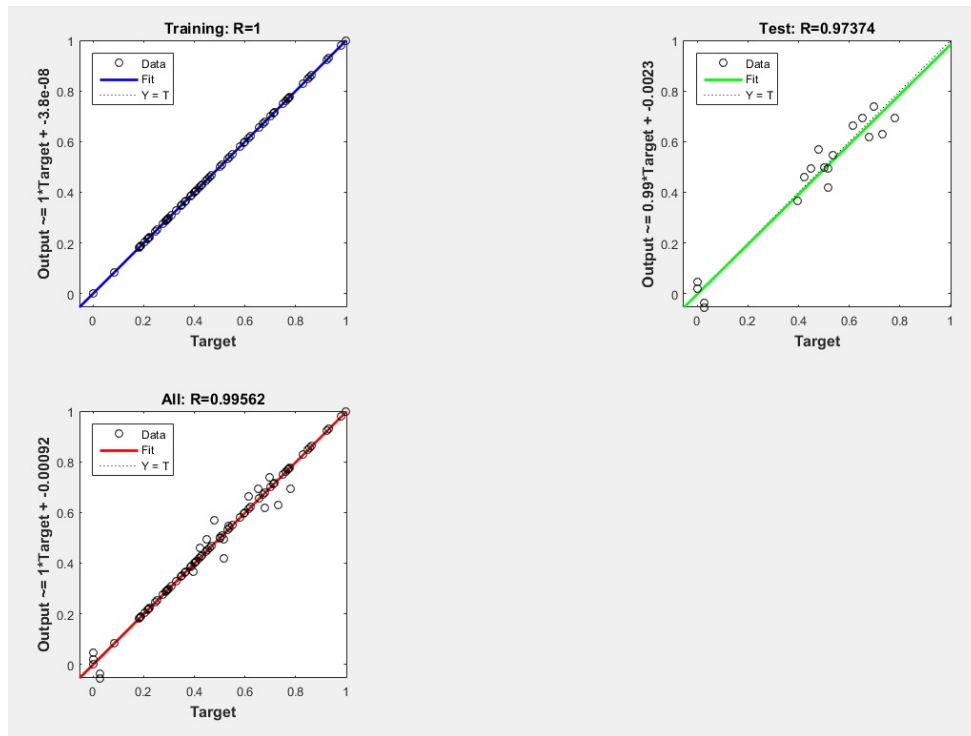
Figure 3. Actual versus predicted regressions for the training, validation, and testing datasets.

The data (Table 1 and Table 2) were normalized and introduced to the model as:

$$Z = \frac{X - \min(x)}{\max(x) - \min(x)},$$

(2)

where x is the input values of Table 1 and Table 2. Thus, the normalized outputs should be decoded and compared to the actual values in Table 2 using Eq. (2). Table 4 provides the decoded outputs.

Table 4. MLP predictions.

Specimen	7-Day Compressive Strength (MPa)	28-Day Compressive Strength (MPa)	Initial Water Absorption (%)	Ultimate Water Absorption (%)	Tensile Strength (MPa)	Flexural Strength (MPa)
Control	19.00	22.00	2.21	3.89	2.49	3.78
MS 10	24.00	29.00	1.58	2.35	3.11	4.80
MS10 PP2	23.00	27.80	1.62	2.41	3.30	5.28
MS10 PP2 S4	26.00	31.30	1.77	2.55	3.72	6.06
MS10 PP2 S8	25.80	32.00	1.89	2.68	3.97	6.66
MS 15	22.50	26.50	1.79	2.69	2.79	4.44
MS15 PP2	21.20	25.80	1.84	2.77	2.98	4.74
MS15 PP2 S4	23.80	28.50	1.97	2.85	3.16	5.58
MS15 PP2 S8	25.00	29.00	2.09	3.00	3.41	6.06
MS10 Na3	26.80	31.50	1.42	2.00	3.31	5.16
MS10 Na3 PP2	25.50	30.00	1.44	2.05	3.57	5.64
MS10 Na3 PP2 S4	27.85	32.43	1.60	2.16	3.89	6.47
MS10 Na3 PP2 S8	29.00	35.00	1.76	2.34	4.08	7.26
MS10 Na5	25.19	29.09	1.71	2.56	2.85	4.52
MS10 Na5 PP2	23.20	27.00	1.75	2.65	3.07	4.92
MS10 Na5 PP2 S4	24.72	27.95	1.87	2.71	3.40	5.64
MS10 Na5 PP2 S8	26.50	30.80	2.02	2.86	3.62	6.48

The differences between the experimental and numerical were measured to evaluate model performance further (Table 5). According to Table 5, the differences were minimal, suggesting that the proposed model had an excellent and reliable performance.

Table 5. Differences between the experimental and numerical quantities.

Specimen	7-Day Compressive Strength (%)	28-Day Compressive Strength (%)	Initial Water Absorption (%)	Ultimate Water Absorption (%)	Tensile Strength (%)	Flexural Strength (%)
Control	0.00	0.00	0.00	0.00	0.00	0.00
MS 10	0.00	0.00	0.00	–1.76	0.00	0.00
MS10 PP2	0.00	0.00	0.00	–1.65	0.00	0.00
MS10 PP2 S4	0.00	0.00	0.00	–1.42	0.00	0.00
MS10 PP2 S8	0.00	0.00	0.00	–1.21	0.00	0.00
MS 15	0.00	0.00	0.00	–1.19	0.00	0.00
MS15 PP2	0.00	0.00	0.00	–1.08	0.00	0.00
MS15 PP2 S4	0.00	0.00	0.00	–0.98	0.00	0.00
MS15 PP2 S8	0.00	0.00	0.00	–0.79	0.00	0.00
MS10 Na3	0.00	0.00	0.00	–2.56	0.00	0.00
MS10 Na3 PP2	0.00	0.00	0.00	–2.44	0.00	0.00
MS10 Na3 PP2 S4	3.28	4.62	–0.98	–2.50	–1.05	4.55
MS10 Na3 PP2 S8	0.00	0.00	0.00	–1.78	0.00	0.00
MS10 Na5	–2.81	–3.88	1.68	–1.29	1.09	0.96
MS10 Na5 PP2	0.00	0.00	0.00	–1.25	0.00	0.00
MS10 Na5 PP2 S4	4.94	6.82	2.17	2.41	0.26	7.82
MS10 Na5 PP2 S8	0.00	0.00	0.00	–0.97	0.00	0.00

Fig. 4 compares the model outputs to the actual values. As can be seen, the estimates and actual values were in good agreement, suggesting that the proposed ANN is efficient and effective.
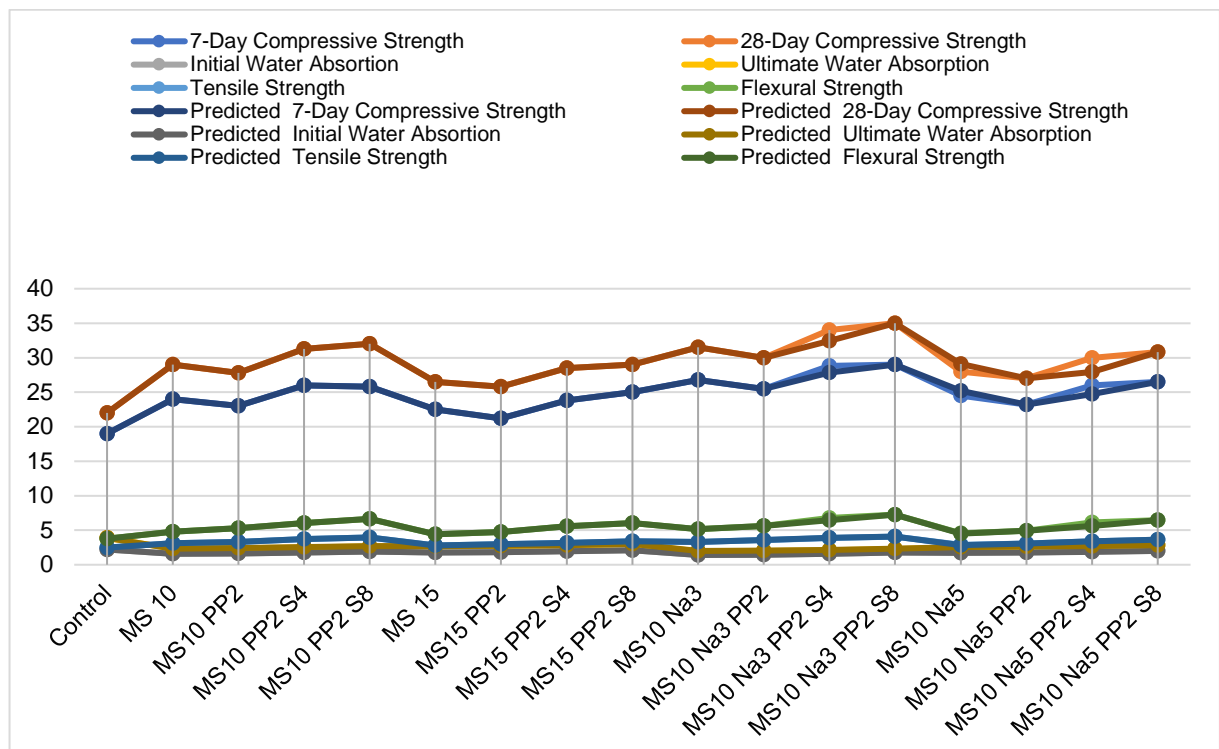

Figure 4. Comparison of experimental and numerical quantities.

4. Conclusion

(1) This study employed an ANN model to estimate the mechanical properties of fiber-reinforced lightweight concretes containing silica fume (MS) and Nano silica.

(2) The inputs included the fractions of cement, Silica Fume, Nano-silica, scoria, superplasticizer, and polypropylene and steel fibers, whereas the outputs involved the 7- and 28-day compressive strengths, initial water absorption, ultimate water absorption, tensile strength, and flexural strength. The experimental data of 17 concrete specimens were adopted from.

(3) Using an ANN requires determining the optimal number of hidden layers and neurons in a trial-and-error process to obtain the most accurate outputs.

(4) Although the predictive performance of an ANN model is limited to the training data, the model can be re-trained using new training algorithms to cover a broader range of inputs.

(5) The model estimates were in good agreement with the experimental data, suggesting that the model was efficient and produced reliable outputs.

(6) The maximum error was calculated as much as 4.94 %, 6.82 %, 2.17 %, 2.56 %, 1.09 %, and 7.82 % for the 7-day compressive strength, 28-day compressive strength, initial water absorption, ultimate water absorption, tensile strength, and flexural strength, respectively.

(7) Future studies are suggested to evaluate different coarse- and fine-grained aggregates and reinforcement fibers and incorporate a more significant number of specimens to obtain more comprehensive results. Furthermore, using recycled aggregates, e.g., rubber and asphalt aggregates in concrete fabrication is crucial to avoid environmental degradation.

References

1. Bargi, K. Fundamentals of Earthquake Engineering. Tehran, Tehran University Press, 2001. ISBN: 978-964-03-4325-8.

2. Babu, D.S., Ganesh Babu, K., Tiong-Huan, W. Effect of polystyrene aggregate size on strength and moisture migration characteristics of lightweight concrete. Cement and Concrete Composites. 2006. 28 (6). Pp. 520–527. DOI: 10.1016/j.cemconcomp.2006.02.018.

3. Demirboğa, R., Örüng, İ., Gül, R. Effects of expanded perlite aggregate and mineral admixtures on the compressive strength of low-density concretes. Cement and Concrete Research. 2001. 31 (11). Pp. 1627–1632. DOI: 10.1016/S0008-8846(01)00615-9.

4. Al-Khaiat, H., Haque, M.N. Effect of initial curing on early strength and physical properties of a lightweight concrete. Cement and Concrete Research. 1998. 28 (6). Pp. 859–866. DOI: 10.1016/S0008-8846(98)00051-9.

5. Demirdag, S., Gunduz, L. Strength properties of volcanic slag aggregate lightweight concrete for high performance masonry units. Construction and Building Materials. 2008. 22 (3). Pp. 135–142. DOI: 10.1016/j.conbuildmat.2006.10.002.

6. Institution, B.S. BS EN 206: 2013 Concrete. Specification, performance, production and conformity 2013.

7. Shannag, M.J. High strength concrete containing natural pozzolan and silica fume. Cement and Concrete Composites. 2000. 22(6). Pp. 399–406. DOI: 10.1016/S0958-9465(00)00037-8.

8. Mehravaran, M., Sohrabi, M. Improving Properties of Concrete Containing Taftan Pozzolans using Nano silica. 5th National Conference of Civil Engineering. 2010. Mashhad, Iran. 7 pp. (in Persian).

9. Qing, Y., Zenan, Z., Deyu, K., Rongshen, C. Influence of nano-SiO2 addition on properties of hardened cement paste as compared with silica fume. Construction and Building Materials. 2007. 21 (3). Pp. 539–545. DOI: 10.1016/j.conbuildmat.2005.09.001

10. Li, H., Zhang, M., Ou, J. Abrasion resistance of concrete containing nano-particles for pavement. Wear. 2006. 260 (11). Pp.1262–1266. DOI: 10.1016/j.wear.2005.08.006

11. Ji, T., Mirzayee, A., Zangeneh-Madar, Z., Zangeneh-Madar, E. Preliminary study on water infiltration of concrete containing nano-SiO$_2$ and silicone. 2009.

12. Gesoğlu, M., Güneyisi, E., Alzeebaree, R., Mermerdaş, K. Effect of silica fume and steel fiber on the mechanical properties of the concretes produced with cold bonded fly ash aggregates. Construction and Building Materials. 2013. 40. Pp. 982–990. DOI: 10.1016/j.conbuildmat.2012.11.074

13. Mahoutian, M., Behradi-Yekta, S. Effects of Steel and Polypropylene Fibers on Mechanical Properties of Lightweight Concretes Containing LECA and Pumice. 1st National Conference of Lightweight Concrete. 2011.

14. Hajmohammadian Baghba, M., Hashemi, S.A.H, Kalbasi Anaraki, K, Hashemi, E.S. Influence of polypropylene-fiber on the mechanical properties of self-compacting-concrete with recycled aggregates. Magazine of Civil Engineering. 2020. 99 (7). Article no. 9905. DOI: 10.18720/MCE.99.5

15. Zehtabchi, A., Hashemi, S.A.H., Asadi, S. Predicting the strength of polymer-modified thin-layer asphalt with fuzzy logic. Construction and Building Materials. 2018. 169. Pp. 826–834.

16. Ibragimov, R., Bogdanov, R., Korolev, E. The effect of metal and polypropylene fiber on technological and physical mechanical properties of activated cement compositions. Case Studies in Construction Materials. 2022. 16. Pp. e00882. DOI: 10.1016/j.cscm.2022.e00882

17. Bayraktar, O.Y., Eshtewı, S.S.T., Benli, A., Kaplan, G., Toklu, K., Gunek, F. The impact of RCA and fly ash on the mechanical and durability properties of polypropylene fibre-reinforced concrete exposed to freeze-thaw cycles and MgSO$_4$ with ANN modeling. Construction and Building Materials. 2021. 313. Pp. 125508. DOI: 10.1016/j.conbuildmat.2021.125508

18. Morsy, A.M., Abd Elmoaty, A.E.M., Harraz, A.B. Predicting mechanical properties of engineering cementitious composite reinforced with PVA using artificial neural network. Case Studies in Construction Materials. 2022. 16. Pp. e00998. DOI: 10.1016/j.cscm.2022.e00998.

19. Alshihri, M.M., Azmy, A.M., El-Bisy, M.S. Neural networks for predicting compressive strength of structural light weight concrete. Construction and Building Materials. 2009. 23 (6). Pp. 2214–2219. DOI: 10.1016/j.conbuildmat.2008.12.003.

20. Altun, F., Kişi, Ö., Aydin, K. Predicting the compressive strength of steel fiber added lightweight concrete using neural network. Computational Materials Science. 2008. 42 (2). Pp. 259–265. DOI: 10.1016/j.commatsci.2007.07.011.

21. Saoudi, B.S., Haddadi, S.H. Predicting creep deformation of asphalts modified with polymer using artificial neural networks. Magazine of Civil Engineering. 2021. 101 (1). Article no. 10106. DOI: 10.34910/MCE.101.6

22. Abdulla, N. Application of artificial neural networks for prediction of concrete properties. Magazine of Civil Engineering. 2022. 110 (2). Article no. 11007. DOI: 10.34910/MCE.110.7

23. Ofrikhter, I.V., Ponomaryov, A.P., Zakharov, A.V., Shenkman, R.I. Estimation of soil properties by an artificial neural network. Magazine of Civil Engineering. 2022. 110 (2). Article no. 11011. DOI: 10.34910/MCE.110.11

24. Hopgood, A.A. Intelligent Systems for Engineers and Scientists: A Practical Guide to Artificial Intelligence. CRC press, 2021. DOI: 10.1201/9781003226277

25. McCulloch, W.S., Pitts, W. A logical calculus of the ideas immanent in nervous activity. The bulletin of mathematical biophysics. 1943. 5(4). Pp. 115–133. DOI:10.1007/BF02478259. URL: https://doi.org/10.1007/BF02478259

26. Rosenblatt, F. The perceptron: a probabilistic model for information storage and organization in the brain. Psychological review. 1958. 65 (6). Pp. 386. DOI: 10.1037/h0042519

27. Rajasekaran, S., Febin, M.F., Ramasamy, J. V. Artificial fuzzy neural networks in civil engineering. Computers \& Structures. 1996. 61 (2). Pp. 291–302. DOI: 10.1016/0045-7949(96)00044-2

28. Lai, S., Serra, M. Concrete strength prediction by means of neural network. Construction and Building Materials. 1997. 11 (2). Pp. 93–98. DOI: 10.1016/S0950-0618(97)00007-X

29. Basma, A.A., Barakat, S.A., Al-Oraimi, S. Prediction of cement degree of hydration using artificial neural networks. ACI Materials Journal. 1999. 96 (2). Pp. 167–172.

30. Oh, J.-W., Lee, I.-W., Kim, J.-T., Lee, G.-W. Application of Neural Networks for Proportioning. ACI Materials Journal. 1999. 96 (1). Pp. 61–67.

31. Ghasemzadeh, M.S.H., others. Effect of Silica Fume and Nano Silica on Mechanical Properties of Fiber-Reinforced Lightweight Concrete. 2018.

Information about authors:

Hamidreza Moradi,
ORCID: https://orcid.org/0000-0003-3715-5180
E-mail: hamidrezamoradi1360@yahoo.com

Seyed Amir Hossein Hashemi, PhD
ORCID: https://orcid.org/0000-0001-8385-9272
E-mail: hashemi@qiau.ac.ir

Heavy-weight concrete with increased early strength

S.I. Pimenov ✉ (iD) **, A.R. Galautdinov** (iD)

Kazan State University of Architecture and Engineering, Kazan, Russia

✉ *sergeypimenov12 @yandex.ru*

Abstract. Production process rate is the most important thing in industrial engineering of concrete and reinforced concrete products, which heavily depends on duration of concrete handling strength development. One of the methods of processes' intensification of concrete structure formation is steam treatment. However, destructive processes developing in concrete in some instances during its long steam treatment at the temperatures above 40°C necessitate reducing its duration. This is achieved through the use of methods of further intensification of concrete structure formation processes, one of which is hydromechanical activation of binder. Research results of joint effect of hydromechanical activation of cement binder and following steam treatment on kinetics of heavy-weight concrete strength development are presented in the paper; special aspects of hydration and structure formation of cement stone are studied. We found an increase in strength development rate of heavy-weight concrete during isothermal warming temperature increment. Technological parameters of steam treatment of concrete based on cement binder under hydromechanical activation are determined for preparing B30–B60 grade concretes using components for B25 heavy-weight concrete. Received results are of substantial interest to construction industry and can be used in prefabricated concrete and reinforced concrete technology, which gives the opportunity to reduce energy intensity of production and end product cost.

1. Introduction

Improvement of the effectiveness of manufacturing processes of construction materials and products can be rated by how much the production duration is reduced and the costs are cut while maintaining or increasing the quality and marketability of the finished products in comparison with analogs. The research on rational combination of certain task components at hand is currently of great interest with respect to manufacturing process of concrete and reinforced concrete products [1]–[3].

Production process rate is the most important thing in production management, which heavily depends on duration of concrete handling strength development. The reason for this is that duration of concrete curing under normal conditions as per Russian State Standard GOST 10180-2012 until attainment of its handling strength far exceeds duration of all other manufacturing processes and necessitates increase of production area.

Processes' intensification of concrete structure formation is possible due to the use of technologic, chemical and thermal methods [4]–[9]. These methods provide different rate acceleration of processes of concrete structure formation and hardening, for which reason applicability of each of them is specified by conditions of production [10]–[15].

At the present time thermal methods of processes' intensification of concrete structure formation and hardening have widespread application in concrete and reinforced concrete production [16]. One of these methods is steam treatment (ST) that helps to get handling strength of products in a short time frame.

Moreover, ST mainstreaming into manufacturing process of concrete and reinforced concrete production makes it possible to largely increase form reuse.

However, it should be noted that apart from constructive processes that are conditioned by acceleration of structure formation and corresponding hardening of concrete structure under ST, destructive processes can also be initiated by volumetric changes of constituents of concrete, by internal deformations, by capillary pressure and moisture movement [17], [18]. Moreover, the effectiveness of ST is relatively not too high as a consequence of low performance coefficient of curing rooms that is within 45 %, which contributes to high cost of end products and lower market competitiveness.

Based on the aforesaid the question about ST duration reduction by the way of intensifying concrete structure formation processes is growing more urgent. One of the effective ways to increase concrete structure formation kinetics is mechanical activation of binder in water medium, or hydromechanical activation (HMA) [5], [10]. Intensification of concrete structure formation processes at early period of hardening during HMA of cement binder is conditioned by increase of mix contraction and also by accelerated primary phase ionic yield into mortar [19]–[23].

Another way to increase the rate of concrete strength development is introduction of plasticizing agents [24]–[26] into concrete composition that provide additional duration reduction of initial period of hydration that defines element formation of primary structure (crystalline hydrates and gel) [15], [27]–[29]. Besides, reduction of induction and crystallizing periods of concrete structure formation during HMA in the presence of chemical admixtures becomes agent for negative effect deficiency of binder hydration retardation by chemical admixtures. In this regard, HMA of cement binder in the presence of chemical admixtures provides a massive scale-up of ultimate bending and compression strength of concrete and reinforced concrete products in early period of hardening.

The question about combined influence of HMA processes of cement binder and following concrete ST on its structure formation kinetics is of great practical interest calling for substantial research.

The purpose of the present study is development of heavy-weight concrete with increased early strength by the way of HMA of cement binder including in the presence of chemical admixtures and further ST.

2. Materials and Methods

During experimental investigations we used the following raw components of concrete:

– Portland cement *CEM* II/A-P 32.5N produced by Ul'ianovskiy plant as per Russian State Standard GOST 31108-2016;

– fine aggregate: enriched sand of Kamsko-Ust'inskoe mineral assets with fineness modulus 2.7;

– coarse aggregate: granite macadam of Urals mineral assets 5–20 mm in size;

– water: plumbing potable water as per Russian State Standard GOST 23732.

For experimental research, we used B25 grade heavy-weight concrete with slump of concrete cone equal to 7–9 cm; the mixture ratio of cement : sand : granite macadam was 490 : 555 : 1315.

We chose "Relamix T-2" superplasticizer based on sodium salts of polymethylenenaphthalenesulfonic acids and formaldehyde with accelerating curing effect produced as per technical conditions 5870-002-14153664-04. Its content in concrete mix composition was 1 % by weight of cement.

HMA of cement binder was made in rotary-pulsed equipment (RPE) RPE-0.8-55A-2.2UZ produced as per technical conditions 5132-001-70447062.

For preparation of concrete mix at the first stage, we combined the required quantity of "Relamix T-2" additive and estimated quantity of gauged water. Then we mixed 50 % by total mass of cement and exposed the received mix to HMA in RPE for 2 minutes. After that we added the remaining portion (50 %) of cement, fine aggregate and coarse aggregate into the received suspended mixture and mixed in job mixer for 5 minutes. With the received concrete mixtures, we made test cube specimens with the dimensions of 10×10×10 cm.

To experimentally investigate the influence of isothermal warming temperature of concrete test cubes on their compression strength development kinetics during ST, we prepared four compositions:

– No.1 – reference specimen (unmodified composition without HMA of cement binder);

– No.2 – specimen based on cement binder under HMA in RPE;

- No.3 – specimen based on cement binder modified by "Relamix T-2" additive (without HMA of cement binder);
- No.4 – specimen based on cement binder under HMA in RPE in the presence of "Relamix T-2" additive.

Hereafter concrete specimens were exposed to ST as follows:

- curing of specimens for 2 hours at a temperature of 20 °C;
- temperature increase for 2 hours in curing room equipped with a microprocessor-based two-channel temperature controller, in accordance with set of rules SP 130.13330.2018;
- isothermal warming for 10 hours at different temperatures (30 °C, 40 °C, 80 °C) in according to SP 130.13330.2018 in curing room;
- temperature decrease for 2 hours.

Ultimate compressive strength of concrete specimens at 1, 3 and 28 days after ST was defined according to Russian State Standard GOST 10180-2012.

Special aspects of hydration and structure formation of cement stone were measured by the way of X-ray diffraction analysis (XRDA) and differential thermal analysis (DTA). During X-ray diffraction analysis diffractometer "D2 Phaser" produced by "BRUKER" company (Germany) was used. Powder mounts according to Bragg–Brentano geometry with the use of monochromated CuK-α radiation ($\lambda = 1.54178$ Å) in step SCAN mode were studied at the following measurement modes and factors record:

- tube tension – 30 kV;
- current – 30 mA;
- scan step – 0.02°;
- scan rate – 1°/min;
- angular range of scan according to Bragg–Brentano (BB) geometry – 3-60°.

Diffractograms received on the results of experimental investigations were compared with reference diffractograms. To do so, we accessed an international card-index database of powder diffractograms, PDF-2 ICDD.

During differential thermal analysis derivatograph SDT Q600 produced by MOM company was used. Platinum lidded crucibles were used in a form of sample-holder, incinerated aluminium oxide – in a form of master sample. The analysis was carried out in helium that was pumped under quartz glass closing thermo-couple of sample and master sample. During the analysis we registered differential thermal curve. Samples' mass was 150–250 mg, sensitivity of balance – 100–200 mg, sensitivity of DTA-channel – 250–500. Specimens were heated in the temperature range from 20 °C to 1000 °C, the heating rate was 25 °C/min.

For carrying out experimental investigations of special aspects of cement stone hydration and structure formation we prepared specimens of 4 compositions:

- No.1/S – reference specimen (unmodified composition without HMA of cement binder);
- No.2/S – specimen based on cement binder modified by "Relamix T-2" additive (without HMA);
- No.3/S – specimen based on cement binder under HMA in RPE in the presence of "Relamix T-2" additive.
- No.4/S – specimen based on cement binder under HMA in RPE in the presence of additive "Relamix T-2" with the following ST at isothermal warming temperature equal to 80°C.

3. Results and Discussion

Table 1 shows experimental results of the influence of isothermal warming temperature of concrete specimens No.1–4 during ST according to the mode received in Materials and Methods section on kinetics of concrete compressive strength development. There is ultimate compressive strength of heavy-weight concrete specimens in the numerator and increase of ultimate strength (%) relative to the specimens, hardening of which took place under normal conditions as per Russian State Standard GOST 10180-2012, in the denominator.

Table 1. Influence of isothermal warming temperature of concrete specimens during ST on kinetics of concrete compressive strength development.

No. of composition	Isothermal warming temperature, °C	Ultimate compressive strength, MPa		
		Day 1 of hardening	Day 3 of hardening	Day 28 of hardening
No.1	Standard curing	8.5	26	44.3
	30	<u>10.2</u> 20	<u>27.3</u> 5	<u>46.07</u> 4
	40	<u>11.5</u> 35	<u>30.2</u> 16	<u>50.1</u> 13
	80	<u>14.7</u> 73	<u>33.1</u> 27	<u>50.5</u> 14
No.2	Standard curing	14.2	29.8	52.8
	30	<u>18.6</u> 31	<u>31.7</u> 6	<u>54.4</u> 3
	40	<u>19.6</u> 38	<u>33.6</u> 13	<u>57.3</u> 9
	80	<u>28.5</u> 101	<u>39.4</u> 32	<u>60.7</u> 15
No.3	Standard curing	18.4	35.1	60.8
	30	<u>22.08</u> 20	<u>39.8</u> 13	<u>63.2</u> 4
	40	<u>27.1</u> 47	<u>40.4</u> 15	<u>65.0</u> 7
	80	<u>44.5</u> 142	<u>50.0</u> 42	<u>66.9</u> 10
No.4	Standard curing	30.6	41.4	70.3
	30	<u>36.1</u> 18	<u>46.7</u> 13	<u>72.4</u> 3
	40	<u>41.0</u> 34	<u>51.2</u> 24	<u>73.2</u> 4
	80	<u>50.5</u> 65	<u>59.6</u> 44	<u>74.5</u> 6

As we can see from Table 1, an increase of kinetics of concrete strength development during isothermal warming temperature increment can be observed for all compositions. The attained results analysis is illustrative of the largest increase (in relation to the specimens hardened under normal conditions) in ultimate compressive strength at day 1 for the specimens No.3 modified by "Relamix T-2" additive. The highest absolute values of ultimate compressive strength at days 1 and 28 can be observed in composition No.4 (compressive strength is increased by 13 % at day 1 and by 11 % at 28 days in comparison with No.3 specimens at isothermal warming temperature of 80°C). The attained results show the effectiveness of HMA of cement binder in the presence of superplasticizer in cooperation with the following ST upon criterion of increase of heave-weight concrete strength development.

The attained results helped to define dependences of curing time of heavy-weight concrete until its attainment of required strength grade on the concrete ST temperature of composition No.4 according to the mode received in part 2. The results of experimental investigations are shown in Table 2.

Table 2. Curing time of heavy-weight concrete until its attainment of required strength grade on the concrete ST temperature of composition No.4.

Concrete grade	Curing time for attainment of required concrete grade at isothermal warming temperature during ST (°C)			
	Standard curing	30 °C	40 °C	80 °C
B30	2 day	1.5 day	1 day	–
B40	7 day	4 day	2 day	1 day
B50	22 day	19 day	14 day	10 day
B60	–	–	–	28 day

As we can see from Table 2, curing time of heavy-weight concrete until its attainment of required strength grade can be drastically reduced by increasing isothermal warming temperature during ST. For example, the time of concrete strength grade attainment equal to B40 can be reduced by 6 days, strength grade attainment equal to B50 – by 12 days.

Substantial reduction of curing time of heavy-weight concrete until attainment of required strength grade is conditioned by increase of kinetics of concrete strength development and connected with special aspects of structure formation and hydrated formation of new growths. To detect such special aspects, XRDA and DTA of cement stone specimens were made. Fig. 1 shows diffractograms of cement stone specimens at day 1 (vertical axis – Bragg angles in degrees, horizontal axis – relative diffraction reflection of minerals in pulses per second).
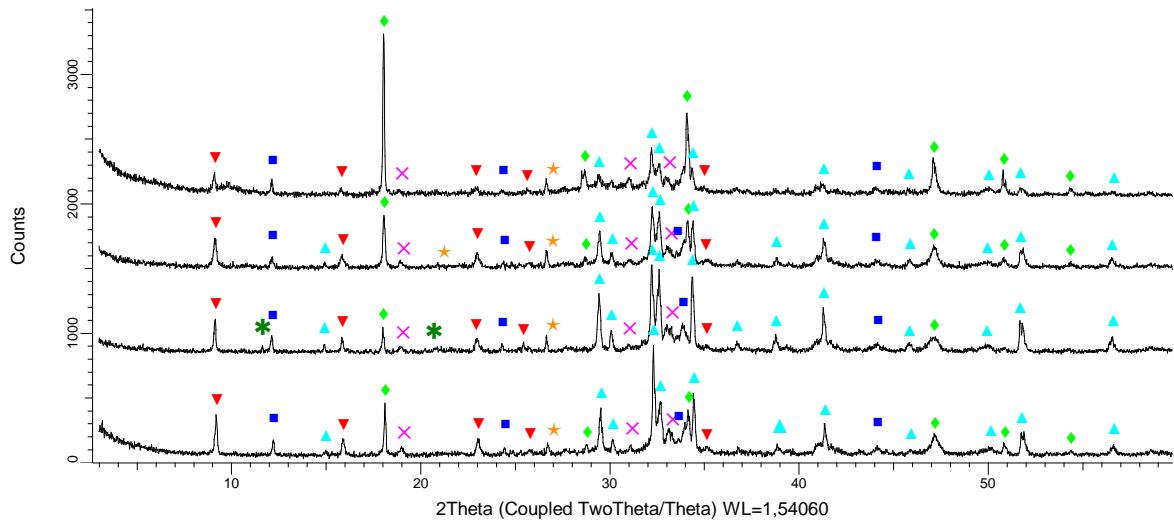

**Figure 1. Diffractograms of cement stone specimens made
of compositions No.1/S–4/S at day 1 (numeration bottom-up)**

Symbol legend: ★ – SiO_2; ▼ – $Ca_6Al_2(SO_4)_3(OH)_{12}*26H_2O$; ✕ – $Ca_2SiO_4\alpha$-Ca_2SiO_4; ▲ – Ca_3SiO_5; ◆ – $Ca(OH)_2$; ■ – $Ca_2(Al, Fe^{+3})_2O_5$; ✳ – $Ca_2SO_4*2H_2O$.

According to the findings most of ettringite is formed in specimen No.1/S, minimum – specimen No.4/S. Minimum of initial minerals of clinker $Ca_2SiO_4\alpha$-Ca_2SiO_4 and Ca_3SiO_5 (alite and belite) and maximum of hydrated calcium silicates (CSH) can be observed in the cement stone specimen made of the composition No.4/S, which is illustrative of fuller binder hydration providing high concrete strength. In the compositions No.1/S and No.2/S equitable quantity of initial minerals of clinker can be observed, which is illustrative of negative effect deficiency of "Relamix T-2" admixture on cement hydration kinetics and on structure formation processes of cement stone.

In Table 3 quantitative mineral composition of the cement stone specimens No.3/S and No.4/S is shown.

Table 3. Quantitative mineral composition of the cement stone specimens

No. of specimen	Quantitative mineral composition, %								Sum, %
	SiO_2	$Ca_6Al_2(SO_4)_3(OH)_{12}*26H_2O$	Ca_2SiO_4 α-Ca_2SiO_4	$Ca_2(Al, Fe^{+3})_2O_5$	$Ca(OH)_2$	Ca_3SiO_5	$CaCO_3$	$Ca_2SO_4*2H_2O$	
3/S	4.91	10.12	16.85	13.78	9,52	44.82	–	–	100
4/S	5.83	8.18	10.08	21.11	24.97	29.83	–	–	100

Data analysis shown in Table 3 provides evidence of intensification of binder hydration processes in the cement stone specimen No.4/S under curing in comparison with the specimen No.3/S, which agrees with research results [30], [31]. For instance, quantity of alite reduction by up to 1.5 times can be observed along with quantity increase of calcium hydroxide by a factor of 2.6.

Thermograms of the cement stone specimens of compositions No.3/S and No.4/S are shown in Fig. 2.
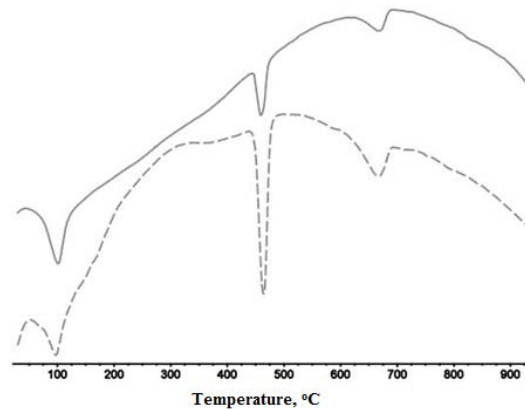

**Figure 2. Thermograms of the cement stone specimens of compositions No.3/S
and No.4/S at day 1 (numbering scheme from up to down).**

Substantial increase of endothermic effect in the interval of temperatures 440–480 °C that describes removal of chemically combined water from compounds of calcium hydroxide according to the formula: $Ca(OH)_2 \rightarrow CaO + H_2O$, provides evidence of its significant content in the cement stone specimen No.4/S. This confirms the results received during XRDA and agrees with research results [30].

4. Conclusion

1. The authors revealed an increase in kinetics of strength development in heavy-weight concrete test specimens during isothermal warming temperature increment. The findings are comparable with the results of fundamental investigations about the influence of curing temperature on kinetics of concrete strength development. The highest absolute values of ultimate compressive strength at days 1 and 28 can be observed in the concrete specimen received with previous HMA of cement in RPE together with "Relamix T-2" additive.

2. The synergistic effect of HMA of cement binder in the presence of "Relamix T-2" additive with the following ST was established, which makes it possible to significantly increase the early strength of concrete. As the result, at 80°C of isothermal heating on the first day of hardening, the concrete specimens obtained corresponded to B40 grade, which is justified by the lowest content of ettringite and initial clinker minerals ($Ca_2SiO_4\alpha$-Ca_2SiO_4 and Ca_3SiO_5), as well as the largest amount of calcium hydrosilicates (CSH) and hydroxides calcium ($Ca(OH)_2$). This indicates a more complete hydration of the binder causing an increased strength of heavy concrete.

3. The required isothermal warming temperature during ST of concrete based on cement binder under HMA in RPE in the presence of "Relamix T-2" additive was found, and duration of this cement binder hardening for concrete with B30 to B60 grades was also found while using components suitable for B25 grade heavy-weight concrete production.

4. As the result, positive influence of HMA of cement binder in the presence of superplasticizer followed by ST of the specimens based on it on processes of structure formation and on kinetics of heavy-weight concrete strength development was determined, which is of increased practical interest for the building materials industry.

References

1. Ansari, R., Egbelakin, T., Mbachu, J., Rasheed, E.O. Maximizing the productivity of the precast concrete plants by implementing the lean management system. The 5th Annual New Zealand Built Environment Research Symposium (NZBERS) 2017, E. Auckland, New Zealand. 2017. (October). Pp. 87–97.

2. Ray, B., Ripley, P., Neal, D. Lean Manufacturing A Systematic Approach to Improving Productivity in the Precast Concrete Industry. PCI Journal. 2006. 51(1). Pp. 62–71. DOI:10.15554/pcij.01012006.62.71.

3. Artamonova, O., Chernyshov, E., Slavcheva, G. Factors and mechanisms of nanomodification cement systems in the technological life cycle. Magazine of Civil Engineering. 2022. 109(1). DOI:10.34910/MCE.109.6.

4. Pohl, M., Obry, S., Zysk, K.-H. Operating experience with a vertical roller mill for grinding blastfurnace slag and composite cements. Cement international. 2012. 10(2).

5. Pimenov, S.I. The special aspects of structure formation of cement stone after hydromechanical activation of cement. Scientific journal of construction and architecture. 2019. 2(54). Pp. 77–88.

6. Prokopec, V.S. The influence of mechanical effect on activity of binder. Construction materials. 2003. 9. Pp. 28–29.

7. Fathollah, S. Applied Activation Techniques on Cement-Slag Mortars and Concretes.2012. 301 p.

8. Fathollah, S. Mechanical activation of cement–slag mortars. Construction and Building Materials. 2012. 26(1). Pp. 41–48. DOI:10.1016/j.conbuildmat.2011.05.001.

9. Shepelenko, T.S., Vatin, N.I., Zubkova, O.A. Hydration and structure formation of Chloride-Activated Cement Paste. Journal of Civil Engineering. 2020. 100(8). DOI:10.18720/MCE.100.9.

10. Pimenov, S.I. Heavyweight concrete based on hydromechanochemically activated binder. IOP Conference Series: Materials science and engineering. 2020. DOI:10.1088/1757-899X/890/1/012098.

11. Mukhametrakhimov, R.Kh., Galautdinov, A.R. Mechanoactivated gypsum cement puzzolan binder based on modified low-grade raw material. Izvestiya Kazanskogo gosudarstvennogo arhitekturno-stroitel'nogo universiteta. 2018. 1. Pp. 187–195.

12. Pimenov, S.I. Features of the structure formation of cement stone after hydro-mechanochemical activation of cement. Russian Journal of Building Construction and Architecture. 2019. 3(43). Pp. 46–58.

13. Kuznecova, T.V. High-early cement development at A.V. Volzhenskii studies. Construction materials. 2000. 2. Pp. 20–21.

14. Mukhametrakhimov, R., Galautdinov, A., Lukmanova, L. Influence of active mineral additives on the basic properties of the gypsum cementpozzolan binder for the manufacture of building products. MATEC Web of Conferences. 2017. 106. Pp. 03012. DOI:10.1051/matecconf/201710603012.

15. Kaprielov, S.S., Karpenko, N.I., SHejnfel'd, A.V., Kuznecov, E.N. Influence of organomineral modifying agent MB-50 on structure and deformability of cement stone and high-strength concrete. Concrete and reinforced concrete. 2003. 3. Pp. 2–7.

16. Dvorkin, L.I., ZHitkovskij, V.V. Method of calculation of cement-water ratio of steam-cure concrete. Construction-engineering journal. 2019. 6(90). Pp. 15–27. DOI:10.18720/MCE.90.2.

17. Travush, V.I., Karpenko, N.I., Erofeev, V.T., Vatin, N., Erofeeva, I.V., Maksimova, I.N., Kondrashchenko, V.I., Kesarijskij, A.G. Destruction of powder-activated concrete with fixation of destruction by a laser interferometer. Journal of Civil Engineering. 2020. 95(3). Pp. 42–48. DOI:10.18720/MCE.95.4.

18. Pedrosa, H.C., Reales, O.M., Reis, V.D., Paiva, M. das D., Fairbairn, E.M.R. Hydration of Portland cement accelerated by C-S-H seeds at different temperatures. Cement and Concrete Research. 2020. 129. Pp. 105978. DOI: 10.1016/j.cemconres.2020.105978.

19. Gusev, B.V. Nanopatterning of concrete materials. Industrial and civil construction. 2016. 1. Pp. 7–10.

20. Balczár, I., Korim, T., Hullár, H., Boros, A., Makó, É. Manufacture of air-cooled slag-based alkali-activated cements using mechanochemical activation. Construction and Building Materials. 2017. 137. Pp. 216–223. DOI: 10.1016/j.conbuildmat.2017.01.121.

21. Izotov, V.S., Mukhametrakhimov, R.Kh., Galautdinov, A.R. The way of gypsum cement puzzolan binder compounding. RU 2550630 C1. 2015.

22. Izotov, V.S., Mukhametrakhimov, R.Kh., Galautdinov, A.R. The way of gypsum cement puzzolan composition compounding. RU 2552274 C1. 2015.

23. Selyaev, V.P., Nizina, T.A., Balbalin, A.V. Analysis of mechanoactivation influence on properties of cement mixes with polyfunctional admixtures. Vestnik Volzhskogo regional'nogo otdeleniya Rossijskoj akademii arhitektury i stroitel'nyh nauk. 2014. (17). Pp. 203–208.

24. Smirnova, O.M. Compatibility of portland cement and polycarboxylate-based superplasticizers in high-strength concrete for precast constructions. Magazine of Civil Engineering. 2016. 66(06). Pp. 12–22. DOI:10.5862/MCE.66.2.

25. Dvorkin, L.I. The influence of admixtures of multifunctional modifier on properties of cement-ash fine grain concrete. Construction-engineering journal. 2020. 93(1). Pp. 121–133. DOI:10.18720/MCE.93.10.

26. Bily, P., Fladr, J., Chylik, R., Hrbek, V., Vrablik, L. Micromechanical characteristics of high-performance concrete subjected to modifications of composition and homogenization. Journal of Civil Engineering. 2020. 2(94). Pp. 145–157. DOI:10.18720/MCE.94.12.

27. Afanas'ev, D.A., Sarkisov, Yu.S., Gorlenko, N.P., SHepelenko, T.S., Cvetkov, N.A., Zubkova, O.A., Shevchenko, M.Y. Increase of pozzolanic activity of cement by ways of spin chemistry. Fundamental'nye issledovaniya. 2017. (7). Pp. 15–19.

28. Izotov, V.S., Sokolova, Y.A. Chemical additives for concrete modification. Paleotip, 2006. 244 p.

29. Galautdinov, A.R., Mukhametrakhimov, R.K. Set-retarding plasticizers for improving the effectiveness of gypsum-cement-pozzolan binders. ZKG International. 2018. (11). Pp. 52–57.

30. Berdov, G.I., Vinogradov, S.A., Bernatskij, A.P. The influence of steam curing on structure and properties of cement stone. Construction materials. 2017. (5). Pp. 81–85.

31. Mironov, S.A., Malinina, L.A., Malinskij, L.N., Kupriyanov, N.N., Berdichevskij, G.I., Markarov, N.A., Kajser, L.A., Chekhova, R.S., Dovzhik, V.G., Brusser, M.I. Guidelines for the heat treatment of concrete and reinforced concrete products. Moscow, 1974. 32 p.

Information about authors:

Sergey Pimenov, PhD in Technical Sciences
ORCID: https://orcid.org/0000-0002-2636-2822
E-mail: sergeypimenov12 @yandex.ru

Albert Galautdinov, PhD in Technical Sciences
ORCID: https://orcid.org/0000-0001-9999-6925
E-mail: galautdinov89 @mail.ru

Research article

UDC 539.3

DOI: 10.34910/MCE.118.10

Spatial stress-strain state of earth dams

D.J. Jurayev[1] , **N. Vatin[2]** , **T.Z. Sultanov[1]**, **M.M. Mirsaidov[1]** ✉

[1] "Tashkent Institute of Irrigation and Agricultural Mechanization Engineers" National Research University, Tashkent, Uzbekistan

[2] Peter the Great St. Petersburg Polytechnic University, St.Petersburg, Russia

✉ theormir@mail.ru

Keywords: earth dam, plane and spatial models, body forces, hydrostatic pressure, stress-strain state, variational equation, core indentation

Abstract. The study is devoted to the stress-strain state (SSS) of various earth dams analyzed using a spatial model. The article provides a detailed review of well-known scientific publications on the SSS assessment of dams. In this article, a mathematical model was developed to assess the SSS of earth dams using a spatial model based on the Lagrange variational equation, considering real geometry, properties of the material, and non-homogeneous design features of structures. A technique was developed for solving spatial problems to assess the SSS of earth dams by the finite element method using the program developed by the authors and the ABAQUS software. The adequacy of the mathematical model and the accuracy of the results obtained were verified by solving test problems. The SSS of the Ghissarak ($H = 138.5$ m), Sokh ($H = 87.3$ m), and Pachkamar ($H = 70.0$ m) earth dams under the action of body forces and hydrostatic water pressure was studied. It was established that the greatest displacements were observed on the crest and in the zone of the dam core; an account for nonhomogeneous design features significantly affects the resulting displacement field in the core zone; a spatial deformed state of the structure occurs near the banks; positive stress (not considered in a plane model) arises in a small area in the upper part of the core near the crest, caused by the crest indentation by the lateral surcharge.

Citation: Jurayev, D.J., Vatin, N., Sultanov, T.Z., Mirsaidov, M.M. Spatial stress-strain state of earth dams. Magazine of Civil Engineering. 2023. 118(2). Article no. 11810. DOI: 10.34910/MCE.118.10

1. Introduction

When designing earth dams in seismic regions, the problem of choosing a computational model for studying their SSS (SSS), and the dynamic behavior, in general, arises. In most cases, when studying such types of structures, simplified plane calculation models are used.

Simplified calculation models cannot describe many of the effects of the spatial work of real structures. This causes an overrun of the material and the inability to provide the required margin of safety and reliability of the structure.

The solution to this problem, considering the above factors, can be most fully and accurately obtained using numerical methods, for example, the finite element method (FEM) or the finite difference method (FDM) [1–6] using a spatial model of structures.

To date, there are a number of scientific papers devoted to the risk of damage and the assessment of the SSS of earth dams in plane and spatial settings.

Despite the increased requirements for dam safety in the process of design, construction, and operation, there is a certain risk of accidents in earth dams.

It was noted in [7] that the risk factors for earth-rock dam breach change with time during the operation period. At that, a static risk analysis limited to a certain time cannot satisfy the needs of a comprehensive assessment and early warning. Therefore, in this article, a model of a dynamic Bayesian network was developed to study the dynamic characteristics of the probability of the breach of earth dams.

In [8], the risks associated with the failure of a rock-earth dam were analyzed from two points of view: the probability of a dam failure and the associated loss of life. To calculate the probability of dam failure, an analysis based on fuzzy event tree method was proposed. The proposed method and model were applied to a dam of the reservoir in Jiangxi Province.

In [9], the results of studies on numerical modeling of the process of earth-rock dams breach were summarized. However, there is still a significant gap in the versatility of computer software and technology for visualizing the breach process of a dam. It is expected that more efforts should be made in the future to investigate a detailed, physically based numerical model of a rockfill dam, and more attention should be paid to the application of visualization technology in simulating the process of dam failure.

In [10], the assessment of deformations of a compacted embankment dam partially supported by a tailing dam was considered using a two-dimensional and three-dimensional finite element model with PLAXIS and TOCHNOG programs, respectively. The modelling was done to simulate the complete stage of dam construction with compacted embankment and filling of the dam reservoir from a tailings dump. The results obtained made it possible to present and understand the deformation mechanisms that occur during the construction of the overpass and the filling of the reservoir.

In [11], using a specially developed computer program, a study was conducted on the impact of the stressed state of the dam on the stability coefficients of its slopes under the main and special combination of loads. The method of circle-cylindrical sliding surfaces was used. The study was conducted for a rock-earth dam with a height of 133 m. It was found that under high seismic impacts due to the formation of zones of soil decompaction, the stability margin of the upper slope was lower than the normative one.

In [12], an attempt was made to give an insight into the 3D probabilistic analysis of a dam by examining the reliability of a real earth dam using field measurements and comparing the 3D results with the 2D ones. It was established that the use of a three-dimensional computational model in a probabilistic analysis could give smaller estimates of the probability of dam failure compared to an analysis based on a two-dimensional model. The results showed that the use of a coarse mesh could lead to an underestimation of the failure probability, especially for 3D cases.

In [13], a new method for analyzing the failure risk caused by surges, landslides, and coast instability was proposed, taking into account the spatial variability of material parameters. Based on the theory of random fields, a method for modeling the spatial variability of material parameters was proposed and the most dangerous sliding surfaces of the slope of the reservoir banks with a minimum value of safety factors were determined.

Reference [14] analyzes the data of time measurements of the horizontal and vertical displacements of the dam under its own weight and water pressure in the reservoir at Ikpoba River dam. The calculation and adjustment of each measurement were conducted at different time points and separately. Analysis of the results showed that nine points of the dam moved to a horizontal position, while at 10 points the horizontal displacements did not change. Vertical displacement occurred in seven points, while in 13 points the vertical displacements did not change, both outside and along the crest of the dam.

In [15], the seismic response of the Pacoima dam site was estimated by performing a three-dimensional analysis using the boundary element method. The nature of the displacement and force caused by the scattering of seismic waves in the dam section was assessed. The calculation results were compared with the registered ground motion. A 4.3-magnitude earthquake recorder was used to analyze site response at Pacoima Dam in 2001. Estimation of the displacement of various points of the dam on both sides of the canyon in time showed a decrease in the amplitude of motions with an increase in the height of the points under consideration. The results obtained showed that the spatial nature of the dam point motion with time was due to the effect of the relief along the canyon.

The results of studies of the stress state in the longitudinal and transverse directions of various sections of a concrete dam, taking into account the sequence of dam erection, were presented in [16]. The purpose of the study was to search for the optimal SSS of the dam in terms of the formation of the minimum stress state of concrete.

In [17], on the basis of detailed monitoring data of the project of the high arch dam, the characteristics of the spatiotemporal evolution and the relationship of deformation of the valley and the dam were analyzed. The effect of valley narrowing deformation on dam deformation was modeled using the 3D Finite Element Method (FEM). A model for monitoring the safety of the deformation of an arch dam was developed,

considering the impact of the deformation of the valley. At the same time, the deformation of the dam was expanded into components of water pressure, temperature, valley deformation, and time effect.

In [18], the models of the global system of the Koyna dam were constructed using the ABAQUS software, considering dam-reservoir-foundation interaction. Results of uncoupled models showed overestimated predicted stability and damage detection parameters in the dam. The effect of clay and stone foundations on the resistance to crack propagation in the dam was assessed.

In [19], the SSS and dynamic characteristics of models of two different earth dams were studied. The studies conducted have shown that for some types of earth dams it is possible to use a plane model for the preliminary assessment of the stress state. Some features of the stress state in the spatial case were revealed, indicating dangerous areas with the highest stresses, and the nature of eigen oscillations that cannot be described using a plane model.

In [20], the SSS of earth dams under the action of harmonic load was numerically studied. A two-dimensional problem for the cross-section of a dam was studied using the equation of state, considering structural changes in the moisture properties of soil. The problem was solved numerically – by the method of finite differences. The results were presented in the form of graphs and were analyzed.

The study in [21] presents a comparative method for assessing the SSS of earth dams under the action of static load using plane and spatial models. The results of the assessment of the SSS of earth dams using these models were presented. Some features of the stress state in the spatial case were revealed, which cause the emergence of dangerous zones with the highest stresses.

Articles [22, 23] give a detailed analysis of well-known publications devoted to various models and methods, and the results of studying the stress state of earth dams, taking into account the elastic-plastic properties of soil. A mathematical model, methods and algorithm were constructed to assess the SSS of earth dams in a plane statement under various impacts, with account for the elastic-plastic properties of soil, non-homogeneous structural features and the level of reservoir filling. The strength of earth dams with a height of 195 m was estimated using the Coulomb-Mohr strength theory.

The paper [24] presents the results of studies of natural oscillations and harmonic responses of the elements of the Kenyir dam power station in Terengganu (Malaysia). Dynamic characteristics of the power plant were determined using the ANSYS software. The amplitude-frequency response for the points of the structure was obtained in a large frequency range by applying a force to the structure. A real-scale 3D model of the Kenyir dam power station was built using Solid Works software and ANSYS software. The maximum deviation of 0.90361 m in the z direction was obtained at a resonant frequency of 5.4 Hz.

The results of explosive tests of the highest Masjed Soleiman earth dam in Iran were presented in [25]. During the in-situ tests, 23 eigenfrequencies and 16 dam vibration modes were determined. Along with this, a numerical analysis was conducted, and the comparison of its results with the test results showed that the best matches were obtained at low vibration modes for a dam model with a massive foundation, and at higher vibration modes, the best results were obtained for a dam model with a massless foundation.

In [26], for numerical simulation of the SSS of the impervious element in the body of the dam of the Gotsatlinskaya HPP, a mechanical model of soil materials taking into account the elastic-plastic properties of soil was used. Various numerical studies were conducted to assess the SSS of the systems under consideration.

The study in [27] presents the analysis data of methods for modeling the SSS of hydro-technical structures using computer systems. Quantitative evaluation was performed using the RSCI database in terms of both the number of publications and their citation, a qualitative analysis of abstract information, and full-text publications.

The study in [28] presents the results of the numerical simulation of the SSS of the diaphragm of a rock-fill cofferdam made of concrete by the method of bored piles. A feature of the operation of the diaphragm in the body of the cofferdam, which distinguishes it from the working conditions in the body of the dam, was revealed. The greatest danger to the strength of the concrete diaphragm is the bending strain. It was established that hydrostatic pressure causes displacement in the diaphragm, which, in turn, causes tensile stresses that are dangerous for concrete.

The research performed in [29] is devoted to the results of numerical studies of the SSS under seismic impact of an intensity of 9 points on a 16-m-high rock-fill cofferdam, the impervious element of which is a concrete diaphragm made of bored piles. It was revealed that the presence of a rigid concrete diaphragm in the center of the dam worsens the seismic resistance of the cofferdam and leads to the stability violation of the upper slope of the cofferdam.

The above review of studies on the SSS and dynamic behavior of earth dams in a spatial setting is very limited.

Despite their shortcomings and advantages, all these publications have their scientific and practical significance.

Therefore, the study and assessment of the SSS of earth dams in a spatial formulation, taking into account various features of the structure and comparison of the results with the ones obtained in a plane formulation, and determining the possibility of their use in assessing the strength of dams, are urgent problems.

The purpose of this study is to develop a mathematical model and methods for solving spatial problems and studying the SSS of various earth dams and assess the possibility of using a plane model of a structure, which can adequately describe the SSS of earth dams.

2. Methods

2.1. Mathematical model

A non-homogeneous spatial system is considered, i.e. an earth dam (Fig. 1a) occupying the volume $V = V_1 + V_2 + V_3$. The surfaces of the lower slope $\sum_3$ and the crest $\sum_2$ are stress-free. This system (Fig. 1a) is under the action of body forces $\vec{f}$; hydrostatic water pressure $\vec{p}$ is applied to surface $\sum_1$ on site S_p.

It is necessary to determine the components of the displacement vector, the strain and stress tensors in the body of the spatial system occurring under the action of its own weight and hydrostatic pressure of the reservoir water (Fig. 1a).
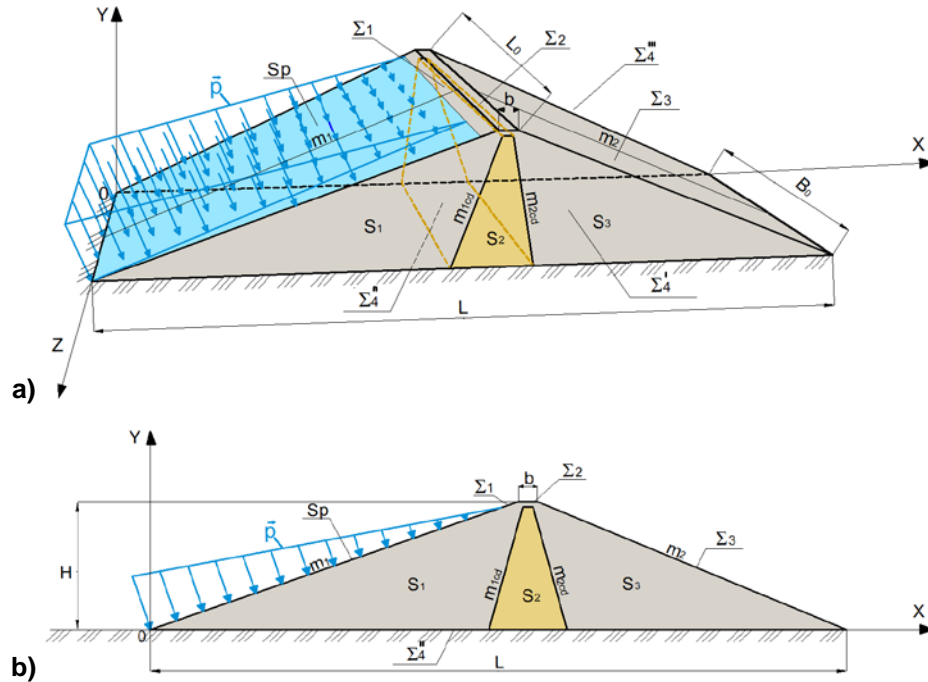
Figure 1. Non-homogeneous system: a) a spatial model of the mid-section of the dam; b) a plane model of the mid-section of the dam.

Here: $\sum_4^{''}$ is the area of foundation, $\sum_1$, $\sum_3$ are the areas of upper and lower slopes, respectively, $\sum_2$ is the crest area, $\sum_4^{'}$, $\sum_4^{'''}$ are the area of a dam connected to the mountain range, S_p is the area where the hydrostatic water pressure $\vec{p}$, acts, V_1, V_3 are the volumes of the upper and lower prisms, V_2 is the volume of the core, L_0 is the length of the dam crest, b is the width of the crest, B_0 is the width of the foundation along the alignment, L is the width of the foundation cross-section, m_1, m_2 are the upper and lower slope ratios, respectively, m_{1cd}, m_{2cd} are the slope ratios of upper and lower parts of the core.

To simulate the SSS occurring in a spatial system (Fig. 1a), the principle of virtual displacements is used; according to it, the sum of virtual works of all active forces acting on the system during virtual displacements is zero [5], i.e.:

$$\delta A = -\int\limits_{V} \sigma_{ij} \cdot \delta\varepsilon_{ij} dV + \int\limits_{V} \vec{f} \cdot \delta\vec{u} dV + \int\limits_{S_p} \vec{p} \cdot \delta\vec{u} d\sum = 0, \quad i, \ j = 1, \ 2, \ 3 \tag{1}$$

Physical properties of the body are described by the relations between stresses σ_{ij} and strains ε_{ij} in the following form [30]

$$\sigma_{ij} = \lambda\varepsilon_{kk}\delta_{ij} + 2\mu\varepsilon_{ij} \tag{2}$$

and the Cauchy relations [30]

$$\varepsilon_{ij} = \frac{1}{2}\left(\frac{\partial u_i}{\partial x_j} + \frac{\partial u_j}{\partial x_i} \right), \tag{3}$$

kinematic boundary condition is also used:

$$\vec{x} \in \sum\nolimits_{4}^{`} + \sum\nolimits_{4}^{``} + \sum\nolimits_{4}^{```} : \vec{u} = 0, \tag{4}$$

Here $\vec{u}$, ε_{ij}, σ_{ij} are the components of displacement vector, strain and stress tensors; $\delta\vec{u}$, $\delta\varepsilon_{ij}$ are the isochronous variations of the components of displacement vector and strain tensors; ρ is the density of the body material; $\vec{f}$ is the vector of body forces; $\vec{p}$ is the hydrostatic water pressure acting on the surface S_p; λ and μ are the Lame constants; $\theta = \varepsilon_{kk}$ is the volumetric strain; $\vec{u} = \{u_1, \ u_2, \ u_3\} = \{u, \ v, \ w\}$ are the components of displacement vector of the body point; $\vec{x} = \{x_1, \ x_2, \ x_3\} = \{x, \ y, \ z\}$ are the coordinates of the body point for solving spatial problems $i, \ j, \ k = 1, \ 2, \ 3$, and plane problems $i, \ j, \ k = 1, \ 2$.

It is necessary to determine in the body of the dam (Fig. 1a) the functions of displacements $\vec{u}(\vec{x})$, strains $\varepsilon_{ij}(\vec{x})$ and stresses $\sigma_{ij}(\vec{x})$ arising under the action of body $(\vec{f})$ and surface $(\vec{p})$ forces that satisfy equations (1)-(3) and boundary conditions (4) for arbitrary virtual displacements $\delta\vec{u}$.

The purpose of solving this problem is to determine how adequately the solution to the problem for a plane strain state for a given system (Fig. 1b) reflects the processes occurring in spatial systems (Fig. 1a).

The considered variational problem (1)–(4) is solved by the finite element method [31]. To solve the spatial problem, a finite element in the form of tetrahedra with 68493 degrees of freedom is used, and for the plane problem, triangular finite elements with 5734 degrees of freedom of the system are used.

The procedure of the finite element method allows us to reduce the considered variational problem (1)-(4) to a system of non-homogeneous high-order algebraic equations, i.e.:

$$\left[K\right]\{u\} = \{P\}, \tag{5}$$

Here: $\left[K\right]$ is the stiffness matrix for the considered body (Fig. 1); $\{u\}$ are the sought-for components of displacement vectors in the nodes of the finite element (after partitioning the body into finite elements); $\{P\}$ are the components of external (body and surface) forces acting on the nodes of the finite element.

When solving the above tasks, the computer calculation program developed by the authors was used for solving plane problems, besides, the well-known ABAQUS software was used to solve both plane and spatial problems.

3. Results and Discussion

To check the adequacy of the mathematical model and the accuracy of the results obtained, a test problem was solved using plane and spatial models.

The stress state of a rectangular long parallelepiped (Fig. 2) is considered under the action of distributed load P. The parallelepiped rests on an absolutely rigid and sliding base: $y = 0$; $u = 0$; $\sigma_{12} = 0$; $\sigma_{13} = 0$.
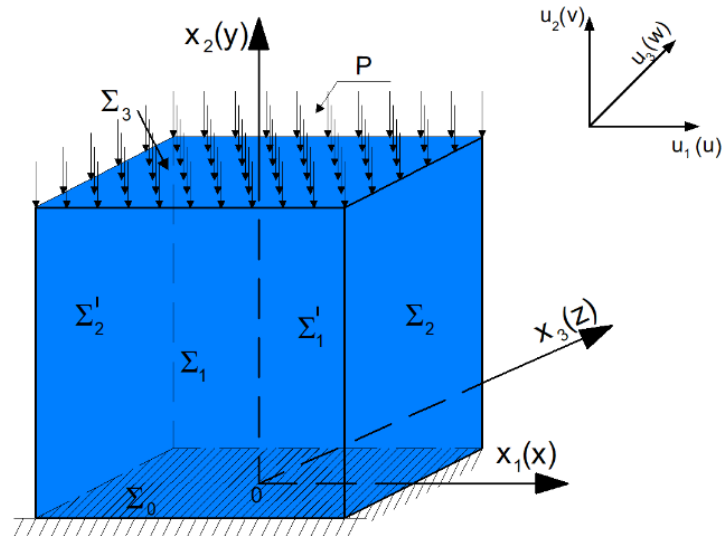

Figure 2. Deformable parallelepiped located on a sliding base.

It is necessary to determine the components of displacement vector $(u,\ v,\ w)$ and the components of stress tensor $(\sigma_{11},\ \sigma_{22},\ \sigma_{12},\ \sigma_{23},\ \sigma_{33},\ \sigma_{13})$ at any point of the body (Fig. 2).

The exact solution to this problem in a plane formulation is given in [32], and the solution has the following form:

$$u = \frac{\nu(1+\nu)}{E} x; \quad v = -\frac{(1-\nu^2)}{E} y; \quad \sigma_{22} = -P; \quad \sigma_{12} = \sigma_{21} = \sigma_{11} = 0.$$

The numerical solution to this problem was obtained using the computer program developed by the authors and the ABAQUS software using plane and spatial models, the results obtained were compared with exact solutions [32].

When solving this problem, the following initial data were used: $P = 1.0$; $a = b = 1.0$; $E = 1.0$; $\nu = 0.25$. A comparison of the numerical and exact solutions obtained using a plane model is given in Table 1, and the solutions obtained using spatial models are given in Table 2.

Table 1. Comparison of numerical and exact solutions of plane problems for some points of the body.

№	Coordinates of the point		Exact solution [32]		Numerical solution obtained by the authors	
	x	y	u	v	u	v
1	0.25	0.0	0.07812	0.000	0.07750	0.000
2	0.50	1.0	0.15625	−0.9375	0.15600	−0.9290
3	0.50	0.375	0.15650	−0.3515	0.15300	−0.3650
4	0.50	0.75	0.15650	−0.7031	0.15500	−0.7100
5	−0.375	1.0	−0.11718	0.9875	−0.09975	−1.000
6	−0.375	0.0	0.11718	0.000	−0.09375	0.000
7	0.840	0.66	0.02667	−0.6191	0.02651	−0.6184
8	−0.058	0.64	−0.01843	−06017	−0.01847	−0.6017

Table 2. Comparison of numerical and exact solutions obtained using spatial models.

№	Name	σ_{11}	σ_{22}	σ_{33}	σ_{12}	σ_{13}	σ_{23}
1	Exact solution [28]	0	−1	0	0	0	0
2	Numerical solution obtained by the authors	-55 E-18	−1	-222 E-18	-44 E-18	-266 E-18	-310 E-18

A comparison of the results obtained (i.e. numerical and exact solutions) given in Tables 1 and 2 shows that the numerical solutions in both cases were obtained with high accuracy. Consequently, the results obtained with these models and techniques make it possible to estimate the stress state of various bodies not only of a simple structure but also of rather complex structures with sufficiently high accuracy.

The SSS (SSS) of three different dams under the action of body forces and hydrostatic water pressure was studied using plane and spatial models: Ghissarak, Sokh and Pachkamar earth dams located on the territory of the Republic of Uzbekistan. When studying the effect of water on the SSS of the dams, various levels of reservoir filling were considered.

The SSS of these dams was studied using the above mathematical models and methods under the action of hydrostatic water pressure in the upstream head, the own weight of the structure, considering the actual physical and mechanical characteristics of soils and design features of the dams under consideration.

The hydrostatic water pressure in the upstream head of the dam was taken as an external influence, according to the following formula [33]:

$$\vec{p} = \rho_0 \cdot g \cdot h, \tag{6}$$

Here, ρ_0 is the density of water; h is the level of reservoir filling.

The study is conducted for three dams, built on the territory of highly seismic regions of Uzbekistan, with the following main geometric and design parameters:

1. **Ghissarak dam.** Rock-earth dam with a height of H = 138.5 m is located on the Aksu River in the Kashkadarya region of Uzbekistan. The laying of the upstream slope is m_1 = 2.2, and of the downstream slope m_2 = 1.9; the slope ratio of the loamy core is m_{1cd} = m_{2cd} = 0.15.

Retaining prisms are laid from rock mass with the following physical and mechanical parameters: E = 3600 MPa, specific gravity of soil γ = 1.9 tf/m³, Poisson's ratio v = 0.3. The core is laid from loam with physical and mechanical parameters: E = 2400 MPa, specific gravity of soil γ = 1.7 tf/m³, Poisson's ratio v = 0.35. The transition zone is laid of sandy-gravelly soil. The width of the dam crest is b = 16 m and length L_0 = 660 m, the width of the foundation is L = 634 m, and the width of the foundation along the alignment is B_0 = 140 m.

2. **Sokh earth dam** (H = 87.3 m high) was built on the Sokh River in the Fergana region, with the slope ratio m_1 = 2.5, m_2 = 2.2.

Retaining prisms are laid from pebbles with the following physical and mechanical parameters: E = 3550 MPa specific gravity of soil γ = 2.1 tf/m³, Poisson's ratio v = 0.35. The core is laid from loam with the slope ratio m_{1cd} = m_{2cd} = 0.25 and with physical and mechanical parameters: E = 2400 MPa, specific gravity of soil γ = 1.75 tf/m³, Poisson's ratio v = 0.35. The dam crest is b = 10 m wide and L_0 = 487.5 m long; the width of the foundation is L = 530 m, and the width of the foundation along the alignment is B_0 = 210 m.

3. **Pachkamar earth dam** with a height of H = 70 m was erected in the Kashkadarya region, with slope ratio m_1 = m_2 = 2.25.

Retaining prisms are laid from sand-pebbles with physical and mechanical parameters: E = 3600 MPa, specific gravity of soil γ = 2.25 tf/m³, Poisson's ratio v = 0.3. The core is laid from loam

with slope ratio $m_{1cd} = m_{2cd} = 0.5$ with physical and mechanical parameters: E = 2400 MPa, specific gravity of soil γ = 1.78 tf/m³, Poisson's ratio v = 0.35. The crest of the dam is b = 8 m wide and L_0 = 573 m long; the width of the foundation is L = 634 m, and the width of the foundation along the alignment is B_0 = 217 m.

The calculation results for these dams are the estimation of the components of displacement vectors u, v, w, the components of strain ε_{ij} and stress σ_{ij} tensors for all points of the structure.

The problem is solved using a spatial model and the results obtained are compared with the results of the problem obtained for a plane model in the case of a plane-deformed state of the central cross-section of the structure.

For the convenience of result analysis in the characteristic longitudinal and transverse sections of the dam, isolines (i.e., lines of equal values) of the components of displacements, strains, and stresses are plotted.

Figure 3 shows lines of equal values of horizontal (Fig. 3 a, c) and vertical (Fig. 3 b, d) displacements of the Ghissarak dam, obtained using the plane model under the action of its own weight and hydrostatic pressure of reservoir water, with completely filled reservoir (Fig. 3 c, d) and with empty reservoir (Fig. 3 a, b).
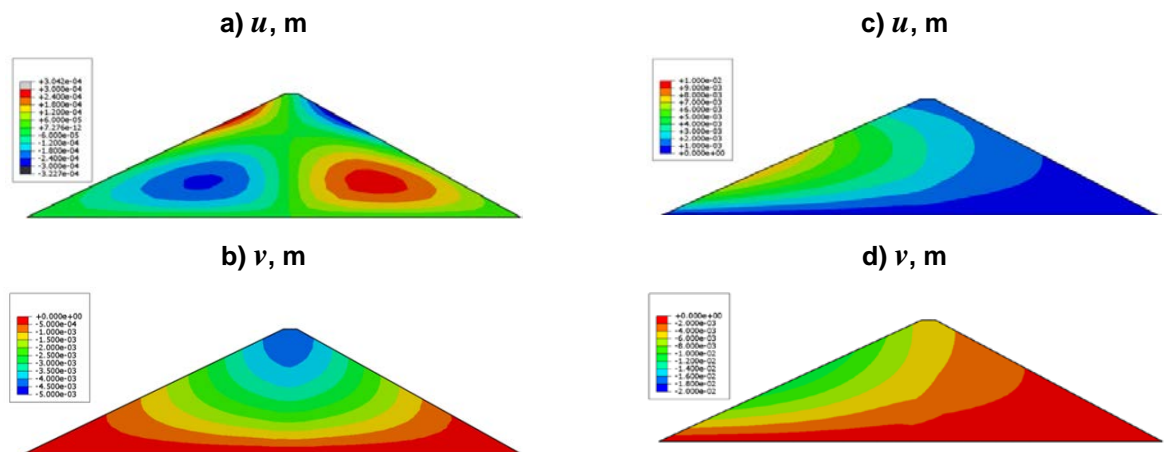
a) u, m   **c) u, m**

b) v, m   **d) v, m**

**Figure 3. Lines of equal values of displacement fields (u and v) of the Ghissarak dam
with completely filled reservoir (c, d) and with empty reservoir (a, b) obtained using a plane model.**

An analysis of the results obtained in a plane formulation (Fig. 3 a, b) shows that the displacements (absolute strain) of points in the body of the dam are approximately symmetrical with respect to the center of the dam. In the core of the dam, the values of horizontal displacements are close to zero, and their values increase towards the centers of the upper and lower retaining prisms. In this case, the displacement of the point in the vertical direction prevails. This is explained by the fact that the calculations were made considering only the own weight of the dam (Fig. 3 a, b). At the points located in the upper levels of the structure, the displacement values are greater than the ones at the points of the lower levels. The highest displacements are observed on the crest and in the zone of the dam core. Consideration of design features, namely the presence of a loam core significantly affects the displacement field only in the core zone.

The value of displacements (absolute strain) of the points of the Ghissarak dam profile (Fig. 3 c, d) in the case of consideration of hydrostatic pressure and body forces significantly changes the strain pattern in the upstream head. At that, the symmetrical distribution of strain relative to the center of the dam is violated in the body of the dam, and the absolute strain of the dam significantly depends on the level of water filling; this is especially evident when calculating the completely filled reservoir (Fig. 3 c, d). The same characteristic pattern was observed in the study of the SSS of the Sokh and Pachkamar dams.

Fig. 4 shows the distribution of equal values of vertical displacements (i.e., isolines) u_2 (along the x_2-axis) in the longitudinal section of the Ghissarak (a), Sokh (b), and Pachkamar (c) dams, obtained using a spatial model under the action of body forces.
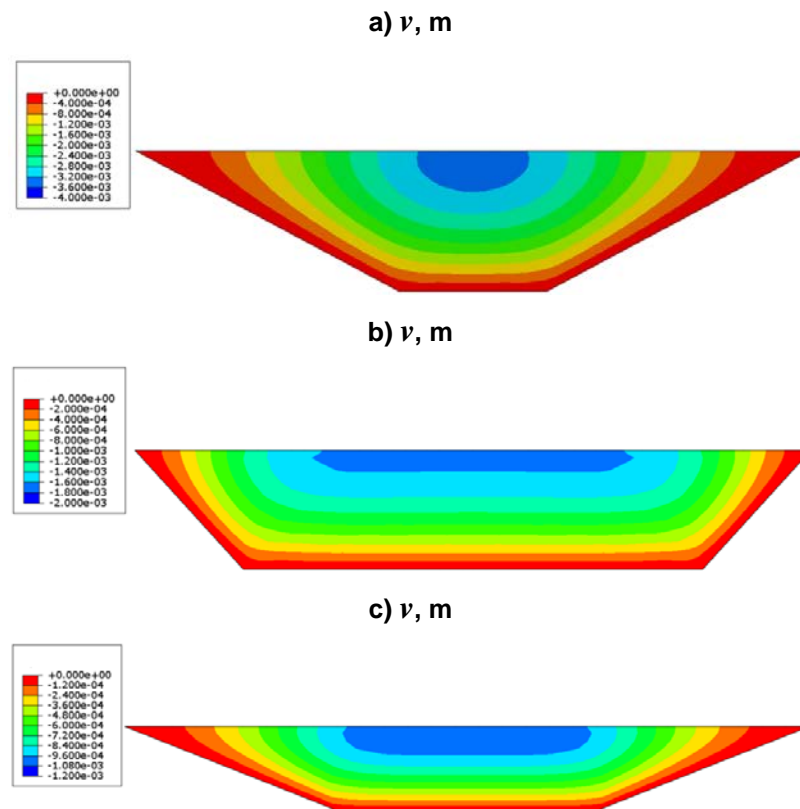
a) v, m

b) v, m

c) v, m

Figure 4. Isolines of equal values distribution of vertical displacements v – (along the y-axis) in the longitudinal section of the Ghissarak (a), Sokh (b), and Pachkamar (c) dams, obtained using a spatial model under the action of body forces

Analysis of the results obtained shows that, in all dams, the values of vertical displacements from the foundation of the dam to the upper levels gradually decrease, and the amplitude values of these displacements depend on the height of the dam.

Along with this, the results in Fig. 4 show that the distribution of equal values of vertical displacements in the longitudinal section of the dam in the Ghissarak dam (Fig. 4 a) differs significantly from the distribution of the same displacements in the Sokh (Fig. 4 b) and Pachkamar (Fig. 4 c) dams.

Having analyzed the distribution of vertical displacements along the length of the longitudinal section, we can see that in the Ghissarak dam the displacement changes dramatically from the middle of the longitudinal length to the left and right banks (Fig. 4 a). This shows that the banks have a significant influence on the dam strain since the geometric parameters of the dam are more consistent with a three-dimensional body.

As for the Sokh (Fig. 4b) and Pachkamar (Fig. 4 c) dams, the banks do not have a significant effect on strains (in the figures this is shown in blue color), i.e. here the use of a plane design model for calculations can be considered justified.

It can be concluded that when modeling the strain state of various dams, a plane calculation model does not always lead to a reliable result.

Figure 5 shows lines of equal values of horizontal σ_{11} (a), vertical σ_{22} (b) and tangential σ_{12} stresses of the Ghissarak dam under the action of its own weight and hydrostatic water pressure when the reservoir is completely filled. These results were obtained for all earth dams under consideration using plane and spatial models at different levels of reservoir filling with water.
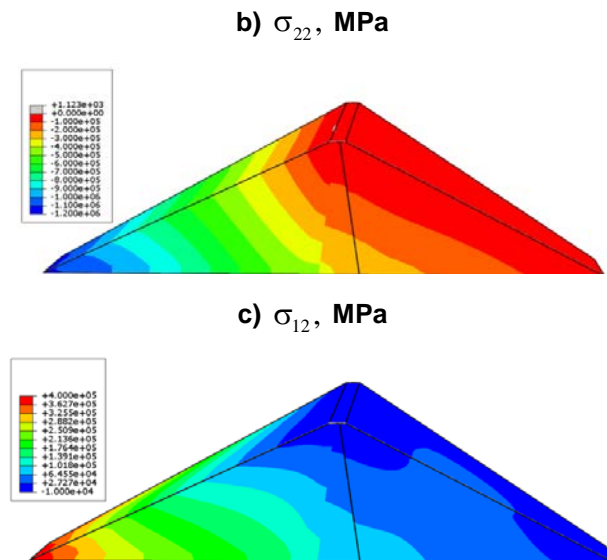
a) σ_{11}, MPa

b) σ_{22}, **MPa**

c) σ_{12}, **MPa**
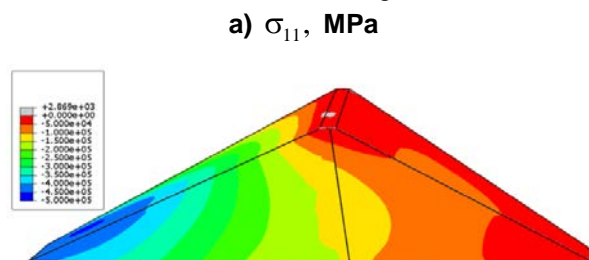
Figure 5. Lines of equal values of horizontal σ_x (a), vertical σ_y (b), and tangential τ_{xy} stresses for the Ghissarak earth dam according to a spatial model at completely filled reservoir.

The results obtained using the spatial model show that in the central part of the Sokh and Pachkamar dams, the conditions of plane strains of the theory of elasticity are observed since in this part there are only three strain components ε_{11}, ε_{22}, ε_{12} and they depend only on the coordinates of the point in the *x0y* plane.

A comparison of the results obtained for the central cross-section of the Ghissarak dam using a spatial model (Fig. 5) with the results obtained by a plane model shows that both statements give an almost similar qualitative pattern of the stress state, but the difference lies in the quantitative overestimation of the stresses obtained with the spatial model, namely, stresses σ_{11}, σ_{22} increase by more than 30 %, the overestimated value of shear stresses σ_{12} is up to 10 %, compared with the plane calculation. At that, calculations by the spatial model show the value of stresses σ_{11}, σ_{22} in the upper part of the dam with a positive value (Fig. 5 a, b), not observed using the plane model. The distribution of stresses along the longitudinal axis of the dam, obtained by the spatial model, shows that a more complex character takes place in the crest and near the end parts of the dam.

For example, in the Ghissarak dam, under the action of body forces, the upper part of the core near the crest rises, i.e. tensile strain occurs. This is apparently explained by the following process: the upper and lower surcharges of denser material and rigidity, press on the cores composed of less rigid material, this, in turn, intends the core and the upper part of the core near the crest rises (in Fig. 5, the positive value of the stress shows this phenomenon).

To verify this phenomenon, a test problem was solved, i.e., this problem was solved using a spatial model for two options of characteristics of the dam core material with modified Poisson's ratios $v = 0.499$ and $v = 0.001$. The result was as follows: at $v = 0.499$, the indentation of the upper part of the core near the crest increased considerably and at $v = 0.001$ no such indentation was observed.

In a certain part of the core near the crest of the Ghissarak dam, we observe the process of bulging of relatively soft soil of the core upwards, apparently due to the fact that the dam is located in a narrow alignment, the left and right banks of the alignment actively affect the SSS of the central part of the dam and soft soil of the core is pressed in.

This phenomenon manifests itself only when using a spatial calculation model. In contrast to the Sokh and Pachkamar dams, the Ghissarak dam is a three-dimensional body in terms of geometric dimensions. Therefore, such a pronounced effect is manifested only in the Ghissarak dam.

In the dams considered in the study, all components of the strain and stress tensor are manifested in the end parts; this shows a spatial SSS of the structures in this part of the dam.

This means that the use of a plane model to assess the SSS of earth dams does not always lead to an adequate description of the SSS occurring in them.

4. Conclusions

1. A detailed review of scientific publications devoted to the assessment of the SSS of various dams was given.

2. A mathematical model and methods were developed for assessing the spatial SSS of earth dams under various static effects, taking into account structural non-homogeneities and the actual geometry of structures using the variational principle and the finite element method.

3. The adequacy of the mathematical model and the accuracy of the results obtained were verified by solving a test problem and the spatial SSS of the Ghissarak, Sokh, and Pachkamar earth dams was studied using a spatial model under the action of body forces and hydrostatic water pressure.

4. It was stated that:

- the greatest displacements were observed on the crest and in the zone of the dam core; an account for the non-homogeneous features of the structure significantly affected the resulting displacement fields in the core zone, and a spatial deformed state of structures occurred near the banks;

- the SSS of real earth dams significantly depends on the commensurability of geometric dimensions of the retaining prisms and the slope ratios, and on the slopes of the dam banks;

- in the upper part of the core (in the central cross-section) of the Ghissarak dam calculated by the spatial model, the distribution pattern of vertical stresses σ_y and strains ε_y changes significantly, compared with the results obtained by the plane model.

- in a small area in the upper part of the core near the crest of the Ghissarak dam, positive stress arises due to the indentation of the core by side surcharges; this is apparently due to the fact that the dam is located in a narrow alignment, the left and right banks of the alignment actively affect the SSS of the central parts of the dam.

References

1. Zareckij, Ju.K., Lombardo, V.N. Statika i dinamika gruntovyh plotin [Statics and dynamics of earth dams]. M.: Energoizdat, 1983. 256 p. (rus)

2. Krasnikov, N.D. Sejsmostojkost' gidrotehnicheskih sooruzhenij iz gruntovyh materialov [Seismic resistance of hydro-technical structures made of earth materials]. M.: Energoizdat, 1981. 240 p. (rus)

3. Ljahter, V.M., Ivashenko I.N. Sejsmostojkost' gruntovyh plotin [Seismic resistance of earth dams]. M.: Nauka, 1986. 233 p. (rus)

4. Konstantinov, I.A. Dinamika gidrotehnicheskih sooruzhenij [Dynamics of hydro-technical structures]. Part 2. L.: Ed. LPI, 1976. 196 p. (rus)

5. Mirsaidov, M.M. Teorija i metody rascheta gruntovyh sooruzhenij na prochnost' i sejsmostojkost [Theory and methods for calculating earth structures for strength and seismic resistance]. Tashkent: Fan, 2010. 312 p. (rus)

6. Mirsaidov, M.M., Sultanov, T.Z. Ocenka dinamicheskoj prochnosti gruntovyh plotin s uchetom nelinejnogo deformirovanija [Evaluation of the dynamic strength of earth dams taking into account nonlinear deformation]. Tashkent: "Adabiyet uchkunlari", 2018. 258 p. (rus)

7. Li, Z., Wang, T., Ge, W., Wie, D., Li, H. Risk analysis of earth-rock dam breach based on dynamic bayesian network. Water. 2019. 11 (11). 2305. DOI: 10.3390/w11112305

8. Fu, X., Gu, Ch.Sh., Su, H.Zh., Qin, X.N. Risk Analysis of Earth-Rock Dam Failures Based on Fuzzy Event Tree Method. Int J Environ Res Public Health. 2018. 15 (5). 886. DOI: 10.3390/ijerph15050886

9. Zhong, Q., Shan, Y., Liu, J. Earth-Rock Dams' Breach Modelling. Dam Engineering. 2020. DOI: 10.5772/intechopen.92893

10. Sidnei Helder Cardoso Teixeira, Paulo Roberto de Paiva, Tennison Freire de Souza Junior, Eduardo Conte. Deformations on a Talings Dam Embankment Due to Its Heightening and Reservoir Filling. Civil Engineering. 2021. DOI: 10.21203/rs.3.rs-528290/v1

11. Sainov, M.P., Gapeev, D.S., Kudrjavcev, G.M. Vlijanie naprjazhjonnogo sostojanija kamenno-zemljanoj plotiny na ustojchivost' ejo [Influence of the stress state of a rock-and-earth dam on the stability of its slopes] Science of Science Internet Journal. 2017. 9(6).

12. Xiangfeng, G., Dias, D., Carvajal, C., Peyras, L., Breul, P. Three-dimensional probabilistic stability analysis of an earth dam using an active learning metamodeling approach. Bulletin of Engineering Geology and the Environment. 2022. 81. 40.

13. Kai, D., Zefa, L., Lu, X., Chen, Ch., Jinbao, Sh., Jiankang, Ch., Zhenyu, W. Analysis of dam overtopping failure risks caused by landslide-induced surges considering spatial variability of material parameters. Front. Earth Sci. 2021. 9-2021. DOI: 10.3389/feart.2021.675900

14. Ehiorobo, J., Ehigiator-Irughe, R. 3-d spatial analysis of deformation at Ikpoba dam from gps data. Journal of the Nigerian Association of Mathematical Physics. 2011. 19. Pp. 493–498.

15. Sohrabi, B.A., Isari, M., Tarinejad, R., Maghami, Sh. Topography effects in pacoima dam site using time-domain three-dimensional bem. Bulletin of earthquake science and engineering Spring. 2019. 6(1). Pp. 23–34.

16. Konstantinov, I., Kuzmin, S., Savchenko, A., Boychenko, P., Nagornya, D. Allowance for sequence of mass concrete dam erection on soils during its stress-strain analysis. MATEC Web of Conferences. 2016. 73(3). 01005. DOI: 10.1051/matecconf/20167301005

17. Zheng, F., Yaqi, L. Deformation characteristics and a safety monitoring model of high arch dam affected by valley narrowing deformation. 11th Conference of Asian Rock Mechanics Society IOP Conf. Series: Earth and Environmental Science. 2021. 861. 042040. DOI: 10.1088/1755-1315/861/4/042040

18. Nariman, N.A., Lahmer, T., Karampour, P. Uncertainty quantification of stability and damage detection parameters of coupled hydrodynamic-ground motion in concrete gravity dams. Struct. Civ. Eng. 2019. 13(2) .Pp. 303–323. DOI: 10.1007/s11709-018-0462-x

19. Mirsaidov, M.M., Toshmatov, E.S. Spatial stress state and dynamic characteristics of earth dams. Magazine of Civil Engineering. 2019. 89(5). Pp. 3-15. DOI: 10.18720/MCE.89.1

20. Khusanov, B., Khaydarova, O. Stress-strain state of earth dam under harmonic effect. E3S Web of Conferences. 2019. 97. 05043. DOI: 10.1051/e3sconf/20199705043

21. Sultanov, T.Z., Yuldoshev, B., Toshmatov, E., Yarashov, J., Ergashev, R., Mirsaidov, M. Strength assessment of earth dams. MATEC Web of Conferences. 2019. 265. 04015. DOI: 10.1051/matecconf/201926504015

22. Mirsaidov, M.M., Sultanov, T.Z., Yarashov, J.Y. Strength of earth dams considering elastic-plastic properties of soil. Magazine of Civil Engineering. 2021. 108 (8). Article No. 10813. DOI: 10.34910/MCE.108.13

23. Mirsaidov, M., Sultanov, T., Yarashov, J., Urazmukhammedova, Z. Estimation of the earth dam strength with inelastic soil properties. IOP Conference Series Materials Science and Engineering. 2020. 883. 012021. DOI: 10.1088/1757-899X/883/1/012021

24. Arbain, A., Mazlan, A.Z., Zawawi, M.H., MohdRadzi, M.R. Vibration analysis of kenyir dam power station structure using a real scale 3d model. Civil and environmental engineering reports. 2019. 29(3). Pp. 048–059. DOI: 10.2478/ceer-2019-0023

25. Jafari, M.K., Davoodi, M. Dynamic characteristics evaluation of Masjed Soleiman Dam using in situ dynamic tests. Canadian Geotechnical Journal. 2006. 43(10). Pp. 997–1014. DOI: 10.1139/t06-059

26. Prokopovich, V.S., Velichko, A.S., Orishchuk, R.N. Stress-strain state of an earth dam with a clay-cement-concrete diaphragm on the example of the earth dam of the Gotsatlinskaya HPP. News of the B.E. Vedeneev VNIIG. 2016. 282. Pp. 87–98.

27. Kulik, K.N. et.al. Analysis of modeling methods of the stress-strain state of the hydro-technical structures for reclamation purposes applying computer systems. Ekologiya & Stroitelstvo. 2018. 1. Pp. 21–26.

28. Sainov, M.P., Tolstikov, V.V., Tarasov, A.A. Study of the stress-strain state of rock-fill cofferdam concrete diaphragm at hinge connection with foundation. The Eurasian Scientific Journal. 2018. 10(1). URL: https://esj.today/PDF/75SAVN118.pdf [reference date: 29.03.2022].

29. Sainov, M.P., Shaimiardianov, I.R. (2018). Study of seismic stability of rock-fill cofferdam with concrete diaphragm. The Eurasian Scientific Journal, 2018. 3 (10). https://esj.today/PDF/03SAVN318.pdf

30. Aleksandrov, A.V., Potapov, V.D. Osnovy teorii uprugosti i plastichnosti [Fundamentals of the theory of elasticity and plasticity]. M.: Higher school, 1990. 400 p. (rus)

31. Bate, K., Vilson, E. Chislennye metody analiza i MKJe [Numerical methods of analysis and FEM]. Moscow: Stroyizdat, 1982. 448 p. (rus)

32. Rekach, V.G. Rukovodstvo k resheniju zadach po teorii uprugosti [Guide to solving problems in the theory of elasticity]. M.: Higher school, 1977. 215 p. (rus)

33. Chugaev, R.R. Gidravlika [Hydraulics]. Energoizdat, 1982. L. 203 p. (rus)

Information about authors:

Doniyor Jurayev,
ORCID: https://orcid.org/0000-0002-3281-3319
E-mail: DiyorbekMuhammadamir@mail.ru

Nikolai Vatin, Doctor of Technical Sciences
ORCID: https://orcid.org/0000-0002-1196-8004
E-mail: vatin@mail.ru

Tahirjon Sultanov, Doctor of Technical Sciences
ORCID: https://orcid.org/0000-0002-6498-5043
E-mail: tohir-zs@mail.ru

Mirziyod Mirsaidov, Doctor of Technical Sciences
ORCID: https://orcid.org/0000-0002-8907-7869
E-mail: theormir@mail.ru

Nonlinear vibrations and dynamic stability of viscoelastic anisotropic fiber reinforced plates

B.Kh. Eshmatov[1] iD *, **R.A. Abdikarimov**[2] iD *, **M. Amabili**[3] iD *, **N.I. Vatin**[4] ✉ iD*

[1] *Almalik Branch, National University of Science and Technology MISiS, Almalik, Uzbekistan*

[2] *Tashkent Institute of Architecture and Civil Engineering, Tashkent, Uzbekistan*

[3] *McGill University, Montreal, Canada*

[4] *Peter the Great St. Petersburg Polytechnic University, St.Petersburg, Russia*

✉ *vatin@mail.ru*

Abstract. Fiber-reinforced plastic composites are one of the most widely used composite materials because they balance well between properties and cost. Despite their widespread use in the aviation and automotive industries, there is currently a lack of effective mathematical models for their calculation under various dynamic loads. The research object of this work is an anisotropic viscoelastic fiber-reinforced simply supported rectangular plate. Two dynamic problems are considered: vibrations of the plate under the influence of a uniformly distributed static load; stability of the plate compressed in one direction. Within the Kirchhoff-Love hypothesis framework, a mathematical model was built in a geometrically nonlinear formulation, taking into account the tangential forces of inertia. By the Bubnov-Galerkin method, based on a polynomial approximation of the deflection and displacement, the problem was reduced to solving systems of nonlinear ordinary integro-differential equations. With a weakly singular Koltunov-Rzhanitsyn kernel with variable coefficients, the resulting system was solved by a numerical method based on quadrature formulas. By using experimental studies, considering the directions of the fibers, the values of the rheological parameters of some plastic materials (KAST-V and EDF) were obtained. The plate's dynamical behavior was investigated depending on the plate's geometric parameters, viscoelastic and inhomogeneous material properties. Results show the importance of taking into account the viscoelastic properties of the material when solving dynamic problems of anisotropic reinforced plates made of composite materials. In particular, when studying the problem of dynamic stability of an anisotropic reinforced plate made of KAST-V, the results obtained in elastic and viscoelastic formulations in some cases differ from each other by more than 20 %.

1. Introduction

Mechanics of composite materials has made great progress in recent years. The application of composite materials in engineering structures considerably improved structures' operational characteristics and, in several cases, create structures that could not be realized with traditional materials. Polymer

composite materials are widely used in diverse engineering fields. A large class of engineering structures relies on the use of composite materials and ceramics (for example, operating under conditions of high temperatures, contact pressures, etc.). Therefore, developing efficient algorithms for solving nonlinear problems of dynamis stability of shells, panels, and plates made of composite materials is important in today's industry.

The development of high-modulus and high-strength boron and graphite fibers joined together in plastic or metal binders arouses great interest in structural elements made of layers, each of which has different mechanical properties. In most cases, these composite materials include many layers of fibers with specific stacking sequences. The dimensions of the structural elements are such that each layer can be adequately modeled as a homogeneous anisotropic layer. Due to the unique characteristics of modern composite materials, interest in the problems of studying the dynamic behavior of anisotropic reinforced layered structures has not weakened in recent years.

An overview analysis of the using various natural fibers to form composites with various matrix materials and the effect of fiber length, chemical processing, and compositions on the dynamic mechanical characteristics of composites is available in [1].

An overview of works related to the study of typical functional capabilities of composites reinforced with natural fibers, including thermal insulation properties, biodegradable properties, and vibration damping properties, are given in [2]. This article concludes that composite materials that fully utilize their functionality rather than mechanical characteristics are important for the future development of composites reinforced with natural fibers. The analysis of some published literature on vibration damping applied to composites reinforced with natural fibers by experimental and numerical methods was carried out here. The effect of reinforcement with natural fibers on the thermosetting and thermoplastic polymer matrix vibration response was considered.

The article [3] investigates the effect of transverse normal and shear deformations on fiber-reinforced viscoelastic beams resting on two-parameter (Pasternak's) elastic foundations. The results were obtained using the refined theory of the sinusoidal shear deformation beam theory and compared with the results obtained using the simple theory of the sinusoidal shear deformation beam theory, the Timoshenko first-order shear deformation beam theory, and the classical Euler-Bernoulli beam theory.

The characteristics of free vibration of rectangular plates reinforced with continuous grading fiber (CGFR) based on elastic bases were studied based on the three-dimensional linear theory of elasticity and the theory of small deformations [4]. The foundation was described by the Pasternak model or a two-parameter model. The CGFR plate was simply supported at the edges and was assumed to have an arbitrary change in the volume fraction of the fiber in the direction of thickness. Displacement functions that satisfy simply supported boundary conditions were used to reduce the equilibrium equations to a set of coupled ordinary differential equations with variable coefficients, which in turn have been solved by differential quadrature (DQM) to obtain natural frequencies. Studies have shown that this method has a high convergence rate, stable numerical performance, and accuracy. The results for a CGFR plate with an arbitrary change in the volume fraction of the fiber in the thickness of the plate were compared with a discrete layered composite plate. They also showed that the use of CGFR plates with graduated volume fractions of fibers has advantages over traditional discretely laminated plates.

The static response of an inhomogeneous fiber-reinforced viscoelastic multilayer plate was investigated in [5] by using the first-order shear deformation theory. Several types of sandwich plates were considered, taking into account the symmetry of the plate and the thickness of each layer. In addition, two cases were considered depending on the viscoelastic material that enters the core or the surface of multilayer plates. To solve equations determining the bending of simply supported inhomogeneous fiber-reinforced viscoelastic multilayer plates, the effective modules method and Ilyushin's approximation method were used. Numerical calculations were carried out to study the effect of the time parameter on deflections and stresses at different values of the aspect ratio, the ratio of sides to the thickness, and the constitutive parameter.

Amabili [6] investigated the dynamic stability of orthotropic thick plates subjected to periodic uniaxial stress and bending stress, considering the inertia of rotation and transverse stress. Based on Bolotin's method, the regions of dynamic instability of plates reinforced with graphite and fiberglass were estimated by solving eigenvalue problems. The influence of material properties and load parameters on the instability region and the index of dynamic instability of orthotropic plates was discussed.

The distorted modes in geometrically nonlinear forced oscillations of angular layered circular cylindrical shells were investigated using the highest order Amabili-Reddy's shear deformation theory [7]. Harmonic forces were applied in the radial direction and simply supported boundary conditions were assumed. The equations of motion were obtained using an energy approach based on Lagrange equations,

which preserves dissipation. Numerical results were obtained using the method of pseudo-arc continuation and bifurcation analysis.

Anisotropic composite plates were evaluated with nanofiber-reinforced matrices (NFRM) [8]. Seven different loading conditions were considered: three for uniaxial loading, three for paired combined loading, and one with three combined loads. The anisotropy had a complete stiffness matrix of 6 by 6, which was satisfied and solved using the Galerkin algorithm.

The influence of some geometric and material parameters on the free vibrations of FML plates (fibrous metal laminates) was studied in [9]. For the analytical solution of the governing equations of the composite plate, the first-order shear deformation theory (FSDT) and the Fourier series method were used.

In combination with the elastic constitutive model and fiber direction, a plastic square plate with two materials (orthotropic and anisotropic) was simulated [10]. Anisotropic characteristics of the thermal field, pressure field, and vibration characteristics of fiber-reinforced PA66 were analyzed using simulation comparisons.

A new nonlinear model of vibrations of reinforced composite thin plates in a thermal environment was proposed [11] by introducing nonlinear thermal and amplitude fitting coefficients. Based on the classical laminated plate theory, the complex module approach, the power function, and the Ritz methods, dynamic governing equations in high-temperature environments for solving nonlinear natural frequencies, vibration characteristics, and damping parameters were obtained. Experimental tests of thin plates made of carbon-epoxy composite CF130 were carried out to test this model.

The article [12] presents a new nonlinear model of vibrations of composite plate structures with amplitude-dependent properties, taking into account the nonlinear characteristics of stiffness and damping by introducing the nonlinearity of the material into the dynamic modeling of fiber-reinforced composite thin plates. In this model, the elastic modulus and loss coefficients were expressed as a function of the strain energy density based on the nonlinear Jones-Nelson material model. These elastic moduli and loss coefficients were characterized as a function of the maximum dimensionless strain energy density using specific parameters at different excitation amplitudes. The power function fitting method was then used to determine the model's nonlinear stiffness and damping parameters. The nonlinear natural frequencies, vibration characteristics, and damping coefficients of the TC300 carbon-epoxy composite thin plate were calculated and measured in a case study.

A Fourier series method based on Mindlin theory and Hamilton's variational principle was proposed [13] for modeling and analyzing the vibration of composite multilayer plates with arbitrary boundary conditions, in which vibrational displacements were sought as a linear combination of a double series of Fourier cosines and auxiliary series functions. Three types of springs with constraints were introduced, and a vibration model was created by combining the Hamilton energy principle to create a general structural model of composite layered materials. The influence of boundary conditions, the laying angle, and the laying layer on the vibration characteristics were analyzed.

The nonlinear dynamic model in a thermal environment was established for modeling a reinforced composite structure made of thin plates [14]. This model uses Hamilton's principle in combination with the classical theory of layered plates, the complex modulus method, and the strain energy method. Nonlinear dependences between elasticity modules, Poisson coefficients, loss coefficients, and temperature change were expressed by the polynomial method. Dynamic equations in a high-temperature environment were derived to solve the inherent characteristics, dynamic characteristics, and damping parameters, considering temperature-dependent properties. The principle of identification of the corresponding fitting coefficients in the theoretical model was illustrated. An experimental test of a thin plate made of carbon-epoxy composite TC500 was carried out to substantiate the correctness of the obtained results. The results of the developed model and experimental tests showed good consistency.

The buckling of a multilayer composite reinforced plate, with porosity effects, was analyzed according to the theory of first shear deformation plates [15]. The properties of the plate material were considered orthotropic properties. Three different models were used considering the effect of porosity in a multilayer composite plate. The Navier procedure was used to solve the problem for a simply supported plate. The influence of porosity coefficients, porosity models, fiber orientation angles, and layer sequences on critical buckling loads was discussed.

Othman, Abouelregal, and Said [16] analytically studied the influence of variable thermal conductivity and initial stress on a reinforced transversely isotropic thick plate. A model of the problem of generalized thermoelasticity with phase delays in an isotropic elastic medium with temperature-dependent mechanical properties was developed. It was assumed that the upper surface of the plate was thermally insulated with a given surface load, and the lower surface of the plate rested on a rigid base. Normal mode analysis was used to obtain analytical expressions of displacement components, power voltage, and temperature

distribution. The results obtained in the presence and absence of initial stress and reinforcement were compared.

The nonlinear Jones-Nelson theory combined with the classical theory of layered plates by Yadav, Amabili, et al. [17]. The polynomial fitting method, the strain energy method, and a damping model of a fiber-reinforced composite thin plate were used. The methods and model were created considering the amplitude-dependent properties. The elastic modulus was expressed as the strain energy density function in this model. The loss coefficients in the longitudinal, transverse, and shear directions were expressed as functions of the excitation amplitude. Three plates made of carbon-epoxy composite TC300 were taken as research objects for the case study. One of them was used to determine the amplitude-dependent coefficients of loss coefficients in fiber-reinforced composites by combining the least-squares method with the polynomial fitting method. The other two plates were used to verify the correctness of the theoretical model. The developed model results, taking into account the amplitude dependence and experimental verification, showed good consistency.

The strict polynomial of a higher order in the thickness coordinate was introduced to develop a theory for doubly curved multilayer composite shells, considering the thickness and shear deformations [18]. By applying the condition of zero transverse normal and tangential stresses on the upper and lower surfaces of the shells, the theory of thickness deformation and shear of the third order with six kinematic parameters was derived. At the same time, the nonlinear terms in all kinematic parameters were preserved. The accuracy of the proposed theory has been tested for static and dynamic reference cases. The results obtained based on the proposed theory were compared with the results obtained using a more complex and computationally time-consuming nine-parameter theory. Isotropic and cross-layered circular cylindrical shells under the action of radial forces and pressure and nonlinear forced oscillations of the cross-layered shell under harmonic radial excitation were considered.

The vibrations of circular cylindrical shells made of a carbon nanotube (CNT) fiber-reinforced composite (CNT-FRC) were studied in a geometrically nonlinear formulation [19]. Vibrations were created due to radial harmonic force, and the process itself was considered viscous structural damping. Elastic properties of randomly distributed CNTs in a polymer matrix (i.e., hybrid matrix) were calculated according to the Eshelby-Mori-Tanaka/Voigt scheme to account for the effect of CNT agglomeration in a hybrid matrix. The resulting hybrid matrix was reinforced with aligned fibers to prepare the CNT-FRC shell plate; its effective properties were evaluated using the Halpin Tsai homogenization approach. The CNT-FRC shell was modeled using von Karman geometric nonlinearity and first-order shear deformation theory (FSDT). According to the Hamilton principle, nonlinear control partial differential equations (PDEs) of CNT-FRC shells were derived. These PDEs were discretized into ordinary differential equations (ODES) using the Galerkin method. The ODES were solved by the incremental harmonic balance (IHB) method combined with the arc length extension method to obtain the frequency-amplitude characteristic of the shell. The influence of various types of CNT agglomeration models, CNT mass fraction, agglomeration parameters, and the sequence of laying layered materials on frequency-amplitude curves corresponding to forced and free nonlinear oscillations of the CNT-FRC shell was studied in detail.

The main purpose of the study [20] was to determine the effect of fiber orientation on the reduction of applied voltage for modeling the structure of a dielectric elastomer and improving its mechanical characteristics. Based on the nonlinear continuum mechanics and large inelastic deformations, the defining relations and equations determining the behavior of viscoelastic dielectric elastomers under harmonic electrical load were extracted and analyzed in various states. The obtained numerical results, such as phase diagrams, frequency amplitudes, and oscillations, illustrate the dynamic behavior of an anisotropic dielectric elastomer with different fiber orientations. Hyperelastic and rheological models were used to consider the viscoelastic properties of the material in combination with electrical coupling.

The analysis of many experimental and fundamental studies shows that most composite materials have clearly pronounced viscoelastic properties [21–23].

Most researchers who have attacked the class of problems mentioned above have considered the solution of problems with such a mathematical statement in an elastic case. In these works, only some properties of construction materials were taken into consideration: the problems were solved either in a linear context or in elastic wave propagation was not taken into account. Even if the problems were solved using a viscoelastic formulation, in many cases, the viscoelastic characteristics of the material were only taken into account in a restricted context. In these cases, viscoelastic properties were addressed by employing the Voight model or by using exponential relaxation kernels. However, mathematical models of problems of viscoelastic systems based on these assumptions cannot describe real processes occurring in shell constructions in early times [21, 23]. The choice of an exponential kernel in calculations was not incidental. The systems of integro-differential equations obtained from the calculations were, by way of differentiation, reduced to the solution of ordinary differential equations, which in most cases used to be solved by the well-known Runge-Kutta's numerical method. To the present day, none of the existing

methods has allowed one to solve such problems with weakly singular kernels of the type of Koltunov's, Rzhanitsyn's, Abel's, Rabotnov's, and others [21, 23].

Badalov, Eshmatov, and Yusupov [24] developed the numerical method based on the use of quadrature rules, which makes it possible to solve a system of nonlinear integro-differential equations with weakly singular kernels of the type of Koltunov-Rzhanitsyn's, Abel's, and Rabotnov's. Verlan, Abdikarimov, and Eshmatov [25] modified this method. The method provides reasonably high accuracy of results, is universal, enables one to solve a wide class of dynamic problems in viscoelasticity, and is economical from computer time consideration. Based on this method, many numerical results have been obtained by Eshmatov, Mukherjee [26], Mirsaidov, Abdikarimov, Khodzhaev [27], and other researchers [28–31] that are in a general agreement with evaluable experiments' data.

This work aims to study the influences of the viscoelastic and anisotropic properties of a material on the dynamical behavior of the plate. For the first time, an integral model is used to consider the viscoelastic properties of materials of an anisotropic structure. The integral mode correctly describes the rheological processes occurring in the studied structure during the entire time. The presented mathematical model makes it possible to obtain sufficiently accurate solutions that are well combined with experimental results.

2. Materials and Methods

The classical Kirchhoff-Love theory is used to construct a mathematical model of the dynamic behavior of a plate made of a material having anisotropic viscoelastic properties under the influence of various external loads (Fig. 1).
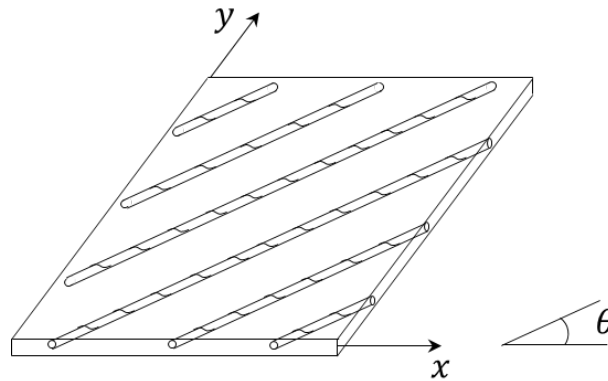

Figure 1. Anisotropic fiber-reinforced rectangular plate.

In this case, following [32–34], the stress and moment resultants have the form:

$$N_x = A_{11}^*\varepsilon_x + A_{12}^*\varepsilon_y + A_{16}^*\gamma_{xy} + B_{11}^*\chi_x + B_{12}^*\chi_y + B_{16}^*\chi_{xy},$$

$$N_y = A_{12}^*\varepsilon_x + A_{22}^*\varepsilon_y + A_{26}^*\gamma_{xy} + B_{12}^*\chi_x + B_{22}^*\chi_y + B_{26}^*\chi_{xy},$$

$$N_{xy} = A_{16}^*\varepsilon_x + A_{26}^*\varepsilon_y + A_{66}^*\gamma_{xy} + B_{16}^*\chi_x + B_{26}^*\chi_y + B_{66}^*\chi_{xy},$$

$$M_x = B_{11}^*\varepsilon_x + B_{12}^*\varepsilon_y + B_{16}^*\gamma_{xy} + D_{11}^*\chi_x + D_{12}^*\chi_y + D_{16}^*\chi_{xy},$$

$$M_y = B_{12}^*\varepsilon_x + B_{22}^*\varepsilon_y + B_{26}^*\gamma_{xy} + D_{12}^*\chi_x + D_{22}^*\chi_y + D_{26}^*\chi_{xy},$$

$$M_{xy} = B_{16}^*\varepsilon_x + B_{26}^*\varepsilon_y + B_{66}^*\gamma_{xy} + D_{16}^*\chi_x + D_{26}^*\chi_y + D_{66}^*\chi_{xy},$$

(1)

where A_{ij}^*, B_{ij}^*, D_{ij}^*, $i, j = 1, 2, 6$ are the operators having the following form:

$$A_{ij}^* \varphi = \sum_{k=1}^{K} \left(\overline{Q}_{ij}^* \varphi \right)_k \left(z_k - z_{k-1} \right), \quad B_{ij}^* \varphi = \frac{1}{2} \sum_{k=1}^{K} \left(\overline{Q}_{ij}^* \varphi \right)_k \left(z_k^2 - z_{k-1}^2 \right),$$

$$D_{ij}^* \varphi = \frac{1}{3} \sum_{k=1}^{K} \left(\overline{Q}_{ij}^* \varphi \right)_k \left(z_k^3 - z_{k-1}^3 \right),$$

$$\overline{Q}_{11}^* \varphi = \left[Q_{11} \cos^4 \theta + \frac{1}{2}(Q_{12} + 2Q_{66}) \sin^2 2\theta + Q_{22} \sin^4 \theta \right] \left(1 - \Gamma^* \right) \varphi,$$

$$Q_{11} = \frac{E_1}{1 - \mu_{12}\mu_{21}},$$

$$\overline{Q}_{12}^* \varphi = \left[\frac{1}{4}(Q_{11} + Q_{22} - 4Q_{66}) \sin^2 2\theta + Q_{12} \left(1 - \frac{1}{2}\sin^2 2\theta \right) \right] \left(1 - \Gamma^* \right) \varphi,$$

$$Q_{22} = \frac{E_2}{1 - \mu_{12}\mu_{21}},$$

$$\overline{Q}_{22}^* \varphi = \left[Q_{11} \sin^4 \theta + \frac{1}{2}(Q_{12} + 2Q_{66}) \sin^2 2\theta + Q_{22} \cos^4 \theta \right] \left(1 - \Gamma^* \right) \varphi,$$

$$\overline{Q}_{16}^* \varphi = \left[Q_{11} \sin \theta \cos^3 \theta - \frac{1}{4}(Q_{12} + 2Q_{66}) \sin 4\theta - Q_{22} \sin^3 \theta \cos \theta \right] \left(1 - \Gamma^* \right) \varphi,$$

$$\overline{Q}_{26}^* \varphi = \left[Q_{11} \sin^3 \theta \cos \theta + \frac{1}{4}(Q_{12} + 2Q_{66}) \sin 4\theta - Q_{22} \sin \theta \cos^3 \theta \right] \left(1 - \Gamma^* \right) \varphi,$$

$$\overline{Q}_{66}^* \varphi = \left[\frac{1}{4}(Q_{11} - 2Q_{12} + Q_{22}) \sin^2 2\theta + Q_{66} \cos^2 2\theta \right] \left(1 - \Gamma^* \right) \varphi, \tag{2}$$

$$Q_{12} = \frac{E_1 \mu_{21}}{1 - \mu_{12}\mu_{21}} = \frac{E_2 \mu_{12}}{1 - \mu_{12}\mu_{21}}, \quad Q_{66} = G_{12}, \quad \Gamma^* \varphi = \int_0^t \Gamma(t - \tau) \varphi(\tau) d\tau.$$

Here K is the number of plate layers, E_1, E_2 are the elastic moduli, G_{12} is the shear modulus, μ_{12}, μ_{21} are the Poisson ratios, θ is the angle characterizing the direction of the fibers relative to the axis OX, Γ^* is the integral operator with the relaxation kernel $\Gamma(t)$.

The relationship between the strains in the median surface ε_x, ε_y, γ_{xy}, χ_x, χ_y, χ_{xy} and displacements u, v, w in directions x, y, z, written by considering the von Kármán type of geometric nonlinearity, in the form [32–35]:

$$\varepsilon_x = \frac{\partial u}{\partial x} + \frac{1}{2}\left(\frac{\partial w}{\partial x}\right)^2, \quad \varepsilon_y = \frac{\partial v}{\partial y} + \frac{1}{2}\left(\frac{\partial w}{\partial y}\right)^2, \quad \gamma_{xy} = \frac{\partial u}{\partial y} + \frac{\partial v}{\partial x} + \frac{\partial w}{\partial x}\frac{\partial w}{\partial y},$$

$$\chi_x = -\frac{\partial^2 w}{\partial x^2}, \quad \chi_y = -\frac{\partial^2 w}{\partial y^2}, \quad \chi_{xy} = -2\frac{\partial^2 w}{\partial x \partial y}. \tag{3}$$

By substituting (1) and (3) into the equations of motion

$$\frac{\partial N_x}{\partial x} + \frac{\partial N_{xy}}{\partial y} + p_x = \rho \frac{\partial^2 u}{\partial t^2}, \quad \frac{\partial N_{xy}}{\partial x} + \frac{\partial N_y}{\partial y} + p_y = \rho \frac{\partial^2 v}{\partial t^2},$$

$$\frac{\partial^2 M_x}{\partial x^2} + \frac{\partial^2 M_y}{\partial y^2} + 2\frac{\partial^2 M_{xy}}{\partial x \partial y} + \frac{\partial}{\partial x}\left(N_x \frac{\partial w}{\partial x} + N_{xy} \frac{\partial w}{\partial y} \right) + \tag{4}$$

$$+ \frac{\partial}{\partial y}\left(N_{xy} \frac{\partial w}{\partial x} + N_y \frac{\partial w}{\partial y} \right) + q = \rho \frac{\partial^2 w}{\partial t^2},$$

the system of nonlinear integro-differential equations in partial derivatives that satisfies the boundary conditions of the problem (the edges are hinged) is obtained. The solution of this system is sought in the form:

$$u(x, y, t) = \sum_{m=1}^{M} \sum_{n=1}^{N} u_{mn}(t) \cos\frac{m\pi x}{a} \sin\frac{n\pi y}{b},$$

$$v(x, y, t) = \sum_{m=1}^{M} \sum_{n=1}^{N} v_{mn}(t) \sin\frac{m\pi x}{a} \cos\frac{n\pi y}{b}, \tag{5}$$

$$w(x, y, t) = \sum_{m=1}^{M} \sum_{n=1}^{N} w_{mn}(t) \sin\frac{m\pi x}{a} \sin\frac{n\pi y}{b},$$

where $u_{mn}(t)$, $v_{mn}(t)$ and $w_{mn}(t)$, m, $n = 1, 2, 3, \ldots$ are the unknown functions of time. Note that eq.(5) gives just an approximation of the in-plane displacements u and v for the given boundary conditions since additional functions should be retained. Substituting the approximating functions (5) into the resulting system of equations and performing the procedure of the Bubnov-Galerkin method, a system of nonlinear ordinary integro-differential equations is obtained. Further, this system is integrated using the numerical method based on the use of quadrature formulas [24, 25].

3. Results and Discussion

The calculations use the simplest and, at the same time, quite common weakly-singular Koltunov-Rzhanitsyn kernel having the form $\Gamma(t) = Ae^{-\beta t}t^{\alpha-1}\left(0 < \alpha < 1\right)$ as the relaxation kernel, where A, α, β are the rheological viscosity parameters determined from the experiments [21, 23]. Experimental studies have shown that weak singular functions most accurately describe the rates of relaxation processes [21, 23]. One of the difficulties of using singular kernels in numerical calculations is their singularity at $t = 0$. A detailed description of the numerical method based on the use of quadrature formulas is given in [24, 25]. The method allows solving systems of nonlinear integro-differential equations, preliminarily transforming singular kernels into regular ones.

In the calculations, the following parameters for plastics: KAST-V (E_1 = 25.5 GPa, E_2 = 14.91 GPa, G_{12} = 4.41 GPa, μ_{12} = 0.2, ρ = 1900 kg/m³) and EDF (E_1 = 24.5 GPa, E_2 = 18.04 GPa, G_{12} = 4.1 GPa, μ_{12} = 0.18, ρ = 1830 kg/m³) have been used. To determine the rheological parameters of the viscosity of these materials for different directions of reinforced fibers, the results of experiments given in [36] have been used. In this paper, based on the experiments, the rheological parameters of the viscosity for some glass-reinforced plastics, such as Textolite, KAST-V, SVAM, and EDF have been obtained. The parameters given in the paper correspond to the samples with directions of reinforced fibers of 0, 45, and 90 degrees relative to the OX axis. The values of the rheological viscosity parameters for samples with an arbitrary fiber orientation were obtained in [37] from experimental results by using interpolation formulas.

The problem of buckling of the anisotropic fiber-reinforced rectangular plate of thickness h with the sides a and b, subjected to dynamic compression along with one of the sides by force $P(t) = P_0 t$ (P_0 is the loading rate) was considered as follows. A problem with a similar mathematical formuation (elastic problem) was considered in [29].

Hereinafter, the following parameters of the plate are used in the calculations (unless otherwise specified): $a = b = 0.5\,m$, $h = 0.5\,sm$, $\theta = 45°$, $P_0 = 2\,MPa\,/\,s$.

As a criterion determining the critical time, it is assumed that the sag of the deflection should not exceed a value equal to the thickness of the plate [35]. In shell structures, the greater the critical time, the more stable it is to dynamic loads.

The following graphs correspond to the results obtained for the midpoint of the simply supported plate. On the graphs, m (meter) is the dimension for the deflection, and s (second) is for time.

Fig. 2 shows the influence of the material's viscoelastic properties on the behavior of anisotropic reinforced plates made from KAST-V and EDF. In general, KAST-V and EDF are materials with different viscoelastic properties. It is evident from the figure that considering viscoelastic properties results in a decrease of the critical time. Especially, it is apparent for plates from KAST-V (A = 0.0208), which have more viscoelastic properties than EDF. The difference in critical times for plates from elastic and viscoelastic KAST-V reaches up to 21 %, whereas this difference is about 2.4 % for plates from EDF. This result shows that it is crucial to consider viscoelastic properties in solving this type of problem.
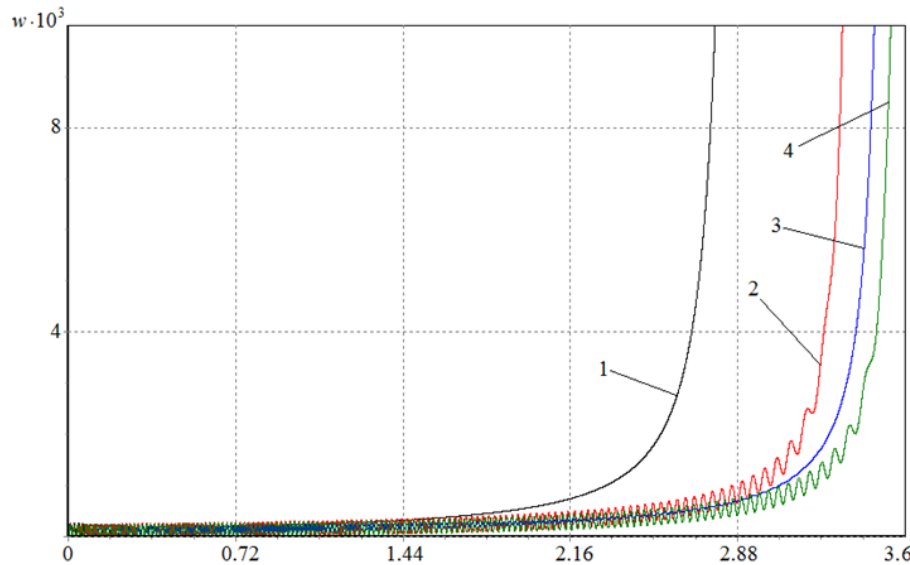

Figure 2. Effect of viscoelastic properties on the behavior of anisotropic reinforced plate from KAST-V (1 – viscoelastic, 2 – elastic) and EDF (3 – viscoelastic, 4 – elastic).

Fig. 3 shows a graph of the changes in the deflections of the midpoints of the plates of various thicknesses. The results show that an increase in plate rigidity due to increased plate thickness leads to a proportional increase in the critical time value.
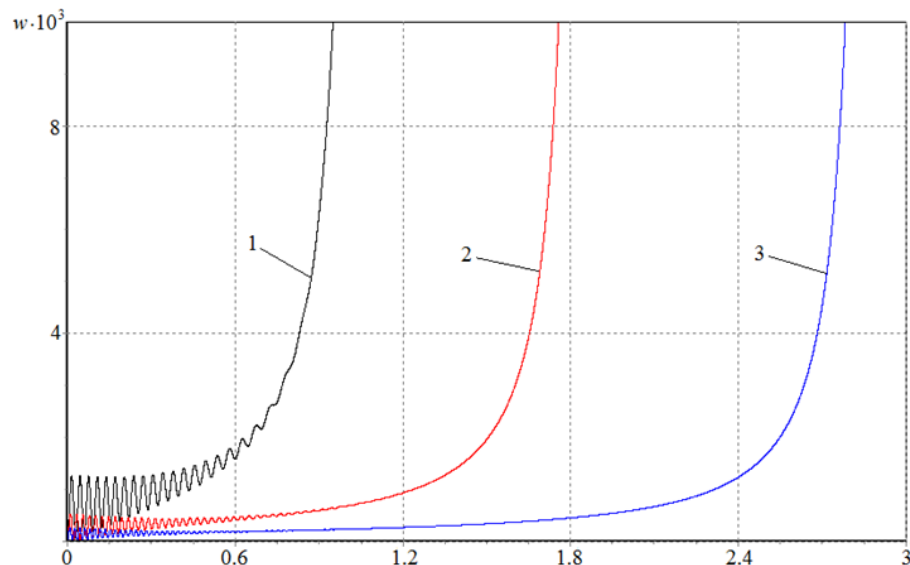

Figure 3. Dependence of the deflection on time for various values of the thicknesses of the plate: 1 – h = 0.3 sm; 2 – h = 0.4 sm; 3 – h = 0.5 sm.

Fig. 4 shows the analogous results for λ = 1; 1.2; 1.4. Here λ is the ratio of plate edges. Therefore, if λ = 1, then the plate is square-shaped. As it is clear from the graph, the increase in one of the edges of the plate increases the critical time.
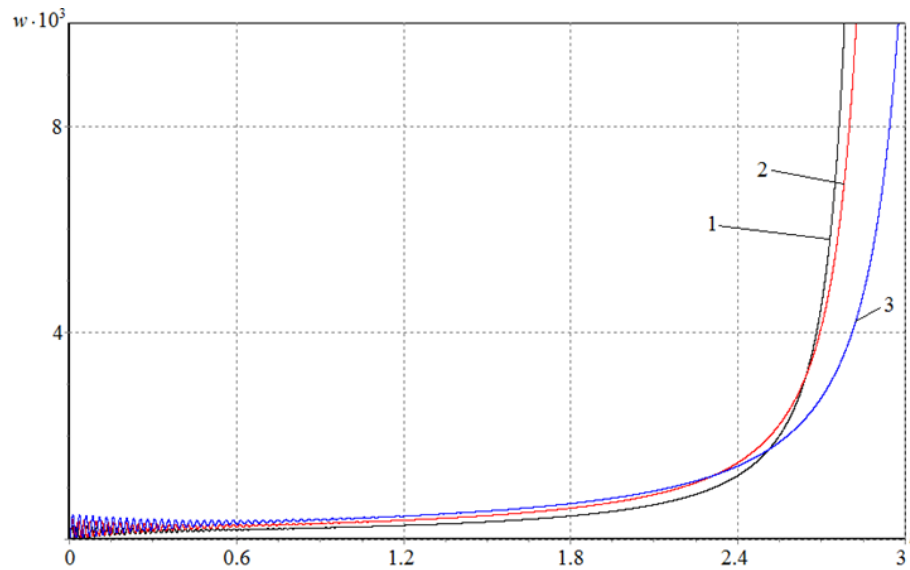

Figure 4. Dependence of the deflection on time for various values of the parameter
λ ($\lambda = a/b$) 1 − λ = 1; 2 − λ = 1.2; 3 − λ = 1.4.

The various curves in Fig. 5 correspond to cases of changes in the deflections of the midpoint of a reinforced rectangular plate at different loading speeds. It should be noted here that in all cases, at the initial moments of time, the changes in the deflections are oscillations that are harmonic in shape, which begin to increase rapidly at certain points in time.
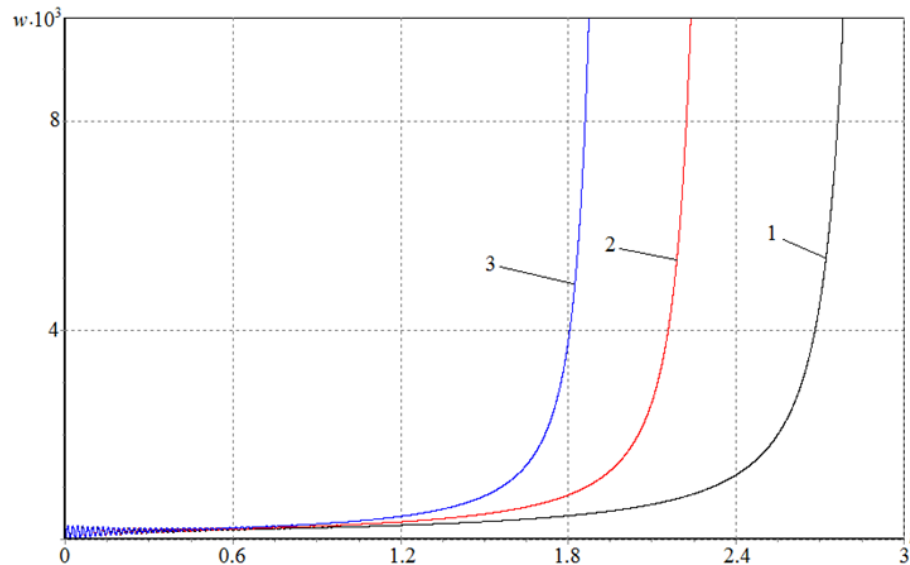

Figure 5. Dependence of the deflection on time for various values of the velocities of loading
1 − P_0 = 2 MPa/s; 2 − P_0 = 2.5 MPa/s; 3 − P_0 = 3 MPa/s.

Fig. 6 shows the influence of changes in the direction of the fibers of the reinforced plate on the dynamic process. As the angle of direction of the fibers increases from 0 to 45 degrees, an increase in the critical time is observed. The difference between the critical time values for single-layer plates with fiber directions of 0 and 45 degrees is 12 %.
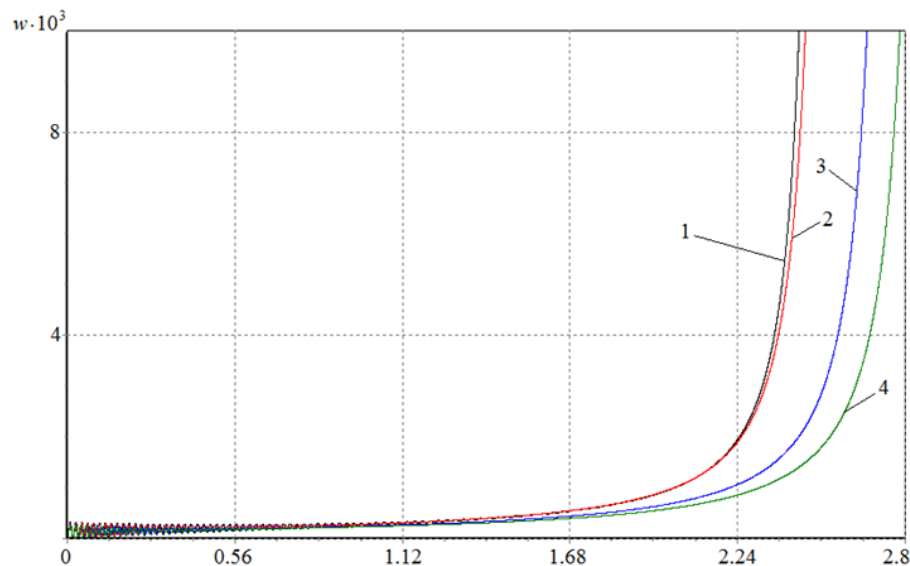
Figure 6. Dependence of the deflection on time for plates with different fiber orientations
1 – 0°; 2 − 15°; 3 − 30°; 4 – 45°.

As mentioned earlier, reinforced composites are a set (composition) of several reinforced layers, each with its own mechanical properties. Thus, by changing the composite structure, it is possible to create contractures, the behavior of which can be predicted in advance.

In this regard, the study of the behavior of laminated reinforced plates with different fiber orientations under the influence of axial compression is of particular interest. Fig. 7 shows the changes in the deflections of the midpoints of laminated reinforced plates made of KAST-V. Moreover, although all these plates have different fiber directions, their thickness is the same. The results show that for two-layer plates with fibers located at an angle of –45 degrees relative to the OX axis in one layer and 45 degrees in another, the critical time values are higher than the others. The layered fiber plate, parallel and perpendicular to the OX axis, has a lower critical time (i.e., it is less stable) than other plates with similar mechanical properties. The difference between the critical time values for the above two-layer plates is 13.3 %.
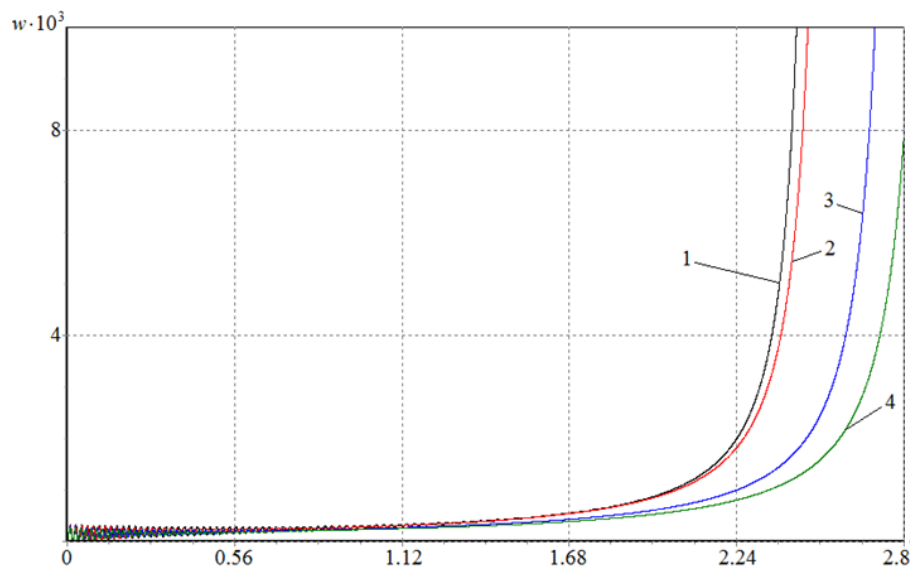

Figure 7. Dependence of the deflection on time for sandwich plates
with different fiber-orientated layers 1 – 0°/90°; 2 – 15°/-15°; 3 – 30°/-30°; 4 – 45°/-45°.

The results of studies of the behavior of reinforced plates for a wide range of changes in their mechanical, physical, and geometric parameters under dynamic compression of one of their sides are shown in Table 1.

Table 1. Critical time values for various geometric and physical parameters of anisotropic fiber-reinforced plates from KAST-V.

№	Geometrical parameters of the plate			Physical parameters		Number of layers	Fiber orientations	Critical time values		
	a, m	b, m	h, sm	q, Pa	v, MPa/s			Elastic problem	Viscoelastic problem	differ. (in %)
1	0.5	0.5	0.5	100	2	1	45°	3.2798	2.7117	21
2	0.6	0.5	0.5	100	2	1	45°	3.3358	2.7338	22
3	0.7	0.5	0.5	100	2	1	45°	3.5262	2.8604	23.3
4	0.5	0.5	0.4	100	2	1	45°	2.0238	1.6522	22.5
5	0.5	0.5	0.3	100	2	1	45°	0.9192	0.7680	19.7
6	0.5	0.5	0.5	200	2	1	45°	3.2110	2.5986	23.6
7	0.5	0.5	0.5	300	2	1	45°	3.1422	2.4982	25.8
8	0.5	0.5	0.5	100	2.5	1	45°	2.6268	2.1806	20.5
9	0.5	0.5	0.5	100	3	1	45°	2.1858	1.8248	19.8
10	0.5	0.5	0.5	100	2	1	0°	2.5984	2.3884	8.8
11	0.5	0.5	0.5	100	2	1	15°	2.7640	2.4038	15
12	0.5	0.5	0.5	100	2	1	30°	3.1046	2.6044	19.2
13	0.5	0.5	0.5	100	2	2	0°/90°	2.5984	2.3830	9
14	0.5	0.5	0.5	100	2	2	15°/-15°	2.7860	2.4152	15.4
15	0.5	0.5	0.5	100	2	2	30°/-30°	3.1396	2.6344	19.2
16	0.5	0.5	0.5	100	2	2	45°/-45°	3.3242	2.7496	20.9
17	0.5	0.5	0.5	100	2	3	45°/-45°/45°	3.2900	2.7168	21.1

The numerical results in the table show that taking into account the viscoelastic properties of structural materials leads to a significant decrease in the critical time value. In some cases, the differences in the results obtained by solving elastic and viscoelastic problems differ from each other by more than 20 %. It is also shown that the direction of the fibers in the structures also significantly affects the value of the critical time. For example, in two-layer plates, the fibers of which have directions at an angle of 45 and −45 degrees, the critical time values are greater than in a single-layer plate of the same thickness, the fibers of which are located at an angle of 45 degrees. This means that by changing the structure of the composite material, it is possible to create structures more resistant to dynamic loads.

4. Conclusions

The study of the dynamic stability of viscoelastic anisotropic reinforced plates, subjected to dynamic compression along with one of their sides, shows:

- It is important to consider the viscoelastic properties of the construction material. The results indicate that the difference in the critical time of elastic and viscoelastic problems is 21 % for plates made from KAST-V.

- The critical time values mainly depend on the direction of the reinforced fibers in each layer. In single-layer and double-layer plates, the difference in the critical time values depending on the direction of the reinforced fibers in places is 12 % and 13.3 %, respectively. An analysis of the results shows that the most resistant to these loads are double-layer plates with fibers located at an angle of −45 degrees relative to the OX axis in one layer and 45 degrees in another.

The results obtained in the work and the conclusions drawn on their basis allow us to accurately predict the dynamic behavior of plates made of reinforced plastics.

References

1. Ashok, R.B., Srinivasa, C.V, Basavaraju, B. Dynamic mechanical properties of natural fiber composites – a review. Advanced Composites and Hybrid Materials. 2019. 2 (4). Pp. 586–607. DOI: 10.1007/s42114-019-00121-8

2. Takagi, H. Review of Functional Properties of Natural Fiber-Reinforced Polymer Composites: Thermal Insulation, Biodegradation and Vibration Damping Properties. Advanced Composite Materials. 2019. 28 (5). Pp. 525–543. DOI: 10.1080/09243046.2019.1617093

3. Zenkour, A.M., Allam, M.N.M., Sobhy, M. Effect of Tranverse Normal and Shear Deformation on a Fiver-Reinforced Viscoelastic Beam Resting on Two-Parameter Elastic Foundations. International Journal of Applied Mechanics. 2010. 02 (01). Pp. 87–115. DOI: 10.1142/S1758825110000482

4. Yas, M.H., Aragh, B.S. Free vibration analysis of continuous grading fiber reinforced plates on elastic foundation. International Journal of Engineering Science. 2010. 48 (12). Pp. 1881–1895. DOI: https://doi.org/10.1016/j.ijengsci.2010.06.015

5. Allam, M.N.M., Zenkour, A.M., El-Mekawy, H.F. Bending response of inhomogeneous fiber-reinforced viscoelastic sandwich plates. Acta Mechanica. 2010. 209 (3). Pp. 231–248. DOI: 10.1007/s00707-009-0157-4

6. Chen, T.-J., Chen, C.-S., Chen, C.-W. Dynamic response of fiber-reinforced composite plates. Mechanics of Composite Materials. 2011. 47 (5). Pp. 549–560. DOI: 10.1007/s11029-011-9233-7

7. Amabili, M. Nonlinear vibrations of angle-ply laminated circular cylindrical shells: Skewed modes. Composite Structures. 2012. 94(12). Pp. 3697–3709. DOI: https://doi.org/10.1016/j.compstruct.2012.05.019

8. Chamis, C.C., Murthy, P.L.N. Vibration of Fiber Reinforced Anisotropic Composite Plates With Nanofiber Reinforced Matrices11-2010.

9. Ghasemi, F.A., Paknejad, R., Fard, K.M. Effects of geometrical and material parameters on free vibration analysis of fiber metal laminated plates. Mechanics & Industry. 2013. 14 (4). Pp. 229–238.

10. Wang, J., Zhang, J., Li, W., Xu, Z. Performance analysis of the plastic square plate based on the fiber reinforced PA66. MATEC Web Conf. 2016. 77.

11. Zu, X., Wu, H., Lv, H., Zheng, Y., Li, H. An Amplitude- and Temperature-Dependent Vibration Model of Fiber-Reinforced Composite Thin Plates in a Thermal Environment. 13 (7) 2020.

12. Li, H., Xue, P., Guan, Z., Han, Q., Wen, B. A new nonlinear vibration model of fiber-reinforced composite thin plate with amplitude-dependent property. Nonlinear Dynamics. 2018. 94 (3). Pp. 2219–2241. DOI: 10.1007/s11071-018-4486-5

13. Xue, Z.C., Li, Q.H., Wang, J.F., Lan, Z.X. Vibration Analysis of Fiber Reinforced Composite Laminated Plates with Arbitrary Boundary Conditions. Key Engineering Materials. 2019. 818. Pp. 104–112. DOI: 10.4028/www.scientific.net/KEM.818.104

14. Li, H., Wu, H., Zhang, T., Wen, B., Guan, Z. A nonlinear dynamic model of fiber-reinforced composite thin plate with temperature dependence in thermal environment. Composites Part B: Engineering. 2019. 162. Pp. 206–218. DOI: https://doi.org/10.1016/j.compositesb.2018.10.070

15. Yüksel, Y.Z., Akbaş, Ş.D. Buckling Analysis of a Fiber Reinforced Laminated Composite Plate with Porosity. Journal of Computational Applied Mechanics. 2019. 50 (2). Pp. 375–380. DOI: 10.22059/jcamech.2019.291967.448

16. Othman, M.I.A., Abouelregal, A.E., Said, S.M. The effect of variable thermal conductivity on an infinite fiber-reinforced thick plate under initial stress. Journal of Mechanics of Materials and Structures. 2019. 14 (2). Pp. 277–293. DOI: 10.2140/jomms.2019.14.277

17. Li, H., Niu, Y., Li, Z., Xu, Z., Han, Q. Modeling of amplitude-dependent damping characteristics of fiber reinforced composite thin plate. Applied Mathematical Modelling. 2020. 80. Pp. 394–407. DOI: https://doi.org/10.1016/j.apm.2019.11.048

18. Amabili, M., Reddy, J.N. The nonlinear, third-order thickness and shear deformation theory for statics and dynamics of laminated composite shells. Composite Structures. 2020. 244. Pp. 112265. DOI: https://doi.org/10.1016/j.compstruct.2020.112265

19. Yadav, A., Amabili, M., Panda, S.K., Dey, T., Kumar, R. Nonlinear damped vibrations of three-phase CNT-FRC circular cylindrical shell. Composite Structures. 2021. 255. Pp. 112939. DOI: https://doi.org/10.1016/j.compstruct.2020.112939

20. Allahyari, E., Asgari, M. Nonlinear dynamic analysis of anisotropic fiber-reinforced dielectric elastomers: A mathematical approach. Journal of Intelligent Material Systems and Structures. 2021. 32 (18–19). Pp. 2300–2324. DOI: 10.1177/1045389X21995879

21. Rabotnov, Y.N. Elements of Hereditary Solid Mechanics. First Thus edition . Moscow, MIR Publishers, 1980. 387 p. ISBN: 978-0714714578.

22. Bogdanovich, A.E. Non-linear Dynamic Problems for Composite Cylindrical Shells. New York, Elsevier, 1993. 312 p.

23. Koltunov, M.A. Choice of kernels in solving problems involving creep and relaxation. Polymer Mechanics. 1969. 2 (4). Pp. 303–311. DOI: 10.1007/BF00860064. URL: http://link.springer.com/10.1007/BF00860064 (date of application: 15.04.2021).

24. Badalov, F.B., Éshmatov, Kh., Yusupov, M. On certain methods of solving systems of integrodifferential equations encountered in viscoelasticity problems. Journal of Applied Mathematics and Mechanics. 1987. 51. Pp. 683–686.

25. Verlan, A.F., Abdikarimov, R.A., Eshmatov, Kh. Numerical modeling of nonlinear problems of the dynamics of viscoelastic systems with variable rigidity. Electronic modeling. 2010. 32 (2). Pp. 3–14.

26. Eshmatov, B., Mukherjee, S. Nonlinear Vibrations of Viscoelastic Composite Cylindrical Panels. Journal of Vibration and Acoustics. 2007. 129 (3). Pp. 285–296. DOI: 10.1115/1.2730532

27. Mirsaidov, M.M., Abdikarimov, R.A., Khodzhaev, D.A. Dynamics of a viscoelastic plate carrying concentrated mass with account of physical nonlinearity of material. Part 1. mathematical model, solution method and computational algorithm. PNRPU Mechanics Bulletin. 2019. 2019 (2). Pp. 143–153. DOI: 10.15593/perm.mech/2019.2.11

28. Eshmatov, B.Kh. Nonlinear vibrations and dynamic stability of viscoelastic orthotropic rectangular plates. Journal of Sound and Vibration. 2007. 300 (3–5). Pp. 709–726. DOI: 10.1016/j.jsv.2006.08.024.

29. Eshmatov, B., Abdikarimov, R., Komilova, Kh., Safarbayeva, N. Dynamics stability of anisotropic fiber-reinforced plate. E3S Web of Conferences 264. 05016 (2021). DOI: 10.1051/e3sconf/202126405016

30. Khodzhaev, D.A., Abdikarimov, R.A., Mirsaidov, M.M. Dynamics of a physically nonlinear viscoelastic cylindrical shell with a concentrated mass. Magazine of Civil Engineering. 2019. 91 (7). Pp. 39–48. DOI: 10.18720/MCE.91.4

31. Abdikarimov, R., Amabili, M., Vatin, N.I., Khodzhaev, D. Dynamic Stability of Orthotropic Viscoelastic Rectangular Plate of an Arbitrarily Varying Thickness. 11 (13) 2021.

32. Ashton, J.E., Whitney, J.M. Theory of laminated plates. Lancaster, PA, Technomic Publishing Co., Inc., 1970. 158 p.

33. Jones, R.M. Mechanics of Composite Materials. New York, McGraw-Hill Book Co., 1975. 450 p.

34. Whitney, J.M. Structural Analysis Of Laminated Anisotropic Plates. United Kingdom, Routledge, 2018. 356 p.

35. Volmir, A.S. The nonlinear dynamics of plates and shells. USA, Ohio, Foreign Technology Division Wright-Patterson Air Force, 1974. 543 p.

36. Tyuneeva, I.M. Relaxation characteristics of glass-reinforced plastics. Polymer Mechanics. 1970. 6. Pp. 492–494.

37. Eshmatov, B.Kh. Nonlinear Oscillations of a Viscoelastic Anisotropic Reinforced Plate. Mechanics of Solids. 2018. 53 (5). Pp. 568–572. DOI: 10.3103/S0025654418080101

Information about authors:

Bakhtiyor Eshmatov, *PhD*
ORCID: https://orcid.org/0000-0003-0198-6679
E-mail: ebkh@mail.ru

Rustamkhan Abdikarimov, *Doctor of Physical and Mathematical Sciences*
ORCID: https://orcid.org/0000-0001-8114-1187
E-mail: rabdikarimov@mail.ru

Marco Amabili, *PhD*
ORCID: https://orcid.org/0000-0001-9340-4474
E-mail: marco.amabili@mcgill.ca

Nikolai Vatin, *Doctor of Technical Sciences*
ORCID: https://orcid.org/0000-0002-1196-8004
E-mail: vatin@mail.ru